A 6-YEAR STUDY OF LONG PERIOD VARIABLE STARS IN THE GLOBULAR CLUSTER NGC 6388

Mohammad A. Aljassim

A Thesis

Submitted to the Graduate College of Bowling Green
State University in partial fulfillment of
the requirements for the degree of

MASTER OF SCIENCE

August 2017

Committee:

Andrew C. Layden, Advisor

John B. Laird

Dale W. Smith

ABSTRACT

Andrew C. Layden, Advisor

We present the results of a 6-year observing campaign conducted using the PROMPT-5 telescope to detect, identify and characterize long-period variable (LPV) stars in the metal-rich globular cluster NGC 6388. LPV stars are asymptotic giant branch stars that exist on a Mira-to-semi-regular-to-irregular continuum in terms of the regularity of their variable behavior. The long time-baseline was found to be fruitful in characterizing that aspect of LPV pulsation that cannot be captured in shorter campaigns. The ISIS image subtraction package is used for variability detection and the production of flux difference photometric data. We have also manually recovered known variable stars with use of their published celestial coordinates. Newly detected sources of variability were ranked on the basis of a variability index. An attempt was also made to quantitatively characterize the positions of LPV stars on the regularity spectrum with a newly defined regularity index, with partial success in the case of known variables. The known and new variables are discussed and characterized and their cluster membership determined with the use of a color-magnitude diagram and the variable's projected distance from the cluster center. Out of 72 variables studied, two of which were found to be duplicated in the literature, 56 are known variables that were detected or recovered. The LPVs detected number to 26 and 16 known and new, respectively. Almost all LPVs' periods are determined using the period-dispersion minimization method. A list of suspected variables, which require higher-resolution observations to confirm, amounts to an additional 22 stars. A period-luminosity relation is determined using the available literature data and our own data.

Dedicated to the love of my life, my shining star, Sara,

And to my sons, Ahmed and Abdulla,

My love for you inspires me, and your love for me sustains me.

ACKNOWLEDGMENTS

I wish to acknowledge my sincerest gratitude to my advisor, Dr. Andrew Layden, a great explainer whose wisdom and expertise have guided and pushed me to a level of knowledge and skill hitherto unimaginable to me. I am forever in his debt for the great opportunity of working on this project, introducing me to this wonderful field, and for his patience and understanding during the time I took to finish this work.

Much thanks and appreciation also go to Dr. Smith, a great educator whose course on stellar structure catapulted my understanding of stars to a level I had only dreamed of before, and whose friendliness and joviality I once thought was impossible to exist in an actual human being. I also wish to thank Dr. Laird, for his trust that I would finish this work, and his review of it is greatly appreciated and will be remembered.

Thanks to Dr. Xi, for the chance to participate in an endeavor that although did not come to fruition, it did impart useful skills that were applied in this work. Thanks also to the great students and professors at the department, without whom these last few years would have been a lot harder, and a lot less fun!

My deepest gratitude goes to my family back home, without whose support I wouldn't have been able to finish this work. I missed them dearly. And to my friends back home, for their hope and inspiration. And thanks to Jasem Mutlaq, for introducing me to astronomy.

The most credit for finishing this, a true shadow co-author, goes to my wonderful wife, Sara. Without her support, help, and sheer time and effort, all of my work would have been for naught!

TABLE OF CONTENTS

LIST OF FIGURES

LIST OF TABLES

CHAPTER 1. INTRODUCTION

Galactic globular clusters (GGC) are dense, gravitationally bound groups of stars that mostly populate the bulge and halo regions, and to lesser degree also the thick disk, of the Milky Way. Each cluster's constituent stars having formed from the same interstellar material at roughly the same time (that is, in a time range that is small relative to their lifetimes), the member stars of globular clusters have long served as important tests of models of star formation and stellar, chemical and physical evolution. By plotting the member stars of a particular cluster on a Color-Apparent Magnitude diagram (CMD) we can get a "snapshot" of the cluster members at a single point in time, with their distribution on the diagram differing mainly according to their initial masses (as they share roughly the same age, chemical composition and distance from Earth), as opposed to being spread along their own individual evolutionary tracks according to mass, age and metallicity.

By virtue of their age and diversity of member stars' initial mass, globular clusters include a lot of variable stars. Variable stars are broadly defined as stars that vary in magnitude and/or color. There are many types of variable stars, with different mechanisms responsible for their variability, but they can be separated into two types: extrinsic and intrinsic variables. Extrinsic variables are those stars whose variability is due to their rotation or the presence of an eclipsing companion star. The other type, intrinsic variables, exhibit variability due to internal conditions related to their composition and evolutionary history, and are ideal "special-case" tests for models of stellar structure, behavior and history. Therefore, by acquiring observational data on them we can inform and constrain those models.

Pulsating variable stars are those intrinsic variables whose change in luminosity results from changes in their radii due to internal processes. These stars' mass, age and (to a lesser

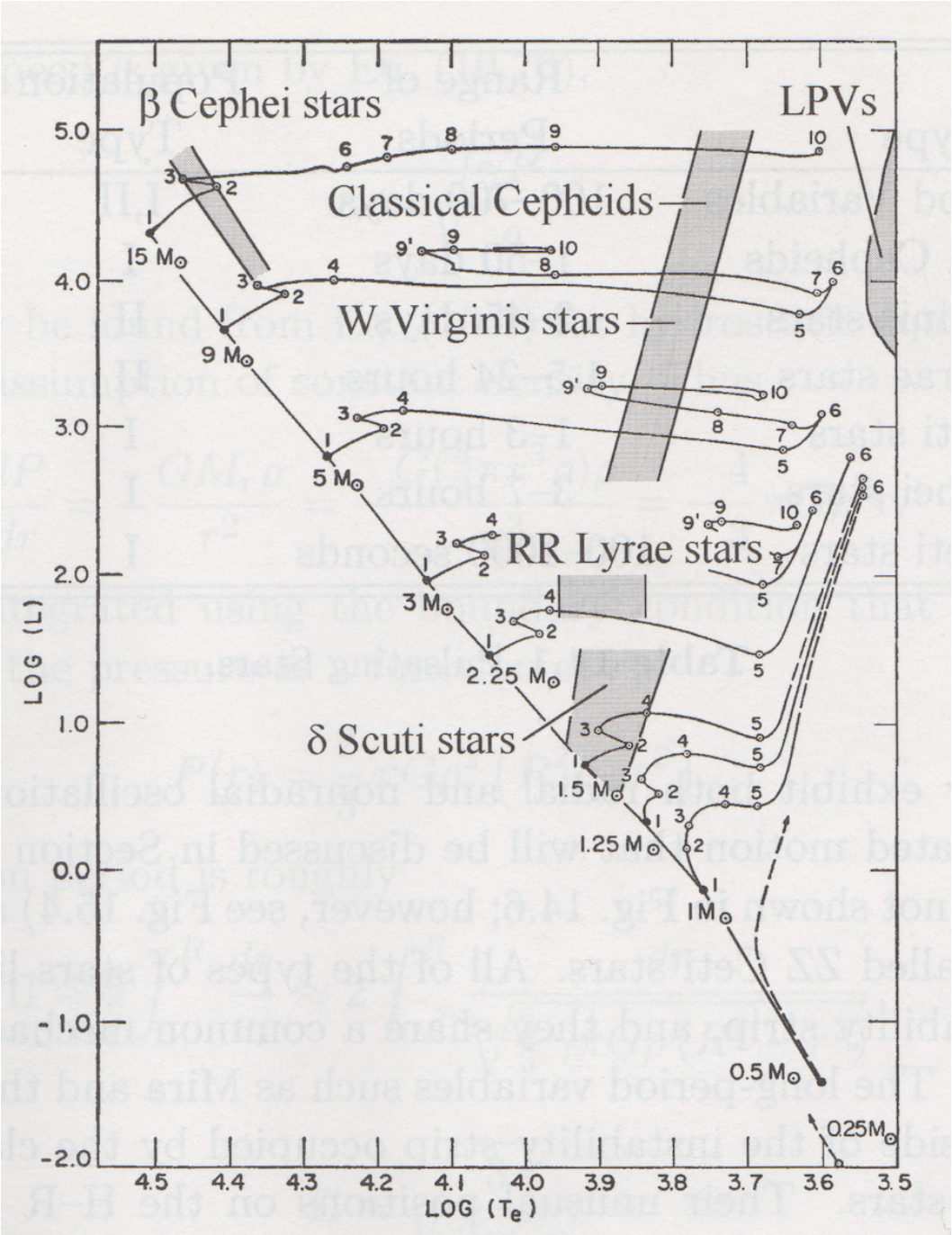

Figure 1.1: HR Diagram with shaded regions denoting pulsating variability. Note regions where LPVs, W Virginis and RR Lyrae variables are located. Evolutionary tracks are incomplete for low mass stars. Source: Ostlie and Carroll, 1996.

extent) metallicity is such that there exists a layer in their atmosphere that alternately turns opaque and transparent in response to high and low pressure respectively as the star pulsates (the kappa mechanism, Ostlie and Carroll (1996)). This alternately traps and releases radiant energy, leading to a cyclic expansion and contraction of the star's atmosphere, with different variable types having different periodicity, regularity and amplitude.

A period is defined as the time required for the star to undergo a pulsational cycle: that is to say, to go from the maximum (or minimum) magnitude, to the next maximum (or minimum) magnitude, and regularity is how consistently the timing and shape of the light curve remains from cycle to cycle. There are regions of instability on the HR diagram where stars exhibit variable behavior (see Figure 1.1), as these regions correlate star luminosity and surface temperature with the internal conditions conducive for pulsation. Of the stars classified in this research, all short-period variables (SPV) were of the Population II Cepheid (P2C) or RR Lyrae (RRL) type, which inhabit the Instability Strip. The long-period variable (LPV) stars inhabit the region correlated with cool giants or supergiants, typically around the red giant branch (RGB) or the asymptotic giant branch (AGB) stellar evolution phase of low- and intermediate-mass stars ($0.5 - 10\ M_{\odot}$).

LPV stars are the variables of special interest to us and, due to the old age and stellar mass variety of GGCs, we can study and characterize many of them by observing one globular cluster while also using information about the cluster's age, distance and chemical composition to gain more understanding about individual member stars' current evolutionary stage than if they were studied separately. Conversely, it is also possible that by documenting and understanding a GGC's member stars' properties, we can gain new insight on the GGC itself.

LPV stars are pulsating variables with long periods of oscillation; a cycle of magnitude change can range from 20 to 2000 days, longer than the shorter, and much better studied, periods of SPV stars. Their pulsational properties can be observed and, combined with their luminosities and color temperatures, are used to characterize and classify them into distinct types: Mira, Semi-regular, and Irregular variables. Gaining more detailed and longer-baseline data on these different types can help further our understanding of their behavior.

The most famous of the LPVs, Miras are cool (~3000 K) red giants, and display a relatively uniform periodicity and regularity in their light curves: when their magnitude is plotted against time, the resulting plot is roughly sinusoidal in nature. The regularity is not absolute, as variations exist cycle-to-cycle: amplitudes and periods change, the former commonly caused by a change in the maximum magnitude of a cycle (see Figure 1.2). As defined by the General Catalogue of Variable Stars (GCVS), their periodicity can range from 80 to 1000 days, and exhibit amplitudes in their variability in excess of 2.5 mag in the V-band. As with most pulsating variable stars, their amplitudes are smaller in longer wavelength passbands, such the near-infrared I-band; their I-band amplitudes are usually less than 2.5 mag (GCVS, 2009). This variability is due to their radial pulsations, which induces these cool red giants to shed their mass. They are related to the semi-regular and irregular LPVs as well, in that they are all RGB, AGB or post-Asymptotic Giant Branch (pAGB) (Sterken and Jaschek, 1996) red giants, and lie on a continuum with respect to regularity and periodicity. Mira LPVs themselves are found on the luminous end of the AGB as plotted on an HR diagram (Sterken and Jaschek, 1996), the next step in their evolution being a planetary nebula by continuous shedding of their atmosphere. Consequently, they are very bright, very large, and spend very little time as a Mira. The

relatively short time spent in this evolutionary stage is therefore of great interest (Sterken and Jaschek, 1996).

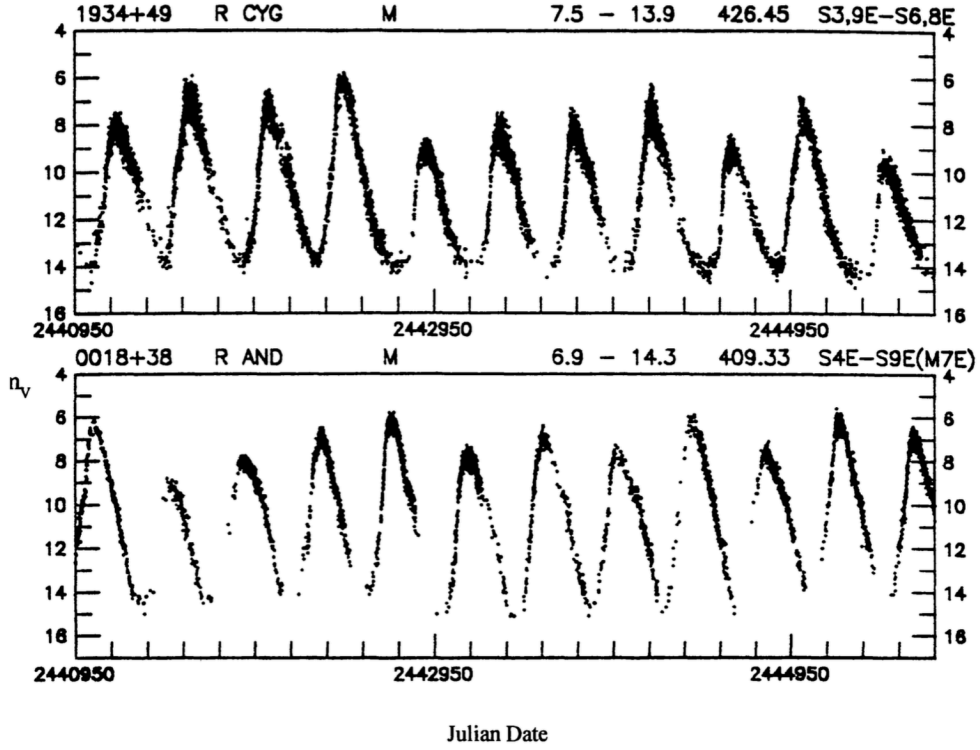

Figure 1.2: Light curves of two Mira variables over 13.2 years: R Cygni (top), R Andromedae (bottom). Source: Mattei (1997).

Semi-regular (SR) LPVs can be thought of as the second-to-Mira variables in terms of regularity, amplitude, and period length. In fact, a main distinguishing characteristic between a Mira and an SR classification is having a visual amplitude less than 2.5 mag (GCVS, 2009). This is due to some edge cases where SR variables can be hard to distinguish from Miras on the basis of cycle uniformity and period length alone (see Figure 1.3 for some examples). Much more diverse than Miras in terms of regularity of period, amplitude, and cycle light curve, they exhibit regularity but with some degree of instability: a changing amplitude and/or mean magnitude, but with the cycle period time remaining relatively constant from one cycle to the next (Sterken and

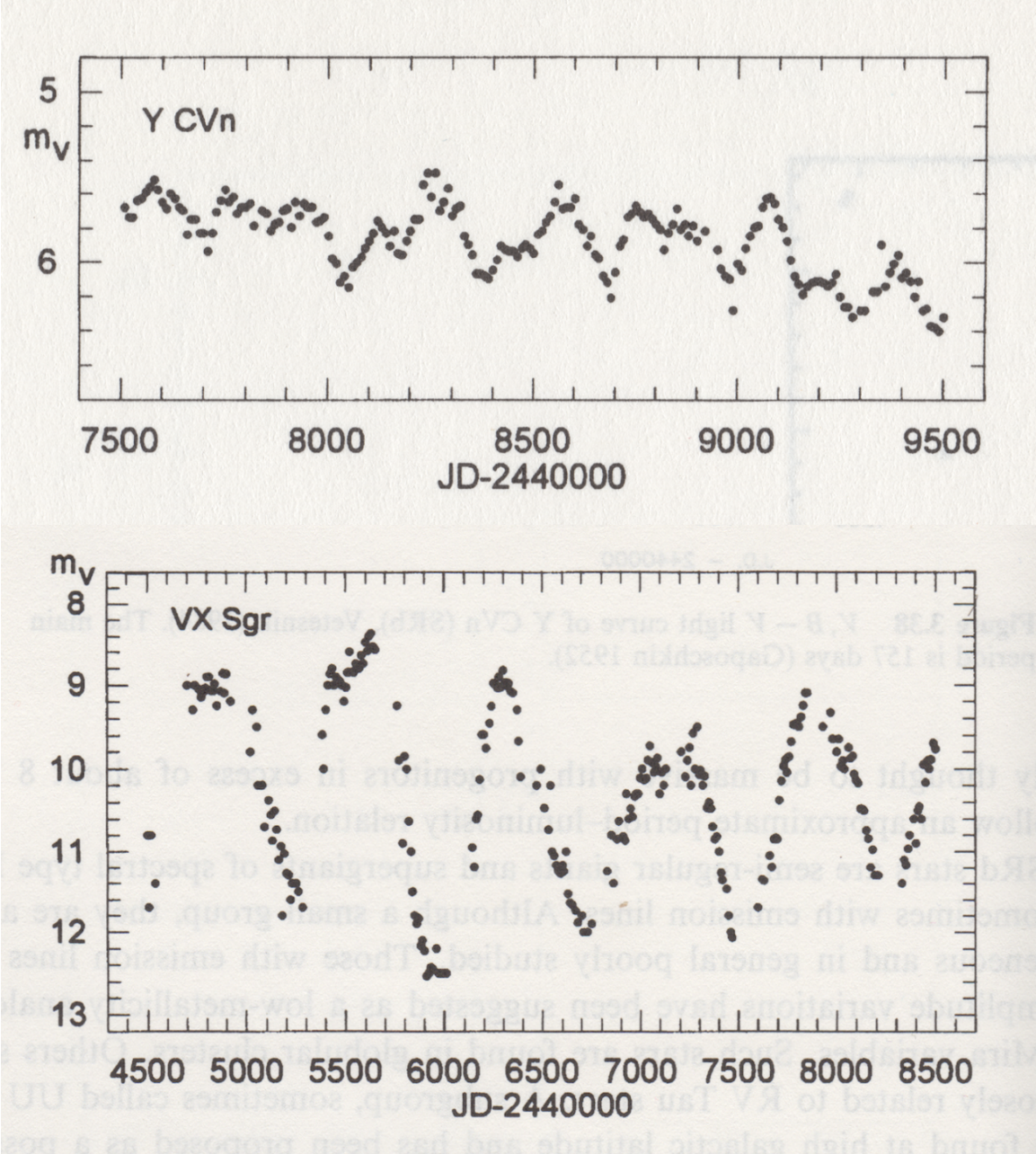

Figure 1.3: Examples of SR light curves: Y Canum Venaticorum over 5.5 years (top), VX Sagittarii over 11.0 years (bottom). Note changing max/min and mean magnitude, possibly due to long secondary period. Source: Sterken and Jaschek (1996).

Jaschek, 1996). That said, they are less instable and chaotic than Irregular LPVs, and thus the distinction remains somewhat subjective. Some semi-regulars exhibit multi-periodic behavior: their variability appears to be the result of a superposition of two or more pulsation cycles with distinct periods, in a manner that can be modeled by a linear combination of sinusoidal functions. This behavior can be (and has been) misidentified as irregular if only a few cycles have been observed, and the only way to be certain is to have more observational data (Sterken and Jaschek, 1996). Semi-regulars are red giants or supergiants, and populate the RGB and early AGB portions of the HR diagram (Otero et al (2016), Samus et al. (2009)).

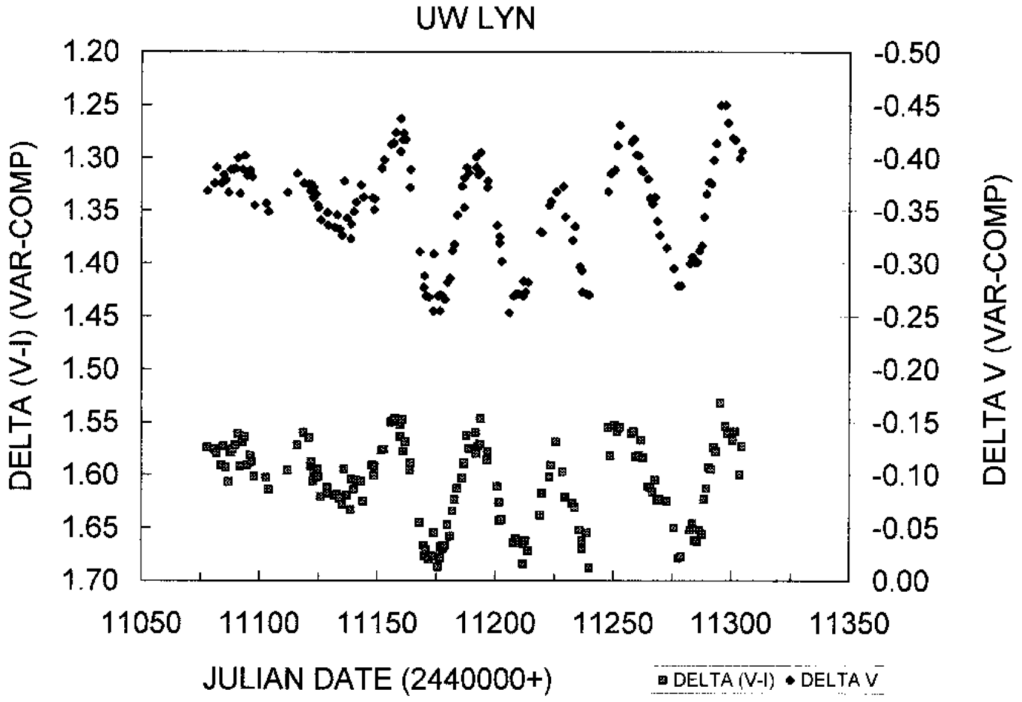

Figure 1.4: Differential magnitude light and color curves of irregular LPV UW Lyn over 10 months: V-Band (top), V-I (bottom). Source estimated period at 30-34 days. Note effective temperature correlating with luminosity. Source: Percy and Wilson (2001)

Irregular (IRR) LPVs lie on the more chaotic end of the regularity continuum. To contrast them against Mira and SR stars, IRR variables exhibit a cycle that is hard to discern as such,

maxima and minima with large variations in value, and a changing mean as well as an unstable period. They do not appear to be easily reducible to multi-periodic sinusoidal basis functions. Again, the line between IRR and SR variables is not clear-cut due to them being on a continuum. They are defined as being slow irregular variables of late spectral type (cool and red) giant or supergiants, with poorly defined periodicity (GCVS, 2009), as can be seen in figure 1.4 (Percy and Wilson, 2001). They also populate the RGB and early AGB portions of the HR diagram.

Although not our main target, it is certain that our variability detection and photometric analysis will yield some SPVs. Any SPVs detected must therefore be characterized and classified in the process of verifying their identity as reported in the literature or, in the case of novel variables, they must be classified in order to be reported as a discovery. The most commonly encountered pulsational[1] SPVs in NGC 6388 are either RR Lyrae (RRL) or Population II Cepheid (P2C), both of which inhabit the Instability Strip. RRL stars are further subdivided into RRab and RRc types, with asymmetric and symmetric light curves, respectively. RRab and RRc have respective typical period ranges of 0.3-1.2 days and 0.2-0.5 days, and variability amplitudes in V-passband of 0.5-2 mag and sub-0.8 mag (GCVS, 2009). RRab and RRc are also commonly reffered to as RR0 and RR1, in reference to their pulsation in the fundamental and first overtone radial modes, respectively. P2C variable stars, also referred to as W Virginis-type variables (hence their GCVS class of CW), are defined as having typical V amplitudes of 0.3-1.2 mag, and are subdivided into CWA and CWB for periods longer and shorter than 8 days, respectively. Potential period lengths can extend up to 35 days (GCVS, 2009).

[1] Other SPV types in NGC 6388 include eclipsing binaries (EC), a single RV Tauri (RV), and an anomalously bright Cepheid (AC) according to the Clement Catalogue (2001). Of those, only the AC variable star was detected in our observations (see chapter 4).

We are searching for variable stars in NGC 6388, which is an exceptional globular cluster: located in the direction of the galactic bulge (l = 345.56˚, b = −6.74˚), it has unusually high metallicity ([Fe/H] = −0.55) (Harris, 1996 (2010 ed.)) for a GGC, which are typically composed of old Population II stars, and thus tend towards lower metallicity.

Despite this high metallicity, there exists a blue extension of the horizontal branch (HB) in the CMD of the cluster (see Fig. 1.5). The HB is a region containing stars that have evolved off the RGB and burn helium in their cores, and it should be redder due to NGC 6388's higher metallicity; an example of the unsolved "Second Parameter" problem of HB morphology. Therefore observing the member LPVs of the cluster over a long time baseline will add to our understanding of how their unique properties relate to their behavior. It might also give us insight into how the hypothesized Second Parameter affects them. The final characteristic of note is that the cluster's absolute visual magnitude, a measure of its total luminosity, is higher than usual (Mv,tot = −9.41 mag (Harris, 1996 (2010 ed.))). This is indicative of a relatively large number of stars, and thus a larger number of potential variables to be found. This is evident in the large numbers of variables discovered in the cluster to date, which stands at 118 variables.

A comparison to a similar, but better known, cluster illustrates why NGC 6388 is unique: 47 Tucanae (NGC 104), abbreviated as "47 Tuc". With lower foreground reddening (47 Tuc's $E(B-V)$ of 0.04 compared to NGC 6388's 0.37) , higher apparent V magnitude (14.06 mag compared to 16.85 mag) and larger half-light radius (3.17 arcmin compared to 0.52 arcmin), 47 Tuc is less attenuated, much brighter and larger than all GGCs except Omega Centauri (NGC 5139), and is well studied as a result. It is similar to NGC 6388 in that it is has almost equal luminosity ($M_{v,tot}$ = −9.42), is also metal-rich (although lower at [Fe/H] = −0.75), and has a

similar number of known variables (122 variables (Lebzelter and Wood, 2005[1])) compared to NGC 6388's. The two clusters notably diverge in 47 Tuc's lack of a blue extension for the HB (see Fig. 1.5). Physical parameters of 47 Tuc sourced from Harris 1996 (2010 ed.)).

Because of NGC 6388's exceptional characteristics, it has been studied by a number of previous researchers. Thus, understanding their work is critical for putting our research in context, as well as giving hints of what to expect from our observations. The first[2] work to mention an LPV in the cluster was by Feast in 1972, who credits Lloyd Evans as suggesting the star (later named V1) as a candidate. Later, more extensive work by Lloyd Evans and Menzies (hereafter abbreviated as LEM, 1973) found 9 LPVs and provided V-I_K color values for them, with V1, V3 and V4 classified as Miras. This work used photographic plates and relied on the blink method for detection and an iris photometer for magnitude measurement. The observational time baseline and cadence was limited to 3 epochs (dark of moon nights) in 2 seasons. More details in a follow-up work that uses the same data indicates that the observations were at most separated by 9 months, not sufficient to give classifications or periods. The follow-up work (LEM, 1977) used the same plates plus additional ones taken later, which were credited but not placed in a time range. They found variables V10 through V12, but again, no classification or periods were given. Additional photometry was provided on all variables, the ones relevant to our work being V-filter amplitudes. Both works provided finder charts for the cluster and known variables.

---

[1] This research used the nomenclature of Clement et al. (2001), but of note is another work by Weldrake et al. (2004), which independently found 100 variable stars but used a different naming scheme.

[2] The Clement catalogue (2001) entry on NGC 6388 notes that star V4 was discovered to be a variable by Shapley and Swope (1940) under the name HV 6570 (or MU Sco). This link was only later identified by Samus et al. (2009).

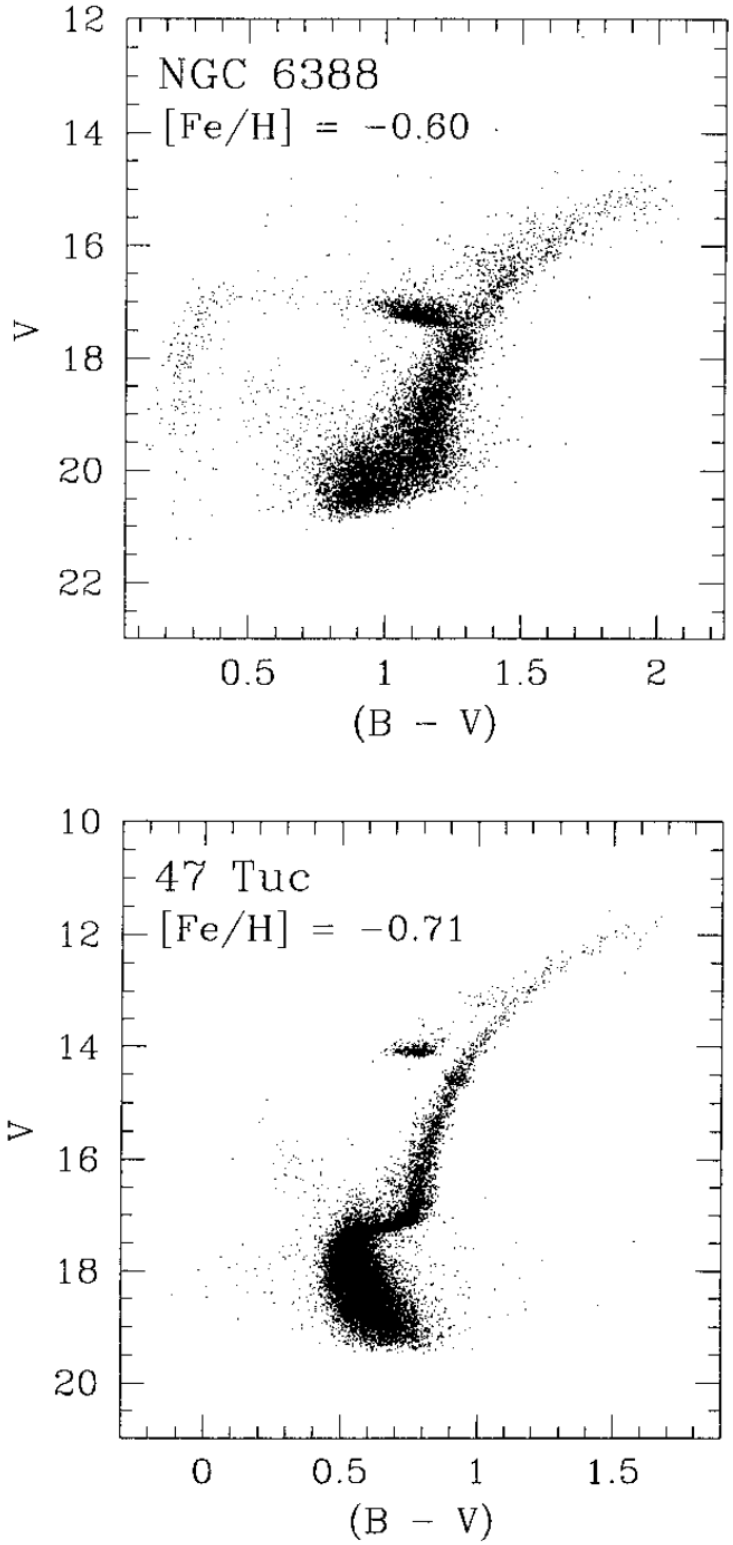

Figure 1.5: The CMD of clusters NGC 6388 and 47 Tuc, top and bottom respectively. Note the "red clump" protruding off the RGB in both, downward-curving HB extension in NGC 6388 but lack of it in 47 Tuc. Source: Rich et al. (1997)

The second work to focus on the variables, Hazen and Hesser (hereafter abbreviated as HH, 1986) also used photographic plates and the blink method for variable detection, while relying on a mixture of visual and iris-based photometry (the latter calibrated photoelectrically). Observation was done in two groups separated by a year: the first group consisting of 13 plates taken over three months, while the last group consisted of 15 plates that were taken in a single month. As would be expected, no information on LPV classification or periods was obtained with such a low number of observations in the interim 9 months, although a new variable (V13) was discovered. B-filter photometry was provided for some of the LPVs. Some SPV stars were also discovered and classified, most being RRL stars with the exception of two eclipsing binaries (V14, V15). Four field variables were discovered as well, and a finder chart was provided for all variables except V1 and V2 because they were too close to the cluster center.

The first CCD-based study of the cluster, Silberman et al. (1994) was also the first of a series of studies (followed by Pritzl et al. (2002) and Corwin et al. (2006)) that uncovered and characterized most of the observable SPV stars in the cluster. Silbermann et al. observed the cluster in observation runs separated by a year, the first of which included three consecutive night's worth of observations while the second included two nights separated by 33 days. This is an observational cadence more suited for SPV detection and characterization, which was noted by the authors. The study used a variety of techniques for variability detection: a computer-based blink method, identifying magnitudes with high-scatter, and correlated color-luminosity changes. The study is the first to rely on the point spread function (PSF) fitting DAOPHOT program for photometry of NGC 6388: B, V, R photometric data was provided for four LPVs and five SPVs, three of the latter of which (V27-V29) are new discoveries. Five suspected SPVs were also noted in the study. Periods, amplitudes and classification were given for the SPVs, but only mean

magnitudes were available for the LPVs. Stars V18 and V19 showed no evidence of variability,[1] although the authors noted they were too blended for accurate analysis. A finder chart for the variables was also provided.

Pritzl el al. (2002) relied on observations in two blocks of four consecutive nights, with the blocks separated by two days, in May and June of 1998. The observations were done in the B and V bands. The chosen cadence proved effective in discovering three new LPVs (V45, V46, V47) and 27 new SPVs (V30-V44, V48-V57), which were, in order of most to least common, RRL, P2C and eclipsing binaries. This is expected given that the observational data's maximum time baseline of 10 days is more suited for SPV discovery and characterization, and not for characterizing LPVs. The study does not classify the LPV type, and does not give periods for the LPVs. It did, however, provide folded light curves and updated photometry, periods, and classification for most of the known SPVs. Photometry was based a on a software package that mainly utilized DAOPHOT, while detection relied on root mean square (RMS) scatter in magnitude values. Finder charts were also provided for the old and new variable stars.

Corwin et al. (2006) used the data from the previous study as the basis for an image-subtraction based photometric analysis and variability detection. The study used the ISIS image subtraction package (Alard, 2000) to do this, and it was chosen for its ability to detect and measure relative flux change in the blended central regions of the cluster. The study managed to discover 11 new SPVs (RRL or P2C type) in the central 2.20 arcmin of the cluster, and provided periods and relative flux-based folded light curves in the B and V bands. Like the previous study, no new information regarding LPVs was provided.

---

[1] Which we now know was partially correct: V19 was not detected as a variable by Pritzl et al. (2002), Corwin et al. (2006) and Cardona (2011). V18, however, was detected and characterized by Pritzl et al. (2002)

A study by Matsunaga et al. (2007) is worthy of mention here. There were few mentions of it in most other literature on the cluster, possibly due to its main focus on determining the distance modulus, and lack of identifying information and finder charts for the variables in question. The study estimated the distance modulus using a period-luminosity relationship determined from Mira variables in the LMC. The study's near-infrared (K_s band) observations took place over a period of five years, with a monthly cadence in a relatively short (April-August) observing season. This was likely sufficient for period estimation, but not enough to characterize the LPVs regularity. The study very likely contained the first periods in the literature for four LPV stars known to be in the cluster at the time, as the study refers to Corwin et al. (2006). It even mentions the discovery of a new Mira, but no identifying information was given for any of the stars. Photometry used the PSF-fitting DoPHOT program, and variability detected by looking for significant magnitude differences from a reference image.

Although not a study focused on characterizing LPV stars, Sloan et al. (2010) provided folded light curves and amplitudes in the far-IR K_S band (2.14 μm) for the stars V3 and V4. The study was focused, rather, on the dust mass-loss rate of LPV stars in GGCs. These light curves were possible because recurrent photometric observations were done with the aim of detecting variability, verifying cluster membership (using the period-K band relation), choosing suitable stars, and finally identifying phase of oscillation during follow-up work. The observations were taken in the J, H and K_S bands, over a period of three years, and with an interval of 40-60 days between observations. The follow up work used the Spitzer Space Telescope's infrared spectrograph instrument, in tandem with individual ground-based observations in the J, H, K and L bands. The mean magnitudes, amplitudes, periods, and resulting folded light curves were determined using Fourier analysis and minimum χ^2 fitting. The periods used were the average of

those determined from the image sets of the three filters. The study also provided magnitudes in the four filter bands of the non-repeating observations, bolometric magnitudes, IR spectra, mass loss rates as well as the aforementioned cluster membership check for the two stars. The LPVs were identified from the then current version of the Clement catalogue (Clement et al., 2001). While the Sloan et al. (2010) study did provide detailed information on these two LPVs, it was too specialized to be comprehensive (only two stars), and too short in time baseline to accurately characterize the LPVs' behavior.

Cardona's 2011 thesis research was the first one to focus on LPVs, and have the cadence and long time baseline necessary to recover and characterize a large number of known and (then) unknown variable stars. With a 2-year baseline and 7 to 10 days between observations, the study was able to recover and characterize 10 known, 23 new, and 7 candidate LPV stars. The study used a combination of ISIS and DAOPHOT for photometry; the former was able to provide relative flux photometry inside the blended central region, while the latter was able to provide apparent magnitude photometry for the stars outside it. A finder chart for the stars was also provided. Of note is that the observations used are part of the data used in our study.

Finally, Skottfelt et al. (2015) is the latest published research on the cluster's variables. The observations were done in groups: the first group over a period of 5 months, and after 195 days the second group was done over a period of six weeks, for a total of about 33 epochs. This was done using a new technology (EMCCD, short for electron multiplying charge-coupled device) that can take very short exposure (as low as 0.01 s) imaging with good signal-to-noise ratios (SNR). The short exposures "freeze" the scintillation to reduce seeing effects, at the expense of low SNR due to the shortness of the exposure time. The resulting series of images are then shifted and stacked to combine their data into one, averaged image with higher SNR while

preserving the higher spatial resolution present in the short exposures. The observations as taken through the system, with a dichroic mirror (effectively a long-pass filter with 650 nm cut-on wavelength) and a camera (whose sensitivity drops to zero above 1050 nm), which in combination are the equivalent of the SDSS i' + z' filters. The system was photometrically calibrated to the I-filter standard with use of isolated cluster stars with known I magnitudes and CMD positions (that said, the study notes that this is an approximation with a corresponding increase in uncertainty). One downside of using the EMCCD was that it was only able to observe a small, square 45 by 45 arcsec area of the sky, so the study focused on the busy central region of the cluster, and as such all newly discovered variables were in that relatively small region (See Figure 1.6 for an idea of how small the field of view is). In addition to recovering 14 known variable stars (all SPVs) and confirming and characterizing 4 suspected variables (V70-V73, discovered by Corwin (2006)), 48 new variable stars (V74-V121) were discovered: 6 SPVs and 42 LPVs.

Both known and new SPV stars, given their short periods and relative regularity, were able to be characterized with the use of folded light curves, giving periods as accurate as 0.0001 days in most cases for those SPVs with periods shorter than about four days. This is reasonable because the stars were observed over several contiguous cycles. Skottfelt et. al. (2015) also estimated magnitudes, periods and amplitudes for the SPV stars. Attempts to characterize the detected LPVs (all of which were new discoveries) were met with partial success: estimated magnitudes, periods and amplitudes were given for 18 LPVs, while for the remaining 24 LPVs only magnitudes and amplitudes were given (with the type assumed to be irregular). Two suspected variables were also discovered.

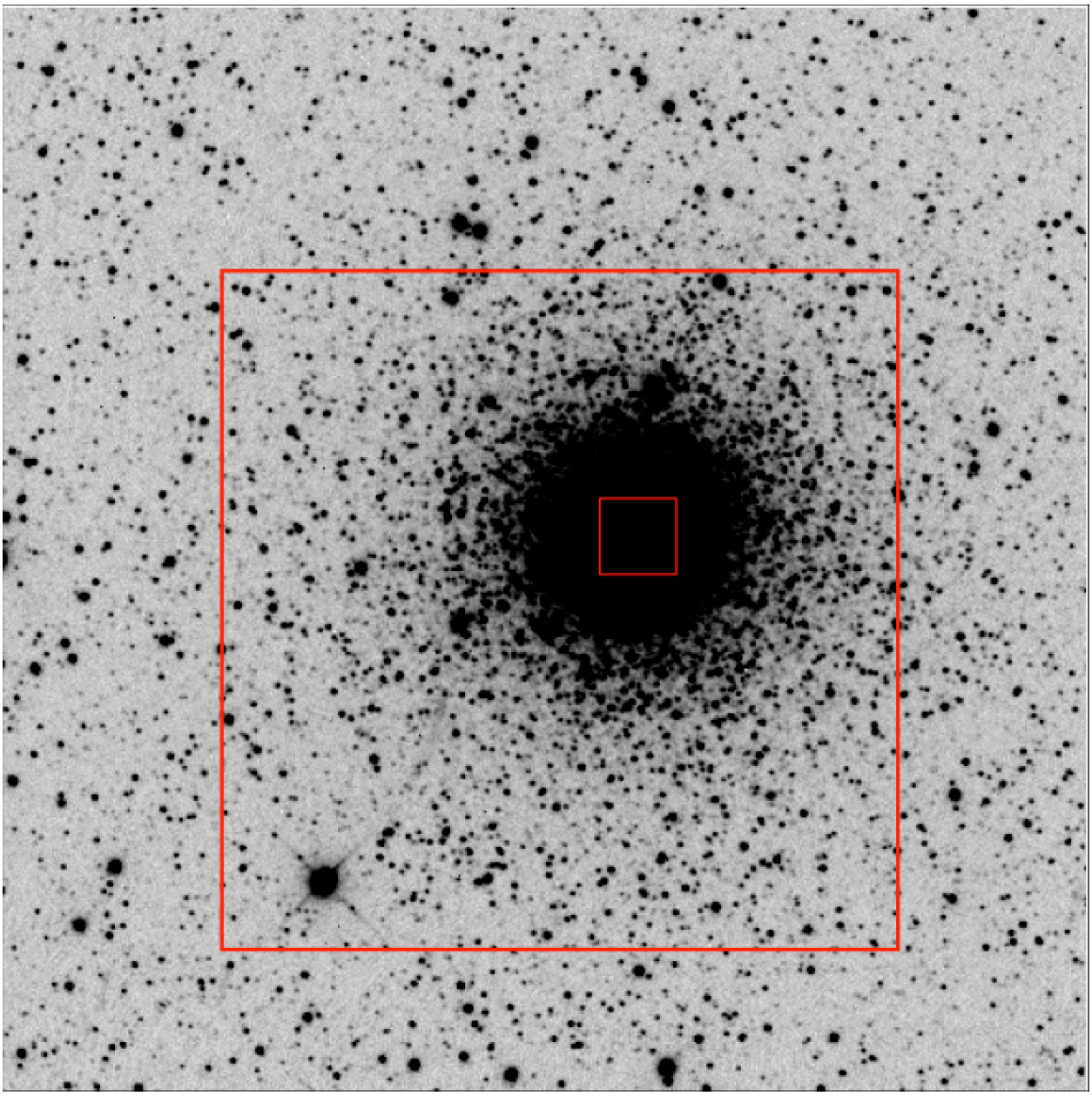

Figure 1.6: comparison between our observation FOV and the narrower one in Skottfelt et al. Note our study's spatial resolution is lower (0.59 arcsec vs 0.09 arcsec)

It must be noted that the LPVs' classifications can be considered subject to change; the length of the observation groups (~ 5 months and 1.5 months) on their own is not enough to accurately characterize the SR and IRR variables with their light curves, which might lack the breadth of data need to determine whether there is cycle-to-cycle uniformity or not. The possibility of irregularity makes extrapolating a behavioral norm from the observed few, widely separated cycles risky, especially for LPVs with longer periods. The LPV variables with estimated periods in the study had a median period of ~57 days, indicating that over half of them had a maximum cumulative observed cycle count of ~3.4, not enough to confirm a behavioral tendency. Finally, the longer time baseline (195 days between the groups), while useful for characterizing the more regular LPVs, does not provide a way to check for the property of regularity.

Incidentally, of the newly confirmed and discovered variables, we have found that at least 6 were also recovered and characterized in Cardona's (2011) research: they are V71/SV2, V73/SV5, V83/NV4, V88/NV11, V93/NV8 and V97/NV12 (as named in Skottfelt et al. and Cardona, respectively). Finder charts were provided by Cardona for the new and old variables that were detected. In sum, at the time of this writing the LEM (1977), Pritzl et al. (2002) and the Skottfelt et al. (2015) studies are the main, most up-to-date sources of published information for the cluster's variables.

Our research will rely on six years' worth of frequent (every 7 to 10 days) observation. With this, we hope to provide an accurate assessment of the behavior and class of LPV stars, specifically their cycle and period uniformity, in order to place them somewhere along the Mira-SR-IRR continuum of cool red variable stars. The resulting light curves can also shed some light on how such stars behave over a longer than previously observed period of time. The nature of

the instrument used will also yield a larger FOV to study the globular cluster's variables than that of the latest published study. As a side benefit of the wealth of observations, we can also improve the periods and light curves of some of the already known SPV stars.

CHAPTER 2. OBSERVATIONS

Our observations of NGC 6388 were undertaken using the University of North Carolina at Chapel Hill-operated PROMPT telescope array. Located at Cerro Tololo Inter-American Observatory in Chile, the automated PROMPT telescopes' main mission is to observe gamma-ray burst afterglows in multiple wavelengths as soon as they are relayed to the array (hence the acronym: Panchromatic Robotic Optical Monitoring and Polarimetry Telescopes). The nature of PROMPT's mission emphasizes swift, multiple concurrent observations, therefore the telescope array is composed of six small-aperture (0.41 m) telescopes mounted on suitably sized off-the-shelf rapid-slew mounts (Reichart et al., 2005). The mount encoder accuracy is sufficient to ensure that the observation target is comfortably within the CCD field of view (FOV) when the telescope is first pointed at the cluster. The tracking is unguided, but the exposure times were short enough so that relatively few images exhibited "trailed" or smeared star images that were severe enough to be rejected, as detailed later in this chapter.

The nature of the primary mission renders the telescope array free for large periods of time, which are allocated for research and educational outreach as prioritized by a web interface system. The large observation time allowed by the array is uniquely suited for our main research purpose of collecting relatively gapless photometry data of NGC 6388 over a long time range. Getting such extended and frequent access on large aperture, professional-grade telescopes is not possible, hence the dearth of long term studies of LPVs in globular clusters[1]; thus the low image scale of our telescope (see below) is an acceptable "trade off", and is an issue that was somewhat ameliorated by using the ISIS Image Subtraction Package (Alard, 2000), which allowed

[1] Of note: some widely cited long-term LPV studies have used data from other long-baseline projects, such as gravitational microlensing surveys (e.g. MACHO in Wood et al. (1999) and Lebzelter and Wood (2007), EROS-2 and OGLE in Beaulieu et al. (2001)), but they were not focused on individual clusters as much as the LMC, SMC and galactic field variables.

photometry work in the busy, “blended” regions close to the cluster core. Use of the package is detailed in chapter 3.

Our primary research goal is to study the pulsation behavior of LPVs in NGC 6388 by tracking their long-term behavior, and identifying their characteristics: amplitude, periodicity of pulsational cycles, and regularity. We also seek to place them along the Mira-SR-IRR behavioral continuum mentioned in Chapter 1, as well as identifying any possible secondary periods. Our observational strategy thus focused on obtaining observations frequently and over a long time baseline as necessary, and reducing the barriers to acquiring these observations.

If all LPVs were as consistent/uniform in behavior as RR Lyrae or Cepheids, this could have been done with widely spaced but infrequent observations (e.g. once a month), with the periodic behavior later determined using any number of methods (e.g. Fourier or phase-based). LPVs, however, can exhibit a large degree of variability cycle-to-cycle, specifically in SR and IRR stars. The need for more data points is therefore of special import for these variables, whose magnitude(s) can change rapidly in the span of a month. We’ve thus aimed for an observational period of one to three weeks, which was chosen due to LPVs being our primary focus. This cadence is an appropriate sampling rate for mapping the brightness curve of a cycle accurately, and thus enabling correct characterization. Conversely, observing with a frequency of less than a week would not be useful for characterizing the behavior of LPVs, which have periods on the order of months. Observing more frequently would consume more of the finite observation time allocated to us, and require more processing time and effort, for too little of return.

LPVs’ relatively long periods necessitate a longer time baseline than that required for SPVs’, but an even longer time baseline than that is required; one long enough to capture as many cycles as possible is necessary. This is because, in addition to individual cycle differences,

LPVs can also exhibit a sort of “meandering mean” ”: this is evident as the amplitude of adjacent maxima/minima pairs remaining roughly consistent but the central point between each sequential pair changing. This is, possibly as a result of a secondary period or simply a feature of irregularity. This behavior can be seen in figure 1.3, and can only be observed over a long time range, hence the multi-year observational seasons. This long-term behavior also further motivates the need for minimizing the gaps between observing seasons, where a possible peak or trough in brightness can occur. In addition to ascertaining regularity, catching the peak/trough of a cycle will help in determining the primary and (if possible) secondary period of an LPV accurately.

Our observational strategy, as outlined so far, is to observe for multiple years while reducing the gaps between those years’ observational seasons. We’ve opted to do this by relaxing some of the limits on astronomical observation in order to extend the observational season (when the cluster is in the Sun’s glare) while not compromising image quality too much. We thus opted to observe through greater air mass numbers, and with the Sun below the horizon at a higher than optimal elevation angle, as detailed further below.

We were able to request observations from the PROMPT array under the aforementioned limits via the Skynet web interface, which automatically queues our observation in a time slot so as to fulfill our request, assuming no higher priority observations were pending for that slot. The Skynet system chooses the time slot that fulfills our observational requirements, which include: target object or celestial coordinates, observational parameters include filters types, image capture order, air mass limits, sun elevation limits, time and date of capture, and which telescope of the array is to take the image. The reasoning for our choice of parameters is explained further below in the chapter.

Where possible, we have opted to request jobs on a single telescope for consistency, because the same CCD and filters remain on that telescope for months or years at a time. The PROMPT-5 was quickly settled upon as one with low demand (due to not being specialized in polarimetric or wavelength-specific blue-vs.-red optimized observation) and appropriate filters, and thus was the telescope with which the majority of images were taken. In the cases where images were taken with other PROMPT telescopes, the filter/exposure length and sequence we kept identical, and the differences were corrected for by the ISIS package routines.

The PROMPT-5 telescope and CCD (a 1024x1024 pixel Apogee Alta U47+s) system have a field of view (FOV) of 10 arcminutes, with a plate scale of 0.59 arcseconds per pixel. A full image, with NGC 6388, is shown in Fig. 2.1. We have chosen to perform our observations with two different filters in order to characterize the color of the star and how it changes with time. Our focus on LPVs, which are either red giants or supergiants, motivated the use of the near-infrared *I* filter, which has a 806 nm wavelength midpoint with full width half maximum (FWHM) of 149 nm. The second filter used was the visual *V*-filter, with a 551 nm midpoint and FWHM of 88 nm. The *V* filter was chosen for its long history of use in LPV photometry, so using it would enable our data to be compared against that of other, well-studied LPV stars. After experimenting with different exposure times, we found the following to produce good results: 60 seconds exposure in *V*, a long 50 second exposure in *I* (called I_L), and a short 12 second exposure in *I* (called I_S), repeated *N* times in a single observation session. The exposure lengths selected were a result of instrumentation and target characteristics. The slightly longer *V* exposure is mainly due to the smaller bandwidth of the respective filter, but also due to LPVs' redder color/cooler effective temperature. The short I_S exposures were done in case some brighter stars saturated the pixels in the I_L exposures.

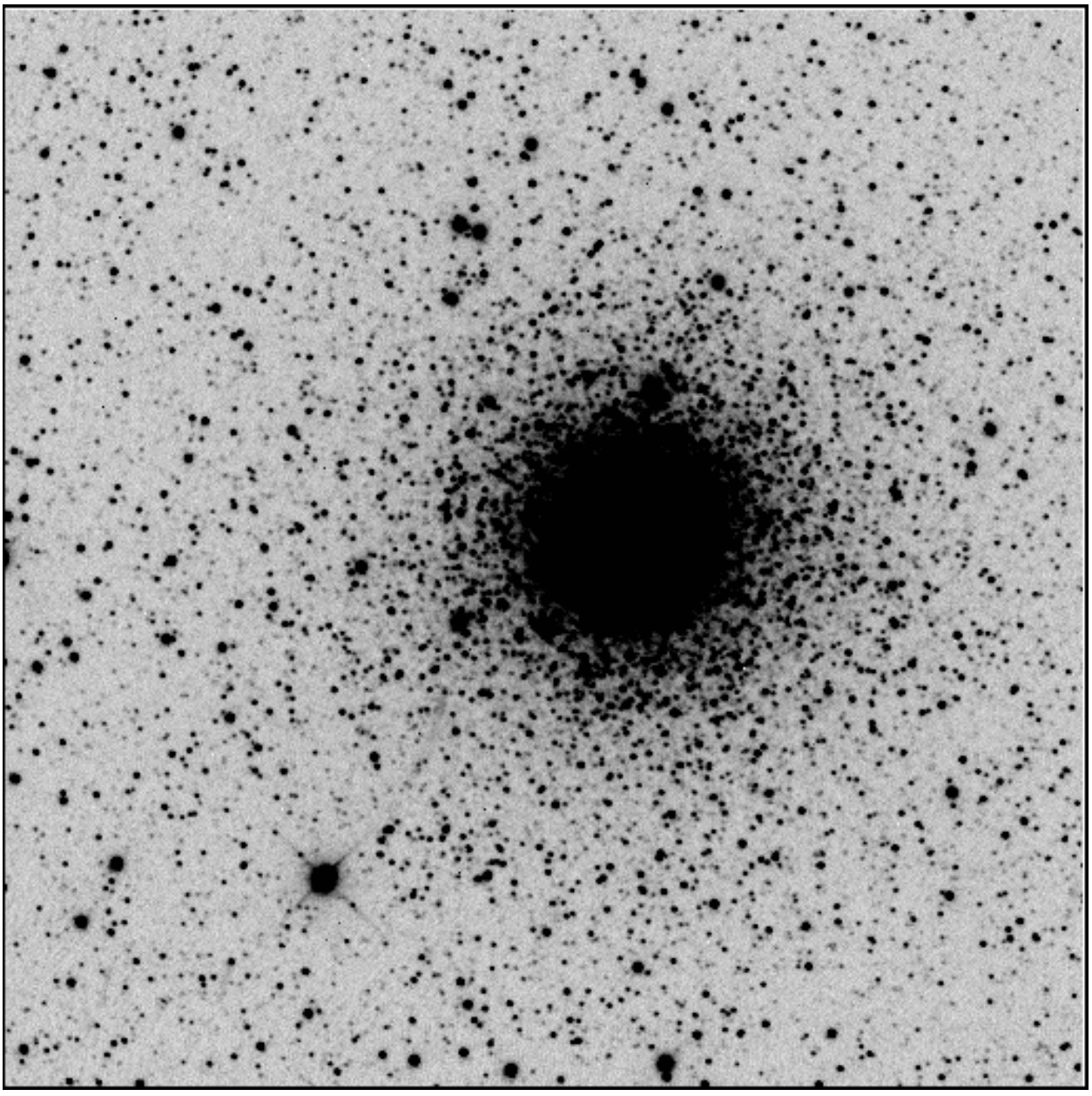

Figure 2.1: Full size, processed reference image of NGC 6388 as taken by PROMPT-5. North is up, east is right.

We obtained the images in the order "V, I_L, I_S, V, I_L, I_S…" to allow the unguided telescope to "drift" stars across several pixels during the sequence, so that images of the same filter/exposure type have a larger offset in star positions on the CCD. This larger offset ensures that an individual star's signal is captured by different pixels in N different images of the same filter/exposure, which prevents persistent capture defects (e.g. hot pixels on the CCD) from affecting the signal. In addition to defect mitigation, having N multiple images (of the same filter type and exposure) also allows us to measure the standard deviation of the measurements.

The number of times the "V, I_L, I_S" sequence was repeated, N, was changed over time. For most nights in the 2009, 2010, and 2011 observing seasons we used $N = 4$, with an additional V exposure at the end of the sequence. Later we reduced this to $N = 3$ for most of the 2012 season, and after Cardona (2011) worked on the first two seasons of the data, I_S exposures were discovered to be of limited use aside from confirmation of periodicity, and thus were stopped in early 2012. For the 2013 and 2014 seasons, we reduced to $N = 2$. For most of the observation sessions, $N > 2$ was used with the thought that, in case of exposures with spurious values, a minimum of three is needed to determine which one is anomalous. The last two seasons forego that ability in exchange for conserving observation time, which is a finite resource. Discrepant values mostly appeared when examining fainter stars, usually the case for RR Lyrae for example, but the large number of available data points from our large number of images made period determination immune to the few (usually one to three) nights that are deviating from the mean behavior. The frequency of observing epochs, or nights, was mostly 3 to 4 times per month. After an initial period of weekly observation in which we experimented with different exposure lengths and settings, our observation frequency varied between about 7 to 10 days, as permitted by sky conditions and the Skynet queuing system.

Finally, the exact length of our observation season was predicated on NGC 6388's air mass, and how dark the sky was. Air mass is a measure of the length of the optical path taken by light from the object through the Earth's atmosphere, and is related to the telescope's elevation angle *h* (the angle between the telescope-object line and the horizon) as follows:

$$h = 90 - \left(\frac{180}{\pi}\right) * sec^{-1}(X)$$

where *X* is the air mass and *h* is in degrees. The formula is an approximation that assumes a plane-parallel atmosphere. For most of the observation season, we have decided to limit observation requests to air mass < 2.0, which corresponds to a minimum telescope elevation of approximately 30 degrees. Sky darkness is determined in part by the Sun elevation angle, which, in our observing requests, we have set to a maximum limit of −16˚ to −18 (i.e. the Sun is more than 16˚ or 18˚ below the horizon).

These two parameters, air mass and Sun elevation, are important due to the effects they have on the oncoming light. Increasing the air mass value induces more deleterious effects caused by having to go through more of the atmosphere. Firstly, it will cause more scintillation and blurring to a star's image, increasing the FWHM and thereby the blending of stars close to each other. Secondly, more of the oncoming light will be absorbed or scattered, reducing the number of photons received and in turn reducing the signal. Thirdly, the background sky brightness will increase, thus increasing the noise in the image. Similarly, the closer the Sun is to the horizon (e.g. at twilight), the brighter the sky background. So, taken all together, the higher the values of the air mass and the sun elevation angle when observing, the lower the signal-to-noise ratio (SNR) and the lower the spatial resolution of the resulting image.

The limits given previously were in use for most of the observation season, but there were periods where different limits were used: for several weeks at the start and end of each

season, the air mass limit was set to 3.0 (equivalent to about 19.5˚ telescope elevation angle), while the Sun elevation angle limit was set to −14˚. In effect, this meant we'd be looking through more of the atmosphere while the background sky is brighter, but this was done to increase the length of the observation season; when the object is just coming out of or going into the glare of the Sun, it remains close to the horizon at astronomical twilight. By relaxing our limits a bit, we gained about 2-3 weeks of observation at beginning and end of the season. In total, we've gained about 5 weeks worth of possible observational data per year at the expense of slightly degraded SNR and resolution, reducing the size of the season gap. This can be seen in Fig. 2.2 below, where the majority of images are of $X < 2$, with the exception of only a few (13.45 percent of total nights) at the start and end of the observing season. It should be noted that the LPVs of interest to us are typically bright enough to endure the reduced SNR, and ISIS can compensate for large variations in sky brightness, which means that those extra nights have recoverable information. Finally, there is the side benefit of the increased likelihood of acquiring observation time; by relaxing our criteria on sun angle, we enter a time when fewer astronomers are willing to take observations, so competition for observing time is reduced.

All told, an observation season tended to start in late January/early February and ended in late October/early November, as NGC 6388 was close to or below the horizon ($X > 3.0$) in the intervening ~2 months. The cluster was successfully observed for 6 years, from 2009 to 2014. This long time baseline is critical due to our focus on LPVs with periods upwards of 100 days, and enables us to accurately characterize the LPV type as well as the small changes that occur due to possibly intrinsic behavior. This is because our observational cadence was sufficient to sample LPV stars throughout the duration of a typical period, and to do so multiple times.

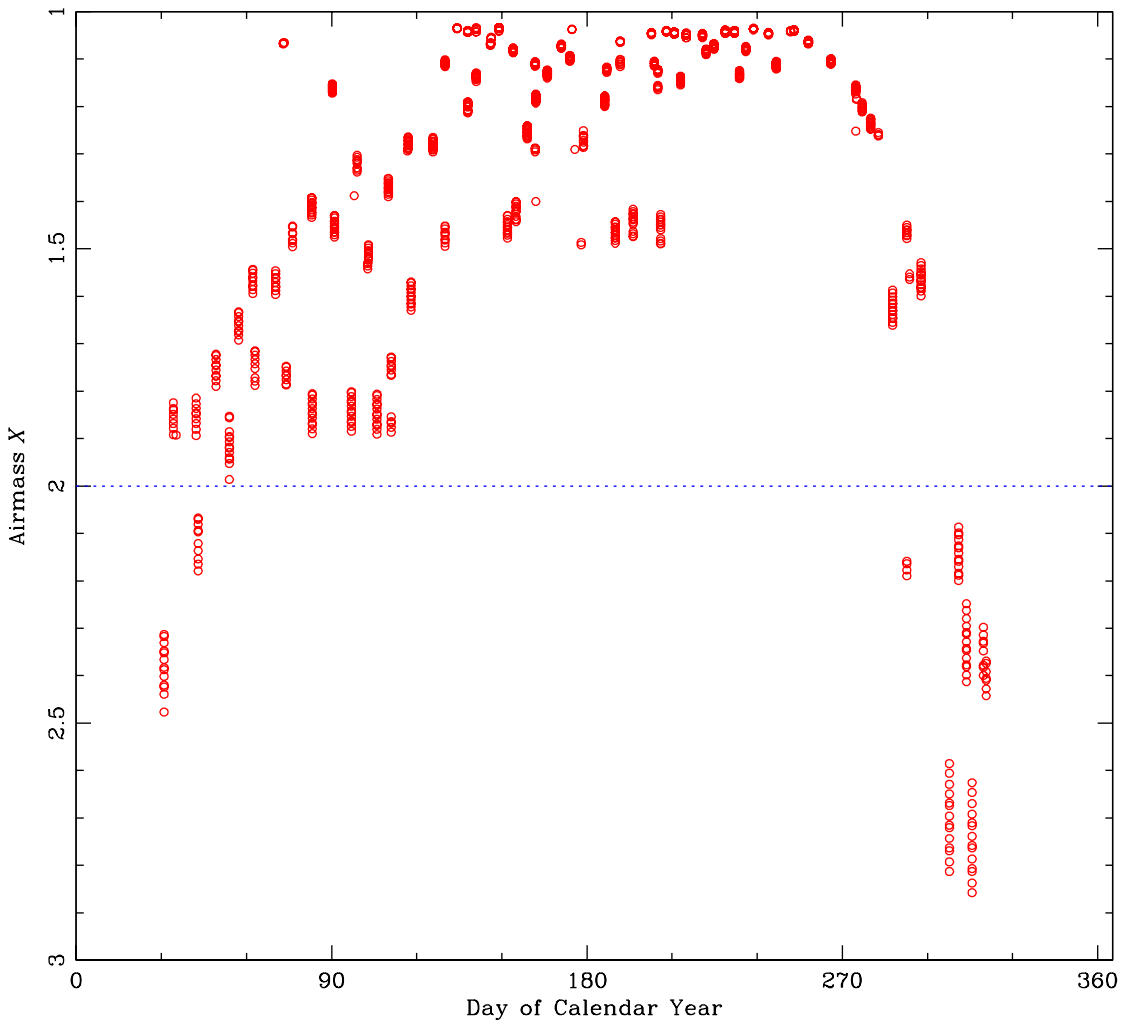

Figure 2.2: Cumulative plot of all images' capture date (day of respective year) versus the airmass through which the image was taken, with each image represented by a circle. Taken over approximately 243 nights, note relative paucity of images with $X > 2$, at start and end of every year's observation season, which happened on 32 nights.

We have managed to accrue a total of 2321 images over 6 years. This introduced two issues: both downloading and processing such a large number of images could be challenging. The PROMPT website does have an option for downloading multiple images at once, but only for those images belonging to the same "observation session" (one requested sequence), with the link to the image package only present on that session's individual webpage. Another difficulty is that the website limits the number of observation sessions listed on a single page to 25, resulting in multiple lists rather than a single, aggregate one. To resolve this issue, we wrote a python script that can output the direct internet addresses of our images by reading those lists. The principle of operation is simple: after saving the session lists (which are in HTML format) to our computer, the script searches the lists for observation session ID numbers. A session ID number is a unique identifier for an observation session that is generated after requesting an observation. By knowing the session IDs, it is a simple matter to generate the addresses of the processed image package (a compressed file containing images that were already processed), as they all share the same address but with different ID numbers. This saves the time of perusing roughly 240 unique session pages for our images.

Finally, we describe how the images downloaded are processed. Image processing for scientific astronomical use of PROMPT images is done to correct for multiple factors that affect the incoming signal from stars. The combination of each telescope's unique optical train and CCD electronics always introduces patterns in the data that are incorrect and not of celestial origin. Thus we cannot directly use the pixel values in the raw images (referred to as "Object" images), but have to use three types of images to adjust the pixel values: Flats, Darks and Bias-Darks (or "Zeros"). Flats are images of a uniform signal source, such as the sky at starless twilight, taken through the same filters used for the Object images. They are used to correct for

vignetting (photons are not distributed evenly over the CCD chip due to optical effects) and different pixel sensitivities in the CCD. Darks are images taken with the CCD shutter closed for the same duration as object exposures, and are used to correct for the "dark current" effect caused by thermal electrons being read out as signals. Zeros are short (~0 second) dark exposures that are used to correct for CCD readout bias, which is the level of charge (or voltage) put on the CCD before every exposure to lift the zero exposure level, so that the noise is properly sampled.

Having over 2300 images to process, we have decided to utilize the Skynet website's built-in image processing ability to correct for the defects that occur in collecting the signal. Thus, the images that are downloaded are not "raw" images with pure CCD readout values, but rather are processed images that are corrected using Flats, Darks and Zeros taken the same day or close in time to the requested Object images. The images are in FITS format, and have the image processing software and correction image dates listed in their header information (the part of the image containing the image meta data, such as filter type, time and date, exposure lengths, etc.) According to the header files, the PROMPT system uses Maxim DL for processing images, the vast majority using versions 4.57 or 4.60 of the software. The Maxim DL website's version release notes mention no changes in the processing utility in the version range used by Skynet, giving us confidence that all 6 years' worth of observations were processed in a consistent way.

CHAPTER 3. ISIS METHODOLOGY

The program used for analyzing the images, the ISIS image subtraction package (Alard, 2000), can take a set of astronomical images and, with correct setup, output an image of the location of variable star candidates and individual star flux difference photometry data. Although this method gives us star flux difference values relative to a chosen reference image rather than magnitudes, it is still able to characterize variable star behavior in important ways: light curve shape, period, regularity and relative amplitude changes of a single star can still be determined.

The ISIS package was chosen because its image subtraction-based photometry is good for blended regions, where methods that can directly get the flux, and therefore instrumental magnitude, of stars do not work due to overlapping star PSFs.

Although our observations have already undergone image processing by the Skynet web interface, ISIS cannot use them directly to perform photometry. The images need further preparation: they need to be organized, catalogued, characterized and modified in order to be useful analyzed ISIS' processing pipeline.

3.1 Pre-ISIS Preparation

As downloaded, the images only have the observed object, filter type, capture sequence number and session in the name such as, for example, "N6388_855351_V_000.fits". To make them more readable to a human user, we've opted to add the date, filter type and exposure length information to the image names for ease of use in future steps. To that end, an additional python script was written to read this critical information out of the FITS file header, and use it to rename the image file name. For example, a typical file is named "12apr26_i2.fits", which lists the year, month, day, filter type and sequence number/exposure length respectively. File names use i1 to i4 for the I_L exposures, i5-8 for the I_S exposures and v1-9 for the V exposures.

Following this, the images were separated by filter type and exposure length into the three previously mentioned types. The IRAF[1] *hselect* command was used to list images by type, after which it was straightforward to separate them using the command line, and do quick checks by reading the names of images in their respective folders. This was necessary because photometry generally requires comparing images taken through instruments of identical sensitivity in the electromagnetic spectrum (in our case, filters with the same midpoint wavelength and bandwidth) in order to obtain accurate results. In addition, the ISIS image analysis routine produces better results with images of roughly the same exposure lengths so as to reduce the amount of convolution done by the program, which can distort the signal.

The main benefit of human-readable names, however, is the ease of use in the rough alignment step. By alignment, we refer to the ideal case where a star will be centered in the same pixels across different images, which is far from the case by default! The untracked nature of the telescope's mount and the slight drifting that occurs between images after the first "slew-to-target" performed by the system means that the images, even those of the same session and mere minutes apart, are not perfectly aligned. In addition to this, the optical train and its connection to the CCD camera will inevitably undergo some degree of flexure, caused by the weight of the telescope shifting through the night, which shifts the image on the CCD chip. There is also the effect of atmospheric distortion, which is not uniform due to changes in air mass as images are taken at different altitudes. A different sort of alignment problem is image orientation, as the telescope is on a German equatorial mount, which means that the telescope and CCD, and hence the images, undergo a 180˚ rotation depending on whether the object is located east or west of the meridian. As a result, in some cases there are images in the same observation session that

[1] Image Reduction and Analysis Facility, a program for reducing and analyzing astronomical data in images developed by the National Optical Astronomy Observatory.

have different orientations, requiring a 180˚ correction to our preferred orientation (where north is up, as seen on an image, and east is right).

Simply correcting orientation, though, is not enough: the other aforementioned factors usually combine to produce misalignments that are large enough as to be uncorrectable by ISIS' automatic image interpolation routine, thus requiring a rough manual alignment. The images must also be trimmed; although ISIS can work on images with roughly the same alignment, it can only do so if they were all of uniform size. As a result, the alignment process requires, after manually adjusting the orientation, trimming the images so as to place a reference star at roughly the same x-y pixel, as well as having a uniform image size. Hence, we have to determine a shared area of the cluster that has been viewed by a majority of the images, and ideally consider that our area of study and analysis.

We have opted to use one particular star as a reference point in order to determine the trims required in each respective image, and thus be able to correct them all in a single batch. Identifying a suitable star for use as a reference with respect to the rest of the cluster, and specifically the cluster center, requires that it be close enough to the center as to reduce any distortion in the distance between it and the cluster center, as distortion is inevitable due to optical train effects, yet also be far enough to be unblended and readily identifiable. We have chosen such a star, marked in Fig. 3.1, above to the left of the cluster center. The next step involves manually examining all of the images captured using the program SAOImage DS9 (an astronomical imaging and data visualization application), correcting the rotation with the IRAF *imcopy* command, investigating the star with the *imexam* routine, and recording the information that is outputted in a list. This information includes the reference star's pixel coordinates, FWHM value, sky background value, and other information that will be used in later steps.

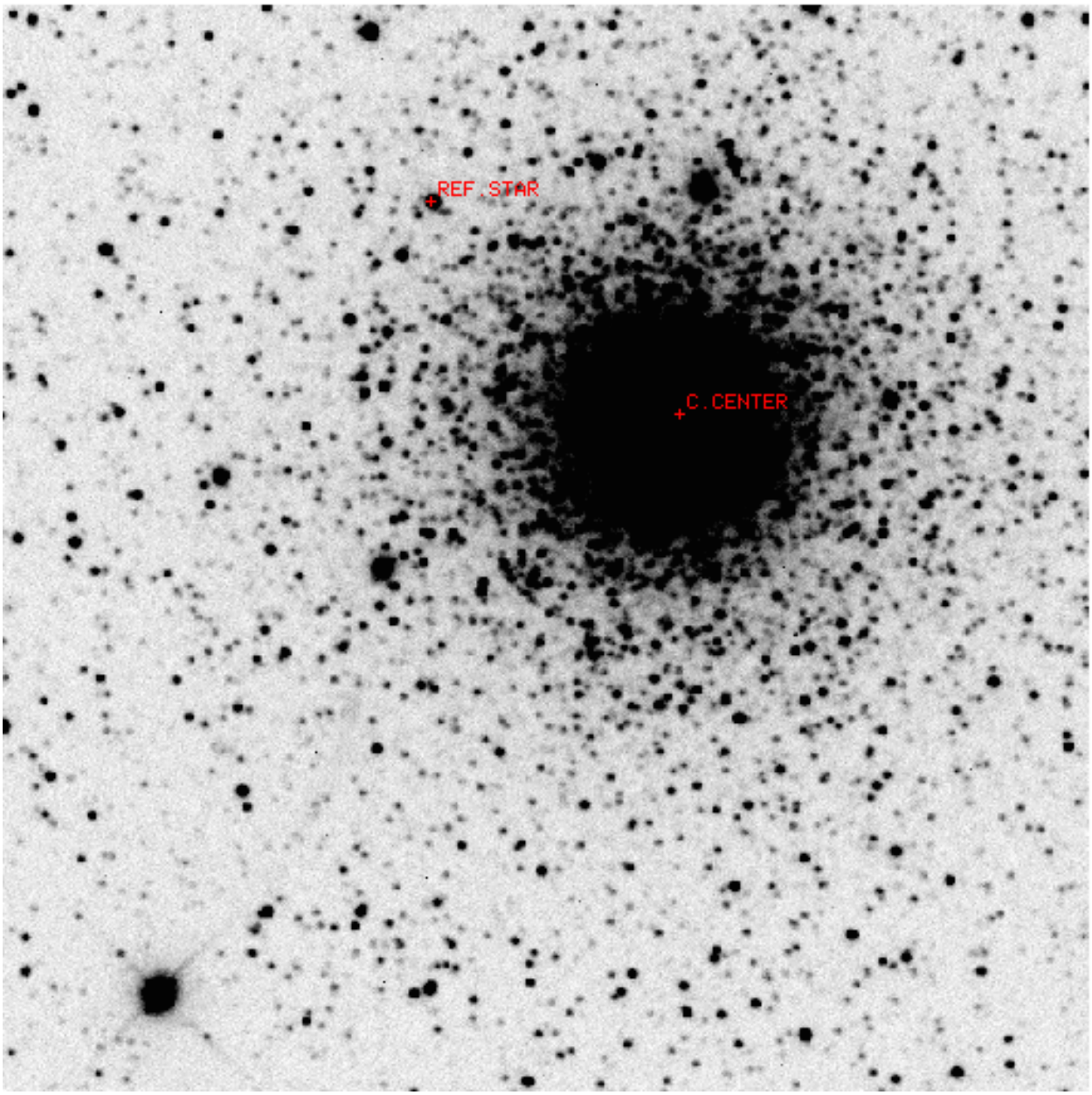

Figure 3.1: Trimmed, offset version of the reference image. The reference star and estimated cluster center are marked.

As we were manually examining and effectively cataloguing all the images, we have also noted the best, low-FWHM images for later use, as well as problematic images. The problems that can render an image difficult to use were usually cloudy skies (resulting in low intensity images), high FWHM due to poor seeing, and mount-induced trailing or tracking "jumps". The last one is the most difficult for ISIS to work with, as it renders the Point Spread Function (PSF) of a star to have two "peaks" on a radial distance-vs-intensity plot.

In order to determine the area shared by most images, and thus the size/FOV of the trimmed images, we necessarily have to know the x-y coordinates of the cluster center in each image, as the shared area will be centered either on or relative to the cluster center. Having recorded the x-y coordinates of the reference star on each image, we are now able to calculate the cluster center coordinates in each image through simple arithmetic. Assuming that the distance between the cluster center and the reference star is constant, the difference in x-y coordinates is also constant. This assumption is accurate enough for rough alignment of the images, as ISIS' interpolation routine can correct for the remaining distortion.

As finding the exact cluster center would require using its celestial coordinates, and as the images' built-in coordinate information is not of sufficient accuracy, we have opted to estimate it. First, we chose a reference image taken from the set of best images. This image, a trimmed version of which is shown in Fig. 3.1, will be the main reference in all subsequent steps relating to alignment, and thus all coordinates will be derived from it. Viewing the reference image at different display contrast levels, the central blended region of the cluster will *appear* to be bigger at different contrast level values. This is due to contrast level changing how brightly pixels are displayed according to their value, an effect akin to changing the exposure length of a photograph (without the commensurate loss of data). Assuming the central region is circle-

shaped, we estimated the horizontal and vertical edges of that region, where stars can be differentiated, and used the midpoint to determine the center for that image scale. By taking the average of those coordinates, we estimated the centroid of the bright inner regions, and in turn the center of the cluster. The estimated (but offset) cluster center is marked in Fig. 3.1. Now that the x-y coordinate differences between the cluster center and the reference star, Δx and Δy, are known, the arithmetic needed to find the center in the other images is rather simple:

$$x_{center} = x_{ref\ star} + \Delta x$$

$$y_{center} = y_{ref\ star} + \Delta y$$

We can now use the list of reference star coordinates to calculate where the cluster center is located in each of the different images, and display them on a plot so as to help determine a suitable size for a shared trimmed image size/FOV. Dr. Layden has written a FORTRAN program that takes the "catalogue" we have made earlier as input and outputs a shortened version of it: essentially a list of the cluster center coordinates, image name and FWHM of each individual image. After plotting these coordinates on a scatter plot (see Fig. 3.2), we found that the images differ widely in where the cluster center lies in their field of view. The plot was then used to determine an ideal-sized trimmed image/shared FOV. However in the course of our research, we have had problems getting ISIS' image interpolation routine (which aligns the images more finely) to work on most of the images. The image interpolation routine will be explained in more detail later, but in short it was later discovered, after experimenting with different reference image settings, that it was correlated to how offset the cluster center was from the center of an image. As such, we have opted to offset the cluster center in the trimmed reference by (77, 76) in the x,y coordinates respectively, while setting the final trimmed image size to be (623, 623). The trimmed, offset reference image is shown in Fig. 3.1.

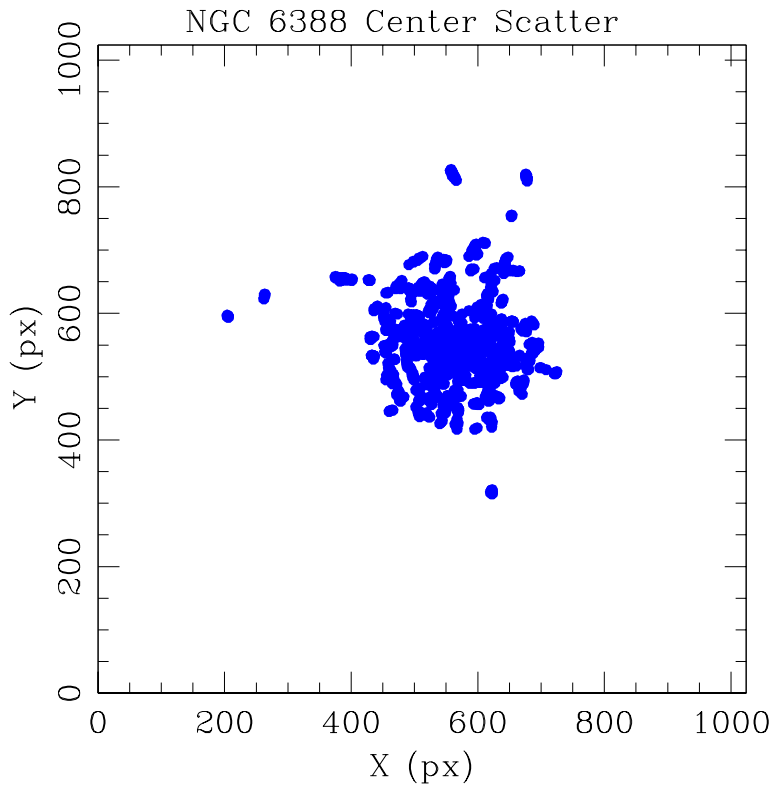

Figure 3.2: A scatter plot of the location of the offset cluster center in all images. Offset performed to combat an image interpolation problem.

The exact size and offset of the trimmed image was determined with the use of a FORTRAN program by Dr. Layden. The program's main purpose is to output a list of commands that effectively trim the images, and the command lists themselves include information on which parts of the image to trim. The program takes the reference image center coordinates (which was shifted to fix the interpolation problem), the list of center coordinates of all images, the full image size, and the desired image size as input, and then produces an IRAF script (a list of preformatted *imcopy* commands) that suitably copies a part of each image into a new, smaller one. This list of commands contain the x, y coordinates of the pixels bounding the "box" to be preserved in the form $[x_1:x_2, y_1:y_2]$, which have values of 0 or 1024 when reaching the edges of an individual image. If the size of this box is smaller than our desired image size, the program flags it, indicating that our desired size is too large due to that particular image's

FOV not including the areas of the cluster we have chosen, and thus has a partial view (hence we refer to them as “partial images”). Using figure 3.2 as a guide, and iterating the program with different trimmed image sizes, we have settled on a final image size of (623, 623) (equivalent to a FOV of 6.13 by 6.13 arcmin) as a good compromise between a wider view and the number of images that are “partial”; The partial images are only 3.13 percent of all the images. The trimmed, offset reference image is shown in Fig. 3.1.

The images can now be trimmed to a smaller but suitably sized partial view of the (now offset) cluster that we have made sure is shared across a large majority of the images. The list of commands output by the program is executed, in effect trimming the images in a single batch, rendering them roughly similar to the trimmed reference image. The list’s flagged partial images are then modified in order to be usable in ISIS; in those images, which have a region of the cluster outside the CCD FOV, the median background sky value along the edge of the trimmed edge is chosen to fill in the missing portion with use of the *imcopy* and *imarith* commands.

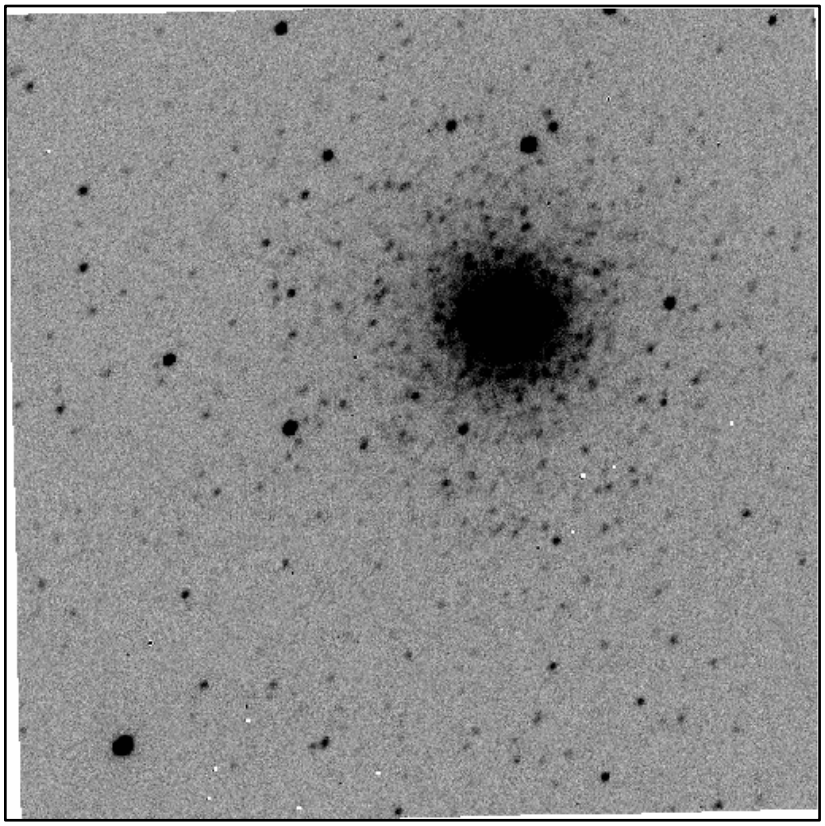

Figure 3.3: Example of a badly interpolated image with zero-value white box masks.

The final modification, before entering the images in the ISIS processing pipeline, involves modifying the pixel values of the images. First, the CCD can measure linearly up to a pixel value of ~50,000 ADU (Analog/Digital Units, a measure proportional to how many electrons were excited in a pixel) so we must cap higher pixel values at 50,000 ADU in order to not use nonlinear data for photometry. The cap is easier to deal with, as it can be considered to be a saturated pixel, and it was done using the IRAF *imreplace* command. In addition, none of the variable stars in our FOV were saturated or had pixel values bigger than the linear limit, thus we did not lose any data.

Second, ISIS works on FITS images whose pixel data is in the short integer format (± 32,768 or $\pm 2^{15}$ ADU), which is remedied by multiplying the pixel values by 0.65532 using the *imarith* command. For reasons that are related to the ISIS interpolation routine, a further step

was added: a floor on pixel values was set, where pixels with values of 1 or less are set to 2. This was done to suppress the white box masks (areas of zero value that are discontinuous with the rest of the sky background, see Figure 3.3 above) that appeared after ISIS interpolation when background sky levels are below an intensity of 2.

3.2 ISIS Processing Pipeline

CCD-based time series image subtraction photometry is simple in principle: a time series of images of a group of stars is taken. They are compared to each other and, using reference stars that are believed to be of constant magnitude, variable stars are identified. Subsequently, their degree of change can be inferred via image subtraction: the object image is subtracted from the reference image, producing the flux difference. Periodicity characterization is then possible by plotting flux difference change over time. Taking observations in different filters was also done, enabling us to observe the brightness change in different wavelength ranges. This is useful because light curves of a star taken in two different filters should behave similarly, serving as a check on the photometry.

That said, in practice a number of problems occur that make image subtraction photometry non-trivial: CCD cameras introduce noise to signals, and the signals themselves were affected by the atmosphere. This includes astronomical seeing, which determines the FWHM of stars observed from Earth, as it causes the stars' images on the CCD to blur and scintillate. This broadens the area over which the signal is received and thus determines the FWHM for a given image. The atmosphere also introduces variable transparency and sky brightness issues from image to image. This means that even images taken through the same instrument are not perfectly identical to each other as to enable a simple image subtraction to take place.

The final obstacle is that the stars being studied may be close enough that their seeing disks blend together, as in our case, in the central region of NGC 6388. This final problem is the main motivation for using image subtraction; even though it can't be used to determine standard magnitudes, it can study stars that are close enough for their PSF patterns to blend, as can be seen in Fig. 3.4 below.

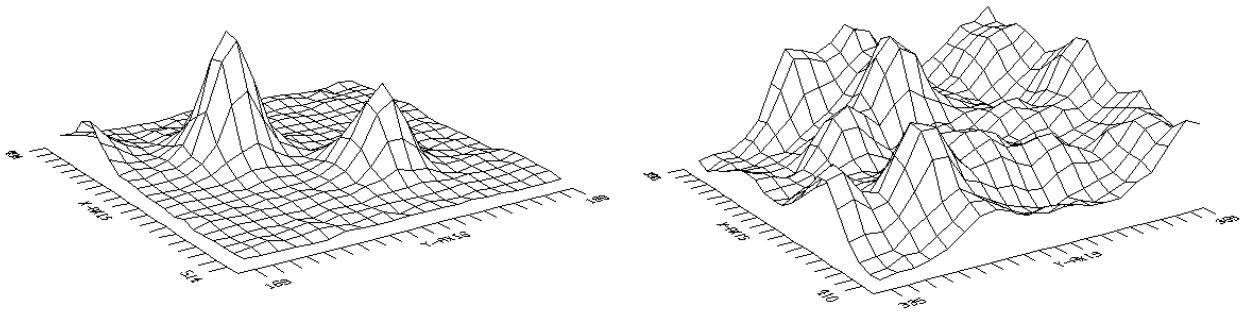

Figure 3.4: IRAF surface plot of pixel values from one of our typical NGC 6388 images, PSF patterns separated on the left, blended core stars on the right.

The ISIS image subtraction package is a difference image analysis (DIA) based photometry software suite that is designed with the aim of minimizing the above problems while also dealing with a large number of images. Written by Christophe Alard (as detailed in Alard, 1998 and Alard, 2000), the software is primarily based on 2D image convolution and subtraction, and works using a set of programs or routines that process the images in a series of steps, with human input and parameter modification needed in between them. We have used version 2.2 in our work, as explained below with an outline of the routines, and the work done to make it work with our images. The three exposure types, V, I_L, and I_S, were processed as separate sets (a requirement for photometry, as explained earlier).

The first step, before running any routine, is setting up the program by providing a list of information on the images. This list should include the name, date, and FWHM value of each

image. In our case, we already have each image's name and FWHM from the cataloguing step, but the dates required more work.

The Julian Date (JD) format used in each image's FITS file had to be converted into Heliocentric Julian Date (HJD) format. This is because JD is Earth-centric, whilst HJD is Sun-centric, which can affect the accuracy of periodicity measurements of the RR Lyrae stars. This occurs due to the Earth's position in its orbit affecting the oncoming light travel time, and thus the observation time of the star, on the order of minutes. Thus RR Lyraes' short periods (7-24 hours, but regular to the level of minutes) might not be determined to sufficient accuracy without using the correction included in HJD. After adding the observatory location to all images' FITS files headers, the HJD was calculated with the IRAF *setjd* command, which uses the JD and location to calculate the correction and adds the resulting HJD to the headers. The *hselect* command is then used to extract the HJD from the headers, as well as the image names. Combined with the FWHM from the catalogue step, we now have the list in a suitable format.

The first routine, *interp.csh*, registers the images. It does this by performing interpolation in order to align them, correcting for small shifts, distortions and rotation differences to make each image as close to the reference image (Fig. 3.1) as possible. This is necessary for the later subtraction step, which requires the stars to have consistent locations across the whole set of images The reference image chosen was identified in the cataloguing step detailed previously, and was chosen for exceptionally high contrast (due to low FWHM and sky background values), and round, stellar images. Three such reference images were chosen, one for each image filter/exposure subset (i.e. V, I_L, I_S).

The interpolation works by selecting a large set of stars on the reference images, and then this set is searched for in the object image being interpolated. In our case, usually 100 to 300 of

the 400-star set are found in a typical object image, with lower numbers corresponding with worse seeing as fainter stars are lost. A two-dimensional polynomial (of order chosen by user) is then fitted to transform the coordinates of the stars in the object image to their coordinates in the reference image. The object image is then resampled using bicubic spline interpolation. The interpolation shifts the original pixel onto a new grid of pixels by interpolating new pixel values based on the old pixel values, which results in an image that sufficiently aligns with the reference image to perform image subtraction later on.

At the first interpolation attempt we ran into the problem of having a very small number of detected stars, no more than 12, for all interpolation attempts. This is much less than the 100 or more stars typically required for a good interpolation, which resulted in a large number (~30%) of failed image interpolations (an example of which is shown in Fig. 3.3). After attempting multiple permutations of the FOV (size, orientation and center) and order of polynomial on test sets of images, we have found that, as explained in above in section 3.1, shifting the cluster away from the center of the image solved this problem. The number of stars increased from the order of 10 to the order of 100 and above, and the interpolated images showed an improvement in quality: significantly less distortion and more stars with consistent positions, and experimental runs of the subtraction step (details below) produced cleaner and more useful subtracted images.

Lacking detailed knowledge of the interpolation routine's algorithm, we can only speculate about the cause. As this was solved by offsetting the cluster center from the image center, and as the number of detected stars rose as the offset was increased at a greater rate than when increasing image size or changing orientation, the problem was probably caused by the isotropic distribution of stars around the cluster center. Further conclusions require more details

of the routine, but this somehow "confused" the routine and caused a smaller number of stars to be detected as shared between object and reference images, which then reduced the accuracy of the interpolation.

Having solved this problem, the routine was tuned to produce the best possible interpolation given the large set of images involved, and after some experimentation, we settled on the polynomial fitting to be first order. Second order polynomial fitting, the default setting of the routine, was found to be especially problematic, as it produced significant warping in interpolated images; the coordinates were transformed as to produce an image with a visually discernable distorted grid, as compared to the source image. It is possible that the large number of stars may have induced an overcorrection in the fitting. Before moving on, we inspect an interpolation log produced by the program, which lists the images along with the number of stars detected, and the amount of correction involved in the fitting. Those images with fewer than 100 stars detected and/or a large degree of correction involved (measured in pixel difference from original location, values greater than ~ 0.3 pix as stated in interpolation log) were inspected visually and, if found to be badly interpolated, were then removed from the images list. The ratio of rejected images, including images rejected in the cataloguing step, is 2.54% of the total.

In one case, one night's *V*-filter images had an unusually short exposure length (6 seconds) that produced a bad interpolation due to the stars' pixel values being below the interpolation routine's detection threshold. They still had salvageable data on some of the brighter stars, and were at the beginning of the observing season and thus important to save, so their original pixel values were increased using the *imarith* command. Multiplying the pixel values by 10 to compensate for short exposure, and adding 300 to lift the minima closer to zero, worked to produce a useful interpolation.

Before the rest of the processing routines are detailed, image convolution as used in ISIS needs to be explained in detail. It is used to transform a given image's seeing conditions into roughly the seeing conditions present in a given reference image in order to perform differential photometry. Convolution is generally defined as a mathematical operation by one function *f* on another function *g*, producing a third function *h*. Function *h* can be an altered version of function *f*. A 1D example of convolution from signal processing theory is shown in Fig. 3.5a below, where *f* can be thought as the object image being operated on by *g*, the 1D convolution kernel matrix, to produce *h*. Mathematically speaking, the operation differs from simple multiplication

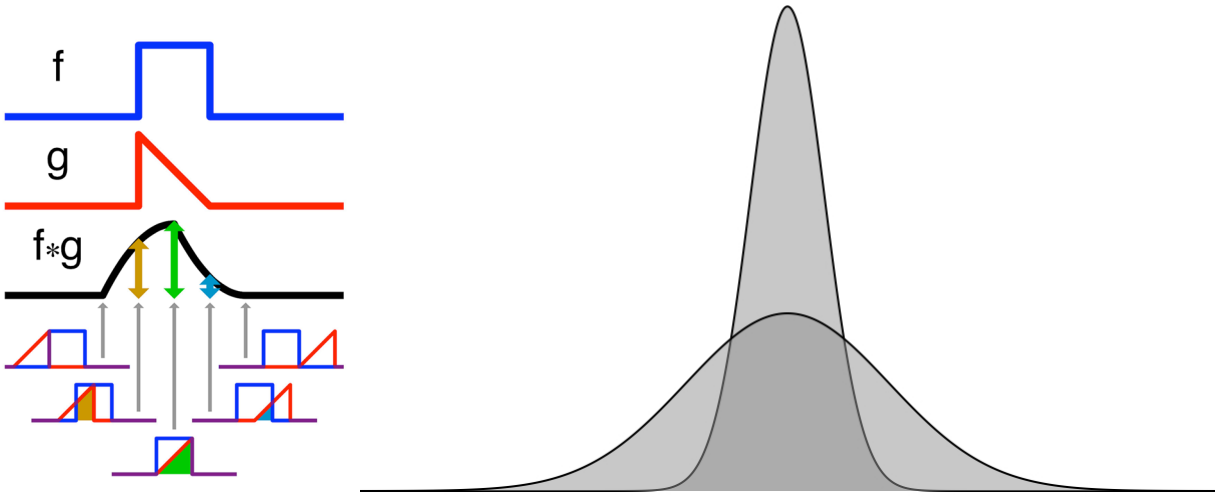

Figure 3.5: Left to right: (a) 1D example of convolution (Author: Cmglee, Wikimedia Commons), (b) Contrast between a "sharp" low FWHM PSF and a "blurry" high FWHM PSF, approximated with Gaussian functions. One can be convolved into resembling the other.

or addition, in that it is a weighted average that takes into account not merely the point (or matrix element in 2D) being operated upon, but also the value of its neighboring points. This can work to produce a running average or smoothing process that "blunts" the edges of points or, the opposite effect, highlighting or "sharpening" them.

This concept can be expanded into 2D convolution. In essence, it is an image processing technique that relies on transforming one image, considered as a set of values mapped to a plane grid, into another one by a convolution kernel, a matrix. We need to convolve a reference image *R* using kernel *K*, as to be minimally different from object image *I*, and do so on an individual basis. In terms of least squares, we minimize the sum:

$$\sum_i([R \otimes K](x_i, y_i) - I(x_i, y_i))^2 \qquad (1)$$

The normalized kernel *K* in the case of ISIS is approximated as a matrix[1] of functions, each of which is composed of a finite[2] basis set of Gaussian functions multiplied by 2D polynomials as described in in section 3 of Alard (2000). The matrix of such functions is thus a linear system and easy to solve using least squares (Alard, 1998). The Gaussian functions are also normalized between separate images, so a kernel can only minimally transform a variable star's PSF function so as to account for seeing differences, sharpening or smoothing in order to achieve a desired FWHM. Fig. 3.5b shows an illustration of different Gaussian functions that can be convolved to achieve this. This preserves the variability, while being able to transform images of different seeing conditions into roughly the same seeing conditions.

2D Convolution is the principle behind most filters used by photographers when editing digital images, and thus an analogy can be drawn as to illustrate: we are effectively "blurring" the reference image when the object image has worse seeing and higher FWHM and, conversely, "sharpening" the reference image when the object image has better seeing and lower FWHM, and to do so using a kernel that is a matrix of functions. This is done separately over each sub-area of the reference image, such that an individual sub-area of the transformed (that is to say,

[1] In practice, ISIS subdivides the image into smaller sub-images in which the convolution is done independently. Thus there are actually multiple such matrices per image.
[2] We've used the default value of three terms in the basis set, which was sufficient for our data.

convolved) reference image resembles its equivalent sub-area in the object image as closely as possible, while still preserving the evidence of variability.

Before convolving the reference image to the seeing conditions of the object images (in the image subtraction step detailed further below) , a *master* reference image needs to be created. Even though we already have an excellent reference image, being just one image means that it would have comparatively more noise, and possibly defects, than a composite reference image. Using the *ref.csh* routine, a set of images of great quality is combined to build the master reference image. We have opted to use combined images made using the best nights in our research, totaling 14 combined images per exposure type, and were created using the IRAF *imcombine* command. Nights chosen were usually the ones with the best seeing, but other factors were also taken into account: low sky background, saturation level and very low tracking errors. The advantage of using combined images is the increase in SNR, the amelioration of individual image defects (e.g. hot pixels, cosmic rays) and sampling artifacts.

The master reference image is built in a way that is somewhat the reverse of the image subtraction step described earlier, in that it is the 14 combined images that are convolved to match the reference image. This process of convolving images of higher FWHM (due to being combined, and of worse seeing than reference image) to lower FWHM will involve some inevitable inaccuracy due to extrapolation, but it is a tradeoff and has the additional benefit of improving the SNR in the resulting reference image. Once the images are transformed to match the reference image, each individual pixel's outlier values (as present in different images) are rejected (using a 3-sigma difference from the median condition) in order to rid the images of defects or anomalies, and are then stacked, producing the final master reference image. Three

such master reference images were built, one for each image subset (V, I_L, I_S), using the reference image and combined images from that respective subset.

The *ref.csh* routine produces a better reference image than that produced by simply stacking the images; stacking would preserve any remaining defects, and blur out the stars' PSF by adding images of different seeing, while the *ref.csh* routine convolves them to match the seeing/FWHM in the reference frame first, which is less detrimental to the PSF after stacking, and rejects possibly errant pixel values.

The critical step in the program, *subtract.csh*, is then used to subtract the object image from the master reference image. This cannot be performed directly, however, due to seeing differences, and thus differences in FWHM, which would not translate to accurate flux differences. The routine solves this by convolving the master reference image R, using kernel K, to be maximally similar to object image I, after which the object image is subtracted from the transformed master reference image. This transformation changes the FWHM in the master reference image to be closer to that in the object image, in effect matching the seeing conditions. This operation is repeated for all object images, each subtracted from its unique, transformed, master reference image. This may cause some distortion when convolving the master reference image into better seeing, as it is extrapolating from high to low FWHM, magnifying the noise in the center while ignoring the data at the edges of the larger FWHM. This can occur because, despite being the master reference image, its FWHM has been degraded somewhat by it being the product of the combing of multiple images, and these images *themselves* being of combining individual images.

With the subtracted images now available, the *detect.csh* routine is run to view the areas of variability. This routine does not simply stack the subtracted images, however; doing so will

average out the variability, and even if the absolute value of the pixels is taken, that might stack defects caused by hot pixels and cosmic rays. To reduce false detections, a robust method to remove outlier pixel values while also preserving true variability is needed. For each individual pixel the routine calculates the median value, and then generates a series of absolute deviations D_n:

$$D_n = |x_n - m| \qquad (2)$$

where x_n is the pixel value in the subtracted image, and m is the median value of that pixel across all the subtracted images. The series is in order of descending value (D_1 is largest, D_2 is 2nd largest, and so on). The rejection criterion, as programmed by Alard, is as follows: if half of D_1 is larger than D_2, then both[1] D_1 and D_2 are removed from the series. The remaining series members are then used in recomputing the median m, and in turn using m in computing the mean absolute deviation M:

$$M = \frac{1}{N}\sum_n^N |x_n - m| \quad (3)$$

where N is the total number of an individual pixel's non-rejected values, as taken from N subtracted images. This ensures the deviations are within a reasonable range of values of each other, as would be expected from true variability.

The routine outputs two variability image files, *abs.fits* and *var.fits*, whose pixel values are the mean absolute deviation M and the mean of the absolute normalized deviations M_{norm}, respectively. The mean of absolute normalized deviations is calculated as follows:

$$M_{norm} = \frac{M}{\sigma} = \frac{1}{N}\sum_n^N \frac{|x_n - m|}{\sigma} \quad (4)$$

[1] The lower value absolute deviation that is compared to D_1 can be modified (e.g. D_1 can be compared to D_3 rather than D_2), but we have opted for the default option due to success in obtaining clean variability images (see Fig. 3.6).

where σ is the standard deviation of the retained values of a pixel. These images thus indicate areas of significant variability in pixel value, and were used to detect variable stars. After some memory problems prevented the program from performing the routine on all the images (~700 for V and I_L images), we have settled on using two smaller subsets of all available images: a ~500 subset of best seeing, best interpolated images and a subset containing the 14 combined images used in making *ref.csh*. Both sets span a wide range of time, which ensures that no variables will be missed due to long periods, and were compared against the other due to the better contrast afforded by the small set and the larger set's lack of false positives. Although the smaller number of I_S images did not run into a memory problem, the shorter exposures did not provide any variable detections that were not found in the I_L images. For V, I_L and I_S, the respective *var.fits* image tended to have more contrast than the respective *abs.fits* image, in that new variable detections were much greater in value than the background noise, and thus *var.fits* is more useful for finding the variables. The four final images that were used for variable detection, all produced by running *detect.csh* four separate times (on two subsets of V and I_L images, respectively), are displayed in Fig. 3.6 below. They are the *var.fits* images produced for V and I_L when using the best seeing image subset, and the combined image subset.

As can be seen, the images are not devoid of artifacts, especially around the edges and the brighter, saturated or almost saturated stars. The defects are identified by their square appearance or their location on the edge. These defects affected the output of the next routine, *find.csh*, which uses the *var.fits* images to automatically find the locations of candidate variables, and produces a list of pixel coordinates for such suspected variables (output as file *phot.data*). The significant threshold parameter, which determines the minimum for detection, was adjusted so as to avoid most of the artifacts and noise, while a FORTRAN program written by Dr. Layden was

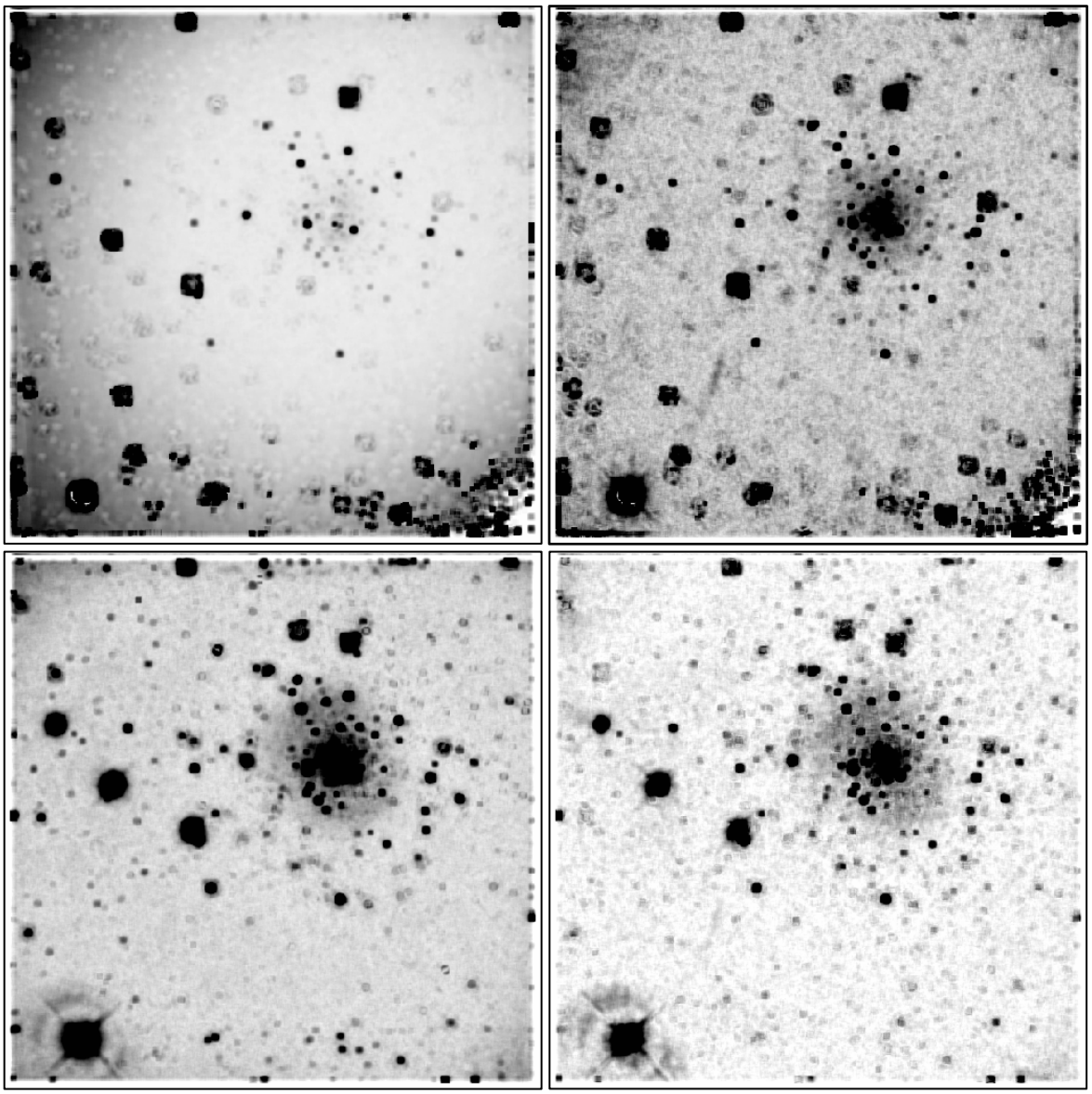

Figure 3.6: *var.fits* images showing suspected variability. Top row is V, bottom row is I_L. Derived from a subset of best and combined images in left and right columns, respectively.

used to automatically remove the edge and bright stars artifacts from the candidate variables lists (built using the V images and I_L images). These two lists are then correlated; in order to identify each respective variable star's pixel coordinates in the V and I_L images, those pairs closest to each other are deemed to belong to the same possible star. There were candidate variables only present in one set of images, but after investigation using the photometric data for signs of variability, it appears three suspected variables were found.

In addition to automatically detecting variables, an attempt was made to manually recover the signal of known variables that were not detected. This was done by transforming known variables' celestial coordinates into the respective pixel coordinates of our master reference image, and adding them to the list of positions to be analyzed. This required plate-solving the master reference image, the process of which is detailed later (in section 4.2.2).

Finally, using the aforementioned list of pixel coordinates of detected and known variability, the *phot.csh* routine is used to produce the differential flux photometry data. A method that is usually used to measure the flux directly, PSF fitting, is used in ISIS on the areas of the subtracted images where candidate variables are located, in which case, the difference in the PSF from the master reference image (to which other images are compared) can be fitted to get the flux difference. The routine's critical parameters that govern the fitting are *radphot* and *rad_aper*, which are defined by Alard (personal website, ISIS tutorial) as "the photometric radius, or the radius of the circle within which the pixels of the object will be fitted in order to estimate the flux (…), and the radius for the flux normalization".

These parameters were experimented with in an attempt to produce results that were consistent with the physical behavior of known variables that were previously studied in the literature generally, and by Cardona (2011) specifically (as that research use some of the same

data as ours). In addition to ISIS, Cardona also used DAOPHOT, which relies on aperture and PSF fitting photometry. This allowed us to see if our parameters had been able to reproduce the characteristic behavior of known LPVs using the same data (from 2009 and 2010) but using our theoretical framework. We have settled upon values of 4 pixels and 8 pixels for *radphot* and *rad_aper*, respectively.

CHAPTER 4. DATA ANALYSIS

The photometric data as output by ISIS needs to be consolidated and analyzed, and the sources of variability examined and, if possible, identified. The known stars must be identified based on their positions first, and characteristics of periodic behavior second, by comparison against findings in previous work. If the stars are new findings themselves, with no mention in the literature, their celestial coordinates are to be determined and periodic behavior characterized quantitatively and qualitatively.

This chapter covers how this was done. Initial results are also summarized, while the individual variable star findings are listed in chapter 5.

4.1 Photometric Data Consolidation

Just getting the photometry is, of course, not sufficient for a full characterization of the variable stars. First, the photometric data have to include some measure of uncertainty if the results are to be interpreted correctly. This measure was estimated by taking advantage of the fact that our individual object images for each night were not combined (save when building the master reference image), enabling the use of multiple data points of a star's intensity at a given night to calculate a standard deviation. This calculation was done en-masse by inputting the photometric data of a suspected variable star, as produced by *phot.csh*, into a FORTRAN program written by Dr. Layden, which then outputs a modified version of the photometric data.

This output is a list of the median and standard deviation photometric values for each observation session, as determined from that session's respective differential flux measurements. Observations are grouped into their individual sessions on the basis of a user-specified time range, which sets a maximum value for gaps between observations. We've set the range to 6 hours, which proved sufficient in grouping nights together, as the largest separation between

same-night observations encountered in the data was found to be ~5.5 hours. It was also small enough that observations cannot be far enough apart to distort LPV and longer SPV period values.

Not all variable star data were averaged over 6 hours; data from RRL and certain W Virgins variables, with periods shorter than 48 hours, can undergo significant distortion if averaged over such a range. This is taken into account by averaging them over a range of approximately half an hour (exact value was 0.499992 hour). This value was chosen as it fits the typical length for an uninterrupted observing session. Thus, if a session is interrupted by a higher-priority observation request, the interrupted images' photometric data would be treated having different observation time.

The data can now be plotted as showing median values with standard deviation bars as an indicator of measurement precision, and consequently of how much confidence we can have in the star's variable behavior as described in the plots. The plots are either regular light curves of the star, which are plots of measured flux difference versus time, or folded light curves, which are a function of phase rather than absolute time (see Fig. 5.11 for examples of both curve types). The analysis and plotting of the periodic behavior is explained in further detail in section 4.3.

The Phase-Dispersion Minimization (PDM) routine is used more thoroughly in section 4.3 to give accurate period values as well as variability and error values of the period of variable stars, but its first use is to give a rough assessment of the nature of the photometric variability: Is it physically real, or just an artifact of ISIS' double use of convolution that was wrongly detected by *find.csh*? Can it be usefully interpreted? If so, is the source an SPV or LPV star? What, roughly, are the type and period of said star? This gives us an understanding of the variable

behavior of the source, and if it appears to behave like a variable star, we can then proceed to possibly identifying it.

4.2 Star Identification

These and other obstacles were overcome with a combination of methods. For positional identification, we cross-referenced with variable star finder charts of differing image scales that were available in the published literature. To use the charts, they were compared by eye against a suitably magnified and oriented portion of our master reference image, with suspected variables' position marked as appropriate given stellar density; the use of individual pixels as markers, for example, was done when examining the densely populated core region (see section 4.2.1).

As a second check based on published star coordinates, and to determine the coordinates of new variable star candidates, an accurate coordinate mapping of the master reference image was done using Digital Sky Survey (DSS) reference stars and IRAF. This coordinate mapping was then used to generate pixel coordinates of the known variable stars in our FOV, which were then compared with known variables' (ISIS-produced) coordinates, both as a check on identity, and as a check on the accuracy of the mapping (see section 4.2.2).

The stars' positional identities were then compared against Cardona's (2011) findings as both an additional check, and in order to identify any deviations from the literature and thus enable correct use of his two-year apparent magnitude data (see section 4.2.3).

Finally, variable behavior-based identification was also done as a consistency check on our identity list where possible: quantitative and qualitative periodic behavior as available in published work, and in Cardona's, was compared to our own measurements (see section 4.2.4).

Where star identity cannot be determined with confidence using a particular method (e.g. the star charts), the next method in line (positional coordinates, to continue the example) is used

to help narrow down which of the known stars we have detected, rather than merely to exist as a check of the method before. If all methods have been exhausted and no known stars with the characteristics that have been observed can be identified in the location of detected variability, it is considered a candidate variable, with potential to be later classified as a suspected or new variable in cluster.

4.2.1 Star Charts

The primary positional identification of detected variability sources is done using finder charts. Due to the modest 0.41 m aperture of the PROMPT telescope, the image scale (0.59 arcsec per pixel) is larger than that of typical professional telescopes (e.g. 0.2 arcsec per pixel for a 4 m aperture), complicating the use of published finder charts. This low resolution meant the suspected variables were closer together, and sometimes hard to distinguish, especially in the blended central region of the cluster, where star density is high enough that multiple variables were detected only a few pixels apart.

After verifying that a particular source is not due to noise or image artifacts by inspecting its photometric data plot (light curve), its position in the *var.fits* image (is it too close to a brighter source or edge) and SNR (can we rely on the data?), the identity of the suspected star is first checked using finder charts in the literature to see if it was already known or suspected to be a variable or candidate.

The finder charts used for the initial identification of LPVs were by LEM (1973, 1977). Although LEM's finder charts are the oldest, and thus the lowest in terms of exposure and resolution due to the use of photographic plates, they had wide FOVs of roughly 4 arcmins, and were able to capture the brightest LPVs on the outer regions of the cluster. These LPVs can be quickly and confidently identified by virtue of their relative brightness, sparsely populated

surroundings, and easily discernable locations relative to nearby star patterns. They were therefore used as initial reference points for correlating other positional identity sources against each other when possible. All known variables in the LEM chart were in our analysis FOV, and were found successfully as detailed in table 4.1 at the end of this chapter.

Next, the finder charts in Pritzl et al. (2002) were used for almost all the SPVs and some of the LPVs. The study's finder charts were of different FOVs, and only marked the variables detected by the study. The study was chosen due to the fact that it included the most up-to-date charts that encompass the entire cluster at moderate resolution. The study also included periods and light curves for some variables, thus presenting linked position and periodic behavior data to compare against our own as a consistency check, as detailed in chapter 4.2.4.

We have listed in table 4.1 the known variables identified using the charts. A majority (65%) of the stars in the Pritzl charts that were also within our analysis FOV were identified. The known stars that could not be identified in our detections were either outside our FOV, were not detected or were manually rejected due to other issues (being too near the artifact-heavy edge of the FOV under analysis, being too dim, or too near a brighter star to yield useful photometry). The star V19, first mentioned in HH (1986), was not detected as a variable, confirming the assertion in the Clement catalog (Clement et al., 2001) of its non-variable nature using a longer time baseline.

The Skottfelt et al. (2015) finder chart has a narrow (45 by 45 arcsec) FOV but a very high spatial resolution that made it ideal for identifying the variables in the central regions of the cluster. It also includes the stars discovered by Corwin et al. (2006) with the exception of V58, V67, and V68, all of which remain without a published finder chart.

However, crosschecking with our suspected variables was complicated by our relatively lower spatial resolution compared to that in Skottfeltet al.: 0.59 arcsec vs. 0.09 arcsec image scale, and FWHM of 2.00 arcsec and 2.36 arcsec (in our V and I_L reference images) vs. 0.42 arcsec. Thus our coordinate precision is lower, and stars' respective PSFs start to blend together in the core. This blending means detected variables' positions can be very close, in a handful of cases as close as a few pixels apart. In such cases, the blending also obfuscates the signals further, making identification, characterization and coordinate determination difficult. For such cases, the full suite of identification methods is necessary for accurate identification.

The less crowded outer regions of the core were compared first, being easier and containing two stars that were already identified using the Pritzl et al. finder charts (V29 and V58), followed by more inner regions.

Comparison in the densely populated core was helped by the use of an image editor to superimpose our detections, using known variables from Pritzl and initial photometry data as calibrators, over the finder chart. They are then compared by eye, and using pixel coordinate differences to figure out the spatial relationships between patterns of detected variables that appear similar to known variables in the chart. In the cases where a detected variable is roughly equidistant from two or more known ones, positional identification and observed periodic behavior are used to determine the correct identity.

The known stars identified in our detections are listed in table 4.1. It should be noted that a minority of the stars in Skottfelt's chart were automatically detected (29.7%), which might be expected given the Skottfelt study's greater resolving power, and signal obfuscation caused by blending. The main properties shared by the undetected stars in the core region, as reported by Skottfelt et al., are the magnitude, and amplitude of variability; the mean of average magnitude

and amplitude of stars successfully detected in the chart (12.42 mag and 0.57 mag) tended to be lower and higher, respectively, as compared to those undetected (13.15 mag and 0.23 mag). This can be due to ISIS' variability images (*vars.fits*) being the result of summing up the absolute deviation from the median. Thus stars with lower amplitudes will have their variability more impacted by noise, small alignment errors, seeing conditions, and blending, as opposed to those with higher amplitudes.

4.2.2 Coordinate Mapping with WCS

Although variable stars can be detected, their relative locations and periodicity measured, and their identities determined without reference to a coordinate system, it is still necessary to plate-solve the master reference image. Plate solving is the process of overlaying celestial coordinates onto an astronomical image, enabling the translation of pixel coordinates into celestial coordinates, and in turn positioning the imaged objects (in our case, variable stars) to greater precision. This is done for multiple reasons: as an additional check on star identity using published coordinates, as a way to identify the stars not present in any star charts (V58, V67, and V68), to enable manual photometry, and to give approximate coordinates of new or suspected variables.

The observed images come encoded with the observed object coordinates from Skynet (the PROMPT telescopes' observation acquisition and control system). However, these coordinates are not accurate enough for our purposes. They are also incomplete, in that they only position the center of the cluster, but do not plate solve to account for image orientation, scale or optical train distortion. After achieving an accurate calibration of the coordinates on our master reference image, the original reported coordinates were different by a translational error on the

order of ~10 arcseconds, as well as non-orthogonal scaling and rotation errors (due to distortion). It was too inaccurate for positional identification or coordinate determination.

We have opted to use a combination of IRAF commands, the SAOImage DS9 image display program, and open stellar image databases to plate solve our image.

Using the DS9 program "Image Servers" utility, it is possible to request plate-solved images from a database that are already encoded with accurate celestial coordinate information. The encoding is based on the World Coordinate System (WCS), defined as a standard for relating pixel positions on a FITS image file with the actual celestial coordinates on the night sky (Mink 2017, WCSTools WCS webpage). This information is placed in the "header" portion of a FITS file.

We requested plate-solved images with WCS information from the SAO-Digitized Sky Survey (Bland-Hawthorn et al., 1993). The DSS image of NGC 6388 with WCS information is not used as a direct astrometric reference due to the small image scale (~ 2 arcsec per pixel), but rather as a way to plot reference stars with known coordinates of sufficient accuracy. We used the reference stars in the USNO-A2.0 catalogue (Monet, 1998) as they are of sufficient accuracy (~0.25 arcsec) to establish our image scale, and can be requested through DS9 for our particular FOV. We started by overlaying markers for the USNO-A2.0 reference star positions on a WCS grid-encoded SAO-DSS image, and then comparing with our reference image. The DSS image chosen is centered on the cluster with a field of view of 10 arcminutes, while the reference stars are limited to those of *R*-bandpass magnitudes brighter than 15 mag. The master reference image was then matched (rotated and scaled) so as to be as similar to the DSS image as possible, star-to-star, given that the DSS image had a wider field of view and lower resolution image scale

relative to our reference image. By comparing the two images, we are able to locate the USNO-A2.0 reference stars in both.

These shared stars can then be used to plate-solve our master image. With the pair of images stored in separate frames in DS9, IRAF's built-in "imexam" profile fitting function was then used to measure the pixel coordinates of each reference star's central peak on the PROMPT master image, which was then recorded and paired with its respective celestial coordinates as acquired from the USNO-A2.0 catalogue. This process was then repeated for a total of 22 stars, which were chosen so as to be as evenly spread across the master image as is possible in order to ensure an accurate solution for the entire field of view. The acquisition of celestial coordinates is done using DS9's "catalog" mouse cursor tool on the DSS image with overlaid reference star positions.

The matched pixel and celestial coordinates pairs were then used in IRAF's "ccmap" function, which outputs a plate solution. The function works by fitting a pair of 2nd degree polynomials to transform pixel values into celestial coordinates. After discarding 4 stars with fitting errors bigger than 1 arcsecond (equivalent to 1.7 pixels in our image), we have achieved a solution with an accuracy of 0.65 and 0.89 arcseconds in right ascension and declination, respectively. The function outputs a solution file that is then encoded into the master reference image using the "ccsetwcs" function. Figure 4.1 shows the now encoded reference image with celestial coordinates overlaid.

With the coordinates mapped, it is now a simple matter to overlay the positions of known variables over the reference image. The IRAF "cctran" function is used, along with a list of up-to-date celestial coordinates of known variable stars (as compiled in the Clement catalogue), to output an equivalent list in the pixel coordinates of the reference image. The DS9 program can

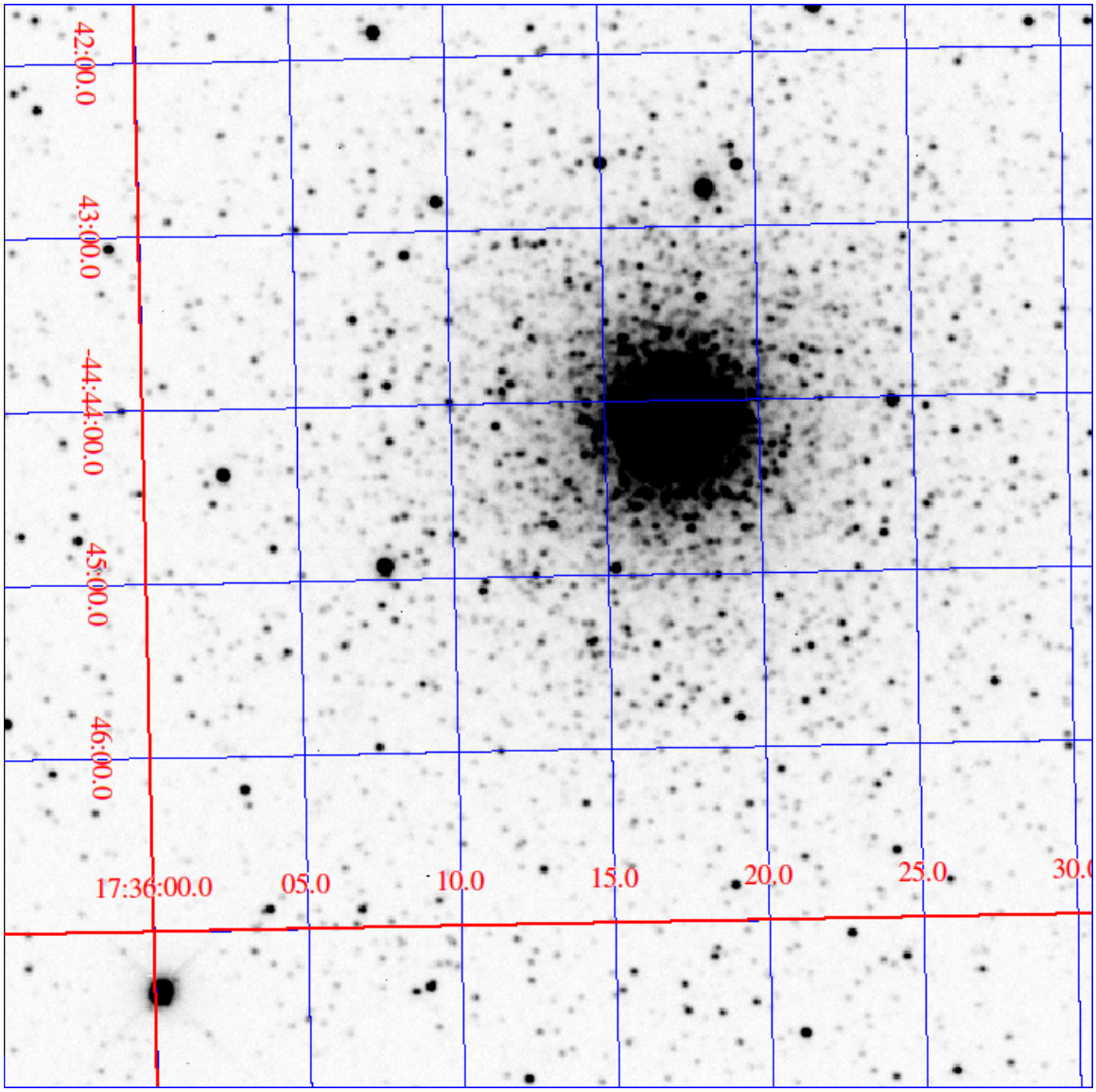

Figure 4.1: Celestial Coordinates mapped over the *V*-filter master reference image. North is up and east is right, so declination is vertical, and right ascension is horizontal, with spacings of one minute of arc and five seconds of time, respectively.

now display the positions of the known variables to good accuracy, as well as the positions of ISIS detections. The stars V58, V67 and V68 were thus located and identified, our previous identified stars checked or, in the more ambiguous cases, narrowed down to one to three candidate identities.

As a check on the precision of our coordinate mapping, we have calculated the difference between our star pixel coordinates, as determined by ISIS' variability detection routine, and the transformed published coordinates. As can be seen in column 6 of table 4.1, the error values are close to those reported by the fitting program. Of note is that the median difference is 0.8 arcsec, or roughly less than 1.5 pixels in our image scale. To further safeguard against positional errors, we have compared our findings to Cardona's (2011) work, and have used the observed variable behavior of a star as two final checks.

4.2.3 Correlation with Cardona (2011)

The variable stars we detected, both known and suspected or new, were then compared to those recovered or discovered by Cardona (2011). This was done because his work used the first two years of our data, and used ISIS and DAOPHOT to get the flux difference and absolute magnitude light curves, respectively. We can thus easily correlate our data to his using both positional and behavioral information, and refer to his magnitude measurements when needed.

Despite being detected in the same object images as some of our own (2009 and 2010), the pixel coordinates of the variables in Cardona's research cannot be used directly: we used a different reference image, had a tighter crop factor in order to accommodate a larger number of images, and had an offset cluster center in order to solve the interpolation problem. Thus Cardona's list of star pixel coordinates were shifted in the x and y axes to be correct in our reference image, which was done by the use of a FORTRAN program written by Dr. Layden.

The extent of the shift was determined using the difference in the pixel coordinates of a reference star between Cardona's reference image and our own. No rotation or scaling was necessary as the basis for his reference image was the same as our own (being chosen from the best night, which occurred in a year we had both investigated).

To link the pixel coordinates of our detected variables, as output by *find.csh*, to Cardona's (now transformed) pixel coordinates, we used a FORTRAN program. The program identifies the closest pair of pixel coordinates in each respective list, and outputs them. The co-identity of each star is then checked: first by eye by comparing his reference image and our own, both marked with the locations and possible identities of the variable stars, and then by comparing the light curve, as generated by our data, and a tentative estimate of the period given by the PDM routine with those in Cardona's work. We are afterwards reasonably certain that we have co-identified the same stars; in summary, 46 variable star candidates were identified as shared between our and Cardona's research, out of a total of 66 stars listed in his work. Of the shared stars, 36 are known in the literature, while 10 suspected variables remain unpublished at the time of this writing. Of the 20 stars not identified, 15 were outside our ISIS FOV.

The remaining five were not detectable or recoverable for unique reasons: First, NV26 was a duplicate detection of V5. Second, NV28 was on the edge of a bright star and Cardona noted the signal might be the result of a "critically resolved" star, as it was only detected by DAOPHOT but not by ISIS. It was suspected to be a SPV with a period of ~3.3 days. Third, NV17's location is in the center of the FWHM (~ 3 pix/1.77 arcsec on the best nights) pattern of a bright star, therefore the variability source could be due to that star's signal noise or pixel saturation. Cardona suspected that it was non-variable. Fourth, V43, an eclipsing variable possibly misidentified by Cardona as NV27, was weakly evident in our variability images

(*var.fits* and *abs.fits*), but was not detected automatically by *find.csh*. This is likely due to V43's dimness, as its maximum (~18.4 mag in *V*-band) is fainter than the minimum of our dimmest detection V26 (an RRc Lyrae with a minima of ~17.8 mag in *V*-band). Fifth and finally, V69, a W Virginis SPV star, was neither detected nor recovered. It was reported in Cardona's work with coordinates and periodic behavior that differ from those reported in the literature: in his work coordinates were offset by ~10 pix (5 arcsec) from the published location, and the period was ~18.03 days while literature values were ~ 3.6 days (Corwin et al. (2006), Skottfelt et al. (2015)). It's possible his photometric data were those of V72, which has a ~ 18 day period (as reported in the literature and successfully recovered in our photometric analysis), but erroneously attributed to V69. Our inability to detect or recover V69 is possibly due to the star's companion variable V80 proximity (within 2.3 arcsec) and brighter magnitude (12.86 mag vs V69's 14.55 mag in I-band), and V69's presence in the busy core region.

In the course of comparing our findings to Cardona's, two significant inconsistencies were found: First, V67 (a W Virginis SPV) was reported with an erroneous location,[1] and low SNR prohibited further characterization. If a novel star was in fact there, it was covered by the ISIS double-convolution edge due to our smaller FOV, and thus could not be detected or recovered. The actual signal of V67 was detected and recovered by us in the I_L exposures. It was detected ~ 4 arcsec offset from its published location, larger than the average offset of 1.0 arcsec. It also had a slightly different period than the literature (~ 2.18 days vs. 2.27 days, respectively). The star's luminosity and amplitude have yet to be published in the literature.

[1] In Cardona (2011) a variable, mislabeled as V67, was detected, but low SNR prohibited any characterization. V67 was listed with erroneous coordinates corresponding to no known or detected source of variability.

Second, V71, an RRab Lyrae SPV star tentatively identified as SV2 by Corwin et al. (2006), was detected but with such low SNR that no physically plausible periodicity was recoverable using PDM. It was detected and the signal recovered by Cardona prior to published confirmation by Skottfelt et al. (2015), but the period reported in Cardona's work differed slightly from the literature (0.8135 days vs 0.854 days, respectively). We do not know the reasons for the discrepancy between our work and Cardona's, and can only speculate that the variable's relatively low amplitude, neighboring brighter stars, and our larger image set might be possible factors for the failed recovery. Literature values of the luminosity and amplitude are 13.96 mag and 0.05 mag in *V*, respectively.

4.2.4 Periodic Behavior Consistency Check

As a consistency check, and when previous methods cannot identify a variable with a high degree of confidence, our light curves and initial period estimates were compared to those in the literature and in Cardona's work. This check was not always possible in the case of LPVs due to our own long time baseline, compared to which no published work has light curves on the same scale. The period estimates and folded light curves of such LPVs may also suffer from a low sample rate (cadence) and short time range of observations, with some known LPVs (V1, V2, V5-V13, etc.) having no published periods. That said, the information is still sufficient to serve as a check of a star's identity. The short periods of SPVs do not present such obstacles, and in most cases periods and type classifications in the literature can serve as excellent identifiers of the star, with the first given by the PDM method while the folded light curve gives the classification of SPVs. This is especially true in the case of RR Lyraes, with their periods on the order of one day enabling an accurate period determination on the order of minutes (0.001 day) or less.

In the case of LPVs, light curve examination by eye can give tentative insight regarding regularity (or lack thereof), and rough period estimates by peak-to-peak/trough-to-trough measurements. In the majority of cases, LPV and SPV, observed periodic behavior has confirmed rather than contradicted the positional identity of a star.

The consistency check results are shown in column 7 left in table 4.1. The column specifies whether a variable star "passes" the test by displaying a period reasonably within (or close to) the precision range of the most recent period value listed in the literature, or "fails" if does not. Variables with no published information relating to their periodicity in the literature could not be checked, and are marked as "NC".

4.3 Periodic Behavior Characterization using Light Curves and PDM method

The consolidation of photometric data, as detailed in section 4.1, allows the plotting of each observation night's measurements as a single point: the median value, with standard deviation bars as error bar analogs. The plots display the median relative flux vs absolute time (in HJD), or versus phase in the folded light curves. The median is used instead of the mean to reduce the influence of extreme values on a night's observations, especially in cases of imaging errors (e.g. tracking issues, seeing changes).

The regular light curve is examined by eye, and by measuring the number of cycles and period of pulsation through peak-to-peak measurement. The evidence of multi-periodicity in pulsational behavior is indicated by the presence of local minima and maxima on ascending and descending flux values, respectively. The regularity of pulsation is evidence by how uniform a star's typical cycle shape is, and although judged subjectively by eye in our work, one way to quantify the cycle-to-cycle uniformity is through the use of folded light curves.

In the folded, also referred to as phased, light curves, the values of multiple cycles are used to show the possible shape of a single typical cycle by using the equation:

$$\Phi = \frac{t_i - t_o}{T} - int\left[\frac{t_i - t_o}{T}\right]$$

to generate the curve. Φ is the phase of an observation, t_i and t_o are the date of the observation i and the earliest observation o, respectively, and T is the probable period of the variable photometric data (determined using multiple methods, as detailed later below). The *int* denotes the *integer* function, which returns only the integer part of the value in brackets.

The typical cycle shape generated is used for SPV classification in a straightforward way: a long time baseline relative to their short period, combined with their uniform pulsation behavior, means the folded light curves show little spread around the implied cycle curve. Thus, they can be easily classified on that basis. This is not the case for LPVs for multiple reasons: with longer cycles, varying degrees of regularity, possible multiperiodic behavior, and as a rule less uniform behavior cycle-to-cycle than SPVs, even for Miras.

The folded light curve can still be used to overcome the aforementioned obstacles: it can indicate regularity by the vertical spread of points at a certain point in the cycle phase. This is due to the curve being generated from the aggregate of multiple cycles, and is seen as how easy it is to discern the characteristic cycle light curve shape: a highly uniform star will have a relatively small spread around the implied cycle curve. The length of our time series has enabled us to perform this operation, one that is more commonly done on SPVs, on LPVs data. Note that the folded light curves in chapter 5 display the aggregated cycle shape twice for ease of visual inspection.

4.3.1 The PDM method

Generating the folded light curve requires a good estimate of the value of the period. The period can be determined through direct measurement but, if the star is regular enough, it can also be calculated using a more accurate and rigorous method. This is done by analyzing the photometric data, in its consolidated form for non-RRL stars, using the IRAF PDM (phase dispersion minimization) routine. First detailed by Stellingwerf (1978), the PDM method is able to give assessments of the suitability of a period value to producing a folded light curve with very small vertical scatter in discrete, separate sections or "bins" of the light curve.

The routine represents a candidate period's suitability using the variable Θ, which is a measure of how suitable a period is at reducing the aggregate per-bin vertical scatter: for a given period, it is the degree of vertical variation in the bins of the folded light curve divided by the variation of the regular, absolute time light curve. In the worst case, the variations are equivalent and Θ is equal to one, but as a candidate period approaches the correct period, the value of Θ is reduced to a global minimum. The value of Θ for the correct period is not necessarily zero due to natural scatter due to photometric detection error (that is, the ability to measure flux off a noisy image), and the star's pulsational irregularities (variation in maximum and minimum magnitudes).

The IRAF PDM routine tests a large user-selected set of periods, and displays a Θ versus candidate periods plot. An example plot, shown in figure 4.2, displays the values of theta for different period choices, with the periods around the local minima in the set being prime candidates for the true period. The PDM routine interface is also able to display a light curve folded to the user's specified period, with error bars, as a way to test candidate periods, and to determine their range of suitability.

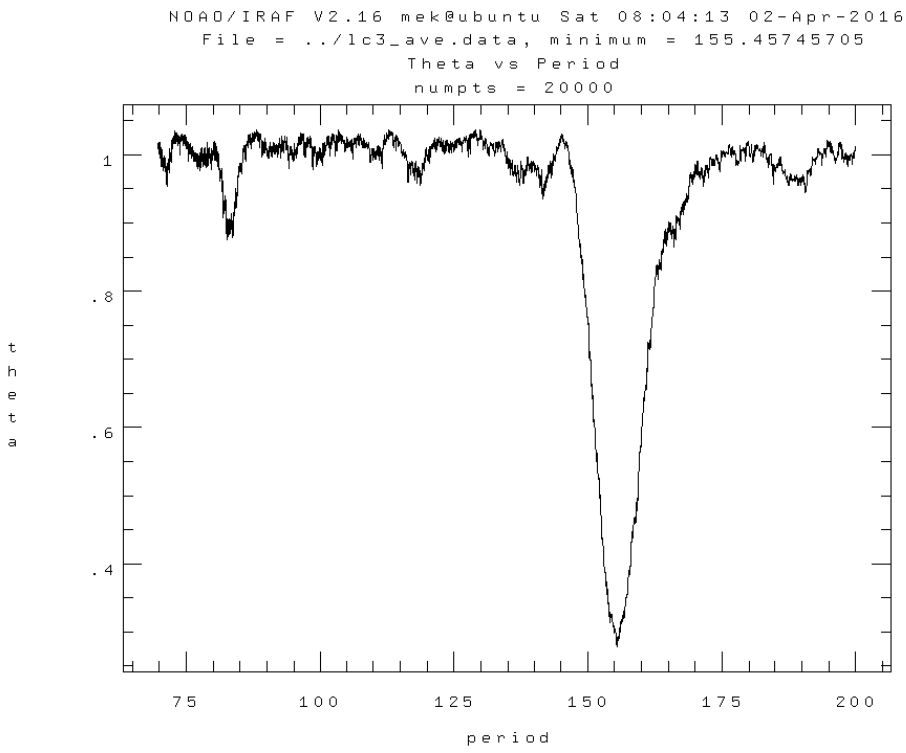

Figure 4.2: Theta vs. Period plot. Large minima at star's (V12) published period.

In our work, the PDM routine was used to give period estimates for all SPVs, and most LPVs given sufficient regularity. For LPVs, the PDM estimates are compared against peak-to-peak measurement for additional insight. We've taken the average of period values as produced from the different filter/exposure (VL, IL, IS) combination where possible. We've determined our period precision as follows: it is the range of period values in which the resultant folded light curve has a single continuous curve that is not aliased, and has sufficiently low scatter to be discerned as a prototypical light curve profile.

Aliases are artifacts of the periodic nature of the data, appearing as area of low theta on the theta-vs-period plot. They produce light curves with two or three peaks, or with non-physical peak-and-trough in the same phase. Aliases are commonly caused by trial periods that are a harmonic of the true period, or due to observational gaps combined with a small number of

observations. The latter was not noted in our analysis, which is expected given our observational cadence and long time baseline, which enabled us to observe multiple cycles at a high frequency. This resulted in not having gaps in the data of a typical cycle profile (e.g. we never lacked observational data of the ascent to the peak luminosity).

4.4 A Summary

What follows are a finder chart for the variable stars successfully detected and/or recovered (see figure 4.3) and tables listing them. Stars successfully detected and/or recovered, both known and new suspected variables, are listed in tables 4.1 and 4.2, respectively. Known stars that were neither recovered nor detected are listed in table 4.3. In total, 56 known variables were recovered, and 38 new or suspected variables were identified. Also, 65 known variables were not recovered, either because they were outside the ISIS field of view, they were too faint, or they were in the crowded cluster core.

Table 4.1: Known Variables

Star ID	Finder Chart	x (px) (V)	y (px) (V)	R_{proj} (arcmin)	Δr (arcsec)	Periodic Behavior Check	Period Observed (days)	Period Lit. (days)	Type (lit.)	Mag. (lit.)	Ampl. (lit.)	Col. (lit.)
V1	L	351.65	369.88	0.345	0.7	NC	180 ± 2.3	-	M	-	-	-
V2	L	405.15	363.43	0.283	1.2	NC	228 ± 3	-	M	-	-	-
V3	L	343.50	440.37	0.690	0.6	Pass	155 ± 2	156.0	M	8.97	0.28	-
V4	L, P	58.59	422.36	3.224	0.8	Pass	251 ± 5	253.0	M	8.47	0.80	-
V5	L	493.92	360.39	1.103	0.5	NC	99 ± 2	-	L	14.6	0.8	-
V6	L	389.36	218.98	1.615	0.7	NC	68.5 +1.7 −1.0	-	L	15.35	0.7	-
V7	L	224.16	288.74	1.826	0.7	NC	105.8 ± 1.0	-	L	15.2	0.8	-
V8	L	398.53	454.99	0.721	0.3	NC	71.5 ± 1.0	-	L	13.7	0.6	-
V9	L	339.71	474.05	0.995	0.5	NC	58.0 +0.7 −0.4	-	L	15.75	0.3	-
V12	L, P	280.58	380.19	1.019	0.6	NC	155 ± 3	-	L	14.6	0.6	-
V17	P	319.47	338.71	0.771	1.1	Pass	0.61142 ± 0.00005	0.611	RR0	16.525	0.85	V
V18	P	333.52	459.70	0.903	0.4	Pass	2.8761 ± 0.0008	2.89	CW	15.616	0.77	V
V20	P	474.38	452.20	1.118	0.7	Pass	0.46745 ± 0.00007	0.467	RR1	16.787	0.36	V
V22	P	499.48	376.41	1.136	0.4	Pass	0.58687 ± 0.00004	0.587	RR0	16.858	1.12	V
V23	P	80.18	411.58	3.002	0.4	Pass	0.33762 ± 0.00004	0.338	RR1	16.893	0.48	V
V26	P	573.20	276.25	2.136	0.2	Pass	0.23877 ± 0.00002	0.2390	RR1	17.403	0.38	V
V28	P	424.65	297.01	0.936	1.0	Pass	0.84089 ± 0.00017	0.840	RR0	16.82	0.8	V
V29	P, S	349.67	390.23	0.346	0.6	Pass	1.8653 ± 0.0003	1.8652	CWB	14.63	0.77	I
V30	P	467.52	368.04	0.833	1.8	Pass	0.95095 ± 0.00018	0.951	RR0?	16.766	--	V
V31	P	585.37	546.80	2.551	1.5	Pass	0.34096 ± 0.00005	0.341	RR1	17.031	0.52	V
V32	ND-F	*320.48*	*334.91*	0.785	N/A	Pass	0.52415 ± 0.00006	0.522	RR1	16.578	0.42	V
V33	P	493.88	525.03	1.764	1.4	Pass	0.55805 ± 0.00007	0.558	RR1	16.747	0.29	V
V36	P	429.37	409.84	0.517	0.7	Pass	3.146 ± 0.001	3.10	CW	15.558	1.05	V
V37	P	385.81	340.90	0.416	1.6	Pass	10.759 ± 0.014	10.0	CW	14.707	-	V
V46	P?	245.53	319.72	1.499	0.9	NC	NR/IRR? (low SNR)	-	-	-	-	-
V49	P	404.67	315.29	0.697	2.3	Pass	0.38425 ± 0.00005	0.384	RR1?	16.925	0.52	V
V50	ND-F	*346.18*	*422.12*	0.535	N/A	Pass	0.36438 ± 0.00005	0.364	RR1?	16.898	0.54	V
V51	P	430.80	337.98	0.639	1.7	Pass	0.39674 ± 0.00005	0.397	RR1?	16.604	0.34	V
V53	P	247.20	443.90	1.473	1.3	Pass	0.9829 ± 0.0001	0.986	RR0?	16.868	-	V
V55	P	411.97	273.69	1.110	2.4	Pass	0.49037 ± 0.00007	0.489	RR1?	16.795	-	V
V58	N/A-D	337.22	372.68	0.473	0.6	Pass	0.6826 ± 0.0002	0.683	RR0	-	-	V
V59	S	394.78	403.40	0.225	0.9	Pass	0.58890 ± 0.00006	0.5888	RR0	15.48	0.39	I
V63	ND-F	*396.80*	*380.51*	0.127	N/A	Pass	2.0376 ± 0.0007	2.038	CWB	14.64	0.73	I
V67	N/A-D	161.40	250.09	2.551	*4.5*	Pass	2.179 ± 0.003	2.27	CW	-	-	V

Continued.

V68	N/A-D	401.71	429.47	0.487	1.1	Pass	0.9370 ± 0.0001	0.946	RR0?	-	-	V
V70	S	389.42	394.70	0.125	1.4	Pass	12.386 ± 0.025	12.38	CWA	13.28	0.24	I
V71	S?	393.28	391.50	0.122	1.3	Fail	NR	0.854	RR0	13.96	0.05	I
V72	S	389.52	367.81	0.160	0.8	Pass	18.026 ± 0.034	18.01	CWA	13.08	0.82	I
V73	S	383.39	370.40	0.125	0.8	Pass	26.16 ± 0.10	26.1	CWA	12.74	1.11	I
V77	ND-F	*387.42*	*372.67*	0.108	N/A	Pass	1.8640 + 0.0007 - 0.0005	1.8643	AC	14.3	0.44	I
V83	S	353.87	350.46	0.438	0.8	*Fail*	68.9 ± 2.0, 110 ± 5	50.68	SR	12.42	0.15	I
V88	S	363.81	378.91	0.204	0.7	*Fail*	71.6 ± 1.4	58.3	SR	12.2	0.35	I
V89	S	379.63	354.34	0.286	1.2	*Fail*	59.3 ± 1.4	70.7	SR	12.42	0.11	I
V90	ND-F	*376.01*	*392.75*	0.124	N/A	*Fail*	*315 ± 10?*	70.8	SR	12.34	0.14	I
V92	ND-F	*350.35*	*376.77*	0.338	N/A	*Pass?*	*110.0 ± 2.5*	114.2	SR	12.6	0.65	I
V93	S	388.74	380.52	0.052	1.0	Pass	158.5 ± 4.0	157	SR	11.97	0.43	I
V95	S (V1)	*352.25*	*370.65*	0.337	(V1)	Pass (V1)	180 ± 2.3	180	SR	11.91	1.06	I
V96	S (V2)	*405.81*	*364.71*	0.280	(V2)	NC (V2)	228 ± 3	-	L	12.51	1.55	I
V97	S	380.92	399.27	0.162	0.5	NC	137.3 ± 3.0	-	L	12.43	0.84	I
V98	ND-F	*381.80*	*395.36*	0.122	N/A	NC (IRR?)	*158.8 ± 0.1?*	-	L	12.52	0.6	I
V101	ND-F	*393.24*	*373.61*	0.130	N/A	NC	45.6 ± 0.3	-	L	12.58	0.26	I
V102	S	360.49	413.65	0.380	0.7	*NC (IRR?)*	*49.5 ± 2.5?*	-	L	12.54	0.21	I
V106	ND-F	*369.79*	*377.65*	0.151	N/A	*NC (IRR?)*	*53.0 ± 1.4?*	-	L	12.28	0.12	I
V107	S	391.89	358.00	0.259	1.3	*NC (IRR)*	*IRR or NR?*	-	L	12.41	0.12	I
V108	S	413.61	388.73	0.295	0.6	*NC (IRR?)*	*43.6 ± 0.6, 39.9 ± 1*	-	L	12.68	0.12	I
V109	S	413.77	371.70	0.312	1.0	NC (IRR)	IRR	-	L	12.63	0.09	I

Table 4.1: Known variables in the literature that were successfully detected and/or recovered. Finder chart column references chart sources with L, P, and S standing for LEM (1973), Pritzl et al. (2002), and Skottfelt et al. (2015), respectively. Star coordinates are in pixels of the master reference image (V-exposure). R_{proj} is the projected radius from the cluster center. Δr is the coordinate difference between published and detected coordinates. Period as observed and in the literature are compared as a consistency check. LPV coordinates, type, magnitude, amplitude and color from Clement et al. (2001). Abbreviations used include ND: not detected, NR: not manually recoverable, NC: not checked (no published period), F: refers to forcing ISIS to manually recover stars not automatically detected. Star type abbreviations: RR0/1 for RR Lyrae type ab/c, CWA/B for W Virginis, M for Mira LPVs, and L for semi-regular and irregular LPVs. Items in italic indicate uncertainty.

Table 4.2: New or Suspected Variables

ID	Filter/ Exp.	x (px) (V)	y (px) (V)	R_{proj} (arcmin)	R.A.	Dec.	Notes
lc1	V, I_L, I_S	219.79	371.22	1.620	17:36:07.92	-44:44:12.97	New LPV variable, IRR, possible period of 45 or 75 days
lc2	V, I_L, I_S	239.05	231.90	2.061	17:36:08.84	-44:45:36.92	Cardona's NV01
lc4	V, I_L, I_S	291.71	487.26	1.369	17:36:12.13	-44:43:04.11	Suspected LPV variable, possibly IRR
lc5	V, I_L, I_S	303.29	483.98	1.271	17:36:12.78	-44:43:06.21	Cardona's NV16, low SNR, type unknown, bright neighbouring stars
lc8	V, I_L, I_S	333.49	524.95	1.481	17:36:14.54	-44:42:41.95	Suspected variable, low SNR, close to artifact
lc13	V, I_L, I_S	350.77	342.90	0.514	17:36:15.29	-44:44:31.55	Cardona's NV02
lc19	V, I_L, I_S	363.39	333.74	0.527	17:36:15.99	-44:44:37.21	Cardona's NV15
lc20	V, I_L, I_S	369.38	340.27	0.446	17:36:16.34	-44:44:33.36	New SPV, low SNR, possible periods of 0.9 or 9 days
lc21	V, I_L, I_S	372.82	322.77	0.604	17:36:16.51	-44:44:43.91	Cardona's NV05
lc22	V, I_L, I_S	372.51	448.41	0.652	17:36:16.65	-44:43:28.41	Cardona's NV06
lc29	V, I_L, I_S	389.44	418.20	0.349	17:36:17.57	-44:43:46.76	Suspected variable, more details needed
lc38	V, I_L, I_S	411.84	418.73	0.444	17:36:18.84	-44:43:46.71	Suspected variable, more details needed
lc42	V, I_L, I_S	436.93	343.08	0.652	17:36:20.16	-44:44:32.46	Suspected variable, close to V51, more details needed
lc44	V, I_L, I_S	439.35	370.04	0.558	17:36:20.33	-44:44:16.29	Suspected LPV, period of 37.5 days detected
lc45	V, I_L, I_S	443.49	282.89	1.146	17:36:20.46	-44:45:08.71	Suspected LPV with period in the range of 200-300 days, low SNR.
lc46	V, I_L, I_S	456.98	426.55	0.834	17:36:21.40	-44:43:42.53	Cardona's NV09
lc47	V, I_L, I_S	488.55	321.92	1.190	17:36:23.05	-44:44:45.78	Cardona's NV14
lc51	V, I_L, I_S	527.97	336.24	1.488	17:36:25.30	-44:44:37.62	Cardona's NV10
lc56	V, I_L, I_S	142.10	417.94	2.404	17:36:03.59	-44:43:43.96	Cardona's NV27
lc62	V, I_L, I_S	206.34	411.51	1.770	17:36:07.21	-44:43:48.60	Suspected variable, more details needed
lc64	V, I_L, I_S	254.74	394.87	1.278	17:36:09.93	-44:43:59.18	Suspected variable, more details needed
lc66	V, I_L, I_S	458.84	405.14	0.766	17:36:21.48	-44:43:55.42	Suspected variable, more details needed
lc67	V, I_L, I_S	490.01	300.59	1.320	17:36:23.11	-44:44:58.61	Suspected LPV with period of 408 days (IL)
lc68	V, I_L, I_S	545.58	379.20	1.588	17:36:26.35	-44:44:12.01	Suspected variable, more details needed
il28	I_L	166.23	492.80	2.399	17:36:05.05	-44:42:59.27	Suspected variable, more details needed
il46	I_L	285.08	403.00	0.993	17:36:11.65	-44:43:54.66	Suspected variable, more details needed
il47	I_L	287.79	584.48	2.195	17:36:12.03	-44:42:05.64	Suspected variable, more details needed
il51	I_L	304.15	294.96	1.170	17:36:12.60	-44:44:59.81	Suspected variable, more details needed

Continued.

il55	I_L	322.64	348.29	0.695	17:36:13.71	-44:44:27.99	Suspected variable, more details needed
il57	I_L	333.16	394.44	0.513	17:36:14.36	-44:44:00.37	Suspected variable, more details needed
il65	I_L	338.48	256.66	1.322	17:36:14.49	-44:45:23.23	Suspected variable, more details needed
il85	I_L	364.15	472.87	0.904	17:36:16.21	-44:43:13.61	Suspected variable, more details needed
il103	I_L	390.58	328.35	0.542	17:36:17.52	-44:44:40.77	Suspected variable, more details needed
il125	I_L	407.86	505.30	1.224	17:36:18.72	-44:42:54.64	Suspected variable, more details needed
il133	I_L	415.74	542.34	1.596	17:36:19.21	-44:42:32.47	Suspected variable, more details needed
il143	I_L	432.04	428.02	0.646	17:36:19.99	-44:43:41.36	Suspected variable, more details needed
il150	I_L	480.12	267.50	1.478	17:36:22.51	-44:45:18.38	Suspected variable, more details needed
il165	I_L	587.33	450.87	2.106	17:36:28.79	-44:43:29.42	Suspected variable, more details needed

Table 4.2: New or suspected variables found that are mentioned in the literature. Photometric data filenames are used as a placeholder for star names. Those with the prefix *IL* were only detected in long, *I*-passband exposures, and could not be found in the other exposures (*V* and I_S). Some were previously detected in the smaller data subset by Cardona (2011), and have the name format NV#. The second column lists the filter/exposure combination which yielded detection and usable photometry. R_{proj} is the projected radius from the cluster center. Celestial coordinates were transformed from ISIS-output pixel coordinates using IRAF's *wcsctran* command and our plate-solved reference image.

Table 4.3: Undetected Stars

Star ID	x (px) (V)	y (px) (V)	R_{proj} (arcmin)	Mag. (lit.)	Ampl. (lit.)	Col. (lit.)	Type (lit.)	Notes
V10	443.37	709.08	3.258	14.45	0.5	V	L	Out of FOV
V11	361.42	731.61	3.434	15.75	0.9	V	L	Out of FOV
V13	1082.28	223.82	7.042	17.1	-	B	L	Out of FOV
V14	86.36	−149.42	6.000	16.179	1.3	V	E	Out of FOV
V15	−302.05	820.80	8.003	16.2	-	B	E	Out of FOV
V16	-67.67	790.83	5.984	16.895	0.26	V	RR1	Out of FOV
V19	452.22	419.86	0.761	-	-	-	CST	Not a variable
V21	488.94	614.94	2.502	17.03	0.87	V	RR0	Out of FOV
V24	334.89	1145.97	7.517	16.8	0.6	B	RR1	Out of FOV
V25	675.75	221.93	3.277	16.15	-	B	L	Out of FOV
V27	483.26	358.55	1.004	16.953	0.46	V	RR1	Faint
V34	63.13	300.60	3.259	17.409	0.36	V	RR1	Faint
V35	495.14	731.55	3.596	17.041	0.18	V	RR1	Out of FOV
V38	378.83	9.55	3.674	18.27	0.46	V	EC	Edge of FOV (convolution artifacts)
V39	545.25	1076.16	6.997	17.996	0.28	V	EC	Out of FOV
V40	490.57	738.29	3.646	18.806	0.39	V	EC	Out of FOV
V41	1044.93	872.49	8.086	17.364	2.2	V	E	Out of FOV
V42	787.33	681.14	4.930	15.724	0.48	V	E	Out of FOV
V43	124.25	415.34	2.575	19.606	1.22	V	E	Very faint
V44	32.94	321.61	3.506	18.082	0.5	V	SX?	Slightly faint, bright companion
V45	657.33	860.94	5.412	-	-	-	L	Out of FOV
V47	858.58	92.35	5.472	-	-	-	L	Out of FOV
V48	428.96	407.43	0.501	16.574	-	V	RR1?	Fainter than bright companion
V52	87.63	53.14	4.362	16.686	0.23	V	RR1?	Slightly faint/low amplitude, bright companion
V54	44.78	345.82	3.357	19.447	0.67	V	EC	Very faint, convolution artifacts
V56	346.63	360.88	0.429	16.825	-	V	RR1?	Faint, in central region
V57	−113.72	698.00	5.792	19.116	0.8	V	EC	Out of FOV
V60	383.72	355.45	0.272	16.19	0.31	I	RR1	Crowded central region, bright companion
V61	362.61	374.51	0.228	15.94	0.83	I	RR0	Crowded central region, 12th and 13th mag. companions
V62	369.51	382.63	0.144	15.79	0.51	I	RR0	Crowded central region, 12th and 13th mag. companions
V64	379.73	368.19	0.153	15.35	0.43	I	RR0	Crowded central region
V65	373.48	411.50	0.298	16.19	0.36	I	RR1	Slightly faint, crowded central region
V66	365.77	367.42	0.238	15.25	0.19	I	RR1	Crowded central region, low amplitude
V69	388.28	365.36	0.179	14.55	0.47	I	CWB	Crowded central region, 12th and 13th mag. companions

Continued.

V74	353.27	356.52	0.401	15.96	0.12	I	RR1?	Crowded central region, low amplitude, 12th mag. Companion
V75	380.65	366.38	0.168	16.07	0.22	I	RR1	Crowded central region, 12th and 13th mag. companions
V76	370.69	393.64	0.168	15.98	0.67	I	RR0	Crowded central region, bright companions
V78	350.79	405.23	0.393	12.8	0.04	I	SR	Crowded central region, low amplitude
V79	388.06	384.00	0.040	12.46	0.05	I	SR	Very crowded core region, low amplitude
V80	385.63	365.31	0.176	12.86	0.2	I	RV	Crowded central region, somewhat low amplitude
V81	375.18	357.62	0.266	12.58	0.08	I	SR	Crowded central region, low amplitude
V82	394.58	401.43	0.207	12.89	0.06	I	RV	Crowded central region, low amplitude
V84	360.37	387.95	0.238	12.85	0.05	I	SR	Crowded central region, low amplitude
V85	379.09	397.63	0.151	13.03	0.07	I	SR	Crowded central region, low amplitude
V86	401.07	395.73	0.208	12.75	0.08	I	SR	Crowded central region, low amplitude
V87	399.89	368.58	0.211	12.99	0.04	I	SR	Crowded central region, low amplitude
V91	385.21	384.61	0.018	12.65	0.05	I	SR	Very crowded core region, low amplitude
V94	396.53	360.36	0.255	13.34	0.06	I	SR	Crowded central region, low amplitude
V99	390.56	382.88	0.063	12.37	0.35	I	L	Very crowded core region
V100	384.05	372.77	0.102	12.53	0.34	I	L	Very crowded core region
V103	384.40	381.43	0.017	12.13	0.2	I	L	Very crowded core region, somewhat low amplitude
V104	387.21	382.15	0.032	12.07	0.15	I	L	Very crowded core region, low amplitude
V105	388.46	373.69	0.102	12.27	0.14	I	L	Very crowded core region, low amplitude
V110	398.86	367.07	0.214	12.38	0.08	I	L	Crowded central region, low amplitude
V111	376.20	384.26	0.079	12.73	0.08	I	L	Very crowded core region, low amplitude
V112	395.34	390.96	0.135	12.88	0.07	I	L	Crowded central region, low amplitude
V113	397.26	408.47	0.281	13.35	0.06	I	L	Crowded central region, low amplitude
V114	364.79	388.03	0.196	12.71	0.05	I	L	Crowded central region, low amplitude
V115	383.05	386.56	0.035	12.11	0.04	I	L	Very crowded core region, low amplitude
V116	413.68	401.97	0.345	13.24	0.04	I	L	Crowded central region, low amplitude
V117	384.06	388.74	0.055	12.83	0.04	I	L	Very crowded core region, low amplitude
V118	382.88	377.90	0.053	12.95	0.04	I	L	Very crowded core region, low amplitude
V119	399.42	382.06	0.151	12.53	0.05	I	L?	Crowded central region, low amplitude
V120	385.63	406.25	0.228	-	-	-	?	Crowded central region
V121	389.76	411.82	0.288	-	-	-	?	Crowded central region

Table 4.3: stars that were neither detected nor manually recovered. In case of the Skotfeltt et al. (2015) discovered stars (whose ID numbers are greater than V77), the main cause for failure was the greater stellar density near the core. Noted are factors that may have impeded detectability and signal recovery.

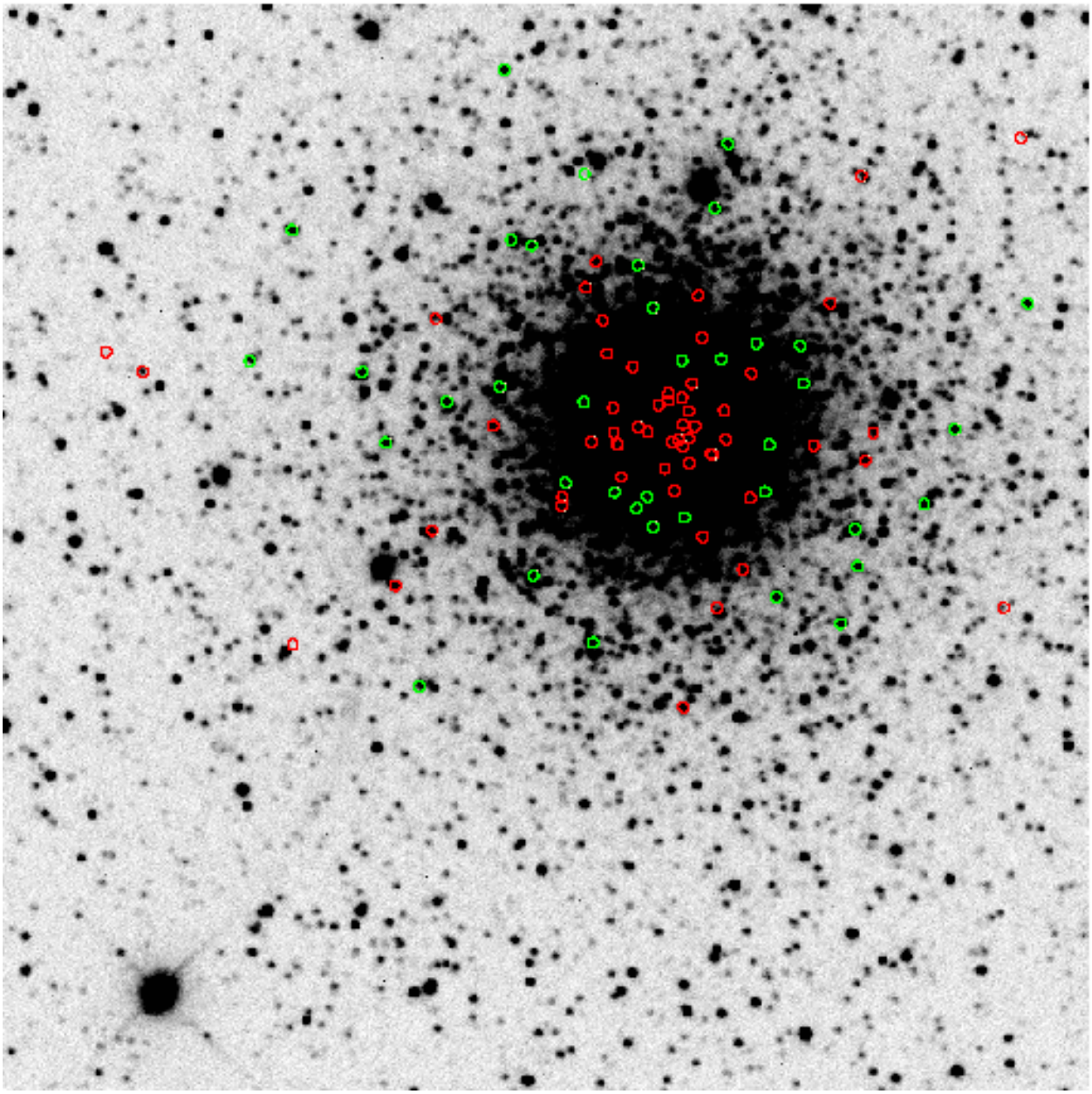

Figure 4.3: A finder chart for variable stars detected and/or recovered. Known variables are red, new or suspected variables are green. The image used was the master reference image in the *V*-band. Note the close adjacency of variable stars in core. The image scale is 0.59" per pixel. Pixel coordinates: (x, y) = (1, 1) at lower-left corner, (x, y) = (623, 623) at upper-right corner. Individual known and new or suspected stars may be identified using the (x, y) pixel coordinates in tables 4.1 and 4.2, respectively.

CHAPTER 5. RESULTS: PHOTOMETRY AND LIGHT CURVES

What follows is the resulting data for suspected variable stars, their characterization, and if available, their history in previous research literature. The photometry data output by *phot.csh* are used to derive a value for the mean and standard deviation from multiple images of the same exposure type taken in the same night, and were used in plotting regular and phase-folded light curves, and in the PDM method for determining the period.

For our folded light curves, the following colors were used to denote time ranges: red first (430 days), then black (600 days), green (600 days) and finally blue (450 days). Colors were used to identify variations in the maxima/minima of LPVs from cycle to cycle, specifically in the case of LPV stars, as those would have completed a low number of cycles during our 6 years of observation.

5.1 Cluster Membership

As a part of variable characterization, we attempt to determine cluster membership. This is done because our aim of studying LPVs in globular clusters, as stated in chapter 1, is to study how the cluster's properties relate to its LPVs variable behavior. As such, an accurate determination of the likelihood of cluster membership is critical.

There are multiple ways to determine the likelihood that a star is a member of a globular cluster: first, position on the CMD relative to the cluster sequence. Second, position relative to the cluster center as seen from Earth (i.e. the projected radius). Third, the star's proper motion, relative to other probable members and to field stars. Fourth, and finally, the star's radial velocity as compared to other members and field stars. The last two methods are not available to us because the spectroscopic and astrometric data required are not available from the PROMPT telescopes.

5.1.1 Color-Magnitude Diagram

The CMD-based method requires magnitude data, and cannot be performed using flux difference photometric data (as output by ISIS). Although we do have data in two passbands (*V* and *I*), they are used to determine the ratio of relative flux amplitudes in V vs. I images as a proxy to the magnitude differences between the respective passbands, but do not measure true V−I color. That does not help with cluster membership, which depends on locating variable stars on the CMD.

Color-magnitude data are thus primarily sourced from Cardona's work (Cardona, 2011), as his two-year dataset is a subset of our own, and used DAOPHOT for color-magnitude photometry. He has performed the field star subtraction needed to characterize the cluster using isochrones, the HB, RGB, and AGB. He has also indicated the location of candidate variables on the CMD, and noted their proximity to the RGB/AGB as good indicators of cluster membership. This was performed on both known and candidate variable stars, a majority of which were successfully recovered in our 6-year ISIS analysis: 46 variable stars, out of Cardona's 66 stars. We have also sourced color-magnitude data from published literature where possible. In the case of unpublished candidate variables, specifically those not in Cardona's work, this type of membership determination is made difficult by the lack of color-magnitude data in the work's results table. There are 28 such stars, about 30% of the total stars recovered. For those stars, Cardona's *V* and I_L non-variable magnitude photometry is available, which was performed on the cluster using the 8 best nights from the year 2010 observing season. DAOPHOT was used for magnitude measurement on a larger FOV than our own. Thus, his photometric data include our own ISIS FOV stars.

The star coordinates in the CMD database have been found to differ from our own, which is to be expected[1] given the different inputs and methodologies; DAOPHOT used an 8-night average with PSF fitting photometry, while ISIS relied on convolution/subtraction of 6 years worth of observation to establish a position. Thus the CMD data were retrieved through a python script that collates[2] all of Cardona's x, y coordinate pairs according to closeness to each other, offsets their coordinates to their approximate position in our own (cropped) ISIS FOV reference frame, and then compares them with our detected variables. The comparison has a search radius of 3 pixels based on the standard deviations of the x, y offsets between a sample of 46 of our stars and Cardona's (see section 4.2.3). They were found to be ~ 1.9 and ~2.1 pixels in x, y respectively, for a maximum displacement of ~2.9 pixels. In case multiple stars were found in the color-magnitude database within the search radius, a visual inspection of ours and Cardona's master reference frames was done to determine which match is the correct one.

As red giant stars, detected LPVs are expected to be of apparent magnitude and color as to be in the RGB and AGB in the cluster's CMD. As can be seen in Fig. 5.1, most of Cardona's detected LPVs lie along it. (Some others do not due to blending effects, to be detailed in the following pages.) Cardona's isochrone was fitted to the cluster after de-reddening, and shifting the V-magnitude with an apparent distance modulus that includes *V*-magnitude extinction parameter A_V. The isochrone was chosen with a metallicity of [Fe/H] = −0.4 dex (Cardona, 2011).

[1] The IRAF *imalign* routine was used to determine the offset between our reference image and that used by DAOMASTER to sub-pixel precision, yet the differences between ISIS and DAOPHOT coordinates remained.
[2] Utilizing the "scipy.spatial.KDTree" class, from the scipy python library (version 0.13.3).

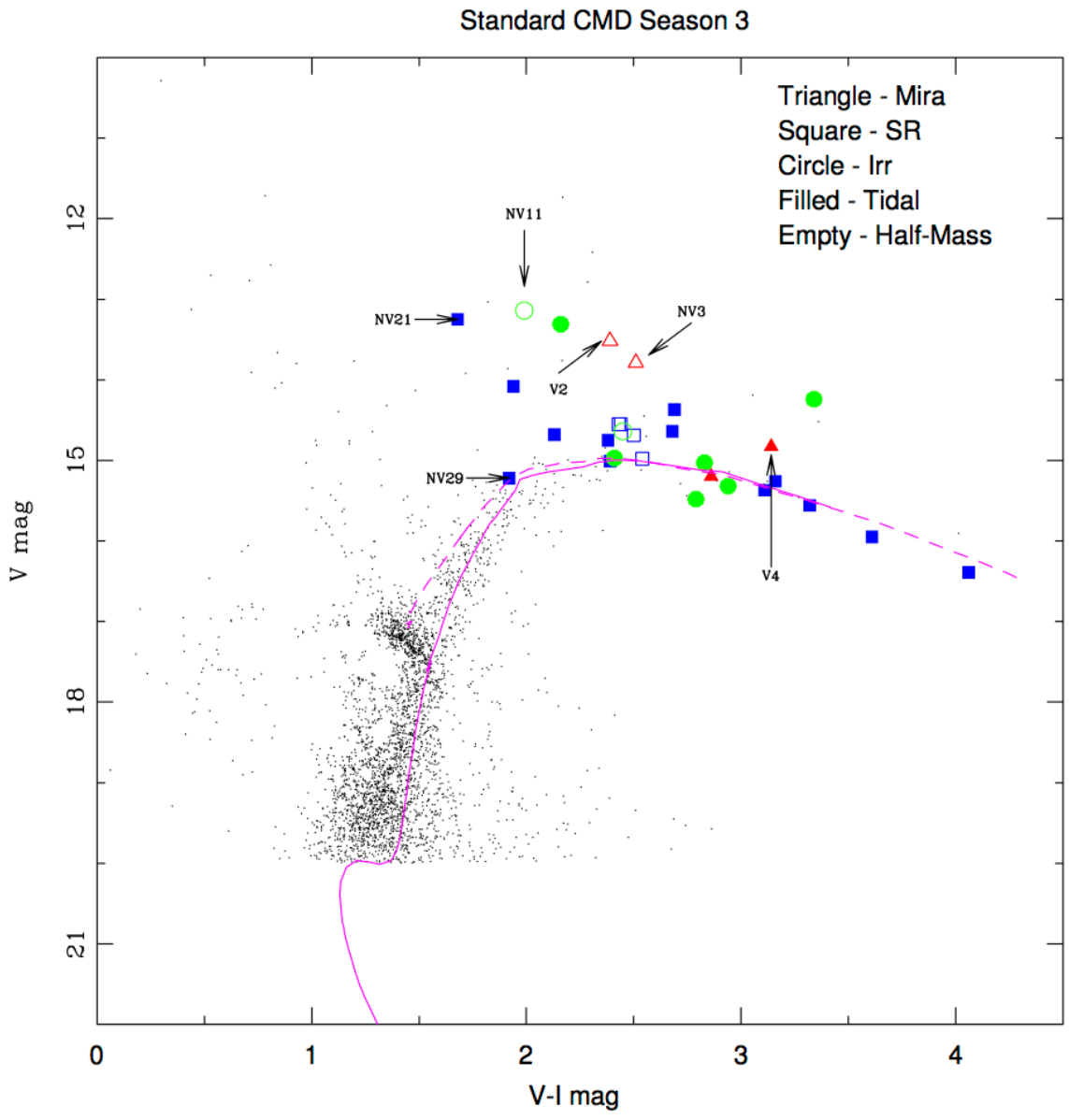

Figure 5.1: CMD from Cardona (2011) using the best nights' photometric data. Marked known and candidate LPVs are Cardona's. Field subtraction, and de-reddening, were performed, and Cardona used isochrones from Girardi (2002), with metallicity [Fe/H] = −0.4 dex. Stars labeled per source notation; NV3 is V1, NV11 is V88).

Fig. 5.2 shows our own known and candidate LPV variables, as determined through positional co-location with Cardona's color-magnitude database. The RGB/AGB has been sourced from Cardona's isochrones. The *V* and *V–I* apparent magnitudes will be affected by interstellar extinction and reddening, the vector of which is shown in Fig. 5.2 as a representation of the effects on the apparent magnitudes. The values of the reddening and extinction of our differential color magnitude, $E(V-I)$ and A_V, were sourced from Cardona (2011) as 0.458 and 1.1, respectively.

The basis for determination of the likelihood of membership of a detected LPV to the cluster is its position in the CMD relative to RGB and AGB; we have defined a region extending above and below the RGB/AGB portion of the isochrones (± 0.3 magnitudes in *V*-passband*)* to account for photometric errors (due to blending and observational limitations), differential reddening[1] across the face of the cluster, and intrinsic apparent magnitude differences (due to the star's variable luminosity and radial distance from cluster center).

We have co-located our stars with those in the color-magnitude photometric database, and plotted those on a CMD (see Fig. 5.2). Our detected LPVs appear along the RGB/AGB, validating their membership, but of note is the spread of some other detected LPVs along the area occupied by non-variable stars that lie in the busy half-light radius of the cluster (roughly $V\sim$ 13-15 mag, $(V-I) \sim$ 1-2mag). This indicates a limitation to the use of the CMD as a membership determinant, and one likely due to the region's high stellar density affecting the photometric measurements due to blending; DAOPHOT's profile-fitting routine can erroneously fit the PSFs of two (or more) unresolved stars using a single profile, lowering the V-magnitude and blue-shifting the color of the brighter and hotter LPVs toward that of their dimmer, cooler

[1] Which was reported to have a maximum value $\Delta E(B-V) \sim 0.1$ mag (Bonatto etl al., 2013)

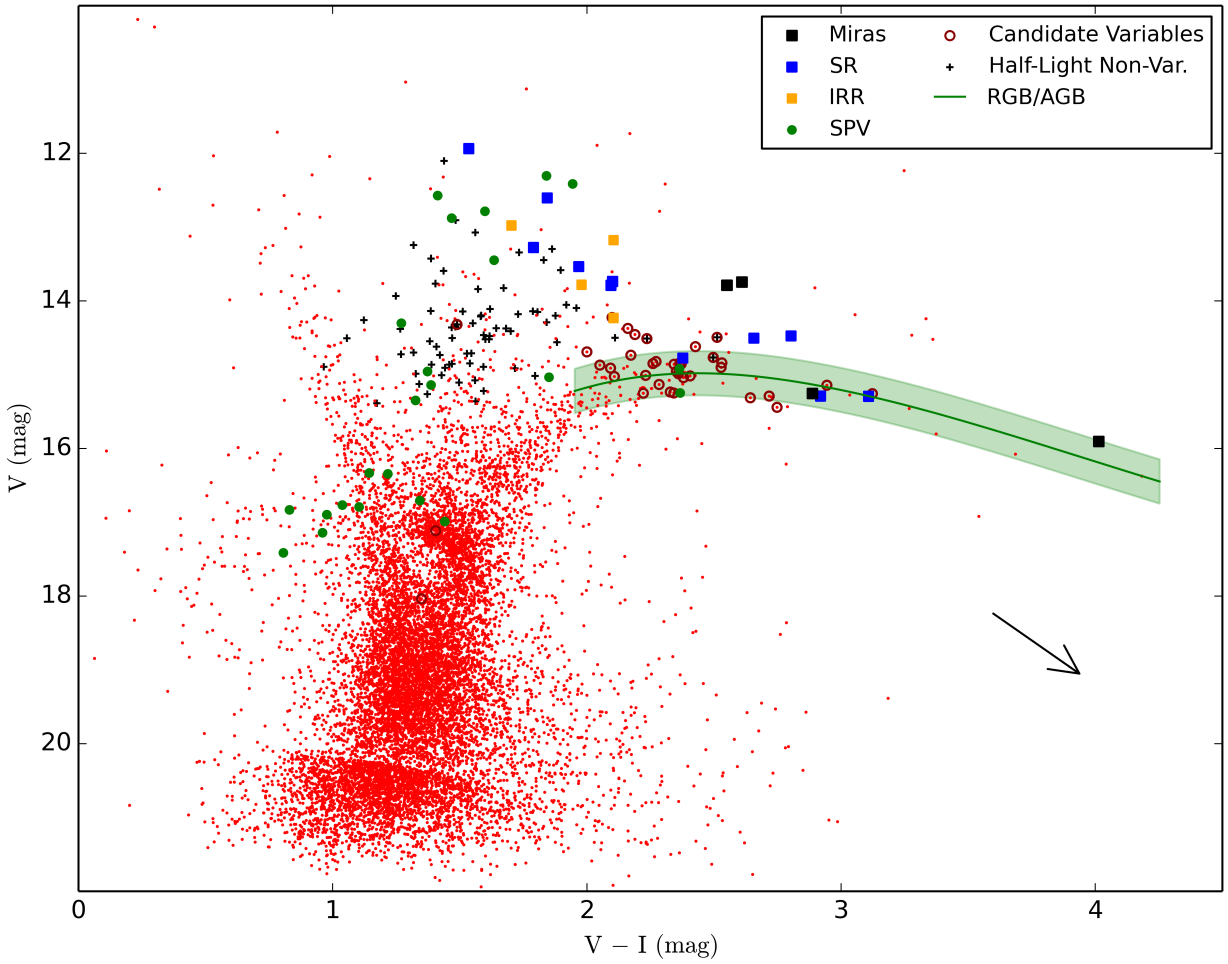

Figure 5.2: CMD with ISIS-detected variable stars marked, data and RGB/AGB sourced from Cardona (2011). The RGB/AGB are marked by a band of ± 0.3 magnitudes in *V*, representing the region where LPVs are expected to appear. Variables are marked by sub-type, but all known LPVs are marked as squares. Non-variable stars located within the half-light radius are marked as black pluses. The reddening vector is represented by the black arrow.

non-red giant neighbors. Thus, the LPVs not on the RGB/AGB appear to be shifting to the location of the CMD inhabited by the non-variable stars that lie within the half-light radius. Other LPVs appear to be brighter than the RGB/AGB (*V > 15* mag*)*, but redder (V-I >2) than the half-light-adjacent LPVs. This is possibly due to having relatively fainter, cooler, or more distant neighbors, or the LPVs are field stars appearing in the foreground relative to the cluster. Known LPV stars identities are annotated on the CMD shown in Fig. 5.3.[1]

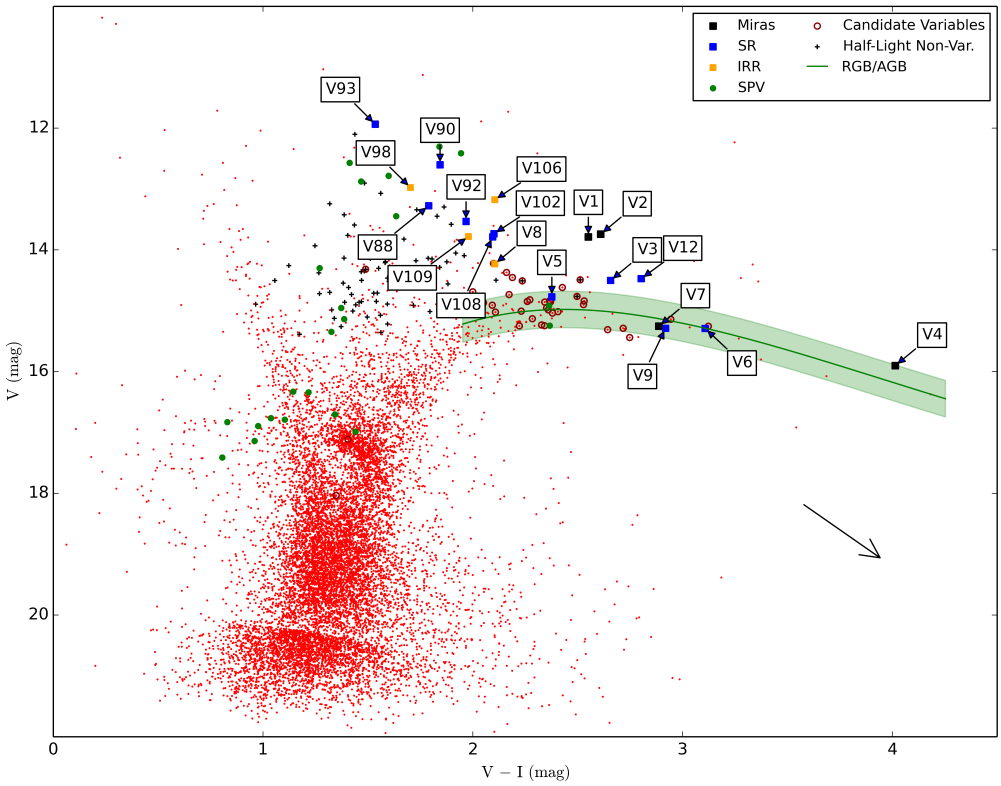

Figure 5.3: similar to Fig. 5.2, but annotated with successfully recovered known LPV stars.

We define the cluster-membership criterion for LPV stars as follows: stars lying on the RGB/AGB, or within ± 0.3 V-magnitudes of it, are more likely to be members. LPVs falling

[1] New LPV stars can be identified on the CMD in Fig. 5.42.

above are less likely to be members, with the likelihood depending on the star's degree of crowding, and hence its proximity to the cluster radius, affecting the photometry. Any LPVs falling below it are likely to be background field stars. Given those limitations, the CMD is used in combination with another criterion: the projected radius of the variable star from the cluster center.

5.1.2 Projected Radius and King Model

The other characteristic to help differentiate between member stars and field stars, one always available, is their projected distance from the cluster center. Closeness to the cluster center is almost definitional to cluster membership: a cluster member must be gravitationally bound to the cluster, and thus must be within the tidal radius of the cluster. To quantify the possibility of membership, the structural parameters of the King model (King, 1962 and 1966) are used. The model relates cluster surface brightness distribution to the mass distribution of the cluster, and therefore the extent of its gravitational influence vs. the Milky Way's. In addition to a cluster's mass concentration, the tidal radius r_t is also influenced by a globular cluster's distance from the galactic center (King, 1962).

The observed parameters describe how concentrated the cluster is: the core radius r_c (the radial distance at which the surface brightness is half of the peak central value), and the half-light radius r_h (the radius of the circle that encompasses half the light power output by the cluster, also referred to as the half-mass radius) (King, 1966). The radii are measured as projected onto the "plane of the sky", i.e. as seen from our Earth-bound viewpoint, an essentially 2D projected

image of a 3D object. These radii inform our understanding of the logarithmic surface brightness distribution plot (Fig. 5.4), which is proportional to star, and thus roughly[1] mass, distribution.

The following empirical relation is used for calculating the tidal radius:

$$r_t = r_c * 10^c$$

where c is the central concentration (King, 1962). We have opted to use the values in the Harris catalogue (Harris 1996, 2010 Edition), which are r_c = 7.2" and c = 1.75, which give r_t = 405", and r_h = 31.2". They were chosen as they lie between Harris' older values (quoted in older literature as c = 1.7, giving r_t = 373") and the larger values found by Lanzoni et al. (c = 1.8, r_c = 7.2", thus r_t = 454").

The larger variance in tidal radius given by studies as recent as the last two decades underlines the uncertainty of the cluster's limits. This is mainly due to the cluster's low galactic latitude ($b \sim -6.7^\circ$), placing it closer to the galactic plane where interstellar dust clouds cause reddening and extinction of the light from the cluster's stars, and field stars along the cluster's line of sight are common. This complicates the typical methodologies of subtracting field foreground and background stars from the cluster stars by color by affecting the instrumental color magnitudes. The measurements are also unevenly affected due to natural non-uniform distribution of the clouds, complicating the use of stellar fields to calibrate the subtraction sample. The galactic plane region also exhibits greater stellar density, which combined with the power low nature of the decrease of the cluster density makes the outer extent of the cluster harder to extricate from the field stars. The greater stellar density also means a larger number of foreground and background field stars will be within the tidal radius as seen from earth, again

[1] Assuming cluster stellar mass uniformity with negligible effects due to mass segregation and a hypothesized intermediate mass black hole (IMBH). The presence of an IMBH remains uncertain and is not definitively discernable from the surface density (Lanzoni et al., 2007, 2013).

complicating the aforementioned methodologies. Luckily, given our narrow FOV, the large variance in the published values of the cluster's tidal radius is not a cause for concern, as can be seen in Fig. 5.5. Our chosen values are marked on NGC 6388's stellar density plot, and on the histogram of recovered variable stars in Fig. 5.4 (top, bottom respectively).

The surface density of recovered variables was found to increase at a rate comparable to general surface density (Fig. 5.4). This gives greater confidence in our criteria for membership based on projected radius, but it must be noted that the surface density of recovered stars drops sharply closer to the core. This can be seen in Fig. 5.5, where the recovered stars appear to stop at the edge of the core radius r_c. This indicates that our detection is incomplete, as to be expected in the dense core region where our aperture's resolving power is too limited to resolve the stars; thus multiple stars' Airy disks overlap and merge, affecting the variability signal by masking it, or interfering with in case of multiple variables in close proximity.

Using the chosen radii and our knowledge of the stellar density distribution of the cluster (Fig. 5.4), we defined categories that rank the likelihood of a variable's cluster membership. These working definitions serve to give a qualitative characterization to augment the information from the CMD to judge a star's cluster membership. Stars outside the cluster tidal radius ($r_p > r_t$) are field stars, by definition, and given our narrow FOV (Fig. 5.5) covers an area entirely within the tidal radius, all of our detected variables cannot be definitively classified as field stars on that basis.

Within the tidal radius, all stars are potential members, but it must be noted that their projected radius only gives an estimate of likelihood because a star, as seen from Earth, could be in front of or behind the cluster, and its proximity is only a coincidence of alignment. Given the aforementioned higher stellar density at NGC 6388's low galactic latitude, the chances of this

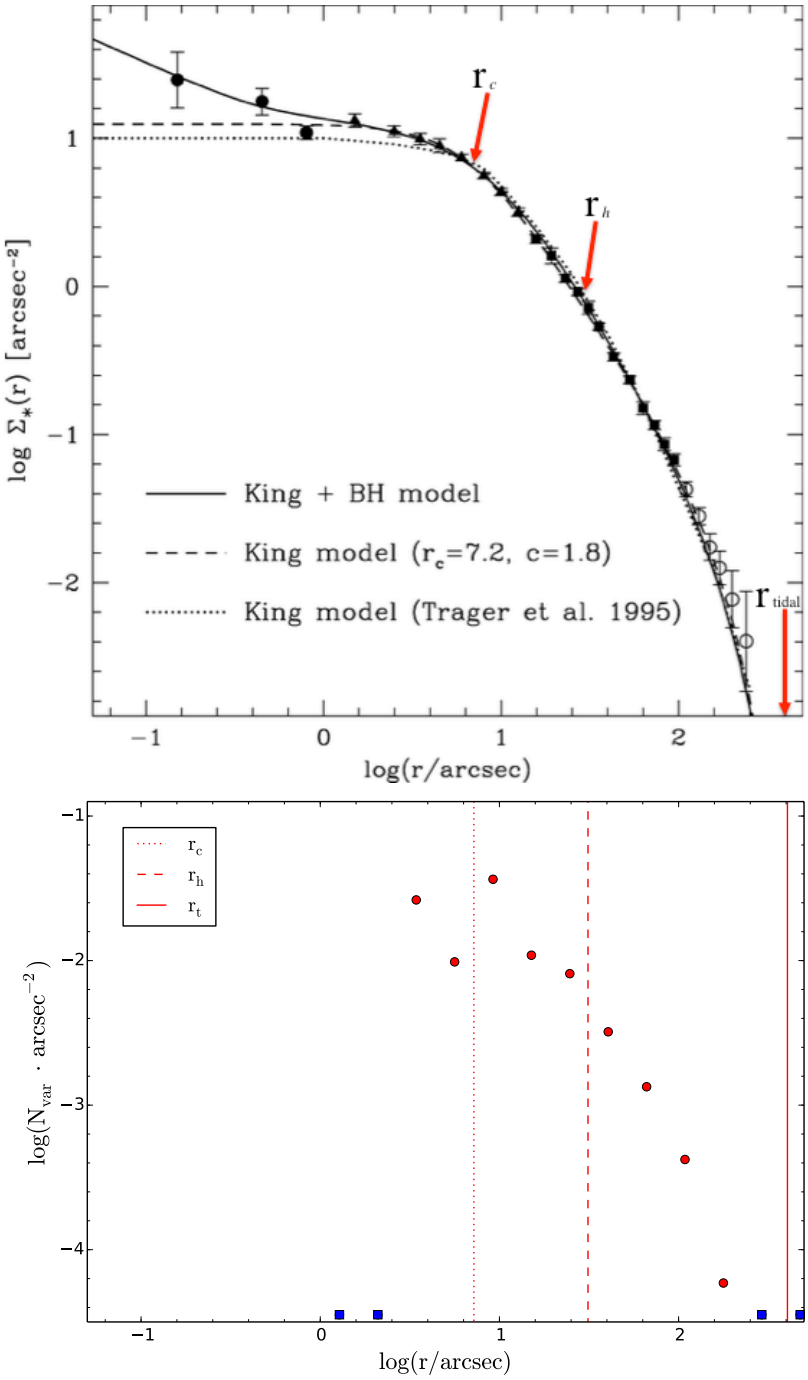

Figure 5.4: Top: projected stellar density distribution of NGC 6388 from Lanzoni et al. (2007) star counts, with background level subtracted. The solid line fit includes hypothesized IMBH effect. Dashed and dotted lines based on King model fits, with respective values for (r_c, c, r_t): (7.2”, 1.8, 454”) from Lanzoni et al. and (7.4”, 1.7, 371”) from Trager et al. (1995). We have marked the position of our adopted values (7.2”, 1.75, 405”), and r_h, with red arrows. Bottom: Our ISIS-recovered stars density distribution, binned per log of r_p. 14 bins at a bin width ~ log(1.64”) to avoid gaps. Structural parameters r_c, r_h, and r_t are marked with red lines. Blue squares indicate zero recovered stars in an annulus, and inner-outer limits (log(0”)-log(3”)) of binning due to lack of stars.

alignment occurring are higher. As such, the projected radius is used in combination with the CMD to determine cluster membership.

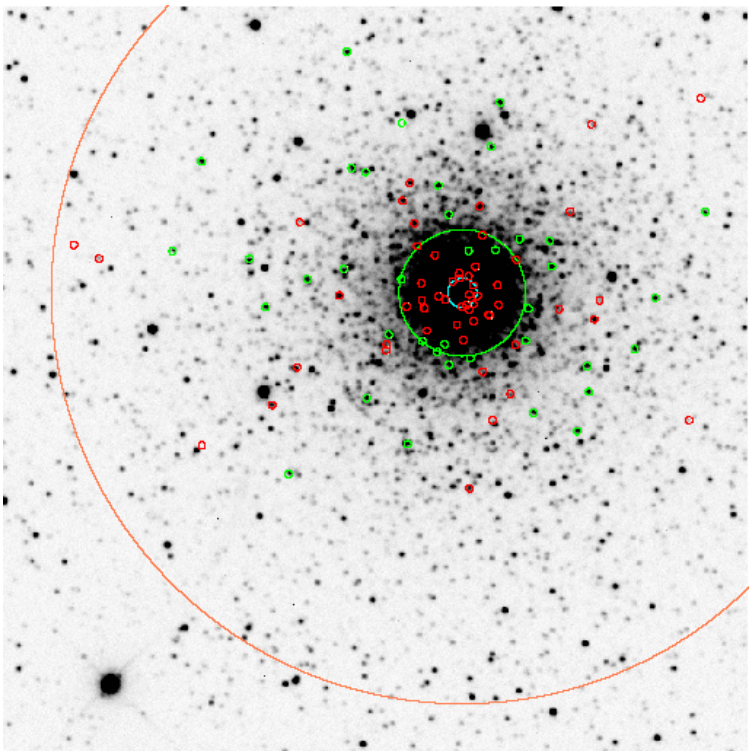

Figure 5.5: A finder chart for variable stars detected and/or recovered. Known variables are red, new or suspected variables are green (see Fig. 4.3 for more details). Colored circles' radii are, in descending order, $\frac{r_t}{2}$, r_h, and r_c. The ISIS FOV is too narrow to include the full tidal radius.

We define stars within the tidal radius but outside the half-light radius ($r_h < r_p < r_t$) as possible cluster members. Closer to the core, we define stars within the half-light radius but outside the core radius ($r_c < r_p < r_h$) as probable cluster members. Finally, we define stars within the core radius as cluster member with a large degree of certainty ($r_p < r_c$). As can be seen in Fig. 5.6, most recovered stars fit in the first two categories (possible and probable cluster members), with only a few near the core that can be considered cluster members with high certainty.

The projected radius' aforementioned limitation of inability to individually identify foreground and background stars is thus countered by reference to stellar density. This is

augmented by the CMD to assess a star's membership based on its brightness and color, which can be used to identify non-member stars, assuming their PSF is not affected by blending. Both criteria will be used in judging an LPVs cluster membership in section 5.4 (Known LPVs), section 5.5 (New LPVs), and section 5.6 (Suspected LPVs).

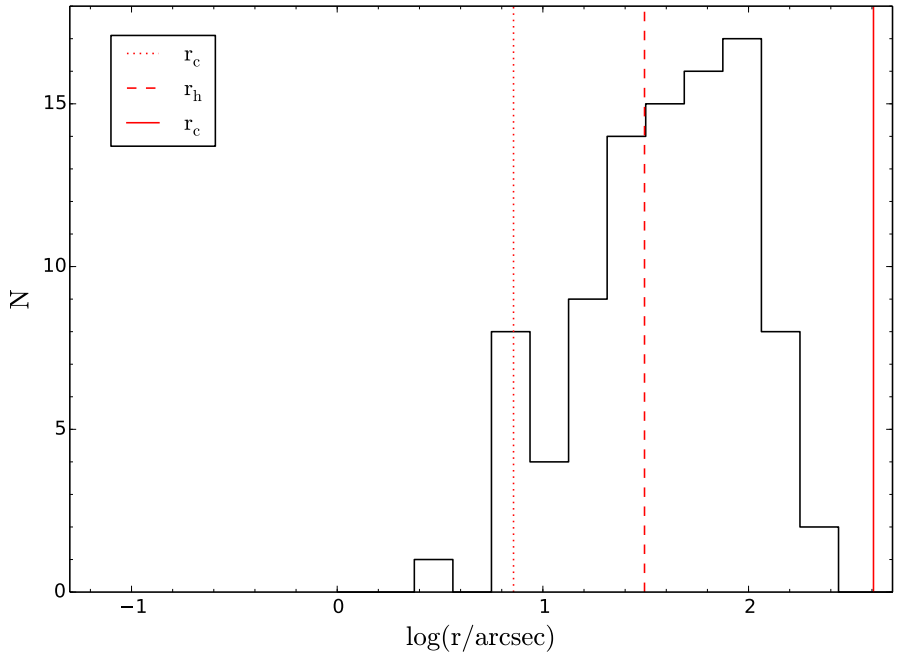

Figure 5.6: A histogram of our ISIS-recovered stars, binned per log of projected radius using 16 bins at a bin width ~ log(1.54"), range log(0") - log(3"). Cluster radial parameters marked in red. Note slightly more bins than Fig. 5.4 (bottom), and the decreasing number of variables encompassed by decreasing radii. Also note the low number of stars recovered inside the core radius r_c due to blending.

5.2 Candidate Variables Selection Criterion

As stated previously, the ISIS variability detection algorithm is quite robust at rejecting obvious statistical anomalies (see chapter 3), and the candidate variables are further manually filtered for glitch-generated variability (e.g. caused by convolution artifacts), as detailed in

chapter 4. After identifying the known[1] variables among the detected variability sources, the remaining candidate variables can be filtered further. The following mathematical formula is used to characterize the variability of the flux difference photometric data of a variable star or variable star candidate:

$$I_{WS} = \frac{1}{N}\sum_{i=1}^{N}\frac{\left|f_i - \bar{f}\right|}{\sigma_i}$$

where I_{WS} is a modified flux-based form of the Welch/Stetson variability index (Stetson, 1996), N is the number of photometric data points, f_i and $\bar{f}$ are the *ith* and median flux difference, respectively. The median flux difference $\bar{f}$ is that for all N data points, and σ_i is the uncertainty of the respective *ith* data point. The formula is slightly modified from Stetson (1996) in using flux difference instead of magnitude, and the inverse of N rather than the inverse of the square root of $N - 1$.

A higher index denotes a higher likelihood of variability being real as opposed to an artifact: for each data point, the larger the deviation from the median, and the smaller the uncertainty in measurement, the greater the contribution to the index. Thus, a larger index indicates there are more measured deviations from the median with low uncertainties. In term of variable stars, that means the index is higher for brighter stars with high amplitudes in areas of relatively low stellar density (i.e. less pollution of PSF with neighboring stars). Fig. 5.7 shows a histogram of the variability index for the known and candidate variables.

[1] Defined as those in published literature and listed in the Clement catalogue (2001), to distinguish them from those that Cardona (2011) discovered, but remain unpublished.

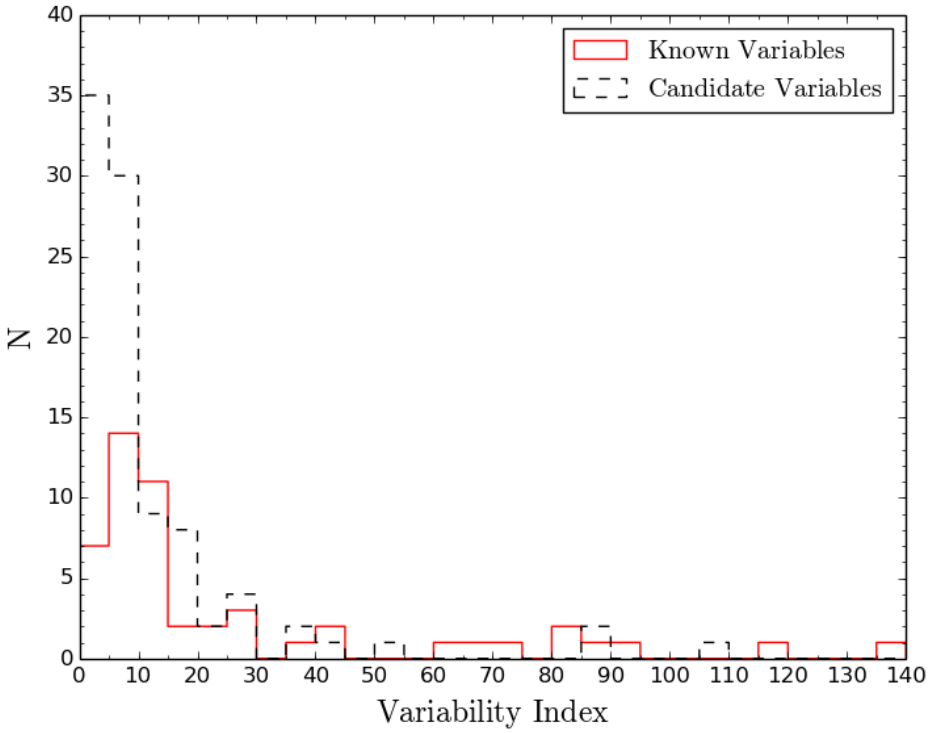

Figure 5.7: a histogram of known and candidate variable stars' variability indices, each bin containing an index range of five. Note four stars were omitted ($I_{WS} > 140$) due to very large values ($I_{WS} > 220$) that cannot be displayed on a linear x-axis.

The histogram (Fig. 5.7) shows that more known stars tend towards the higher index end of the histogram. Given the higher SNR of our I-long observations due to the larger filter bandpass and the fact that our target LPV stars are redder, we have limited our analysis to I_L observations. That said, the same trend was noted in the V and I_S exposures. From inspecting the histogram, promising limits for classifying a candidate variable as new, suspected or false are index values approximately above 20, 20 – 5, and below 5 respectively.

The limits are hard to discern due to the clustering for $I_{WS} < 20$. As in Stetson (1996), we have plotted the histogram with a logarithmic x-axis both to magnify the low-end and to incorporate the high-index stars. To illustrate the spread and concentration of the variables, and to estimate cut-off values for classification, we have also fitted skew normal distributions in a

generalized form. This distribution was chosen to better represent the asymmetric distribution. The fits were separate for known and candidate variables, with probability density function:

$$\mathrm{PDF}(x) = a\frac{e^{-2(x-\bar{x})}}{2\sigma^2}\cdot\frac{1}{2}\left(1+\mathrm{erf}\left(\frac{\alpha(x-\bar{x})}{\sqrt{2}}\right)\right)$$

where x, and $\bar{x}$ are the logarithm of variability index I_{WS} and its median, and a and α are scale and skew parameters, respectively. The skew parameter tended to very large values (~10^4) in an attempt to fit the "long tail" of the histogram, and as such an upper limit of 10 was set for the fit. This was acceptable as the fit was needed only to help visualize the general trend.

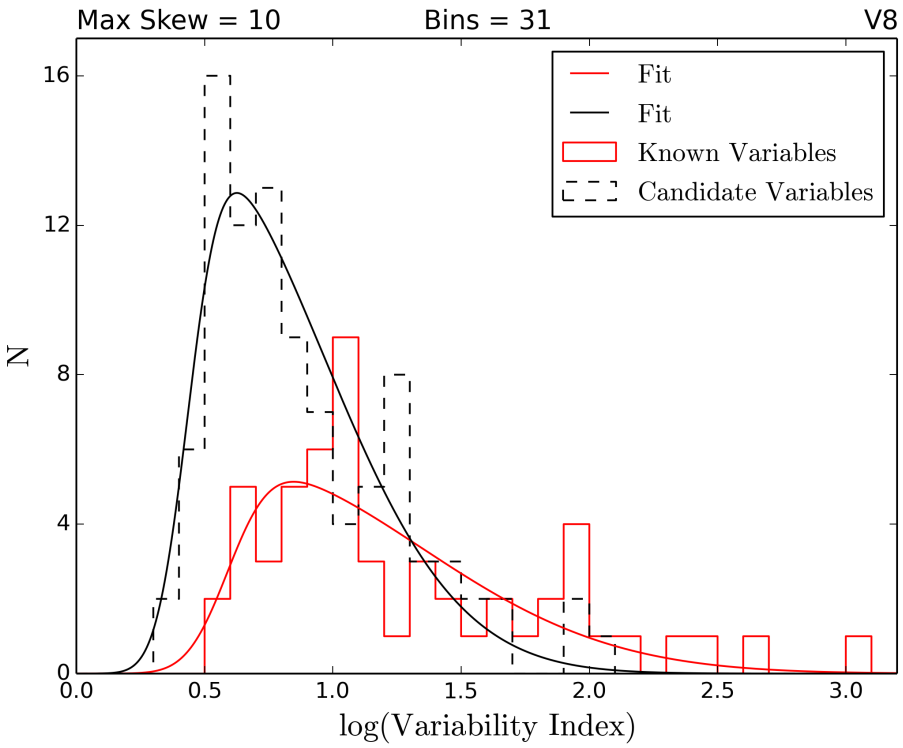

Figure 5.8: A histogram of known and candidate variable stars' variability indices on a logarithmic x-axis, each bin containing an index range of $\log(I_{WS}) = 0.1$. Skew normal distribution fits were applied to each set of variables.

The distribution of known variables is now more clearly separated from the candidates (see Fig. 5.8), with the distributions equalizing at $\log(I_{WS}) \sim 1.3$, which gives $I_{WS} \sim 20$, close to our estimated cut-off point for new variables. Given the distribution, a variable with $I_{WS} > 10$ will be considered a novel variable, 10 – 4 will be considered on an individual basis, while sub-4 variables will be rejected unless they were co-detected by Cardona (2011). The new and suspected variable stars are listed in sections 5.5 and 5.6, respectively.

5.3 Phase Plot Regularity Measure

As a part of variable star characterization, a measure of how regular a star is on a given portion of the phase plot diagram is given. This is done in order to place the star somewhere on the regular-to-irregular spectrum that was discussed in chapter 1, as well as to assess the effect of secondary periods on the primary mode of oscillation. A characteristic of higher-regularity variables that can be seen in their folded light curves is the smaller vertical (the brightness-axis) spread of data points of near-phase around the ideal or median light curve line (see Fig. 5.9). For Mira LPVs', as well as Cepheid and RRL SPVs', data points tend to have a relatively small spread, while those of semi-regular variables that tend towards irregularity or multi-periodicity will have a much larger spread. By measuring and indexing this spread, we can develop an objective measurement for LPVs in addition to relying on human judgment of regularity vs. irregularity.

We have done this using the following procedure: we generate a phase plot for a variable star's flux difference photometric data, which is folded to the primary period (as determined by the lowest value theta using PDM). The data points undergo a 3-sigma rejection process to reject egregious outliers due to image defects, and are then binned such that they are distributed as equally amongst the bins as possible. The standard deviation of the flux difference data points

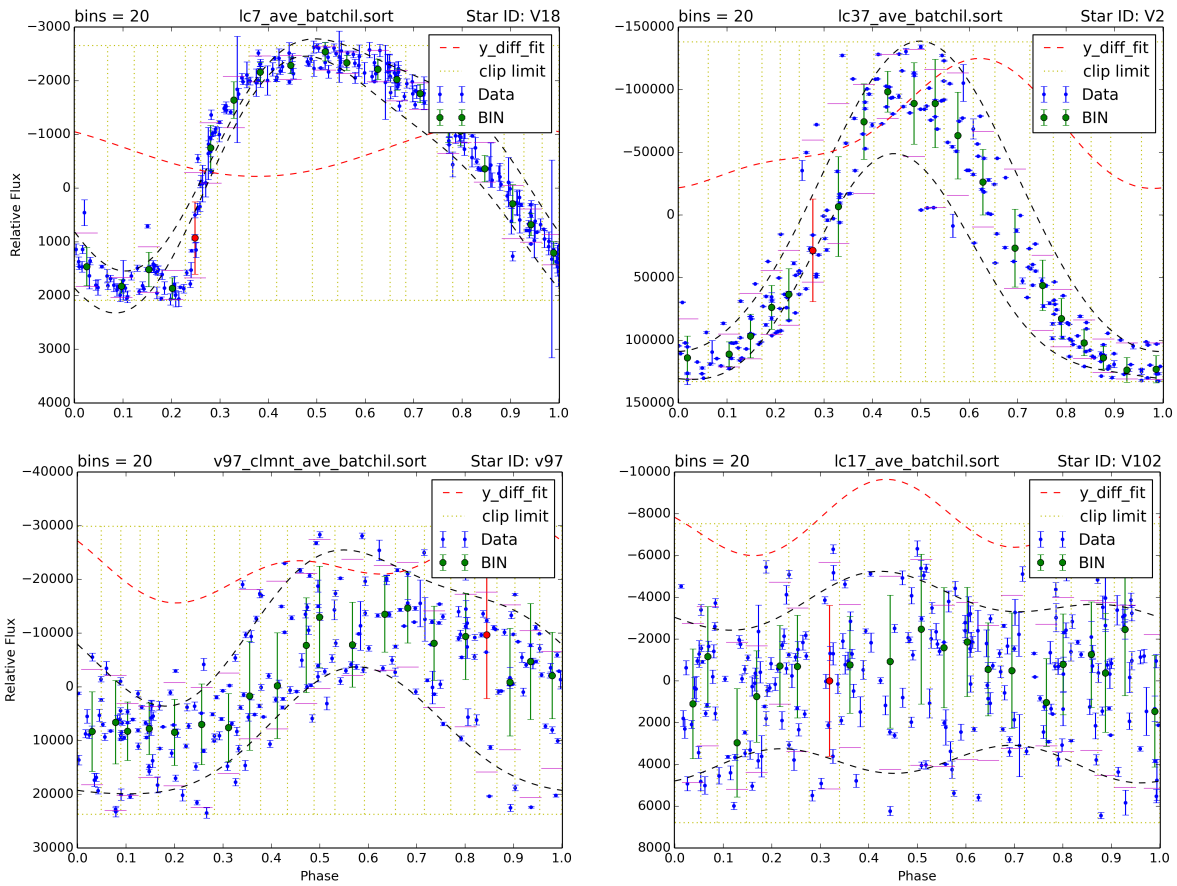

Figure 5.9: A sample of phase plots output by the program. The light curve's upper and lower extent is bounded by 2-term sinusoidal functions for clarity. Bin limits are shown in yellow, and vertical limits bound upper 95%/lower 5%ile of all data points. The median and standard deviation in each bin are represented by green points and bars. The variable stars shown are, in ascending index value: V18, a fairly regular CWA Cepheid (upper left); V2, a regular Mira LPV (upper right); V97, a multi-periodic semi-regular LPV (bottom left); and V102, an irregular LPV (bottom right).

within each bin is then calculated, listed, and the upper 75th percentile[1] value for the list is calculated. Thus the more regular stars, the ones with less vertical spread in flux difference in the phase plot, should have bins with overall lower standard deviations than the more irregular variables. The calculated standard deviation is then normalized over the star's observed flux range:

$$Regularity\ Index = \frac{(\sigma_{bin})_{75ile}}{|f_{max} - f_{min}|}$$

where the numerator is the aforementioned 75th percentile standard deviation amongst the bins, and f_{max} and f_{min} are the maximum and minimum flux difference values. In order to reduce the effect of outlier values, the 99th and 1st percentiles are used in lieu of the maximum/minimum values. The regularity index as defined should then be a measure of how high the relative spread in the star's brightness is amongst its observed cycles, and should be numerically higher for less regular stars with greater cycle-to-cycle variation.

The program to generate the index was coded in python, and outputs diagnostic folded light curve plots as well as regularity indices (see Fig. 5.9). The plots show the bins, which were set at 20 bins per cycle as a compromise between having a large number of data points per bin, but fewer bins, and sampling precision by conversely having more bins but less data points per bin.

As can be seen in Fig. 5.9, the more irregular a variable star is, the wider the spread of values surrounding the median flux value at a given phase of the cycle. The program has successfully approximated the ranking of stars by regularity; see Fig. 5.10 below. Of interest is

[1] Initial attempts at choosing the maximum standard deviation amongst the bins biased the regularity index of regular, but rapidly changing flux against phase, variables towards higher values due to single-bins capturing a rapid change in luminosity.

the predominance of Mira LPVs and WV Cepheid and RR Lyrae towards the lower end, followed by higher index-valued semi-regular and irregular LPVs. The separation point is an

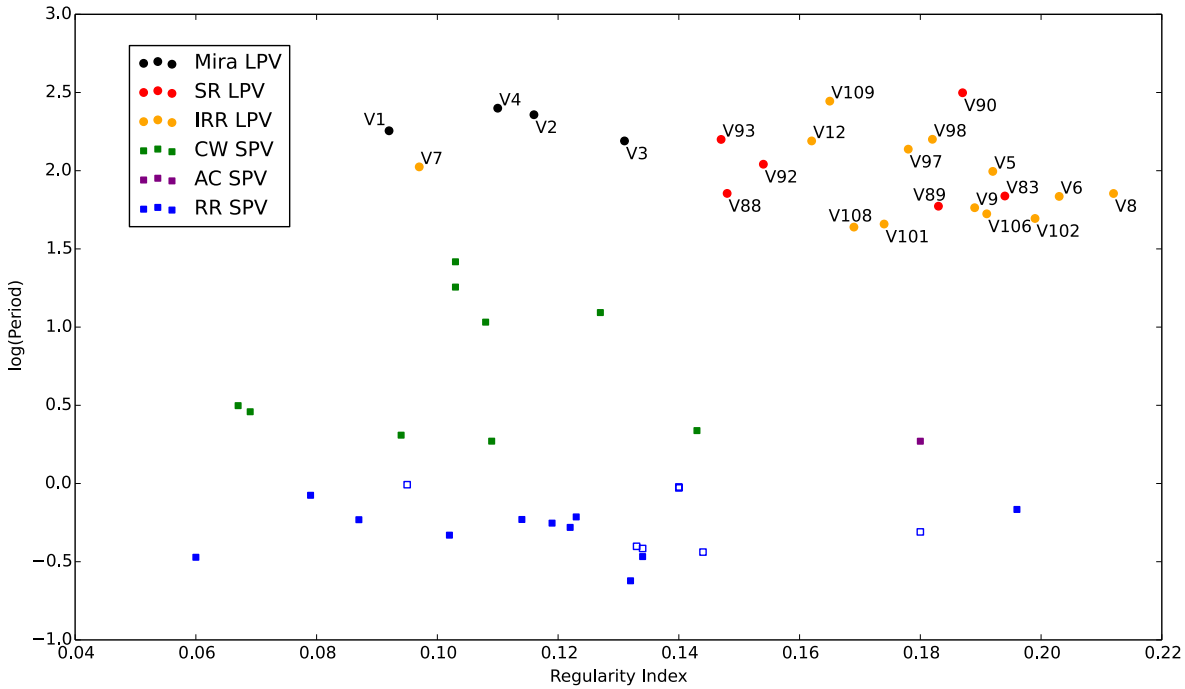

Figure 5.10: known variable stars' regularity indices vs. the logarithm of the period. The logarithmic y-axis is for separating the LPVs from the SPVs. Variable star types sourced from Clement catalogue (2015). Hollow markers denote uncertain classification in source.

index value ~ 0.14, with only three SPVs beyond this point. Of note is that Mira-type V3, and Semi-regular V7, are the most and least irregular of their respective types, and may require re-classification. The index values of known LPV stars are listed in table 5.1

Star ID	Period Obs. (days)	Type (lit.)	Regularity Index
V23	0.33762	RR1	0.060
V36	3.14600	CW	0.067
V18	2.8761	CW	0.069
V28	0.84089	RR0	0.079
V22	0.58687	RR0	0.087
V1	180	M	0.092
V63	2.0376	CWB	0.094
V53	0.9829	RR0?	0.095
V7	105.8 ± 1.0	L	0.097
V20	0.46745 ± 0.00007	RR1	0.102
V72	18.026 ± 0.034	CWA	0.103
V73	26.16 ± 0.10	CWA	0.103
V37	10.759 ± 0.014	CW	0.108
V29	1.8653 ± 0.0003	CWB	0.109
V4	251 ± 5	M	0.110
V59	0.58890 ± 0.00006	RR0	0.114
V2	228 ± 3	M	0.116
V33	0.55805 ± 0.00007	RR1	0.119
V32	0.52415 ± 0.00006	RR1	0.122
V17	0.61142 ± 0.00005	RR0	0.123
V70	12.386 ± 0.025	CWA	0.127
V3	155 ± 2	M	0.131
V26	0.23877 ± 0.00002	RR1	0.132
V51	0.39674 ± 0.00005	RR1?	0.133
V31	0.34096 ± 0.00005	RR1	0.134
V49	0.38425 ± 0.00005	RR1?	0.134
V30	0.95095 ± 0.00018	RR0?	0.140
V68	0.9370 ± 0.0001	RR0?	0.140
V67	2.179 ± 0.003	CW	0.143
V50	0.36438 ± 0.00005	RR1?	0.144
V93	158.5 ± 4.0	SR	0.147
V88	71.6 ± 1.4	SR	0.148
V92	110.0 ± 2.5	SR	0.154
V12	155 ± 3	L	0.162
V109	278.4?	L	0.165
V108	43.6 ± 0.6, 39.9 ± 1(2nd)	L	0.169
V101	45.6 ± 0.3	L	0.174
V97	137.3 ± 3.0	L	0.178
V55	0.49037 ± 0.00007	RR1?	0.180
V77	1.8640 + 0.0007 - 0.0005	AC	0.180
V98	158.8 ± 0.1?	L	0.182
V89	59.3 ± 1.4	SR	0.183
V90	315 ± 10?	SR	0.187
V9	58.0 +0.7 −0.4	L	0.189
V106	53.0 ± 1.4?	L	0.191
V5	99 ± 2	L	0.192
V83	68.9 ± 2.0, 110 ± 5	SR	0.194
V58	0.6826 ± 0.0002	RR0	0.196
V102	49.5 ± 2.5?	L	0.199
V6	68.5 +1.7 −1.0	L	0.203
V8	71.5 ± 1.0	L	0.212

Table 5.1: Recovered known variables' regularity indices, in ascending order from the top. Note the predominance of more regular Miras and SPVs towards the top end. Variable star types are from the literature. The period used to fold our data was determined using PDM.

5.4 Known LPVs

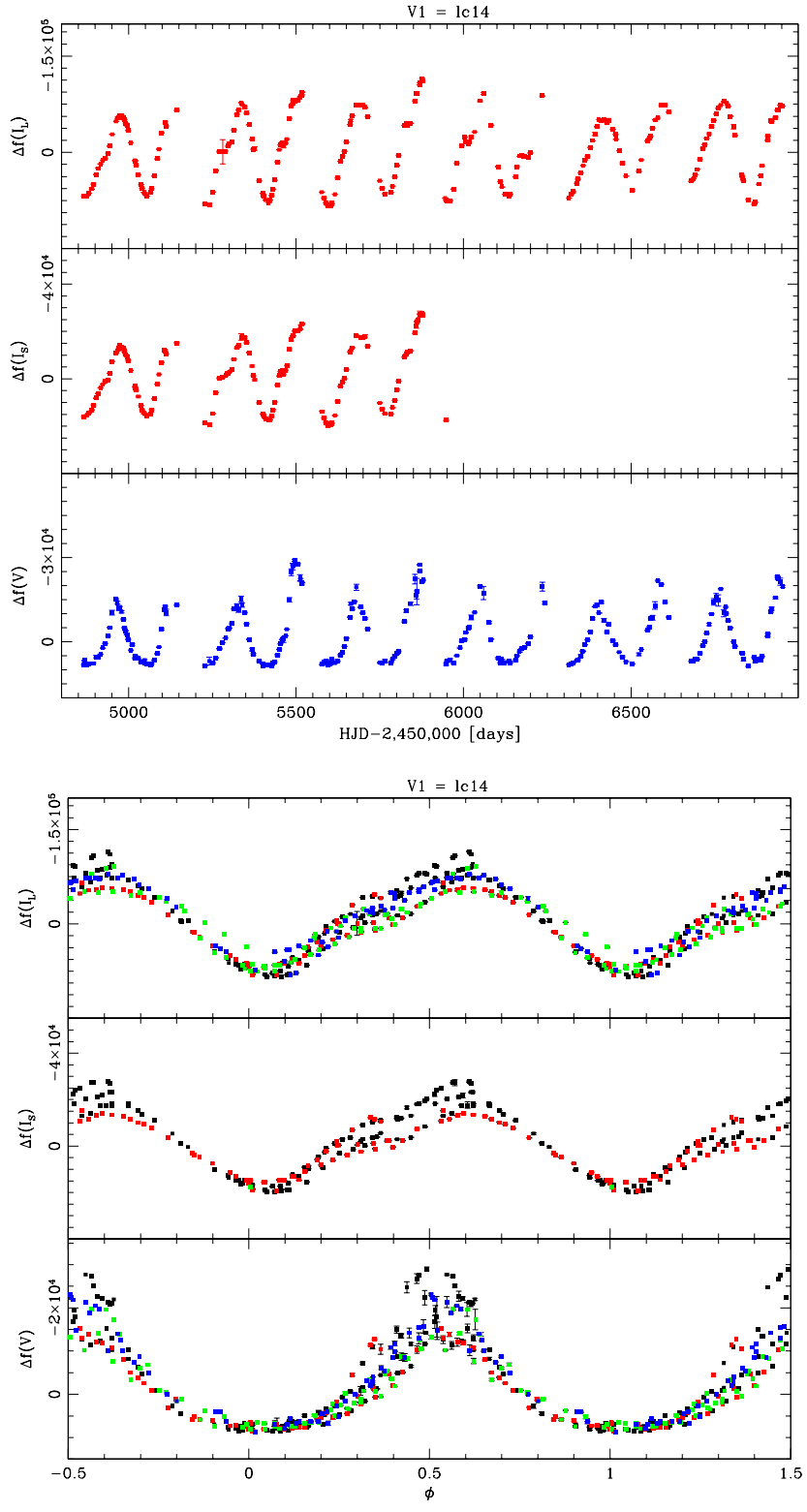

Figure 5.11 Variable V1 ISIS light curve (top), folded light curve (bottom)

Variable V1 (Figure 5.11) is located 0.35 arcmin from the cluster center, putting it near the crowded center region. ISIS was able to extract the light curves, which show evidence of LPV behavior (a long, consistent period, amplitude maxima/minima that are roughly equal, and similarly shaped curves, in all filter/exposure settings.) The IRAF PDM tool produced a period of 180 ± 2 days. The folded light curve confirms this, although it shows some variation in the amplitude of the maxima, particularly in V. The only previous literature that provides a period for this star is Cardona (2011). The period from Cardona is slightly different, 177 ± 3 days, but overlaps with our own, and we can confidently prefer our value based on our greater range of observations, and thus greater number of observed cycles over which we can confirm the regularity of the periodicity of the star. Based on the long period and regularity of the cycle we can classify this star as a Mira-type LPV; the regularity index is ~0.09, the lowest value of all the LPVs we've measured. We must note, however, that Cardona also provides a value for the amplitude that is less than 2.5 mag in both I and V, 0.83 mag and 0.99 mag, respectively. This is out of step with typical Mira variables, whose amplitudes are at least 2.5 mag or higher. The definition of Mira variables, as noted in Sterken and Jaschek (1996), also includes a period of 80 to 1000 days, and a spectral type of Me, Se, or Ce. The period fits the requirement, but the spectral type cannot be determined due to lack of spectral data, which is needed to determine the presence of emission lines (hence lowercase "e" in Me, Se, or Ce). We can say that the star is relatively late in evolutionary stage, as seen in CMD diagram (Cardona, 2011).

Previous literature on V1 prior to Cardona (2011) is sparse; it was discovered by Feast (1972) and confirmed by LEM (1973, 1977), who classified it as Mira, with no period or magnitude information provided since that time. Although Cardona identified it as a new variable star (referring to it as NV3), he was able to provide period and amplitude information.

Another feature of note in V1 are the “shoulders” seen on the rising portion of a cycle, which are more prominent in the I-filter than the V-filter, as can be seen in both the light curve and the folded curve in Fig. 5.11.

While identifying ISIS detections using published star charts, it was found that Skottfelt et al. (2015) have probably misidentified V1 as V95; the published coordinates (Clement catalogue, 2015) of the two stars are separated by 0.54 arcsec, but the finder chart in Skottfelt et al. does not show any bright stars near V95, or any indication of a blended double. If there was a novel variable close to V1 then the reported FWHM in the study of 0.42 arcsec should have rendered it visible on the finder chart. The study also reports that V95 was amongst the least blended of their detected variable stars. In addition, the fact that V1 was one of the first variable stars discovered and classified as a Mira in NGC 6388, means it should yield good light curves that show at least some hints of regularity. V95 was classified as a semi-regular variable on the basis of displaying periodic variability and being on the RGB in the study’s CMD. The study reports a period of 180 days, and a mean magnitude and amplitude in *I*-passband of 11.91 mag and 1.06 mag, respectively, consistent with our own period and Cardona’s measured magnitudes. This measurement further confirms that the classification of this star as a Mira is weak, at best, unless there was blending that was undetected by Skottfelt et al. highr-resolution observations.

The variable star is positioned above the RGB (see Fig. 5.3), meaning it could either be a foreground star, or of hotter temperature and merging shifted it above and towards the cooler end, which is a possibility given the star’s presence near the busy central region. The star’s projected radius places it outside the core radius but within the half-light radius, which by our criterion renders it a probable cluster member.

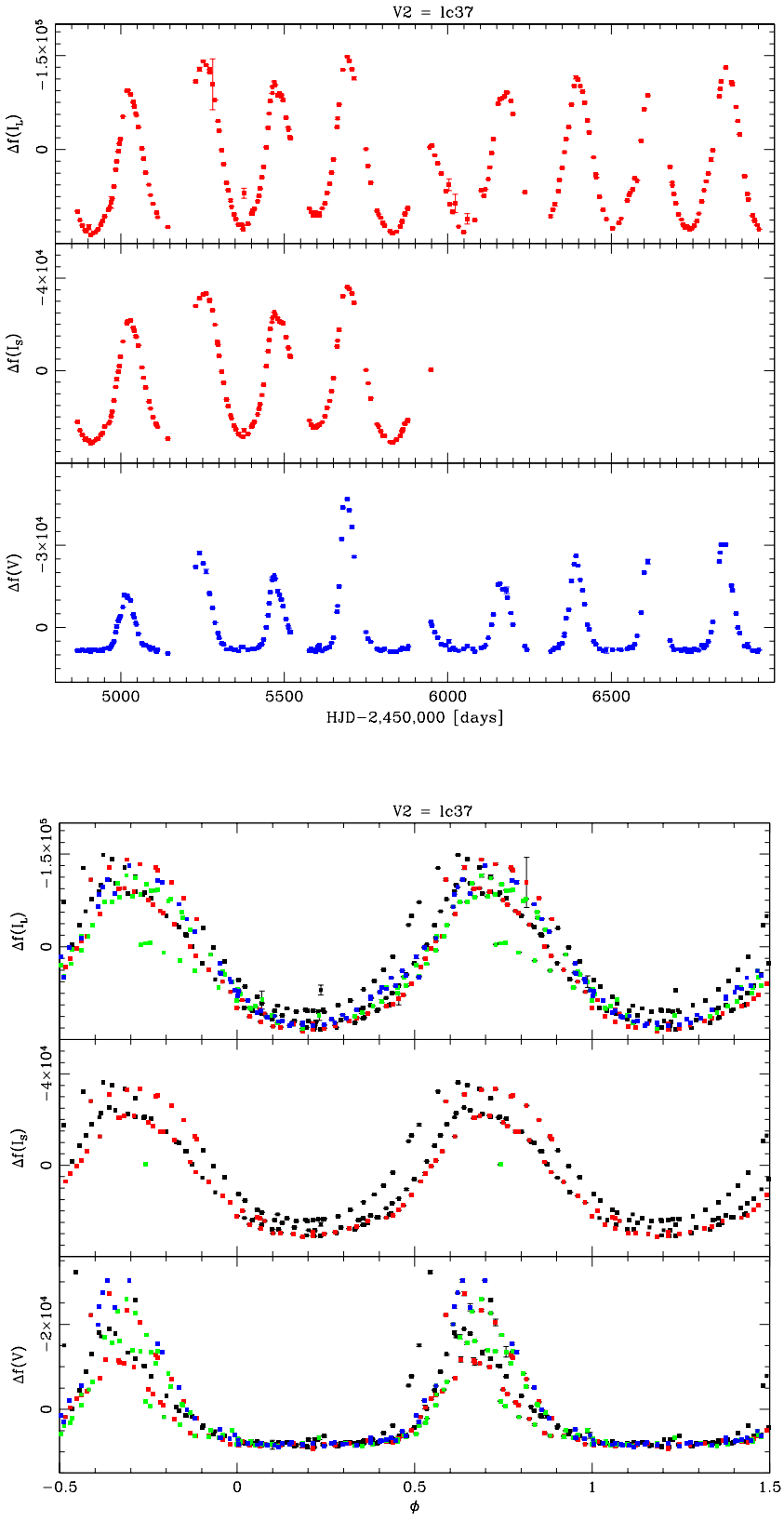

Figure 5.12: Variable V2 ISIS light curve (top), folded light curve (bottom)

Variable V2 (Fig. 5.12) is located 0.28 arcmin from the cluster center, on the edge of the crowded center region. The light curves extracted by ISIS show similar periodic behavior in all filters, but with a variation in maximum flux (and thus amplitude of magnitude variation). The PDM tool gives a period of 228 ± 3 days for both *I* and *V* datasets. We can report, with some reservations, the classification of this star as a Mira variable based on its regularly periodic light curve and long period. The star's regularity index is ~ 0.11 which, of the known Mira-type LPV stars recovered, is second highest after V3 (see Fig. 5.10).

The only previous literature to provide a classification and period is, again, Cardona (2011), which is expected given the long period of the star relative to previous research efforts' short observation baseline or frequency. Discovered and classified as a Mira variable by LEM (1973), it remained without a period or magnitude determination in the literature until Cardona, who gave a period of 227.4 ± 5 days and *I*-filter mean magnitude and amplitude of 11.13 mag and 1.25 mag, respectively. The *V*-filter mean magnitude and amplitude were reported as 13.52 mag and 0.84 mag. These small amplitude values are, again, different from those of typical Mira variables (> 2.5 mag), hence our reservation.

While identifying ISIS detections using published star charts, it was found that Skottfelt et al. (2015) have probably misidentified V2 as V96, much like V1 was misidentified as new variable V96: The published coordinates (Clement catalogue, 2015) of the two stars are separated by 0.91 arcsec, but the finder chart in Skottfelt et al. does not show any bright stars near V96, or any indication of a blended double. For all the reasons listed for V1, we believe V96 if Skottfelt et al. (2015) is the same star as V2. V96 was classified by Skottfelt as an irregular LPV ("L" in GCVS nomenclature) on the basis of being on the RGB but having no detected periodic variability. The study gave mean magnitude and amplitude in I of 12.51 mag

and 1.55 mag. The amplitude being sub-2.5 mag is consistent with our Mira-type definition detailed in chapter 1. Cardona classified it as Mira on the basis of a nearby star merging with V2 affecting the signal and weakening the measured amplitude, but the higher resolution of the Skottfelt et al. observations and their reported lack of blending effects, gives further credence to Cardona's *I*-filter measurements, unless the blending was on a scale smaller than Skottfelt et al. could detect.

The star is located above the RGB (see Fig. 5.3), which is possibly either due to merging affecting the photometric data, or due to it being a foreground star. Merging is a possibility given the star's position in the busy central region. The star's projected radius from the cluster center places it between the core and half-light radii, meaning it is a probable cluster member.

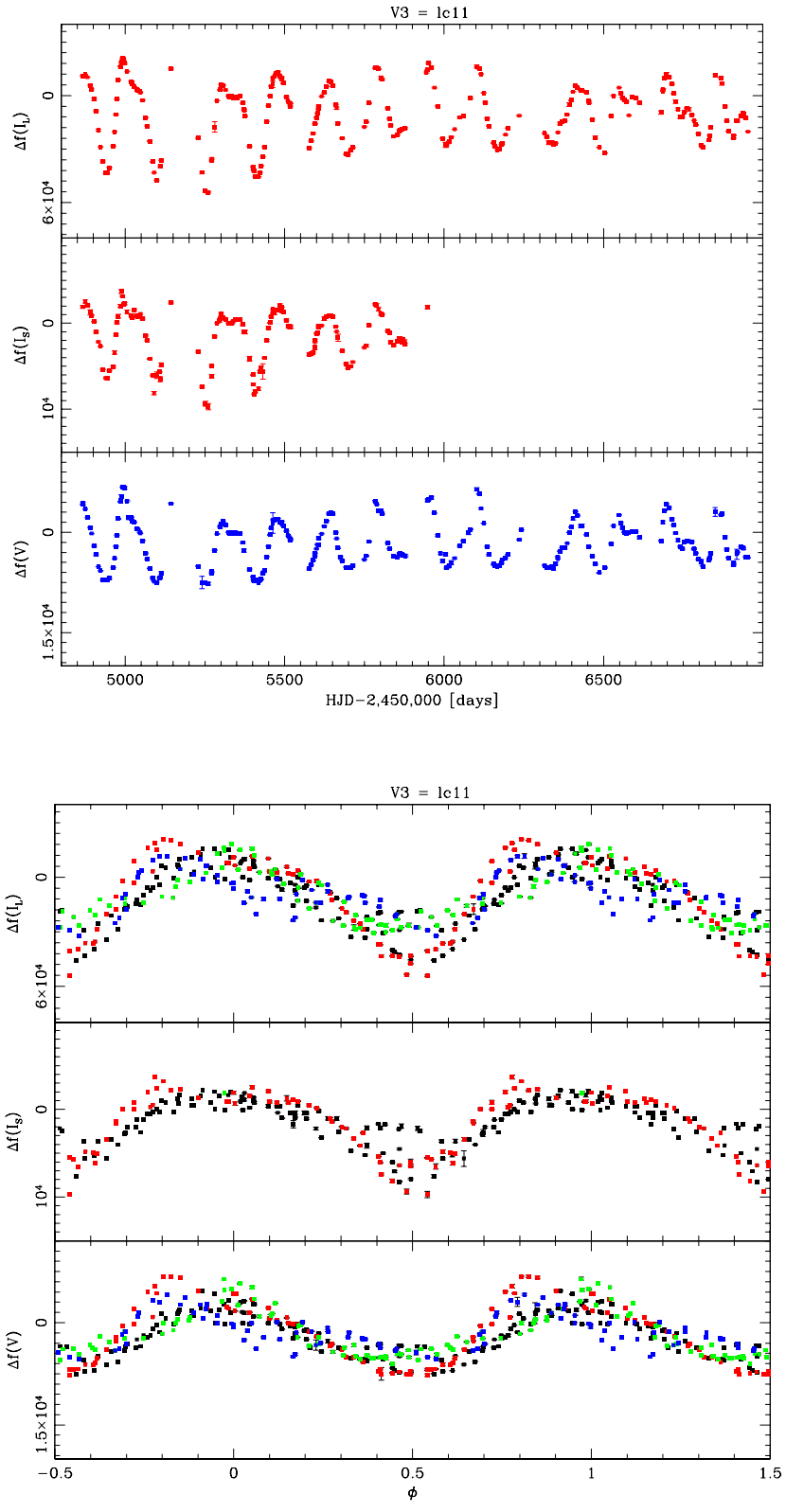

Figure 5.13: Variable V3 ISIS light curve (top), folded light curve (bottom)

Variable V3 (Fig. 5.13) is located farther from the center; at 0.69 arcmin from the cluster center, beyond the half-light radius of 0.52 arcmin (Harris, 1996 (2010 ed.)). The flux difference light curves show periodic behavior that is not perfectly repetitive, and appears to indicate multi-periodic behavior; the light curves in both filters are largely similar, and they both show minima and maxima of varying values, as well as "plateaus", and local maxima/minima (peak/trough pairs). Using the IRAF PDM routine, we found a period of 155 ± 2 days. Folding the curves based on that value, we can see evidence of a periodicity that is somewhat variable in amplitude, but consistent in periodicity, and also variation in the amplitude of the minima and maxima. The star regularity index is ~0.13, the highest of the known Mira-type LPV stars in our work; see Fig. 5.10 to see its position on the index relative to the other Miras. Based on the aforementioned, and using reference light curves (Sterken and Jaschek, 1996), we classify it as a semi-regular LPV star.

Discovered by LEM (1973), and noted then as being "bright", it was also later noted as possibly being of low variability, 0.2-0.3 mag, by HH (1986), with the caveat that it was blended with another star, so they did not provide a magnitude or period. Magnitude and period values were first given by Sloan (2010): K-band mean of 8.97 mag, amplitude of 0.28 mag, period of 156 days. More recent work done by Cardona (2011) over the first two-years of our data found a period of 156.8 ± 4 days, and V-filter and I-filter amplitudes of 0.92 mag and 0.67 mag, respectively. Although our semi-regular classification is in disagreement with the previous classification of Mira by Sloan (2010), we prefer ours due to the length and sampling frequency of our observations in comparison (compare data points in Fig. 5.13 to Fig. 5.14), Cardona's (2011) finding of an amplitude significantly lower than the usual 2.5 mag for Mira-type LPVs.

The relatively high regularity index of the variable, placing it as the least regular of the Miras in the literature by our definition, is also a factor in our classification.

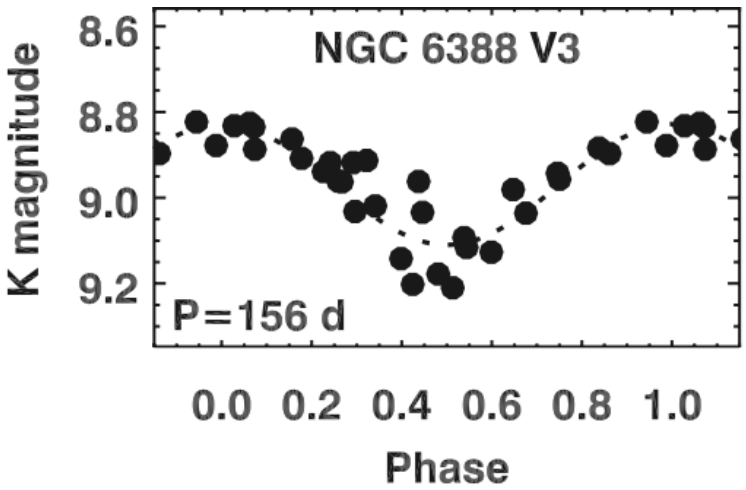

Figure 5.14: Variable V3 folded light curve from Sloan (2010). The mean K-band magnitude was reported in the work as 8.97 mag.

The star's CMD position is slightly above our defined RGB band, thus we cannot use it as evidence of cluster membership; it is possible for the photometric data to have been polluted by another star, or that it is a foreground field star and thus brighter and appears higher than the RGB. The former possibility is less likely due to the star being outside the busy central region; the star's position is outside the half-light radius, but within our defined tidal radius, which by our criterion makes it only a possible cluster member.

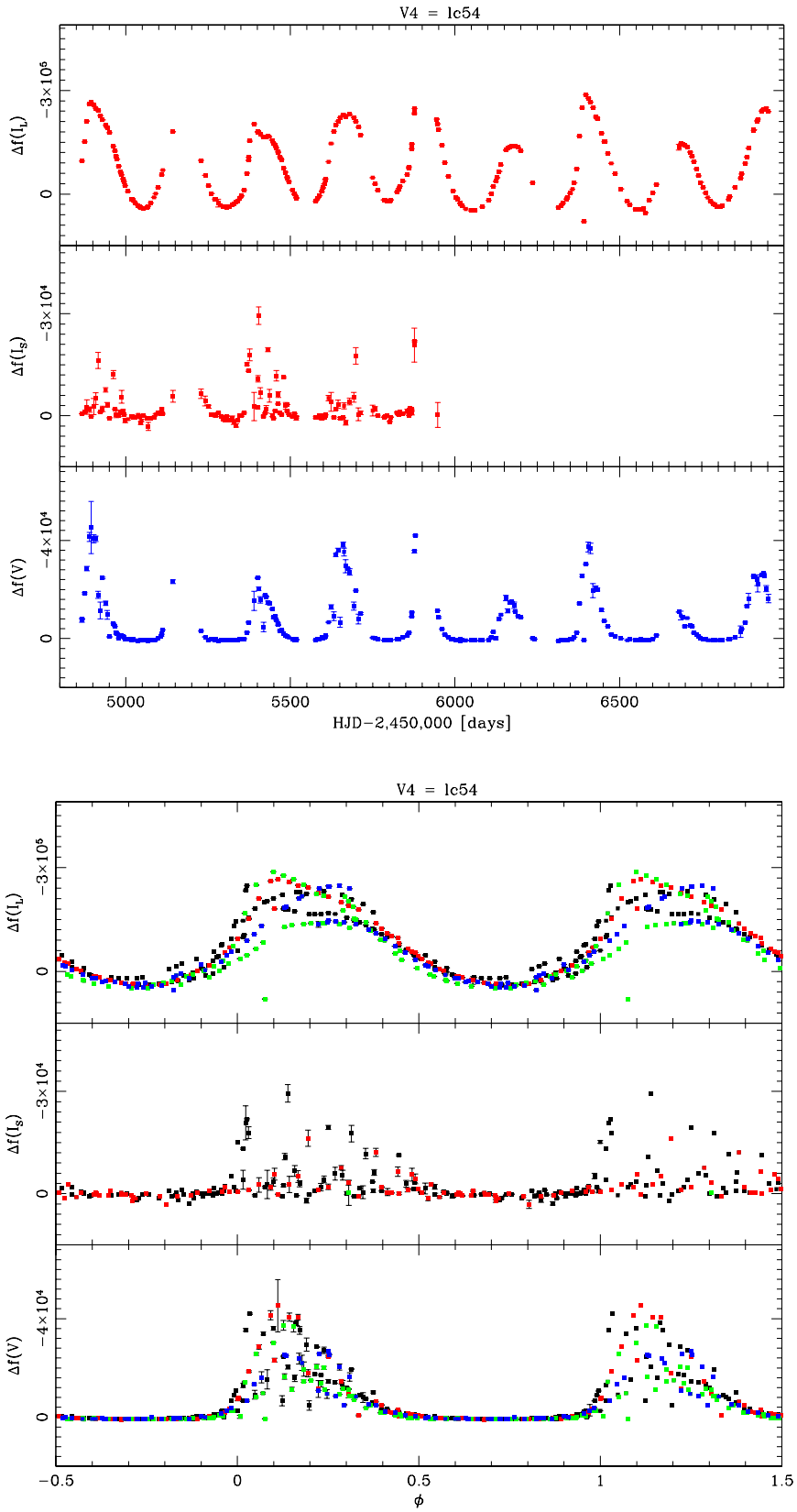

Figure 5.15: Variable V4 ISIS light curve (top), folded light curve (bottom)

Located 3.22 arcmin from the cluster center, variable V4 was one of the earlier detected LPVs in the cluster. As can be seen in Fig. 5.15, the light curve does not display any multi-periodic behavior, and although there are different maximum flux values in different cycles, the variation appears to be generally sinusoidal with the flat portion of the plots an artifact of the linear y-axis (see Fig. 5.16 for confirmation from Cardona (2011)). Using the PDM method we determine the period to be 251 ± 5 days, and the regularity index is ~0.11, third lowest (and most regular by our definition) as can be seen in Fig. 5.10. We can thus safely classify this star as Mira.

V4 is one of the LPV stars discovered early on (LEM, 1973), yet it remained without classification or magnitude/period data until Sloan (2010), who classified it as a Mira with a K-band mean of 8.47 mag, 0.80 mag amplitude, and period of 253 days (see Figure 5.17 for the folded light curve). Cardona's (2011) DAOPHOT work on a subset of our data yielded amplitude values of 5.47 mag in V and 2.730 mag in I. These values confirm the Mira classification as it satisfies the minimum amplitude condition (~ 2.5 mag in the V band). The V-filter amplitude is bigger than the I-filter amplitude, which is in turn bigger the K-band amplitude. This is expected given that pulsational variables' amplitudes are typically larger near the ~600 nm V-passband midpoint, smaller near the redder 800 nm I-passband midpoint, and thus even smaller in redder far-IR K_S band with 2.14 μm ~ 2100 nm midpoint. The larger error bars seen in V relative to I_L (see Fig. 5.15, folded light curve) is likely due to the linear flux-based y-scale and the smaller mean V magnitude of 14.83 mag relative to the mean I magnitude of 11.69 mag (according to Cardona, 2011). The larger I_S scatter is due to the smaller exposure time.

The star's projected radius from the cluster center is outside the half-light radius, but within the tidal radius (as expected for our FOV), which makes it a possible cluster member. However, the star is located on the RGB-band, making it more likely to be a cluster member.

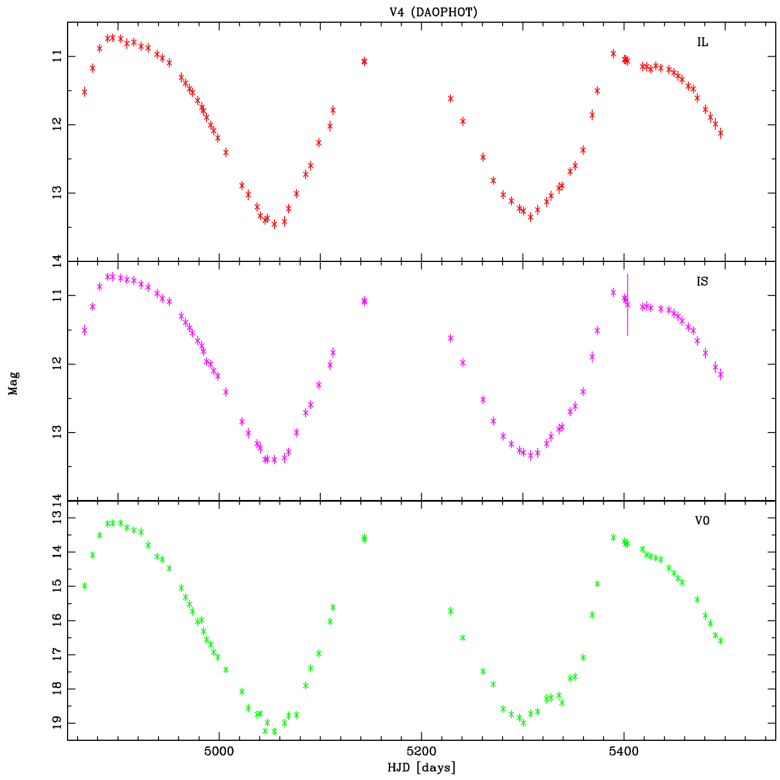

Figure 5.16: Variable V4 DAOPHOT light curve (Cardona, 2011)

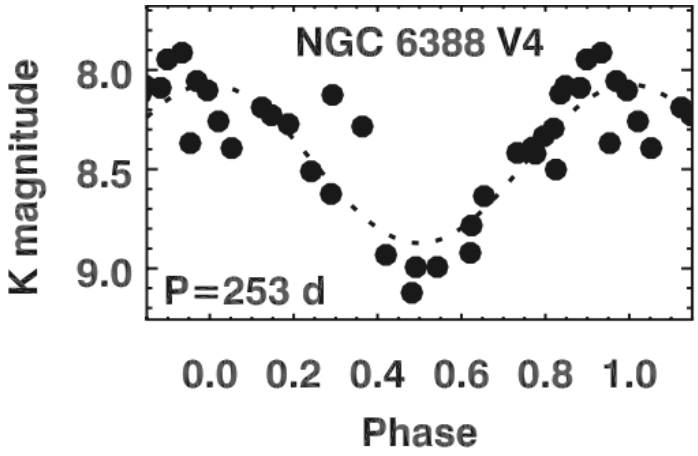

Figure 5.17: Variable V4 K-band folded light curve from Sloan (2010).

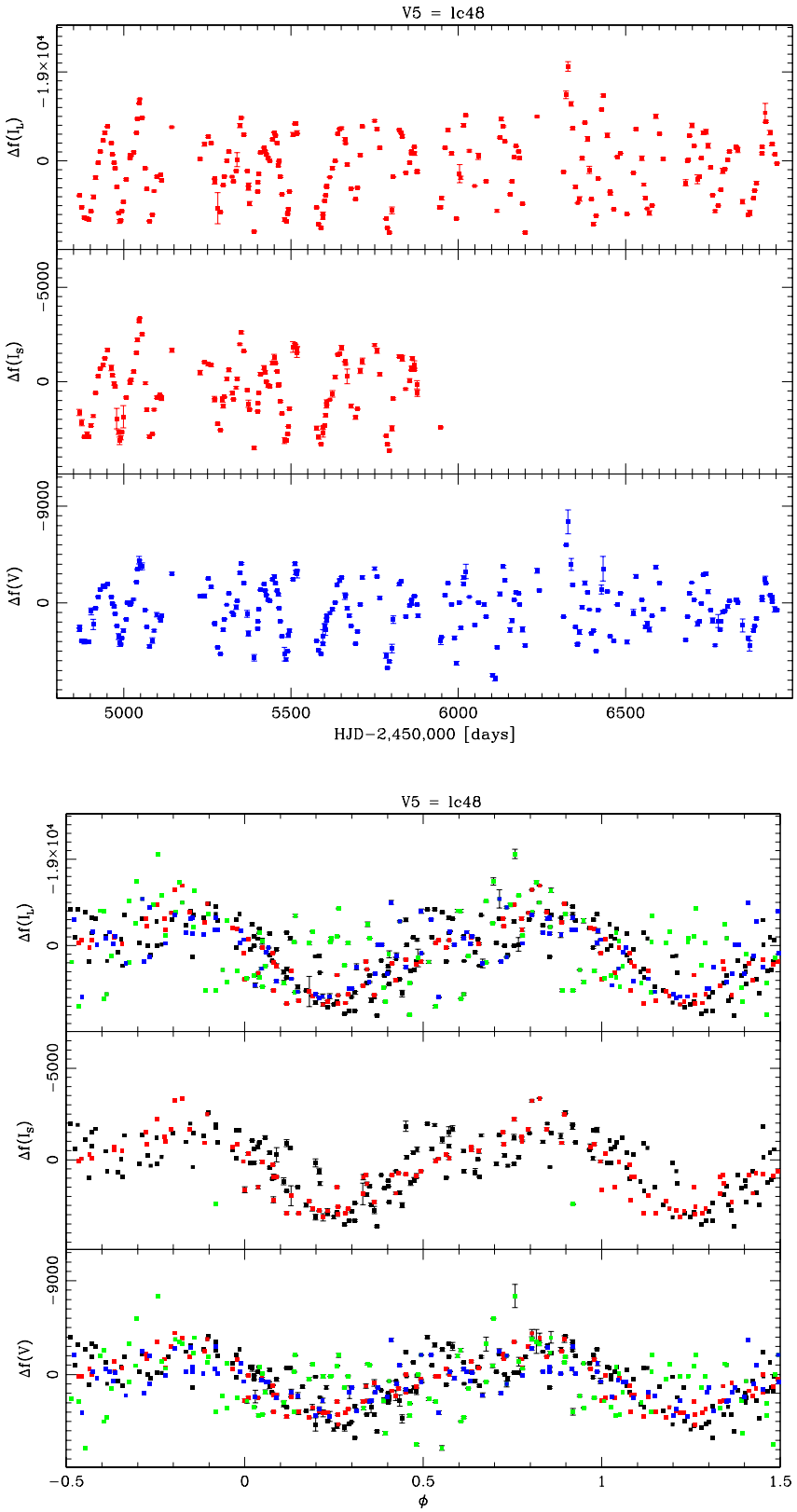

Figure 5.18: Variable V5 ISIS light curve (top), folded light curve p = 99 days (bottom).

Another of the LPVs discovered early on, V5 is located 1.10 arcmin from the cluster center, placing it outside the most blended regions. As can be seen from Figure 5.18, the star appears to lack simple sinusoidal regularity, displaying multi-periodic behavior as evident by closely spaced "double" maxima/minima, and the differences in maxima/minima values present in the folded light curve. It also has a regularity index of ~0.19, placing it with semi-regular and irregular variables on the index (see Fig. 5.10). We can thus classify this LPV star as a semi-regular.

V5's discovery paper (LEM, 1973) identified it as an LPV but did not classify it further, and the first photometry presented (LEM, 1977) provided magnitudes in *I* and *V*, and an amplitude in *V* (0.8 mag). The first CCD photometry by Silberman et al. (1994) was too brief to determine a classification or the variability amplitude. The first classification and periodicity determination was done by Cardona (2011), where the star was also duplicated as a new variable (NV26). It was classified as a semi-regular, with a period of 100.3 ± 8 days, and amplitudes were measured by DAOPHOT to be 0.56 mag and 0.29 mag in V and I, respectively. Cardona's light curve is shown in Fig. 5.19.

The star is located outside the half-light radius, but within the tidal radius (as expected given the ISIS FOV) and thus a possible cluster member. The star's color and magnitude place it within the RGB band that, by our criterion, makes it a likely cluster member.

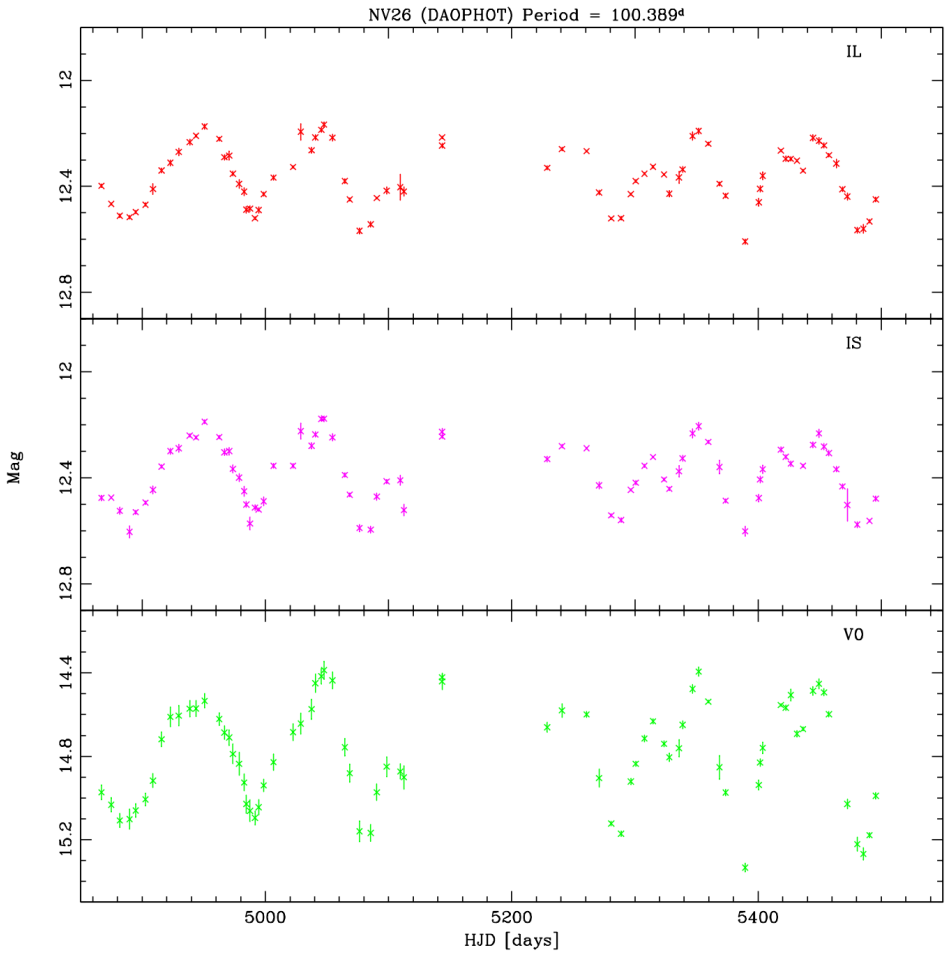

Figure 5.19: Variable V5 DAOPHOT magnitude light curve (Cardona, 2011, where it was listed as NV26)

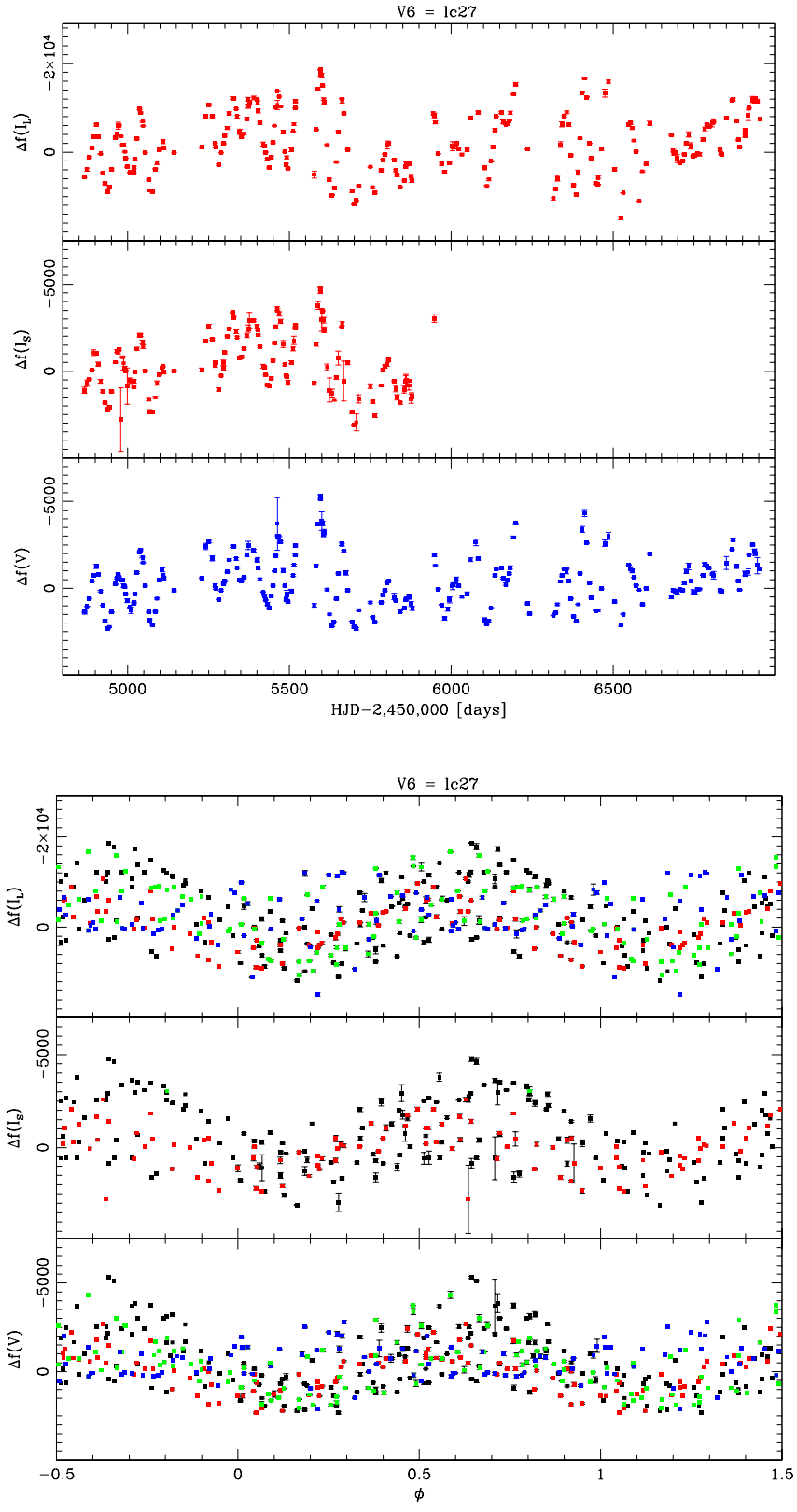

Figure 5.20: Variable V6 ISIS light curve (top), folded light curve (bottom).

Light curves for V6, located 1.62 arcmin from the center are shown in Fig. 5.20. They indicate strong multi-periodic behavior, with a large variation and "doubling" in maxima/minima in both regular and folded light curves. After determining the best period (68.3 ± 2 days) and folding accordingly, the resulting light curves show large variations about the mean. The regularity index is ~0.2, making it by our definition to be the second-least regular of the known LPVs detected. The persistence of a period, despite the variation, led us to classify this LPV star as a semi-regular, while noting that it is edging towards behaving as an irregular as evidenced by the index, and the regular light curves' beats-like shape.

V6 is another early LPV discovered by LEM (1973). Follow up research (LEM, 1977) determined the V-filter amplitude (0.7 mag) but no period or classification. Cardona (2011) provided the first period and classification (69.9 ± 7 days and semi-regular, respectively), as well as a V-filter amplitude of 0.38 mag and an I-filter amplitude of 0.12 mag.

The star lies outside the half-light radius, which by our projected radius criterion makes it a possible cluster member. The star's color and magnitude, as recovered from Cardona's photometric database, place it in the RGB band, which makes it a likely cluster member.

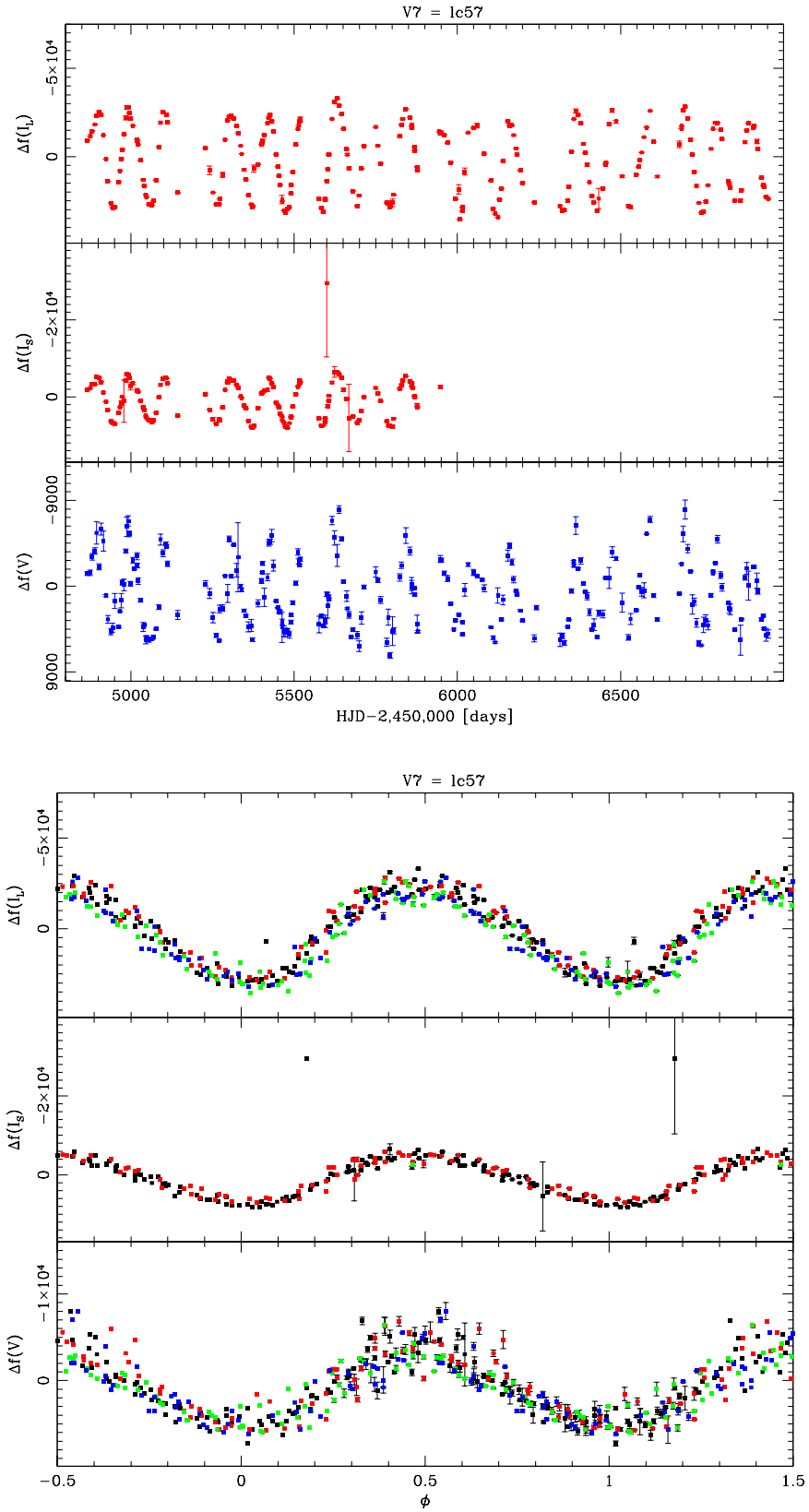

Figure 5.21: Variable V7 ISIS light curve (top), folded light curve (bottom).

LPV star V7 shows (Fig. 5.21) clear signs of regularity. Located at a distance of 1.83 arcmin from the cluster center, farther away than most LPVs, its classification is a choice between Mira and semi-regular; the light curve is characteristically sinusoidal, but a variation in the maxima/minima is apparent. That said, this variation is small, the curve does not show signs of multi-periodicity, and the folded light curve is typical of Mira LPVs. The folded light curve has a regularity index value of ~ 0.1 (see Table 5.1), indicative of a very regular cycle, as it is in the index value range typical of Mira LPVs and CW/RRL SPVs. As such, we classify it as Mira, with a period of 105.8 ± 1.

V7 was discovered by LEM (1973), and follow up work (LEM, 1977) found the amplitude in V to be 0.8 mag. The first CCD photometry by Silbermann et al. (1994) provided magnitudes in V, B, and R, but no periodic behavior-related data due to limited observations only capturing parts of the cycle.[1] Cardona (2011) was the first to do so, listing it under a different name (V5) but as a Mira, with a period of 98.6 ± 3 days, and amplitudes of 1.66 mag and 0.81 mag in the V and I filters, respectively. The differences in V amplitude between LEM (1977) and Cardona (2011) might be explained by the differences in observation time range (1 year vs. 2 years, respectively). There is thus a possibility that V7 is not a Mira, but a semi-regular that tends towards the regular end of the regularity spectrum; the star is not in the busy core region nor does it have a companion close enough to have affected the photometry of Cardona (2011) or earlier studies, and given the definition of Mira-like LPVs having *V* amplitudes greater than 2.5 mag, that would make V7 a very regular semi-regular LPV. The star is outside the half-light radius, thus it is by our criterion a possible cluster member. It is, however, located in the RGB band (see Fig. 5.3), thus it has a higher likelihood of being a member.

[1] Two sets of three-days of consecutive observations, separated by a 400-day time baseline.

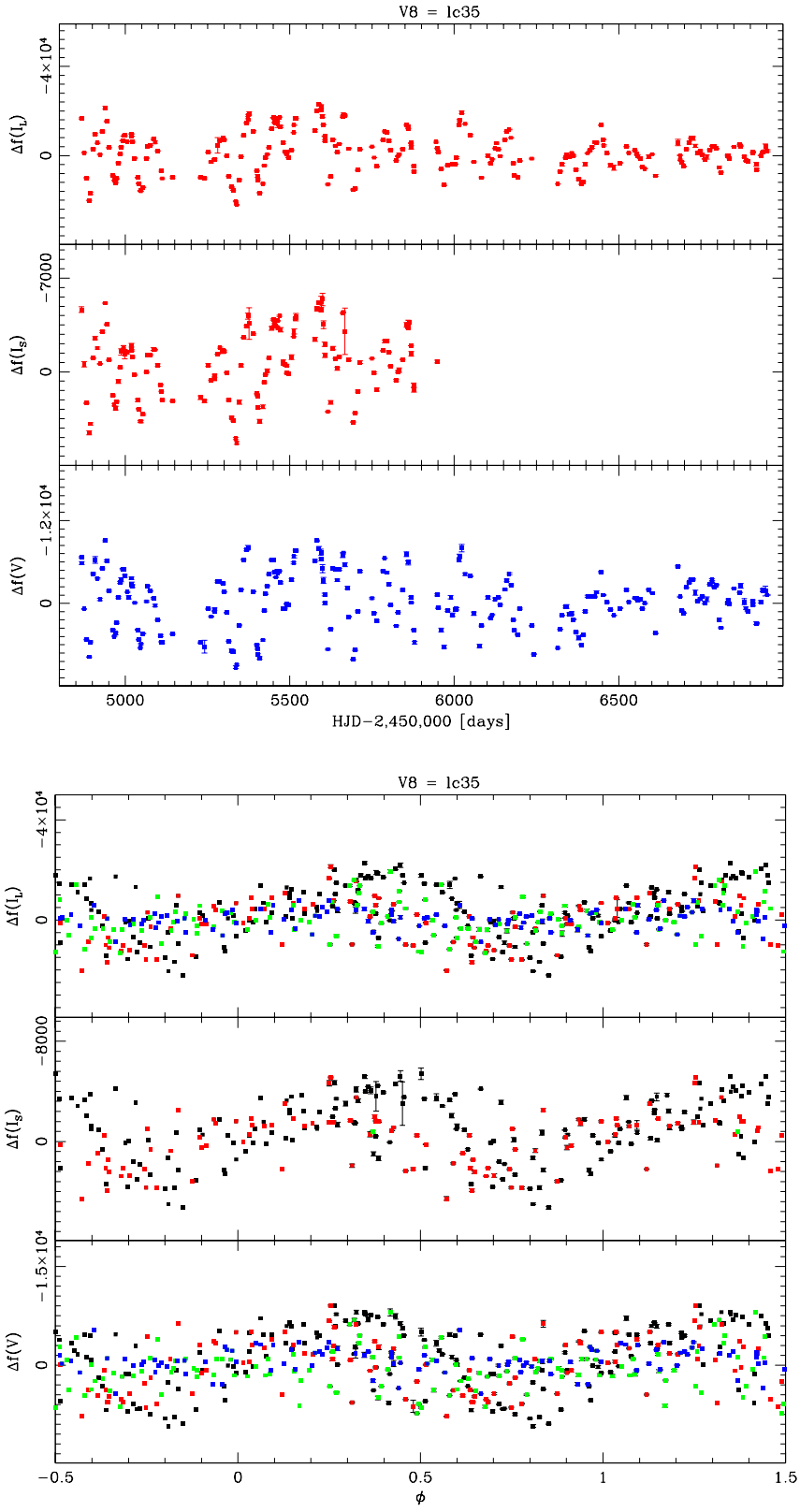

Figure 5.22: Variable V8 ISIS light curve (top), folded light curve (bottom).

The light curves (Fig. 5.22) for LPV V8, located 0.72 arcmin from the cluster center, indicate irregularity; the intensity change does not appear sinusoidal, or even follow a simple multi-periodic pattern as present in stars discussed above. The maxima and minima also vary significantly in their values, with the light curve's peaks and troughs having no uniform value of difference from the mean. This irregularity proved problematic for determining the period, but a combination of the PDM method and simple peak-to-peak/trough-to-trough measurements give a period of 71.5 ± 2 days. Using this information, the resultant folded light curve highlights the aforementioned maxima/minima irregularity, and indicates that different cycles have significantly different periods in comparison to previously discussed semi-regular stars' folded curves. The regularity index of the star at the detected period is ~0.21, the highest value of all known LPVs detected in the cluster. We can thus confidently conclude that this LPV is of the irregular variety.

First announced as an LPV by LEM (1973), follow up work by the same authors (LEM, 1977) gave magnitudes and, relevant to our work, a V-filter amplitude (0.6 mag). It then remained without additional published data or classification until Cardona (2011), who classified it as a semi-regular, with V and I amplitudes of 0.44 mag and 0.33 mag, respectively, over the range of time observed. He also gave a period of 73.9 ± 5 days. As we share the same data (2009, 2010), we can confidently conclude that this classification discrepancy is due to the short time baseline used in Cardona's study (2 years compared to 6 years), and doesn't include the years of 2013 and 2014 where the maxima and minima's absolute values decrease significantly. See Fig. 5.23 below for an illustration of this, as well as an apparent magnitude light curve produced by DAOPHOT.

Variable V8 is outside the half-light radius, and thus a possible cluster member by the projected radius criterion. It is positioned above the RGB band (see Fig. 5.3), possibily due to it being a foreground star, or combined light with a neighboring star, affecting the data. The latter is less likely due to the star being outside the busy central region, thus it remains a possible cluster member.

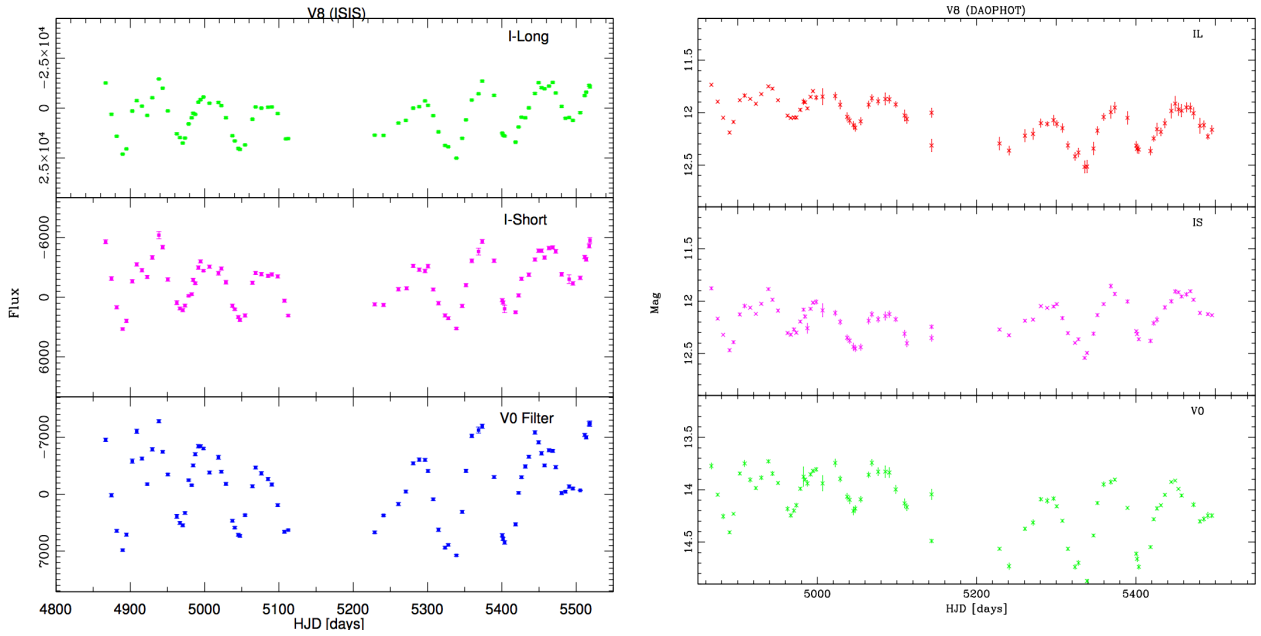

Figure 5.23: Variable V8 ISIS relative-flux light curve Top Left – DAOPHOT apparent magnitude light curve Top Right (Cardona, 2011)

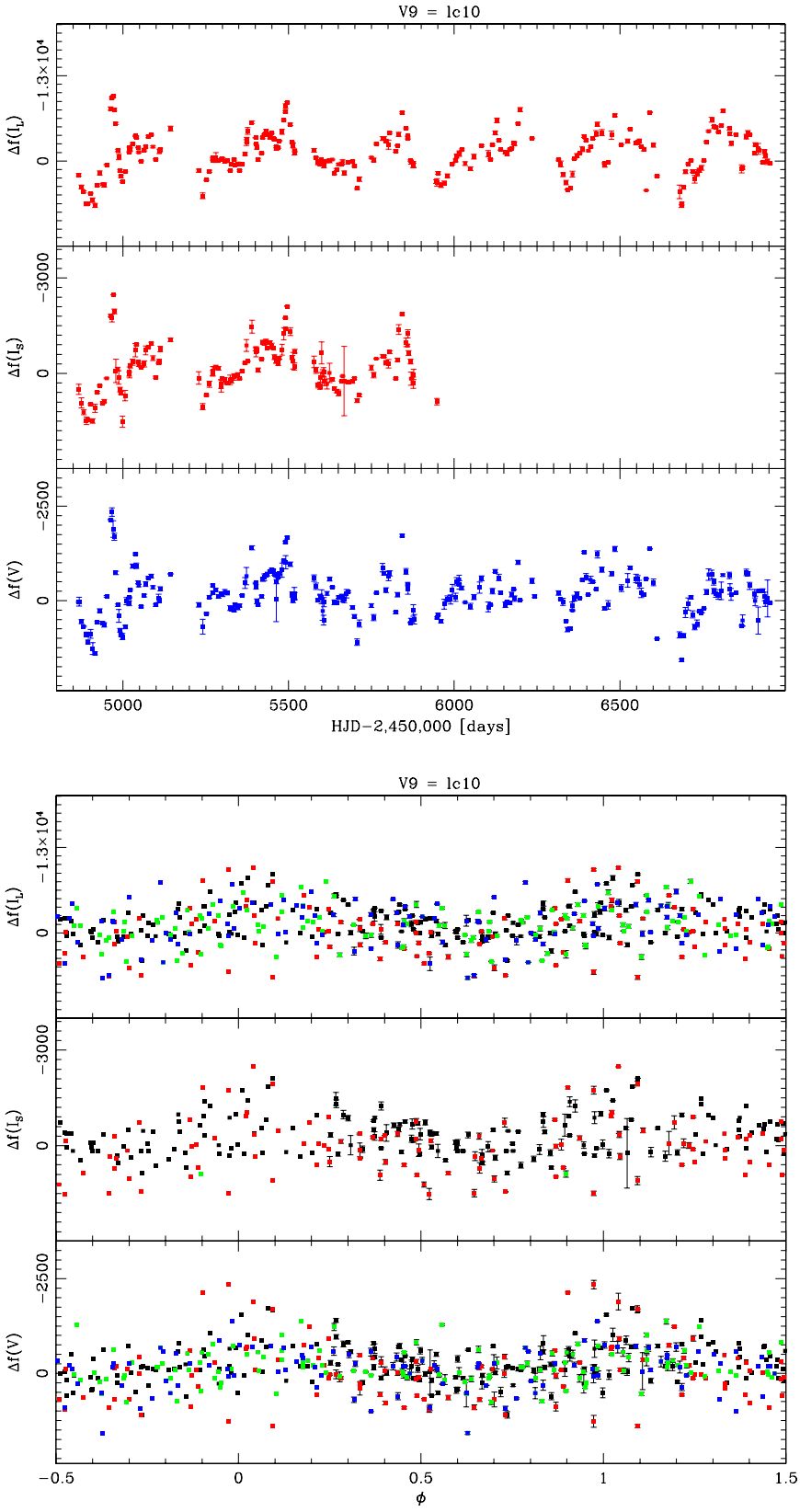

Figure 5.24: Variable V9 ISIS light curve (top), folded light curve (bottom).

The last of the LPVs discovered by LEM (1973), star V9 is located 1.00 arcmin from the cluster center. Again, it displays signs of irregularity more than those of simple multi-periodicity, with a large variation in maxima/minima seen in the regular and folded light curves (Figure 5.24). That said, there does appear to be a repeating pattern that indicates two periods: the light intensity appears to rise, with variation about a mean, before undergoing a large drop. Investigation using the PDM method and light curves found two periods: a small one of 58.0 ± 0.6 days, and a larger one that is roughly 348 ± 100 days. The small one is the primary period, and is confirmed to be accurate via the two methods, but the larger one requires more investigation; it is apparent, but exhibits a large variation, when measured on the regular light curve, and using the PDM method results in alias detection as 348 is a harmonic of 58. The regularity index for the primary period is ~0.19, placing it in the middle of the index range populated by semi-regular and irregular LPVs (see Fig. 5.10). More investigation of the long secondary period (LSP) is required using a FFT (fast Fourier transform) analysis to get an accurate determination, but we have tentatively classified V9 as a semi-regular rather than an irregular LPV, pending further investigation.

V9 was first mentioned in LEM (1973). The follow up study (LEM, 1977) found a V-filter amplitude of 0.3 mag. The first CCD photometry presented (Silberman et al., 1994) did not offer periodic behavior-specific details (e.g. period, amplitude) but offered magnitudes (V, B, R). Its first characterization as an LPV was by Cardona (2011), who found 0.15 mag and 0.04 mag V and I amplitudes, respectively, and a period of 59.50 ± 3 days. It was classified as an Irregular LPV, but it was noted that more data were required for accurate determination.

The star lies outside the half-light radius and thus by our criterion is a possible cluster member. It lies in the RGB band, however, increasing the likelihood of cluster membership.

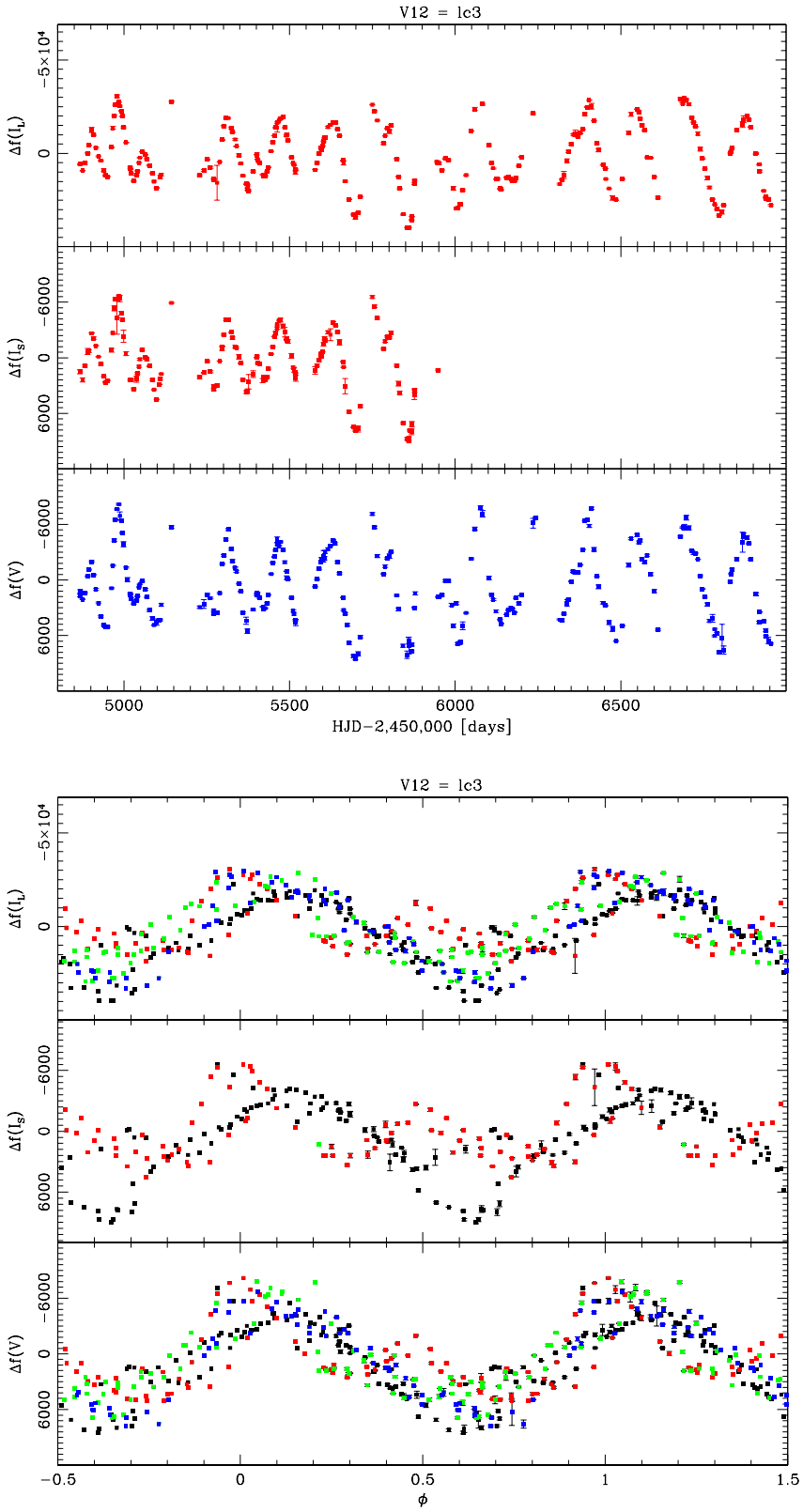

Figure 5.25: Variable V12 ISIS light curve (top), folded light curve (bottom).

Located 1.02 arcmin from the cluster center, star V12 is a textbook example of a semi-regular LPV. Multi-periodic behavior is evident in the light curves in Fig. 5.25 by the presence of doubled-peaks and plateaus, and the maxima/minima absolute values changes. The period was found, through the PDM method, to be 155.2 ± 3 days, and folded light curves were generated appropriately. The folded light curves highlight the aforementioned multi-periodic nature with the variation of maxima/minima, and also indicate a variation in the period that precludes the generation of a "thin", uniform curve, instead generating a curve that varies about the mean in both phase and intensity. The time-series light curves also seem to suggest the presence of an even longer period than the observation time, but more data, plus an FFT analysis, is necessary to verify this. The regularity index was found to be ~0.16, making it one of the more regular semi-regular and irregular LPVs that mostly have values higher than 0.16 (see Fig. 5.10). We can thus safely conclude that this star is a semi-regular LPV.

Discovered by LEM (1977), who supplied B, V, and R-passband photometry and V-filter amplitude (0.6 mag), followed by B-filter photometry by HH (1986). The first CCD photometry was by Silbermann et al. (1994), but they did not provide periodic characteristics. The first to do so, as well as giving a classification, was Cardona (2011), who gave V and I amplitudes of 0.37 mag and 0.23 mag, respectively, and estimated the period to be 81.6 ± 8 days. The large discrepancy with our period value is mostly likely due to his smaller time range, which was confirmed by simple peak-to-peak cycle measurements in our data, as well as using the PDM method on the data subset available to Cardona. It was found that a period of ~82 days corresponding to minimal scatter does exist when only using the 2009 and 2010 data, but that it is reduced in significance when more observational data are available.

V12 is located above the RGB (see Fig. 5.3), so either it is a foreground star or its photometry is affected by merging with a nearby star, somewhat unlikely given its location outside the half-light radius. This outer location means that it is, by the projected radius criterion, a possible cluster member.

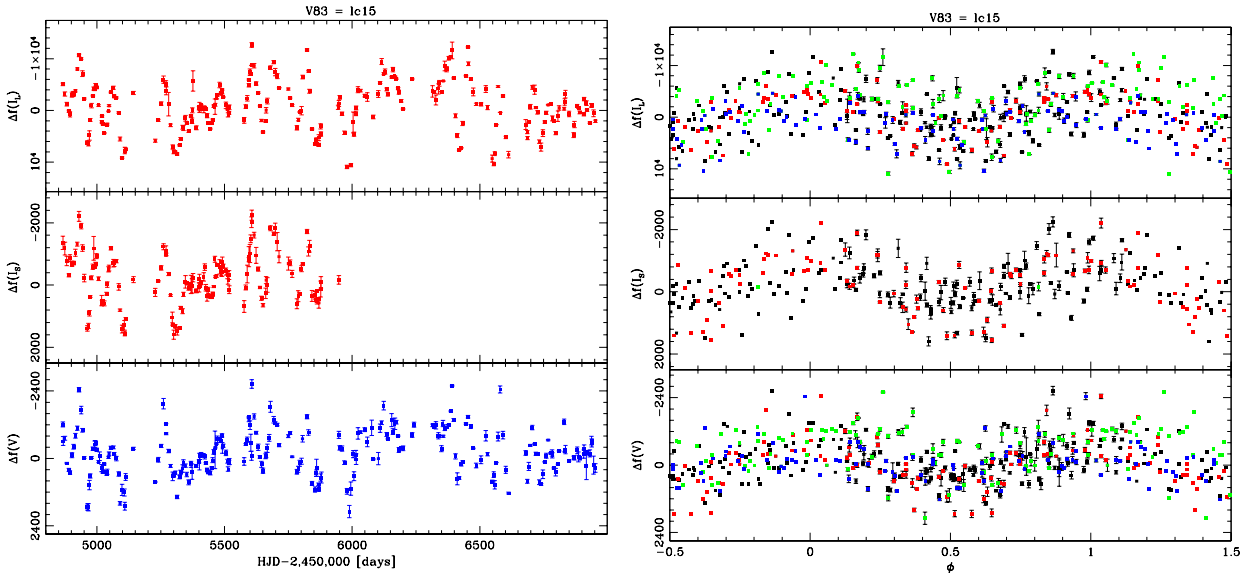

Figure 5.26: Variable V83 ISIS light curve (top), folded light curve p = 68.9 days (bottom).

V83 is an LPV located 0.438 arcmin from the cluster center placing it within the half-light radius and, in our image scale, at the edges of the blended central region. In Fig. 5.26, the light curve displays multi-periodic behavior, which is evident in the close spacing of maxima/minima, and the variation in their values. This is confirmed by the PDM routine: 68.9 ± 2.0 days and 110 ± 5 days are respectively the primary and secondary periods. The secondary period was also confirmed not to be an alias via the PDM routine, where it appeared at the expected value (137.8 days). Folding the light curve at the primary period (see Fig. 5.26) shows the variation caused by the presence of the secondary period.

Discovered by Skottfelt et al. (2015), the star was also identified by Cardona (2011) as an LPV under the name NV4. Cardona gave a similar period as our primary (68.4 ± 4 days), and

hypothesized the presence of an LSP to account for the multi-periodic behavior. Our detected secondary period is smaller than the minimum value (~10 times the primary period) to be considered an LSP, but we cannot rule it out. It was classified by Skottfelt as SR by virtue of its long period (50.68 days), low amplitude (0.15 mag in *I*-bandpass) and presence on the RGB[1].

Given the observational cadence of the Skottfelt study, they have managed to capture ~2 cycles of pulsation, and give a folded light curve. Using peak/trough counting, we have observed it over a minimum of 14 cycles, which is reasonable given that 26 cycles are possible given the primary period's length, our cadence, season length and long time baseline. Thus despite the discrepancy in period value we can confidently assert our own, but note that we are in agreement regarding the semi-regular classification. The regularity index is 0.192, the fifth highest in the index (see Fig. 5.10).

V83's photometric data could not be found in Cardona's database, as no photometric data was found that was for a star within a 3 pixel (~1.8 arcsec) radius V88's location. Although we cannot determine whether it lies on the RGB band or not from our data, Skottfelt et al. (2015) report that it is on the RGB. The star is located within the half-light radius, however, and is thus a probable cluster member.

[1] In the paper, the stars V83-V92, V94, and V95 were classified SR as a group on that basis.

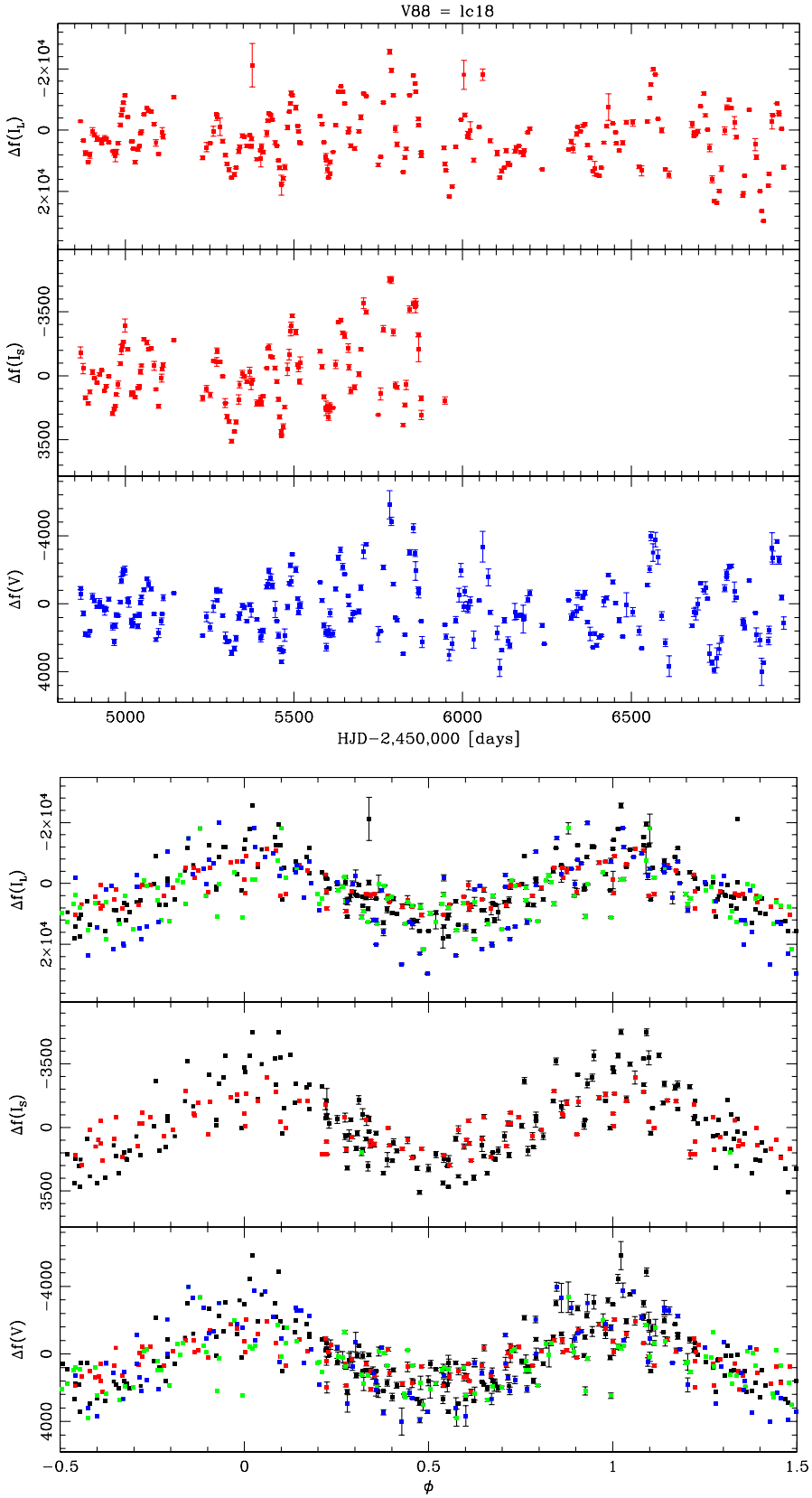

Figure 5.27: Variable V88 ISIS light curve (top), folded light curve p = 71.6 days (bottom)

Variable V88 is an LPV located 0.204 arcmin from the cluster center, within the half-light radius. Due to our image scale this places it within the blended region near the cluster core[1]. As can be seen in Fig. 5.27, it displays a light curve characteristic of multi-periodic LPVs: variation in value and spacing of maxima/minima. Using the PDM routine, only a single period of 71.6 ± 1.4 days was detected, although there may be an LSP present as evident by large maxima and minima at the middle and end of our observational baseline, respectively. A folded light curve with the detected period is shown in Fig. 5.27, in which the variation in maxima/minima values is also evident.

Skottfelt et al. (2015) discovered V88, which was also identified in Cardona's work (2011) as NV11. Part of the group of stars classified by Skottfelt as SR on basis of being RGB stars with long periods and low amplitudes, V88 is actually a star with a relatively high amplitude: 0.35 mag about a mean luminosity of 12.2 mag in the *I*-bandpass. Mira variables generally have amplitudes lower than 2.5 mag in that bandpass (see chapter 1), so this is consistent with our classification. Cardona's DAOPHOT photometry gave an amplitude of 0.14 mag and 0.19 mag in the *I* and *V* bandpasses respectively, and a bigger magnitude range of 0.35 mag and 0.19 mag in *I* and *V* respectively. The similarity between Skottfelt's amplitude and Cardona's range in the *I*-bandpass is likely due to the former's shorter baseline compared to the latter's, but the possibility of blending affecting the values was noted by Cardona. This was noted in reference to his classifying V88 as an SR variable despite having a *V* amplitude lower than the expected 1 mag. The periods detected by Skottfelt and Cardona were 58.3 days and 71.3 days, respectively. Again, the discrepancy is likely due to the difference in time baseline, and

[1] The core radius is 0.12 arcmin (Harris, 1996 (2010 ed.).

Cardona's period being similar to our own is due to sharing the first two years of data. Our best period determination, from thee full 6-year data set, was p = 71.6 ± 1.4 days.

We concur with the above two authors in classifying V88 as an SR variable on the basis of our regular and folded light curves (see Fig.lc18); the former continued to display multi-periodic behavior through six years of observation, while in the latter V88 exhibits a consistent cycle shape. The regularity index is 0.146, making it once of the most regular of the known LPVs (see Fig. 5.10).

V88 is located within the half-light radius, and is thus a probable cluster member. It appears in the region of the CMD populated by most non-variables inside the half-light radius (i.e. cooler and more luminous than the CMD), this is most likely due to merging impacting the photometry, as it was reported to be on the RGB by Skottfelt et al. (2015), who used higher-resolution observations.

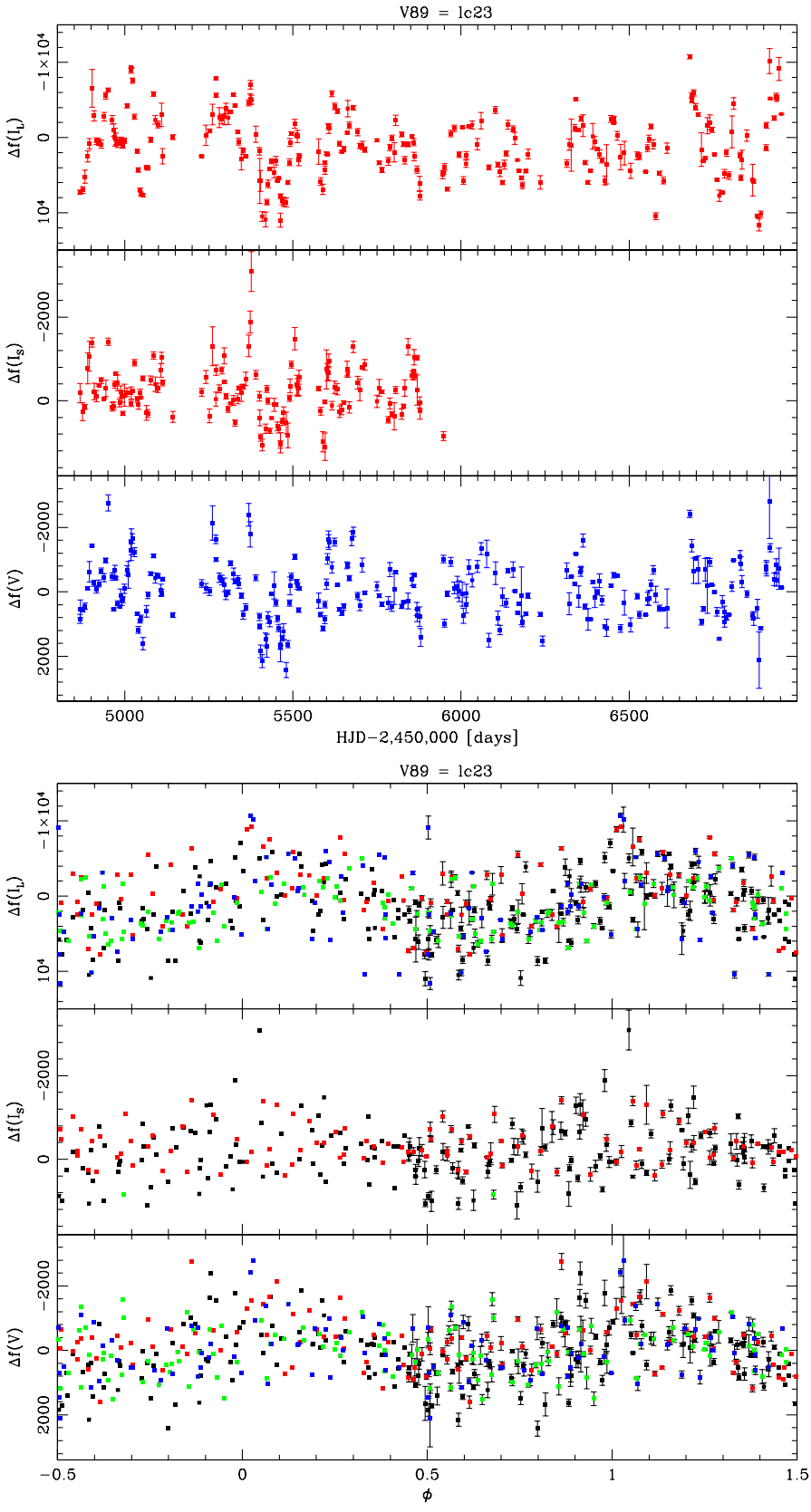

Figure 5.28: Variable V89 ISIS light curve (top), folded light curve p = 59.3 days (bottom).

LPV star V89 is located 0.286 arcmin from the cluster center which, like most Skottfelt et al. (2015) discoveries, is within the blended region near the core. This is evident in the light curves' (see Fig. 5.28) lower SNR as compared to V88. This is possibly due to a combination of lower magnitude and amplitude, and being within ~4 arcsec of another dimmer LPV (V81, which was not detected or recovered). V89's magnitude and amplitudes were given as 12.42 mag and 0.11 mag in the *I*-passband by Skottfelt, who classified it as semi-regular given the periodicity, low amplitude and presence on the RGB.

Our regular light curve displays multi-periodic, semi-regular behavior characteristics: a variation in the maxima/minima and closely spaced peak/trough pairs. A PDM analysis yields a period of 59.3 ± 1.4 days as the primary one; other periods are possible, but could not be definitively determined using the PDM tool. A period discrepancy exists between ours and Skottfelt's (theirs being 70.7 days), but because our cadence and time baseline allowed us to observe more cycles (a minimum of ~15 using peak/trough counting), we can assert our value. The folded light curve produced by the detected period produce a curve with some non-regularity, giving a regularity index of ~0.183 (a value in the middle of the semi-regular/irregular range, see Fig. 5.10). Given the folded light curve's coherence during so many observed cycles, we concur in defining V89 as semi-regular, but note its multi-periodicity.

Given that V89's projected radius is less than our designated half-light radius (0.52 arcmin) of the cluster center, it is a probable cluster member. The color-magnitude information from Cardona (2011) could not be retrieved due to a lack of photometric data in the star's crowded position (a positional search radius of 4 pixels, equivalent to ~2.4 arcsec, was attempted on the database with no returns). However, the discovery paper (Skottfelt et al., 2015) reported it is on the RGB. It is thus very probably a cluster member according to both criteria.

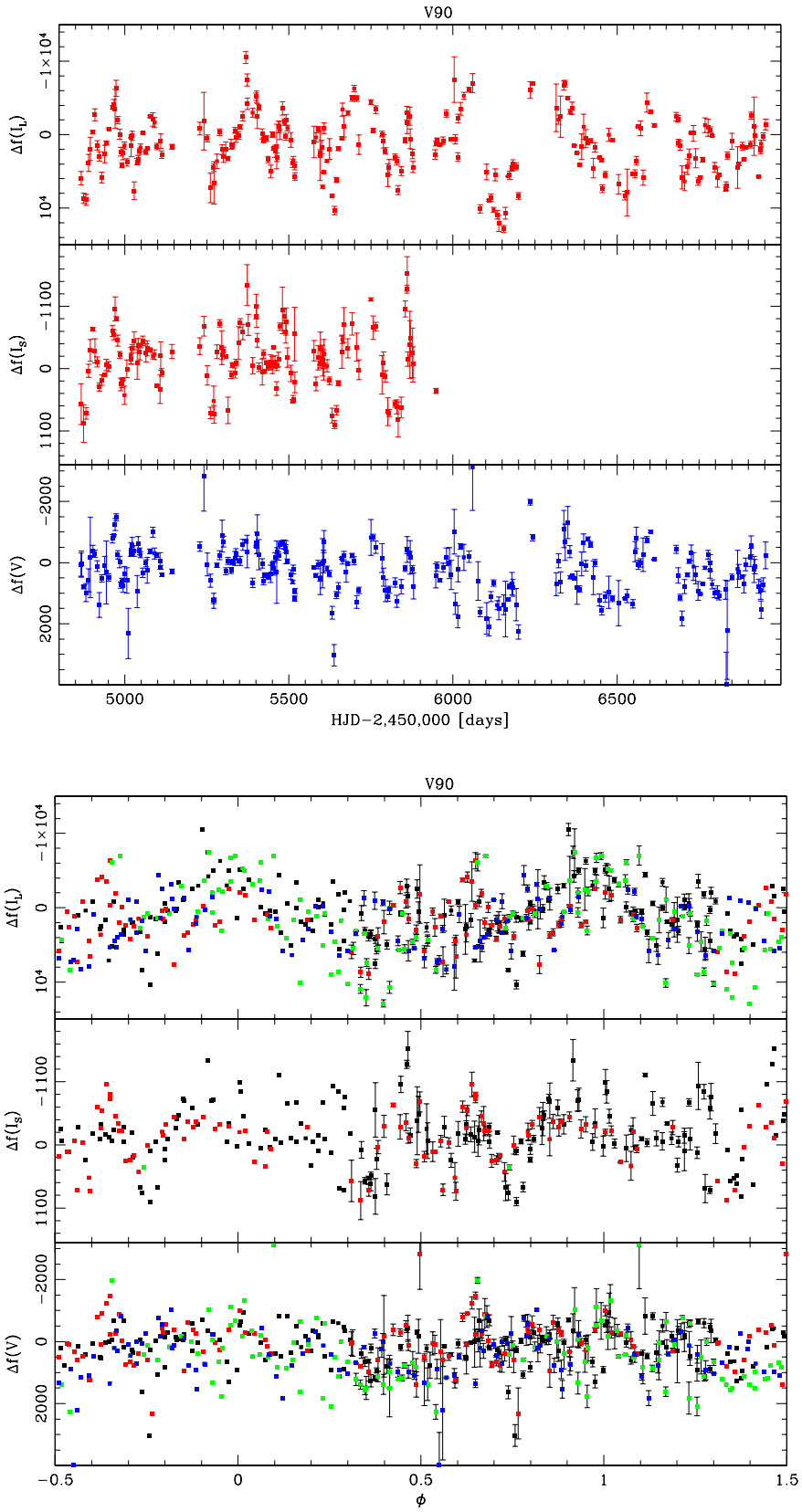

Figure 5.29: Variable V90 ISIS light curve (top), folded light curve p = 315 days (bottom).

Variable V90, an LPV discovered by Skottfelt et al. (2015), is located 0.124 arcmin from the cluster center in the crowded core region. This can be seen in the light curves (Fig 5.29), whose SNR suffers as a result. Also, it was not automatically detected by ISIS, and its flux difference data was manually recovered (as detailed in chapter 4). This is probably due to the crowded region causing blending of multiple stars' PSFs; Skottfelt reported star(s) of similar magnitude blended with V90 which, given their higher resolving power, means our own signal is affected to at least a similar extent. They also give magnitude and amplitude values of 12.34 mag and 0.14 mag in the *I*-passband, respectively. They classified it as semi-regular given the periodicity, low amplitude and presence on the RGB.

Despite the low SNR, our recovered data (see Fig 5.29) still show evidence of significant irregularity in all three exposure types: a variation in the maxima/minima and closely spaced peaks/troughs the evidence multi-periodic behavior. The period reported by Skottfelt, 70.8 days, could not be detected. At best, a primary period of 315 ± 10 days is suspected, but has large variation as can be seen in the folded light curve. Our longer time baseline and higher cadence means we should have observed that cycle many more times than Skottfelt, who only observed roughly two cycles (see Fig. 5.30, below), but our observations were done at a lower resolution. That said, the folded light curve's error bars are smaller than the observed cycle-to-cycle variation. The regularity index for our detected period is 0.187, in the middle of the SR/IRR range (see Fig. 5.10), but given the lower SNR, it cannot be used as a definitive ranking. In sum, we have classified it as an irregular that displays some periodicity, but with reservations due to our lower SNR.

Cardona's work (2011) did not detect V90, but his non-variable photometric data give *I* and *V* magnitudes of 10.76 mag and 12.60 mag, respectively, thus $V - I = 1.84$ mag. This

places it on the CMD portion populated by stars of the crowded half-light radius region (see Fig. 5.2), probably due to, as noted above, blending with another similar-magnitude star(s). Note that the *I* magnitude is similar to the one given by Skottfelt. Thus our CMD does not confirm cluster membership due to blending, but does not rule it out either. Skottfelt et al. (2015) reports that V90 is on the RGB, and given V90's projected radius of 0.124 arcmin places it just outside the core radius, but well within the half-light radius, it is a highly probable cluster member.

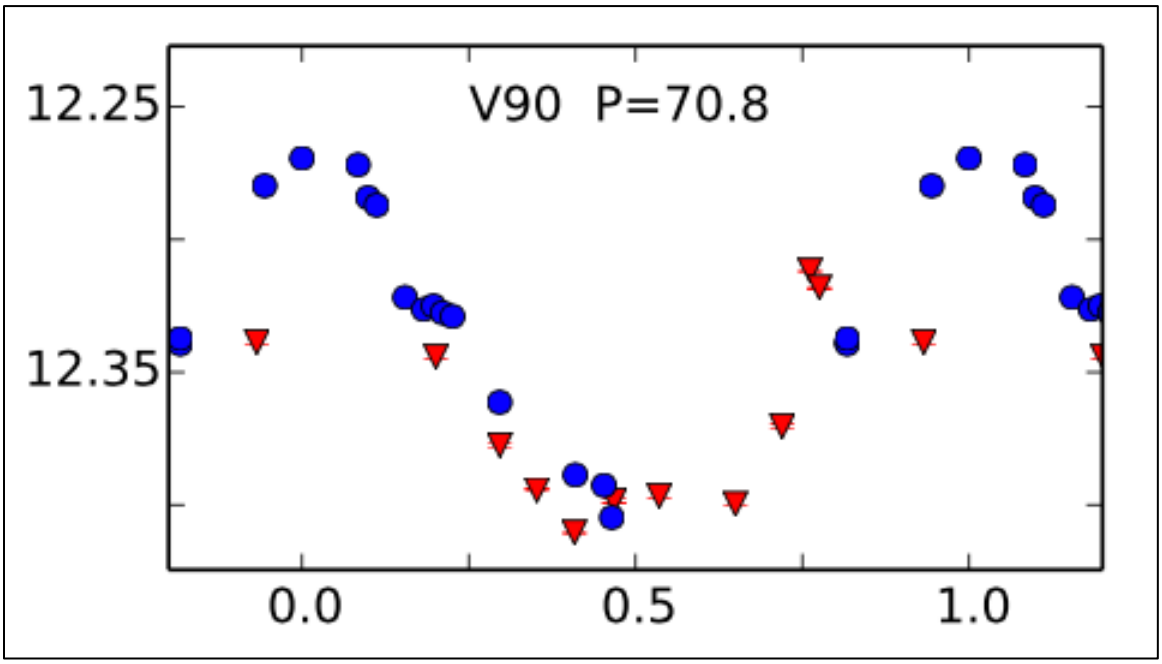

Figure 5.30: folded light curve from Skottfelt et al. (2015) for V90. Note y-axis is the magnitude in the *I*-passband, x-axis the phase of the cycle. Red triangles and blue circles are 2013 and 2014 data, respectively.

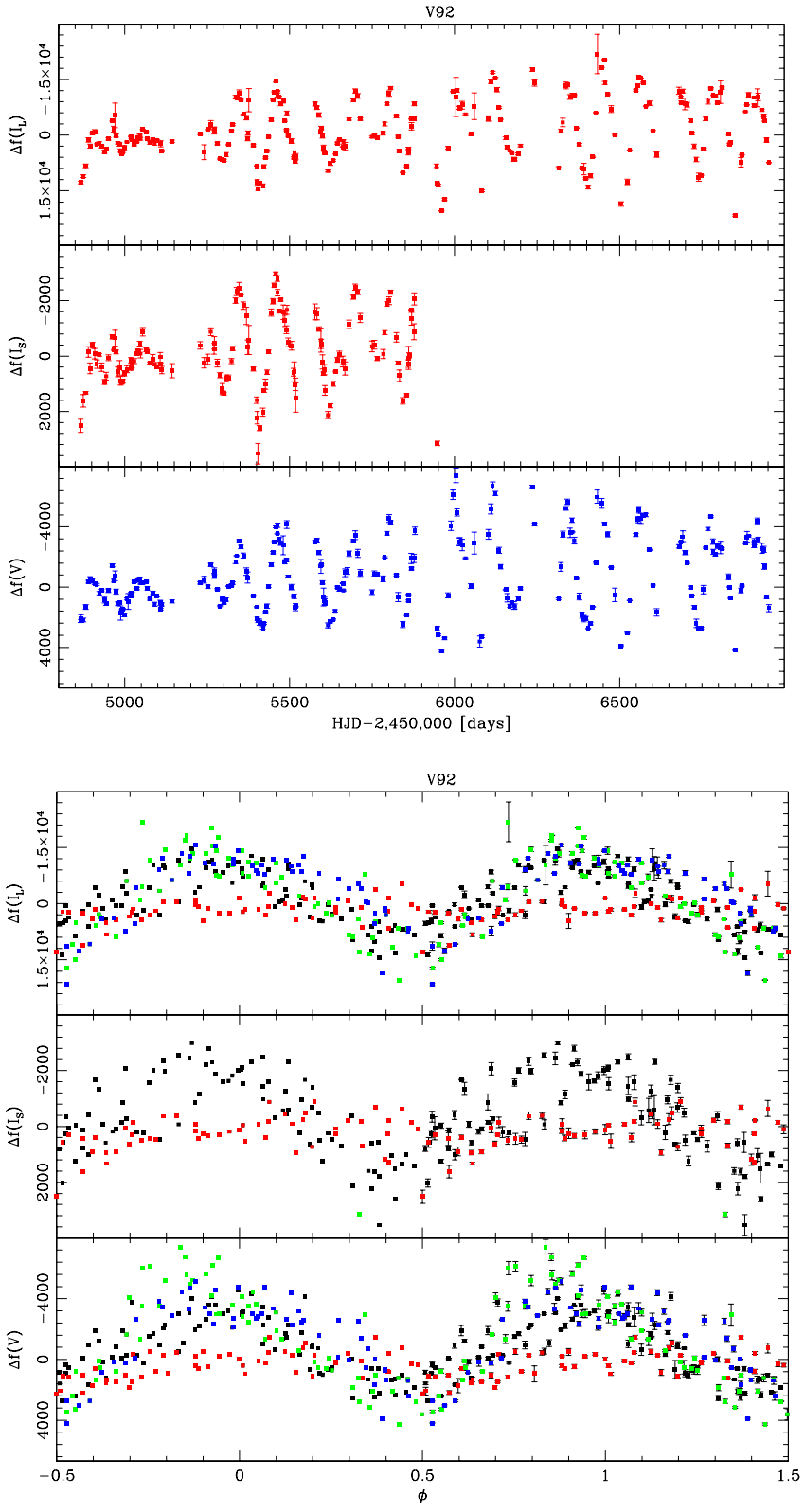

Figure 5.31: Variable V92 ISIS light curve (top), folded light curve p = 110 days (bottom).

V92, another Skottfelt et al. (2015) discovery, is located on the outer edges of the busy central region, with a projected radius of 0.338 arcmin (the half-light radius is 0.52 arcmin). The LPV was not automatically detected by ISIS and was instead manually recovered as described in chapter 4 by using its published coordinates. The recovered data produce good light curves (see Fig. 5.31) that have better SNR than V90's, which is expected given the star's less central location. The regular light curves show the characteristics of a multi-periodic semi-regular star in all exposure types: a variation in the maxima/minima, closely spaced peaks/troughs and hints of a LSP. The PDM analysis detected the primary period of 110.0 ± 2.5 days with ease, but other trial periods could not produce a coherent folded light curve; use of FFT may determine the other periods. The folded light curve's uniform variation is further evidence of this multi-periodicity, as well the regularity index value of 0.154, on the SR end of the Mira-SR transition (see Fig. 5.10). We thus classify this star as a semi-regular, confirming Skottfelt's classification.

Skottfelt gave *I* magnitude and amplitude of 12.60 and 0.65, respectively, and a period of 114.2 days. The amplitude is noted to be higher than that of their other LPVs. The period is close to our value, only slightly outside the period range detected with our PDM analysis, which was most likely due to our longer time baseline and more frequent cadence giving a better primary period than they could. Skottfelt further notes that the star is blended with a star of similar magnitude, although in this case it was not detrimental to the recovery of the data, unlike V90.

Cardona's non-variable color-magnitude data give *I* and *V* magnitudes of 11.57 mag and 13.54 mag, respectively, for a $V - I = 1.97$. This puts the star above the cooler end of the RGB (see Fig. 5.2), at the edge of the region. We speculate that this is due to blending, as the Skottfelt magnitude is sufficiently different as to not be due to variability alone.

V92 is within the half-light radius, and is thus a probable cluster member.

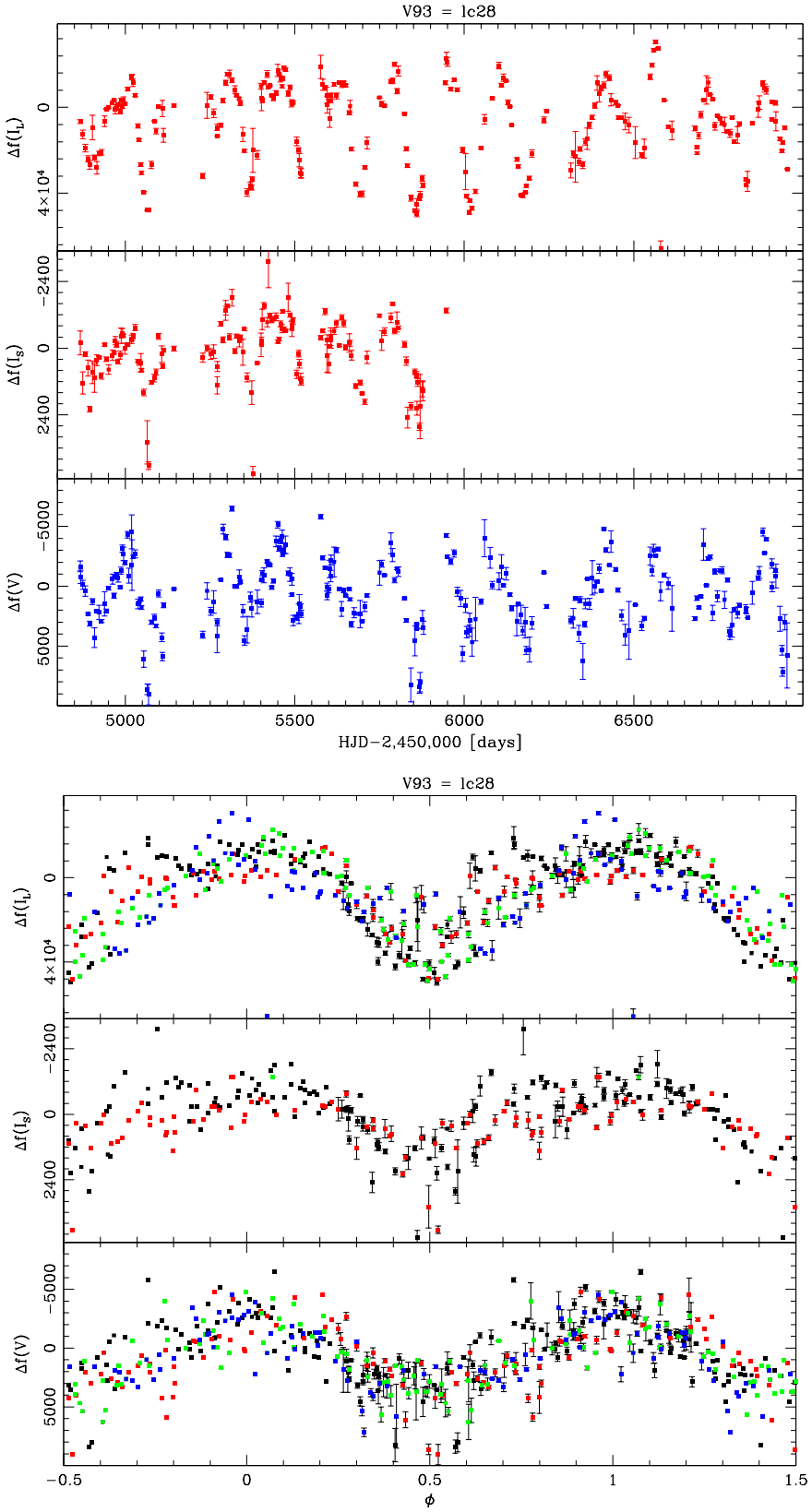

Figure 5.32: Variable V93 ISIS light curve (top), folded light curve p = 158.5 days (bottom).

Located at a distance of 0.052 arcmin, V93 is the closest variable star to the cluster center. Despite this, it was automatically detected and the data recovered successfully (see Fig. 5.32), although with intermittent points of low SNR. One of the Skottfelt et al. (2015) discoveries, it was also identified by Cardona (2011) as NV8, who both gave periods of 157 days and 155 ± 5 days, respectively. Our PDM analysis on the larger data set unavailable to Cardona determined a period of 158.5 ± 4 days. The regular light curves (see Fig. 5.32) display characteristic multi-periodic semi-regular behavior of maxima/minima variation and closely spaced (and small) peak/trough pairs, and there is a uniform variation in the folded light curve. This is confirmed by the regularity index value of 0.147, making it the most regular of our known SR-classified LPVs (see Fig. 5.10). We thus classify it as a semi-regular possibly with other periods, in agreement with Skottfelt and Cardona. Note that Skottfelt's classification was not based on the CMD position.

The *I*–passband magnitudes and amplitudes were reported by Skottfelt as 11.97 mag and 0.43 mag, explaining the ease of relative-flux subtraction photometry despite the star's location. Cardona was not able to perform DAOPHOT photometry due to this very issue (the merging of PSFs of multiple closely spaced stars unresolvable with our limited aperture and image scale). That said, a search of his non-variable magnitude data returned a positional match within 3 pixels (~1.8 arcsec) of our detection*: I* and *V* magnitudes of 10.40 mag and 11.94 mag, respectively. V – I is thus 1.54 mag. The *I*-passband value is higher than Skottfelt's, which with the V-I places the star alongside others within the half-light region (see Fig. 5.2). This is likely indicative of aforementioned blending that hampers DAOPHOT, and thus cannot confirm cluster membership. Its project position is less than the core radius (0.12 arcmin), thus making it a cluster member by our criterion. Note that Skottfelt did not report that V93 was on the RGB.

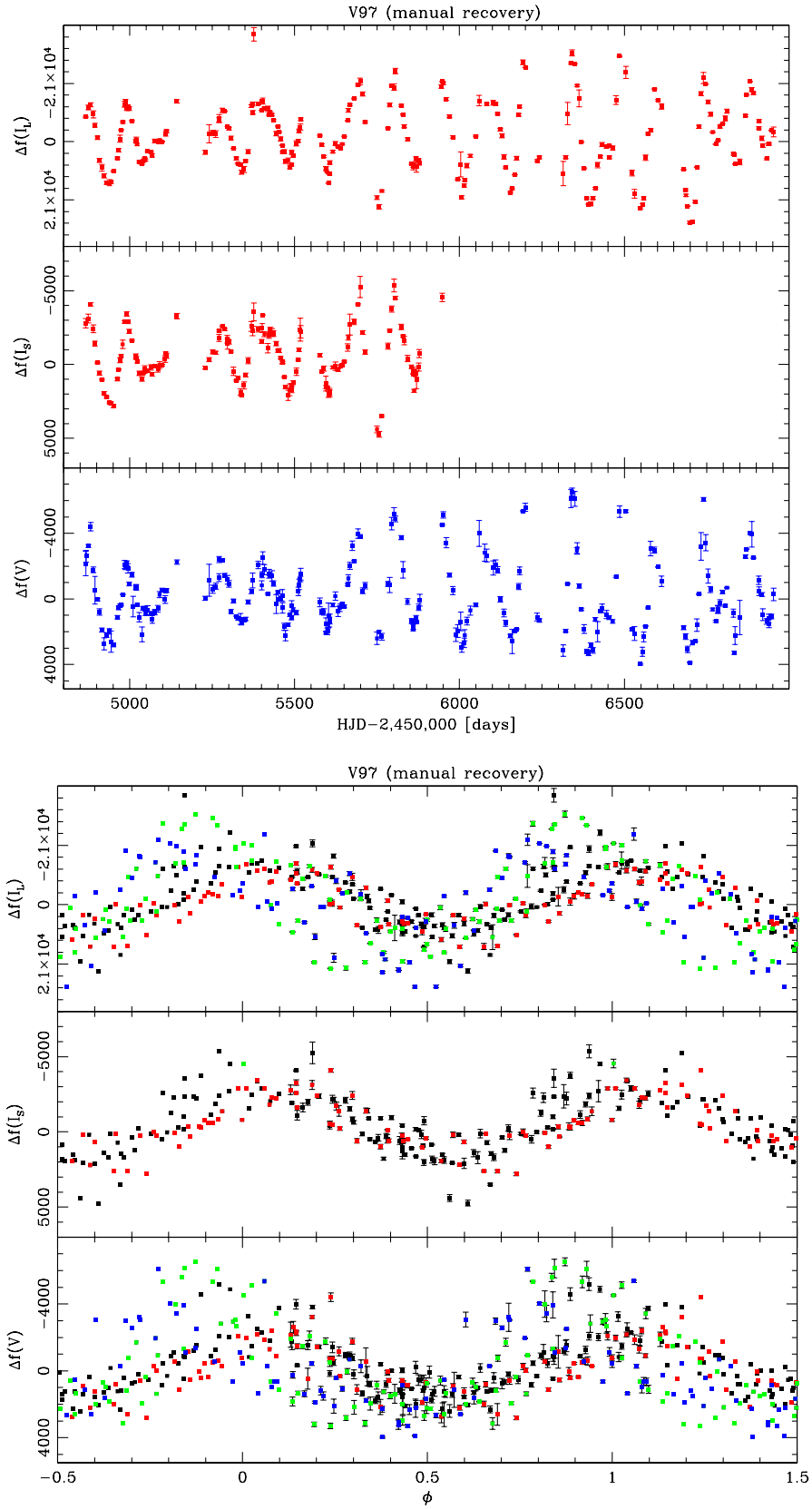

Figure 5.33: Variable V97 ISIS light curve (top), folded light curve p = 137.3 days (bottom).

Variable star V97 is located in the central region at a distance of 0.162 arcmin from the cluster center, as typical with Skottfelt et al. (2015) discoveries. It was also identified by Cardona (2011) as NV12. The star's variability was not automatically detected in our dataset, however, and was manually recovered using published coordinates (see chapter 4). This is possibly due to its close proximity to V98 and V85 (within ~3 pixels of both, or ~1.8 arcsec), making detection close to our ISIS detection threshold, which might have been set lower than Cardona's. The data appear to be good, as the light curves (see Fig. 5.33) display characteristic multi-periodicity, with uniform variation in the folded light curve. PDM analysis returned a period of 137.3 ± 3, in agreement with Cardona (137.7 ± 8 days). Skottfelt classified it as irregular on the basis of RGB position and inability to phase their light curves, likely due to not observing sufficient cycles, but with our longer time baseline and more frequent cadence, we concur with Cardona in classifying it as a semi-regular LPV. Furthermore, the regularity index is 0.178, the mid-range of the semi-regular-to-irregular range.

Skottfelt reports *I*-passband magnitude and amplitude of 12.43 mag and 0.84 mag, respectively. The high amplitude explains the good relative-flux data SNR despite the central location. Cardona could not perform variable DAOPHOT photometry due to blending, but his non-variable data give V and I magnitudes of 12.98 mag and 11.28 mag, respectively, for V-I = 1.70 mag. This places it among other half-light radius stars (see Fig. 5.2), which means merging has likely affected the signal and our CMD cannot be used to confirm membership. Skottfelt did note that the star was on the RGB, however, thus it is likely a cluster. The projected radius of the star is also less than the half-light radius, thus by both our criterion it a highly probable cluster member.

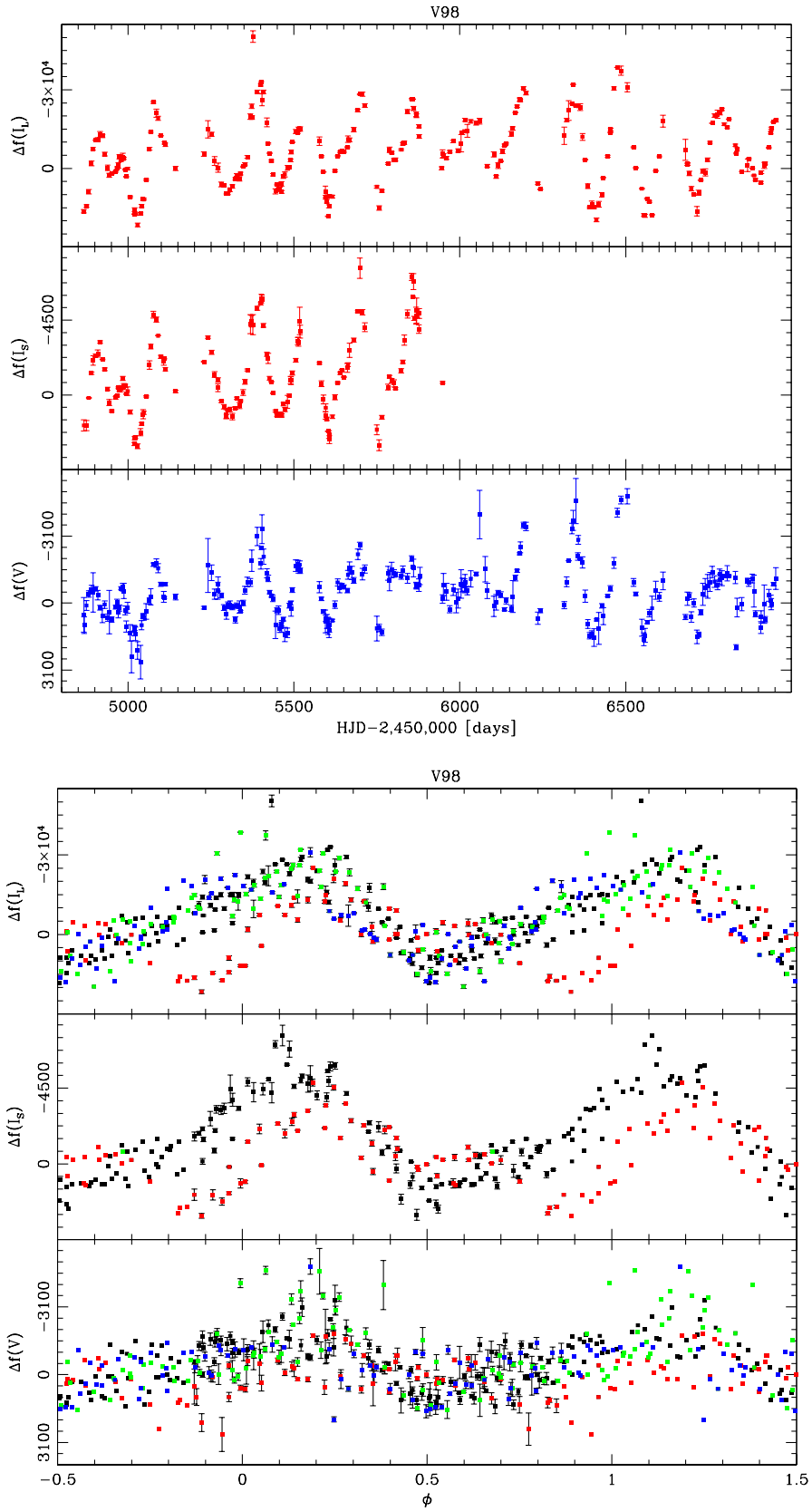

Figure 5.34: Variable V98 ISIS light curve (top), folded light curve p = 158.8 days (bottom).

LPV star V98 is located 0.122 arcmin from the cluster center, at the outer edge of our designated core radius (0.12 arcmin), placing it in a very busy region. It was discovered by Skottfelt (2015), and identified by Cardona (2011) as NV7, as an LPV, but was classified differently by the two studies: Skottfelt classified it as an irregular based on being on the RGB and inability to find periodicity, but Cardona's longer time baseline of two years allowed him to identify a period of 149 ± 6 days. Our own PDM analysis gives a similar value of 158.8 ± 0.1; the narrow tolerance is due to the folded light curve quickly becoming incoherent outside it.

The star was manually recovered, but it was detected in a signal merged with that of V97, with the detected location being the midpoint between the two. The signal was noisy, and manual recovery produced a better, clearer light curve (see Fig. 5.34). This is evident in Cardona's light curve of V98 (see Fig. 5.35), which he noted in his study. Our light curves display characteristics of semi-regular behavior (maxima/minima variation, closely spaced peak/troughs), but finding a primary period using PDM was difficult, with multiple candidates for periodicity producing unphysical light curves. For the detected primary period, the regular index is 0.182, roughly the middle of the SR-to-IRR range (Fig. 5.10). This is expected given the scatter in the folded light curve. We therefore classify it as an irregular, but note the presence of a period. Note it was classified as semi-regular by Cardona, but our longer time baseline allowed us to observe more cycles, and thus better capture the variation in cycle-to-cycle behavior. Skottfelt also classified it as an irregular LPV due to being on the RGB and the lack of detected periodicity (which is expected given their cadence and baseline).

Skottfelt gave *I*-passband magnitude and amplitude of 12.52 mag and 0.60 mag, while Cardona gave *I* and *V* amplitudes of 0.14 mag and 0.68 mag, respectively. Cardona's non-variable photometric data returned *I* and *V* magnitudes of 11.28 mag and 12.98 mag,

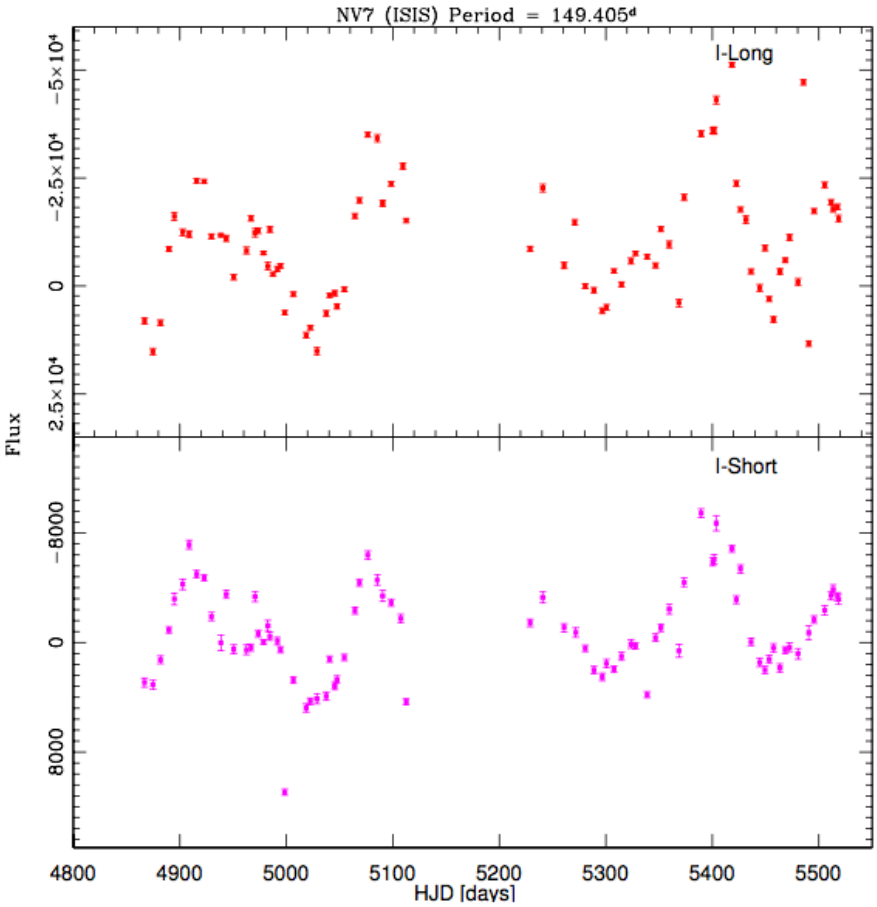

Figure 5.35: Variable V98 ISIS light curve from Cardona (2011), note differences between our shared portions of the light curve, specifically the ~4900-5000 days range in I_L and I_S, possibly due to interference from nearby LPV V97.

respectively, for a $V - I = 1.70$ mag. This places the star in the half-light region of the CMD (see Fig. 5.2), which, combined with the discrepancy with Skottfelt's values, means the star's CMD position was likely shifted due to merging. Skottfelt also noted that the star's photometry was not affected by nearby stars of similar or brighter magnitude, and placed the star on the RGB. The star's projected radius is also ~0.1 arcsec outside the core radius, which makes this star a highly probable cluster member per our criteria.

5.4.1 V101, V102, V106-V108, V109

The known LPV stars V101, V102, V106, V107, V108, and V109 commentary and measurements have been consolidated into a single subsection for brevity, as they share the following characteristics:

1. They were not identified by Cardona (2011).
2. They were discovered by Skottfelt et al. (2015), who classified them[1] as irregular, and did not note the presence of neighboring stars affecting the study's photometry.
3. They are located outside our core radius (0.12 arcmin) but within the half-light radius (0.52 arcmin), making them probable cluster members per our criterion.
4. They exhibit *non*-Mira-like variability, with at least some hints of periodicity.
5. They suffer from classification ambiguity to some degree.

The similarities break down in the following ways:

1. V101 and V106 were manually recovered (see chapter 4), V108 was automatically detected in the I_L exposure type only; the rest were detected normally.
2. Their regularities differ, according to their regular and folded light curve, and their regularity indices place them in the SR-IRR range of Fig. 5.10, but V101, V108, and

1 They were classified en-masse, as part of a group encompassing V96-V118, as irregular LPVs on the basis of being on the RGB and lacking detected periods for good folded light curves.

V109 are clustered at the semi-regular end of the range, while V102 and V106 are nearer to the irregular end. These values do not completely reflect their irregularities. PDM analysis did not yield V107 a primary period, so it lacks an index.

3. Cardona's (2011) non-variable color-magnitude database yielded matches for only V106, V109, V102, and V108. They are all located above the cooler end of the RGB, possibly due to blending or their being field stars in front of the cluster. No matches were found for V101 and V107. Given they all lie inside the busy half-light radius, there is a higher possibility merging may have affected the photometry, but some could yet be foreground stars.

The details of the LPVs are listed in Table 5.2, which is followed by their regular and folded ISIS light curves as available.

Star ID	Period Obs. (days)	Type Obs.	I Mag. (lit.)	I Amp. (lit.)	V Mag.	I Mag.	(V - I)	Rp (arcmin)	Reg. I.
V101	45.6 ± 0.3	SR/IRR?	12.58	0.26	N/A	N/A	N/A	0.130	0.174
V102	49.5 ± 2.5?	IRR/SR?	12.54	0.21	13.74	11.64	2.10	0.380	0.199
V106	53.0 ± 1.4?	IRR/SR? Low SNR	12.28	0.12	13.18	11.07	2.11	0.151	0.191
V107	IRR or NR?	IRR/NR?	12.41	0.12	N/A	N/A	N/A	0.259	-
V108	43.6 ± 0.6, 39.9 ±1	SR, MP	12.68	0.12	13.79	11.70	2.10	0.295	0.169
V109	IRR/288.5?	IRR/SR? Low SNR	12.63	0.09	13.78	11.80	1.98	0.312	0.165

Table 5.2: Known variable stars V101-V109's details. Suspected or uncertain measurements or classifications marked with a question mark. (1st column): Star ID. (2nd column): Period observed is listed primary first, followed by secondary period if present or suspected. (3rd column): Our type classification, with primary tendency/type first, followed by secondary. In a sense, the variable's place on the SR-IRR spectrum. (3rd, 4th columns): Skottfelt et al. (2015) magnitude and amplitude in I. (5th, 6th, and 7th columns): V, I, and V-I magnitudes if available from Cardona's database. (8th column): Projected radius, note all stars are probable cluster members by our criteria. (9th column): regularity index, where available if a primary period is detected.

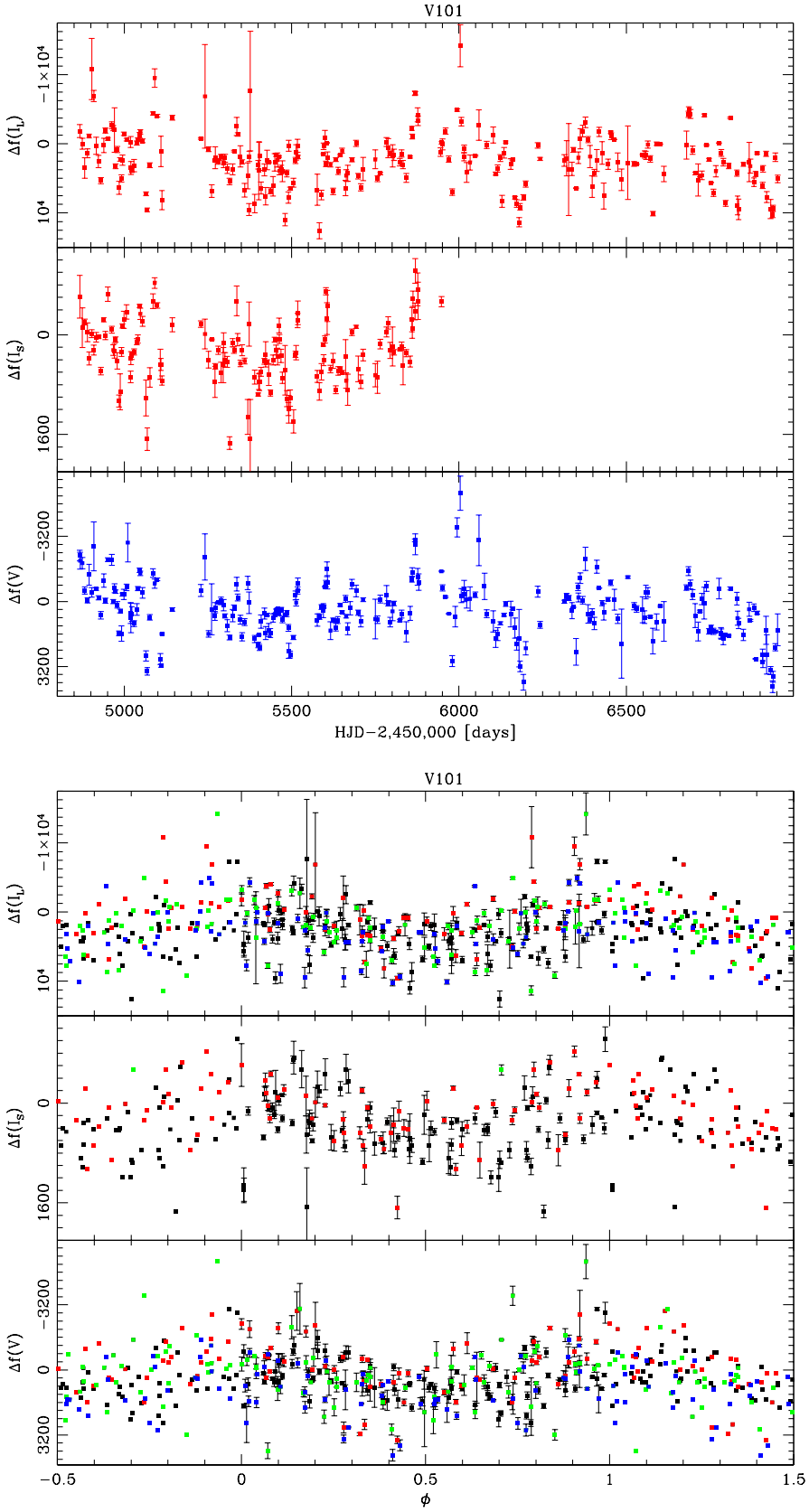

Figure 5.36: Variable V101 ISIS light curve (top), folded light curve p = 45.6 days (bottom).

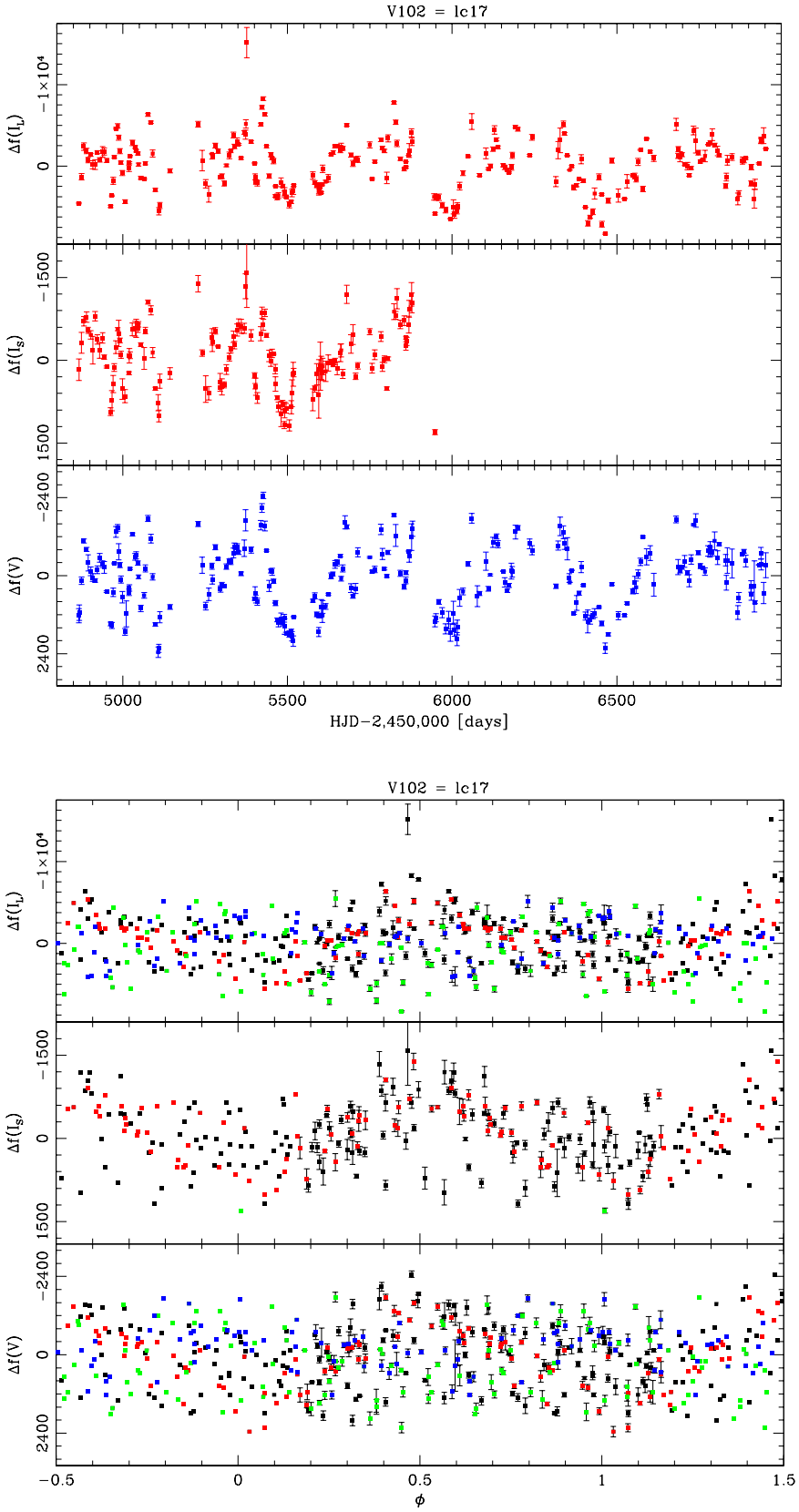

Figure 5.37: Variable V102 ISIS light curve (top), folded light curve p = 49.5 days (bottom).

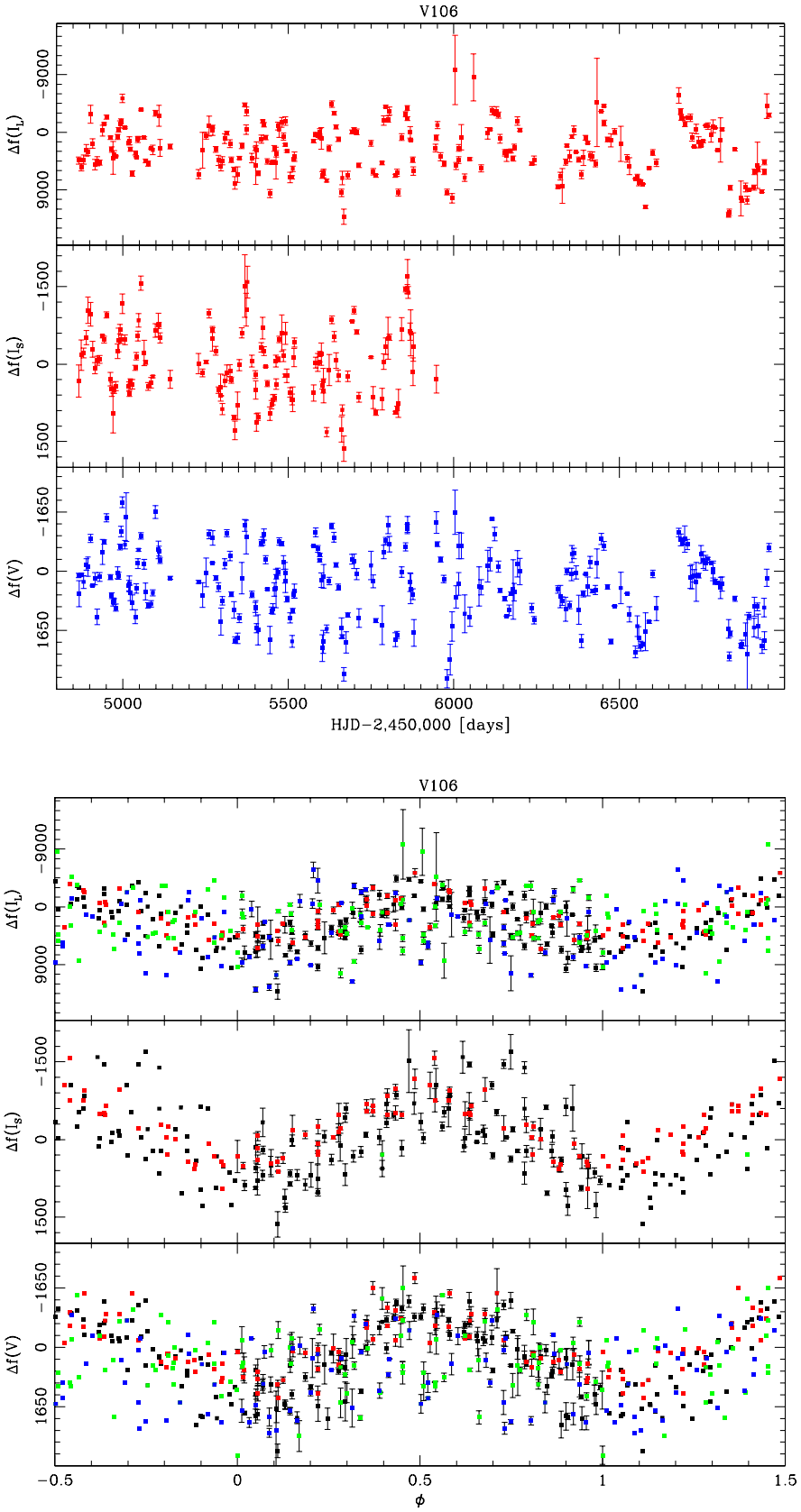

Figure 5.38: Variable V106 ISIS light curve (top), folded light curve p = 53.0 days (bottom).

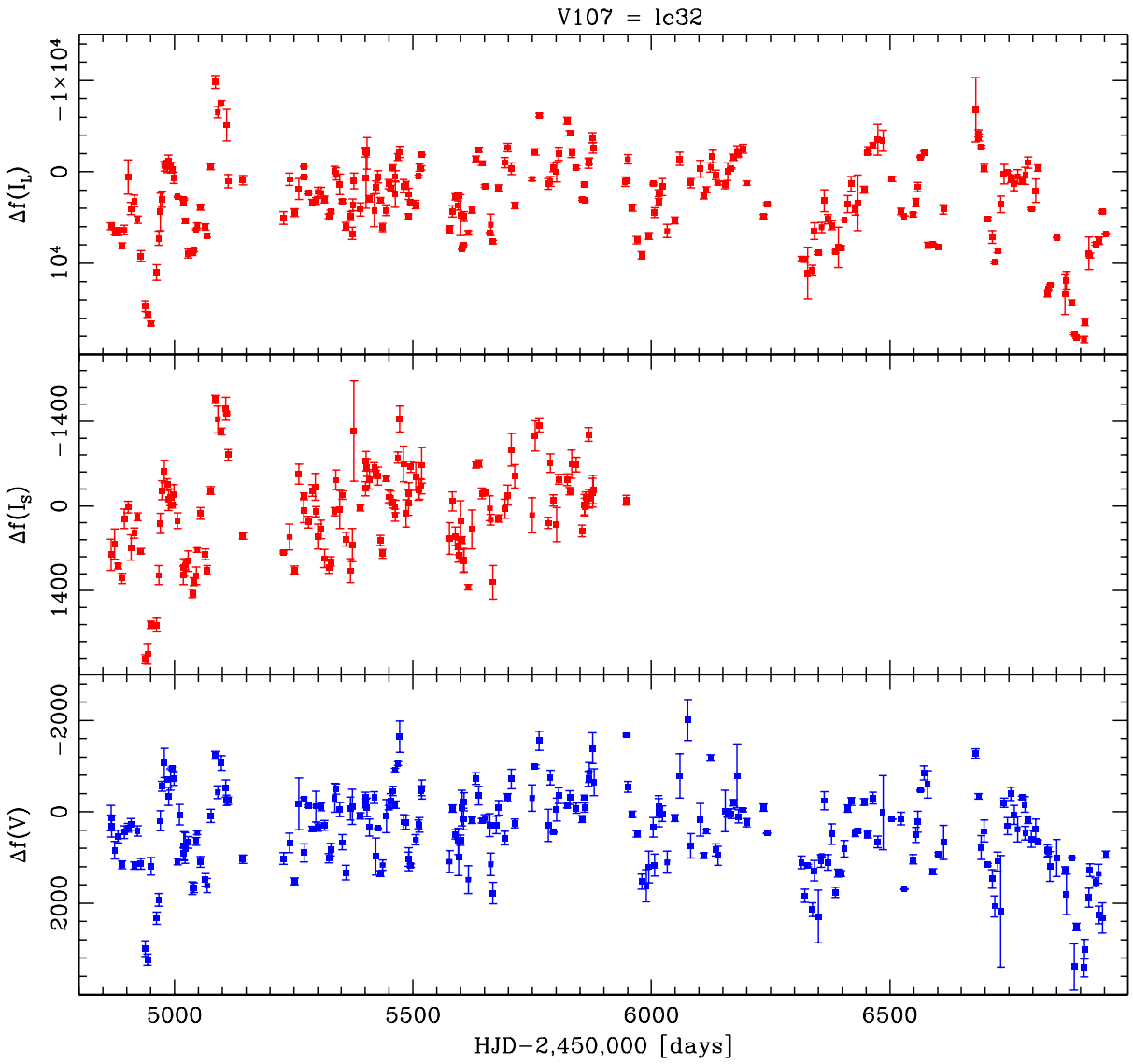

Figure 5.39: Variable V107 ISIS light curve. No primary period detected.

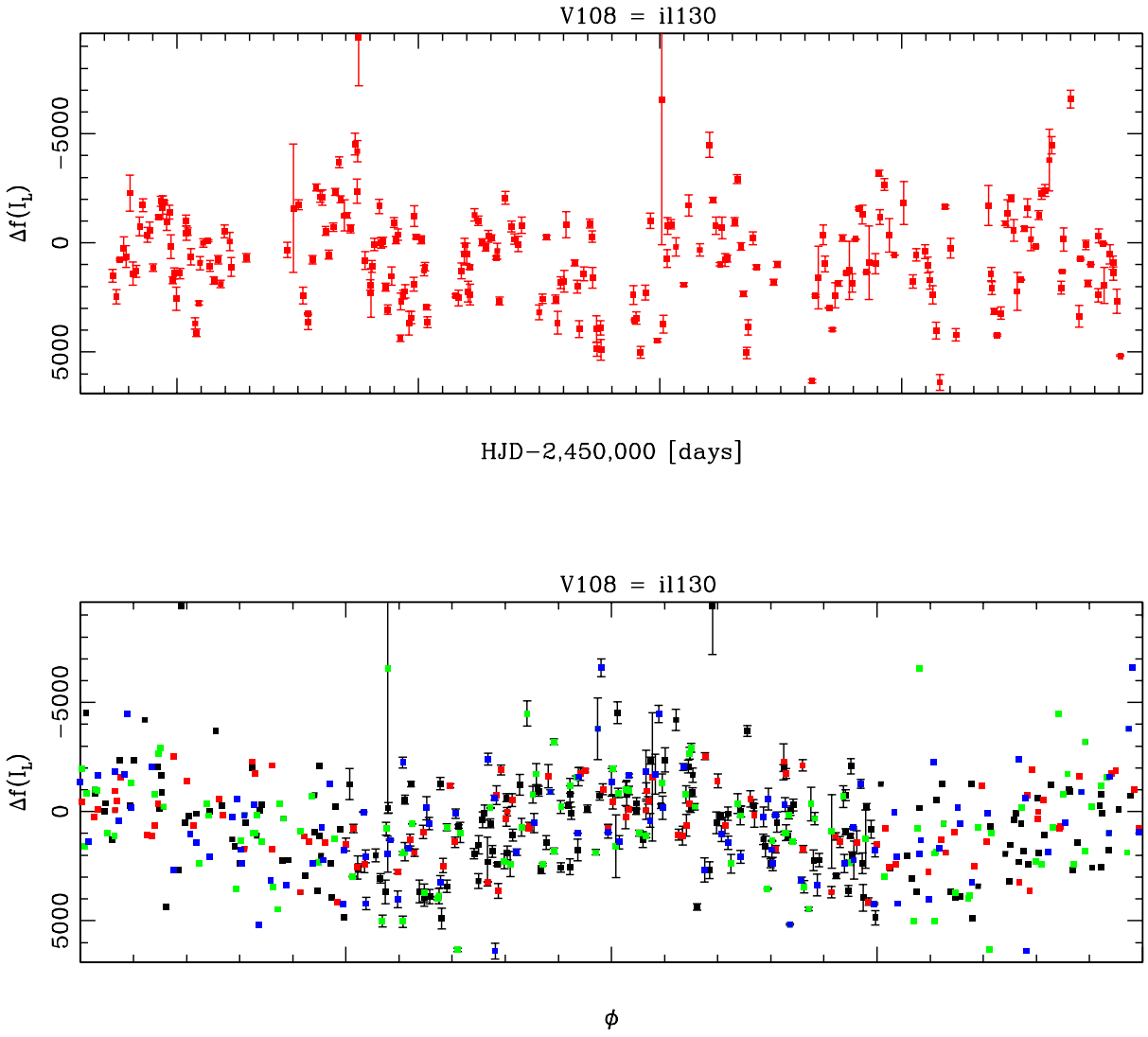

Figure 5.40: Variable V108 ISIS light curve (top), folded light curve p = 43.6 days (bottom).

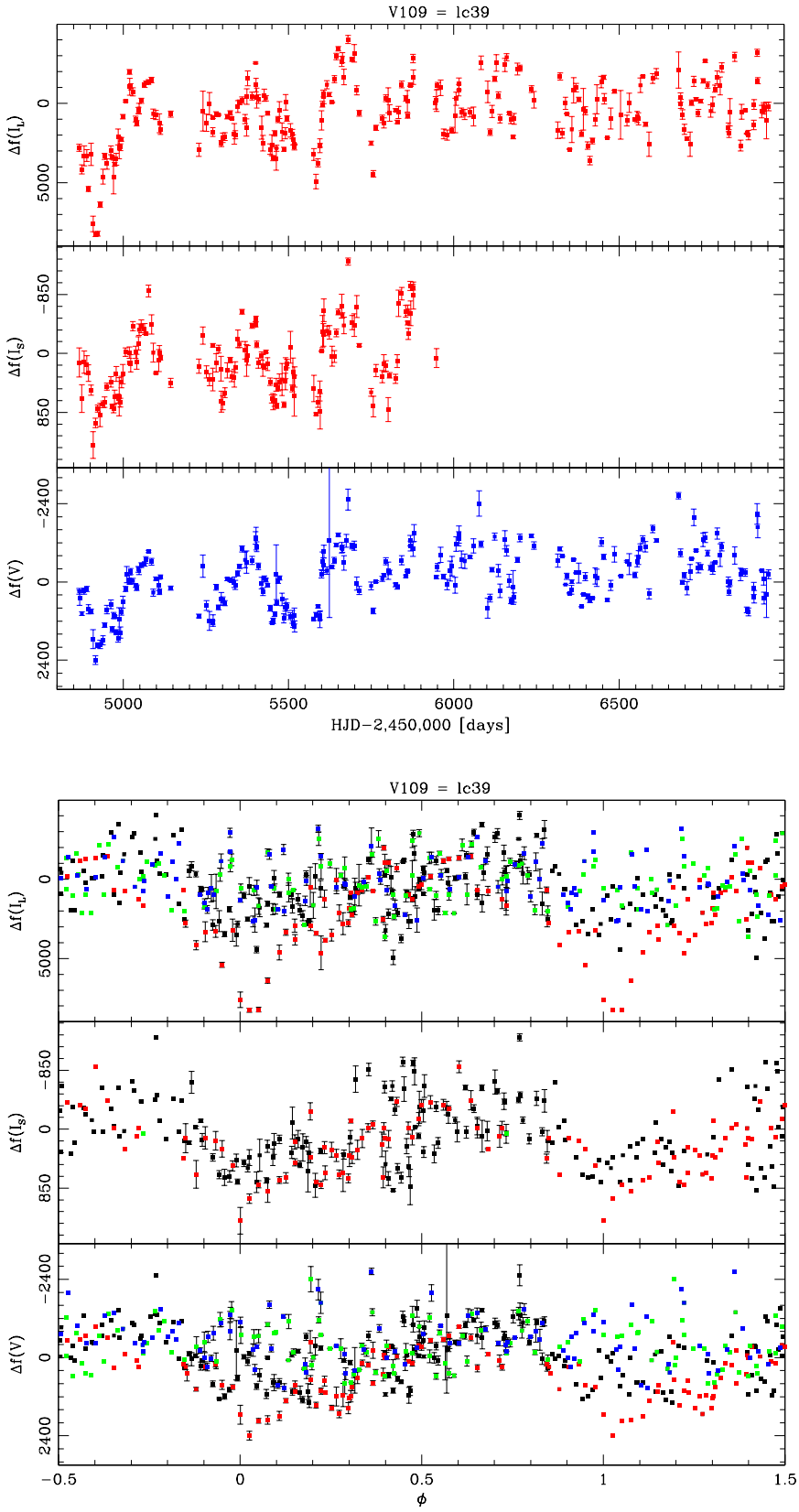

Figure 5.41: Variable V109 ISIS light curve (top), folded light curve p = 278.4 days (bottom).

5.5 New LPVs

This section details the LPVs that were discovered in this work. They were selected from the candidate variables, as described in section 5.2, for satisfying the variability index criterion either sufficiently to be automatically considered a new variable (NV), or enough to be considered for individual examination, after which their light curves and PDM analysis results determined them to be new, undiscovered variable stars with good confidence. The rest were either classified as false-positives, or are classified as suspected variables that need future observations for confirmation. The new variables are examined in more detail and are listed in Table 5.3, while the suspected variables are listed in Table 5.4.

Figure 5.42 shows their positions on the CMD, which was extracted from photometric data from Cardona (2011) as described previously in section 5.1.1, with the RGB band for cluster membership highlighted. It can be seen that most of the detected new variables (NV) lie in the RGB band, which is to be expected given all our discoveries appear to be LPVs. As detailed in the aforementioned section, this is evidence of their being cluster members. Their projected radii vary, with the majority falling outside the half-light radius. This is to be expected given the Skottfelt et al. (2015) FOV was limited to the busy core region, and the limits of our resolving power.

The newly discovered and suspected variables are named after our ISIS data file number in the format “LC#” or, if their data were only recovered in I_L, “IL#”. Having already examined the cluster using a subset of our own data, Cardona (2011) discovered some of our NVs. Therefore, variable stars identified in his work that are still not in the literature will follow his naming scheme of “NV#”.

The periods for the stars that were also identified by Cardona (2011) were sometimes found to have significantly different periods, and as such both our and his periods are listed in the table for comparison.

Newly discovered variable stars are discussed briefly below in groups according to their position on the regularity-to-irregularity spectrum, starting from Mira-like, to semi-regular, to irregular. Many stars straddle categories in the classification system, and thus Table 4.3 indicates on which divide they lie, and which category they are most like. A few examples: SR/M refers to star on the Mira/semi-regular divide, but which we judge to most likely be a semi-regular, IRR/SR is most likely irregular, but displays some semi-regular characteristics such as having a recognizable cycle shape in the folded light curve.

The regularity index was not used as the final determinant, but only as a guide in determining the classification of a star. It was found that highly irregular stars, or those with low SNR observations possibly due to low amplitudes, sometimes have periods with high cycle-to-cycle variation relative to the max/min range of variability. Thus they have lower regularity indices than those encountered previously in semi-regular variable stars with more consistent periodic behavior. It was noted that all had index values greater than 0.15. The details will be discussed in the conclusions section.

5.5.1 Discussion of Variable Groups

NV09: highly regular LPV whose regular light curves display peak-trough pairs near cycle peaks (see Fig. 5.55), evidence of a secondary period that could not be detected. There is also significant variation in the folded light curve. It was therefore classified as a semi-regular with noted regularity. Cardona came to the same conclusion, and supplied amplitude

measurements of 0.13 mag and 0.32 mag in the I and V pass bands, respectively, which is consistent with our semi-regular definition.

LC16, NV01, NV02, NV06: these stars display multi-periodic characteristics as evident in the regular light curves, which show variation in maxima/minima, and closely spaced peak/trough pairs. The phased light curves show some variation that is evidence of cycle-to-cycle differences. LC16's ISIS I_L light curves were noted to differ from the I_S and V light curves, which agree in shape. They were thus all classified as semi-regular LPVs. Note that Cardona classified NV01 and NV02 as semi-regular and NV06 as irregular.

LC45, NV05, NV15: these stars straddle the SR/IRR divide, displaying the aforementioned multi-periodic behavior as well as a possible LSP. NV15 has two periods, which were detected using PDM. They were classified as semi-regulars, with some irregularity, thus confirming Cardona (2011). An LSP is suspected for NV05 beyond the primary 395-day period.

LC1, LC29, LC38, IL143, NV10, NV14: new LPVs that display irregularity as evident in regular light curves, but some periodicity can be discerned in the folded light curve. The regular light curves may also hint at secondary periods. For NV16 and IL143, it is possible that low SNR may have affected the observations, and follow-up observations at higher resolution could reveal multi-periodic semi-regular behavior. They were classified as irregulars, with some noted periodicity. NV10 and NV14 were also classified as irregular by Cardona.

LC5, NV27: these stars display highly irregular behavior, and although signs of a primary period were found using PDM, the folded light curves display such high variation that the typical cycle form is nearly indiscernible.

Star ID	R_p (arcmin)	R_p Category	CMD Pos.	Type	P. (day)	P. (day) (C12)	V Mag	I Mag
LC1	1.620	Pos. CM	RGB	IRR/SR	45.6?, 75?	-	14.84	12.47
NV01	2.061	Pos. CM	RGB	SR	122.8?	73.43 ± 5	15.26	12.13
NV16	1.271	Pos. CM	RGB	IRR	41.94	41.01 ± 4	15.02	12.61
NV02	0.514	Prob. CM	RGB	SR	64.2	64 ± 4	14.77	12.27
LC16	0.899	Pos. CM	N/A	SR	159.4 ± 7	-	N/A	N/A
NV15	0.527	Pos. CM	Above	SR/IRR	138.8, 150.5	144.6 ± 5	14.51	12.28
NV05	0.604	Pos. CM	RGB	SR/IRR	395?	358 ± 7	14.90	12.37
NV06	0.652	Pos. CM	Above, ~0.1 mag	SR	323 ± 20	313.6 ± 12	14.62	12.19
LC29	0.349	Prob. CM	N/A	IRR/SR	318.3 ± 25, 432	-	N/A	N/A
LC38	0.444	Prob. CM	Above, merge?	IRR/SR	496?	-	14.49	11.98
LC45	1.146	Pos. CM	RGB	SR/IRR	226.5 ± 11	-	15.25	13.03
NV09	0.834	Pos. CM	RGB	SR (very regular)	305.9	335.8 ± 13	14.86	12.52
NV14	1.190	Pos. CM	RGB	IRR/SR	350	369.2 ± 12	14.85	12.48
NV10	1.488	Pos. CM	RGB	IRR/SR	274	278 ± 5	15.14	12.20
NV27	2.404	Pos. CM	Below, ~0.1 mag	IRR	47	47.5 ± 5	15.44	12.69
IL143	0.646	Pos. CM	N/A	IRR/SR	280 ± 13	-	N/A	N/A

Table 5.3: New variable stars' details. (1st column): Star ID. (2nd column): Projected radius. (3rd column): Cluster membership category (see section 5.1.2). (4th column): CMD position. (5th column): Our type classification, with primary tendency/type first, followed by secondary. In a sense, the variable's place on the SR-IRR spectrum. (6th column): Period observed is listed primary first, followed by secondary period if present or suspected. Periods without errors go to incoherence quickly, periods with question marks are barely discernable. (7th column): Period in Cardona (2011). (8th and 9th columns): V and I magnitudes if available from Cardona's database.

ID	Filter/ Exp.*	x (px) (V)	y (px) (V)	R_p (arcmin)	Notes and Suspected Period
lc4	V, IL, IS	291.71	487.26	1.369	LPV, possibly IRR, weak signal, p ~ 153 day
lc20	V, IL, IS	369.38	340.27	0.446	SPV, low SNR, p ~ of 0.9 or 9 day
lc44	V, IL, IS	439.35	370.04	0.558	LPV? p ~ 37.5, 450 day
lc62	V	206.34	411.51	1.770	If present, weak signal with p~48.4, V-passband only
lc64	V, IL, IS	254.74	394.87	1.278	p~0.971day
lc66	V, IL, IS	458.84	405.14	0.766	p~20 days, no v0-data?
lc67	IL	490.01	300.59	1.320	Possible LPV with period of 408 days, IL-only
lc68	V, IL, IS	545.58	379.20	1.588	P ~ 0.99-0.95 day
il46	IL	285.08	403.00	0.993	If present, no period detected
il47	IL	287.79	584.48	2.195	If present, p~433.9days, irregular LPV?
il51	IL	304.15	294.96	1.170	If present, p~275.8 day
il55	IL	322.64	348.29	0.695	Busy region, p~423.5 day
il57	IL	333.16	394.44	0.513	P~180
il65	IL	338.48	256.66	1.322	Merged with neighbour? P~397 day
il77	IL	353.00	425.20	0.515	p ~ 0.5days
il85	IL	364.15	472.87	0.904	Suspected variable, more details needed, p~391.7 days?
il103	IL	390.58	328.35	0.542	Suspected variable, more details needed, jun2017 alt p 386
il125	IL	407.86	505.30	1.224	Near bright star, on RGB if present, p~328
il127	IL	410.08	295.55	0.898	P ~ 350-397
il133	IL	415.74	542.34	1.596	P ~ 22.6
il150	IL	480.12	267.50	1.478	If present, p ~ 38 day
il165	IL	587.33	450.87	2.106	no period found, close to edge artifact

Table 5.4: Suspected variables detected in the cluster. Possible periods were detected with the PDM. The variability sources were classified as suspected as per the variability index metric defined in section 5.2, wherein they are either automatically considered new variables, or are considered for individual inspection. The suspected variability sources above were found sufficiently variable star-like in their regular and phase (if available) light curves as to be consider as suspected, but not with high certainty as to be considered new variables. (1st column): Variability source ID. Photometric data filenames are used as a placeholder for star names. Those with the prefix IL were only detected in long, I-passband exposures, and could not be found in the other exposures (V and IS). (2nd column): The filter/exposure combination which yielded the detection. (3rd and 4th column): Source coordinates are in pixels of the master reference image (*V*-exposure). (5th column): Projected radius. (6th column): Brief notes on the variability source's characteristic e.g. possible period, SNR, etc.

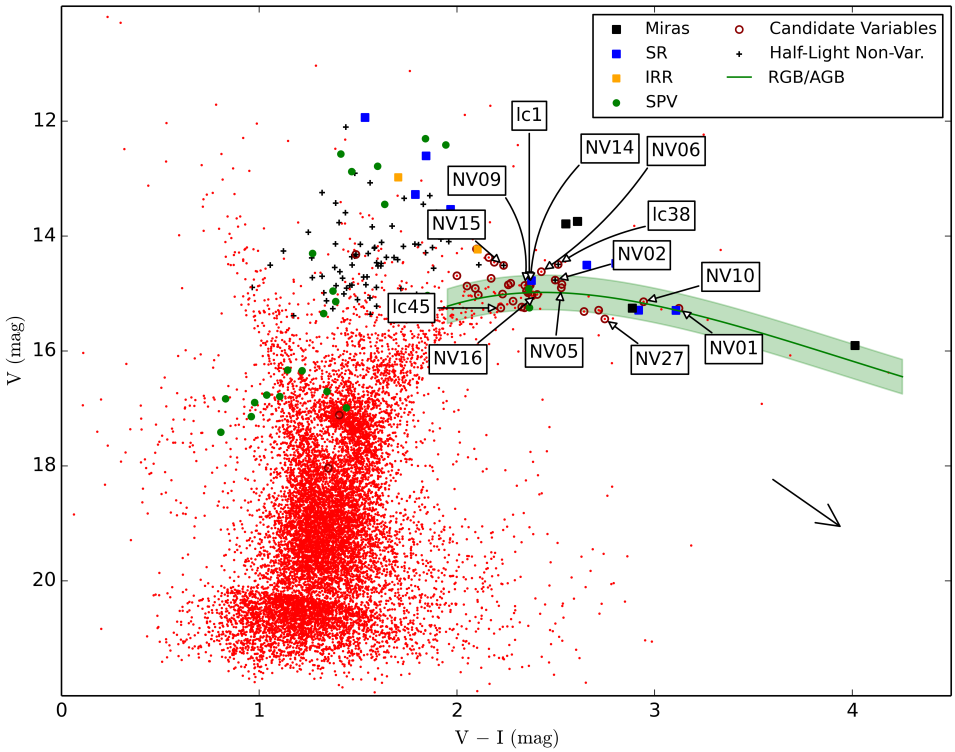

Figure 5.42: New variable stars' positions on the CMD, with the RGB band denoting our membership criterion (see section 5.1.1). Reddening vector represented by arrow.

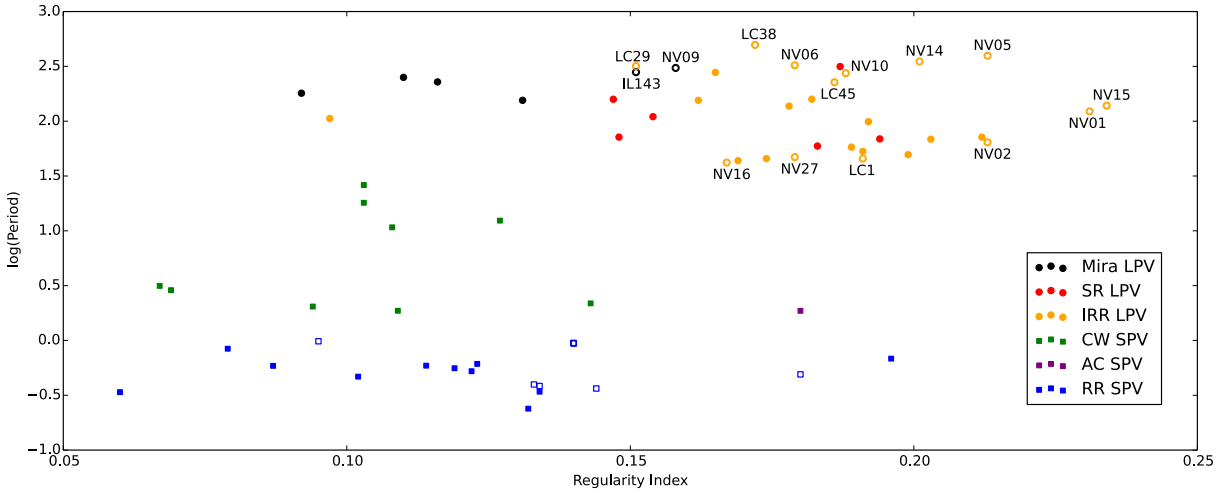

Figure 5.43: New variable stars' regularity indices vs. the logarithm of the period. The logarithmic y-axis is used to separate the LPVs from the SPVs. Known and new LPVs are marked with filled and empty circles, respectively. Known LPV types sourced from Clement catalogue (2015), New LPV types were determined by us. Hollow square markers denote uncertain classification of known SPVs. Note LC16 was not displayed because the period was not detected in I_L.

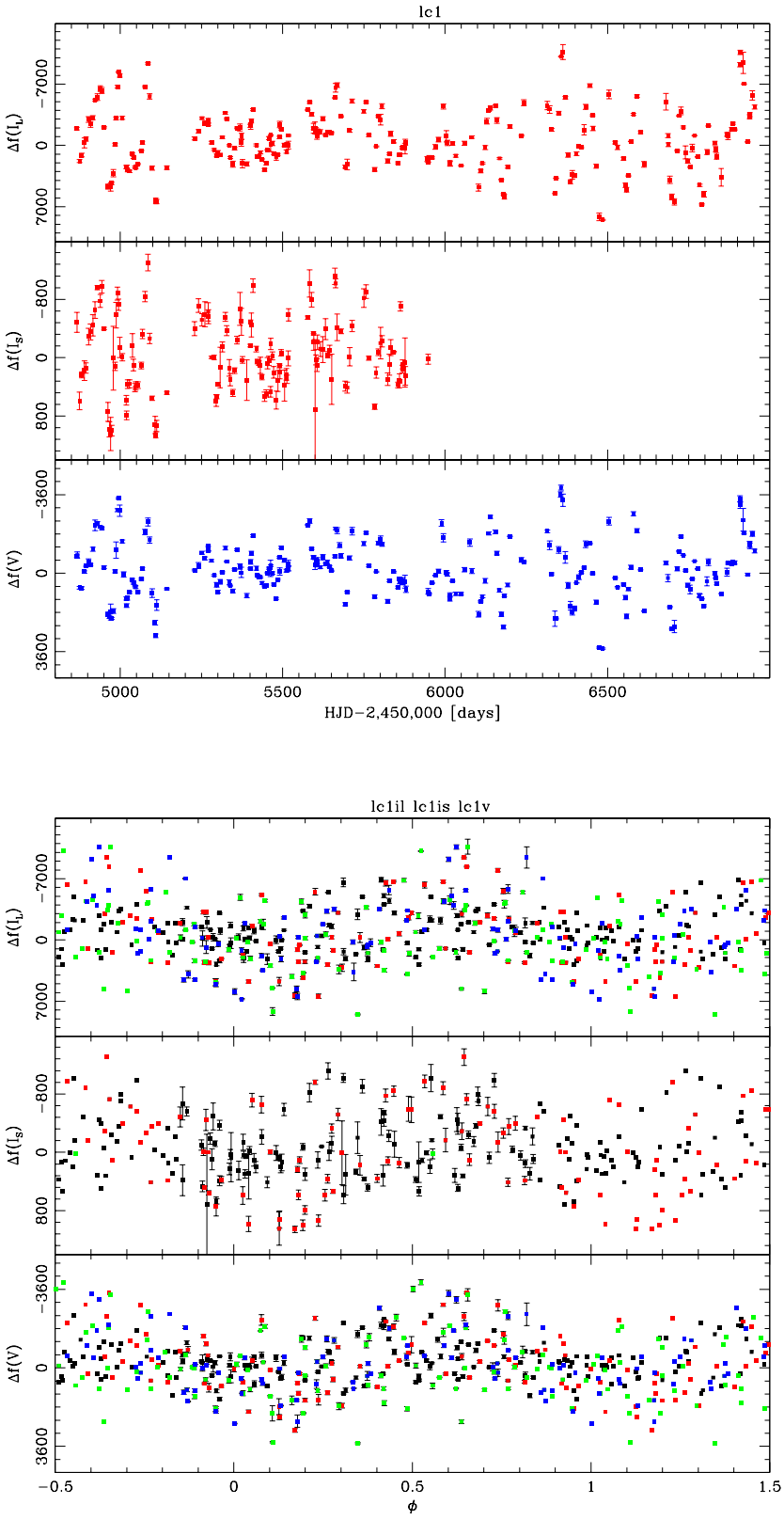

Figure 5.44: Variable LC1 ISIS light curve (top), folded light curve p = 45.6 days (bottom).

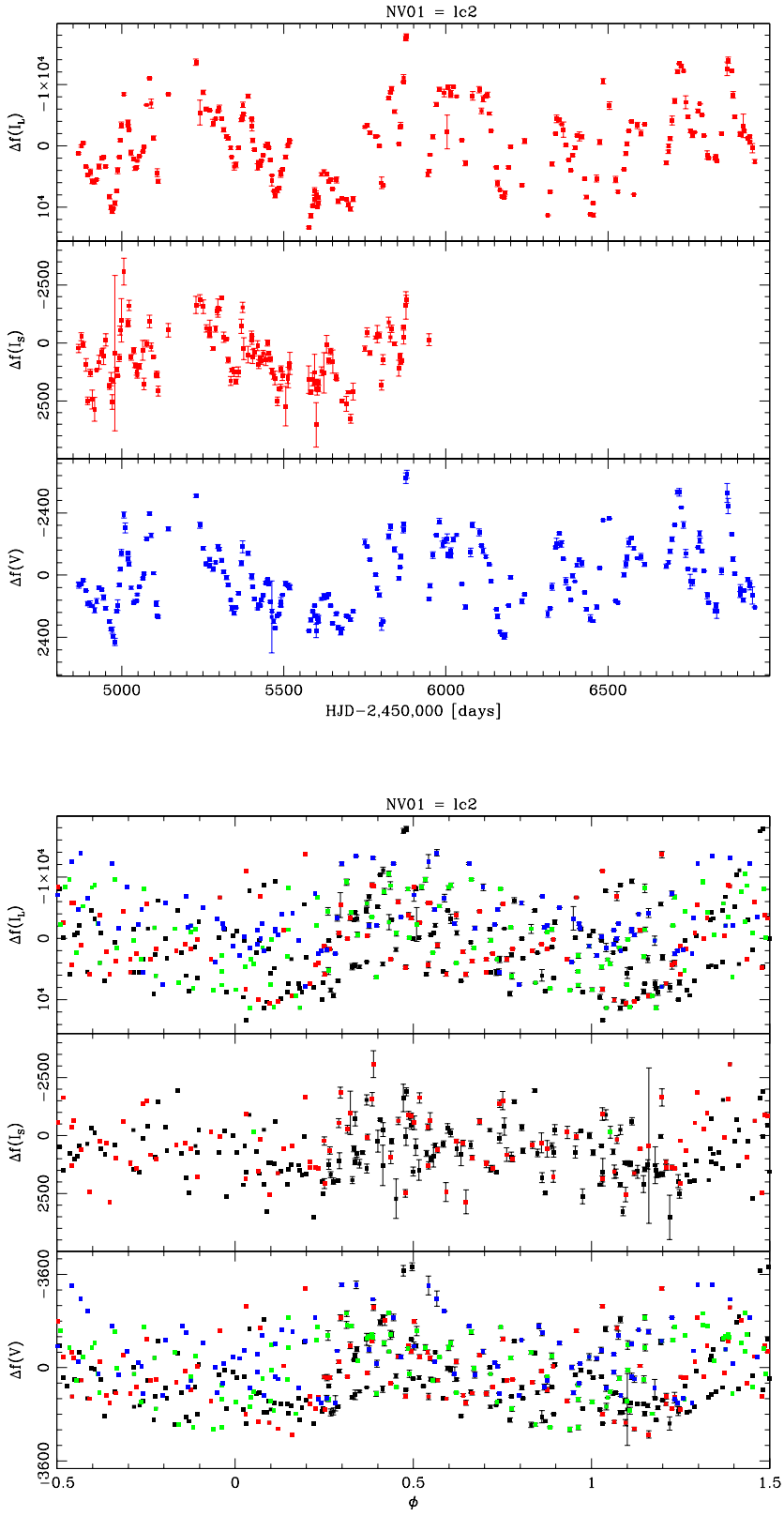

Figure 5.45: Variable NV01 ISIS light curve (top), folded light curve p = 122.8 days (bottom).

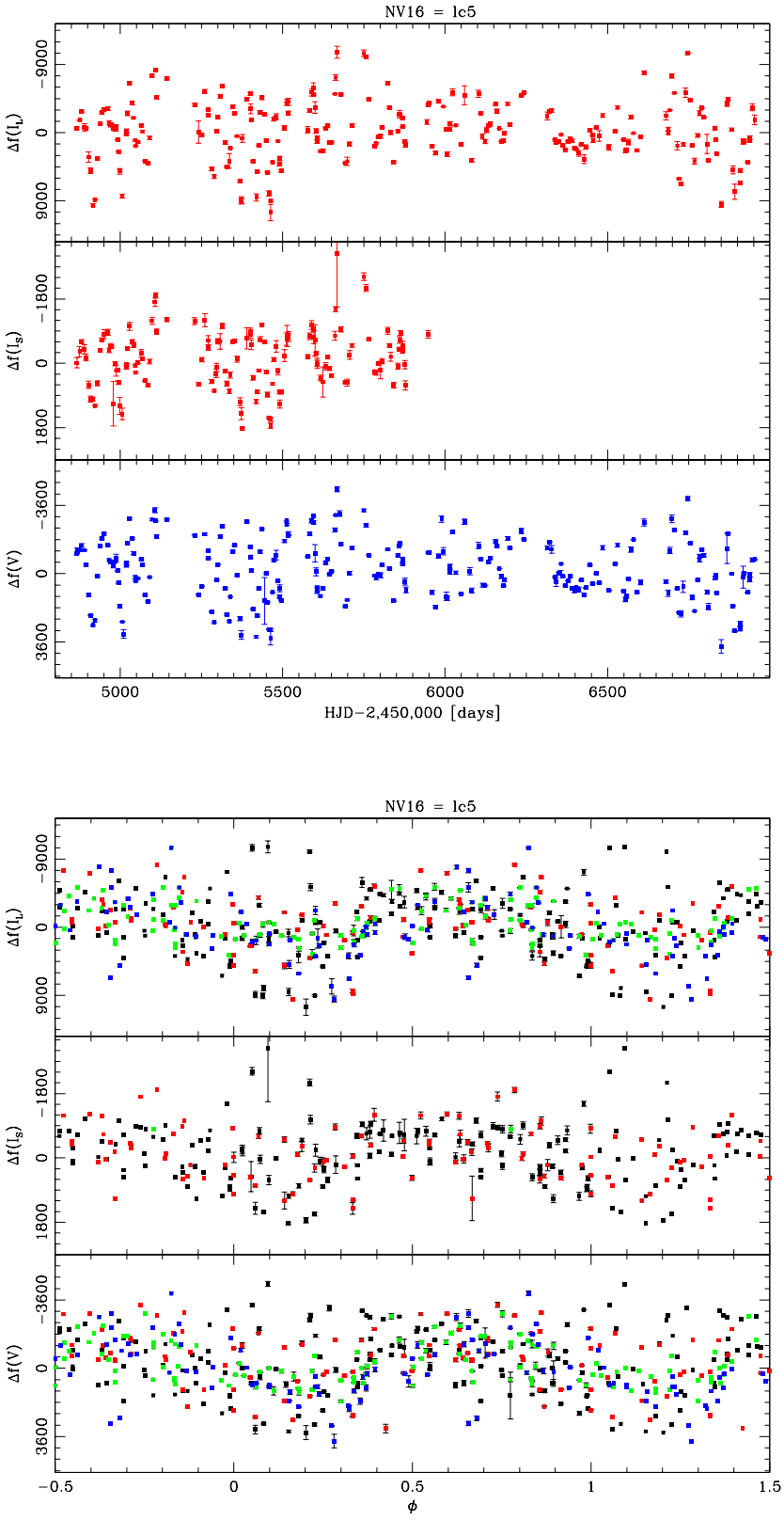

Figure 5.46: Variable NV16 ISIS light curve (top), folded light curve p = 41.94 days (bottom).

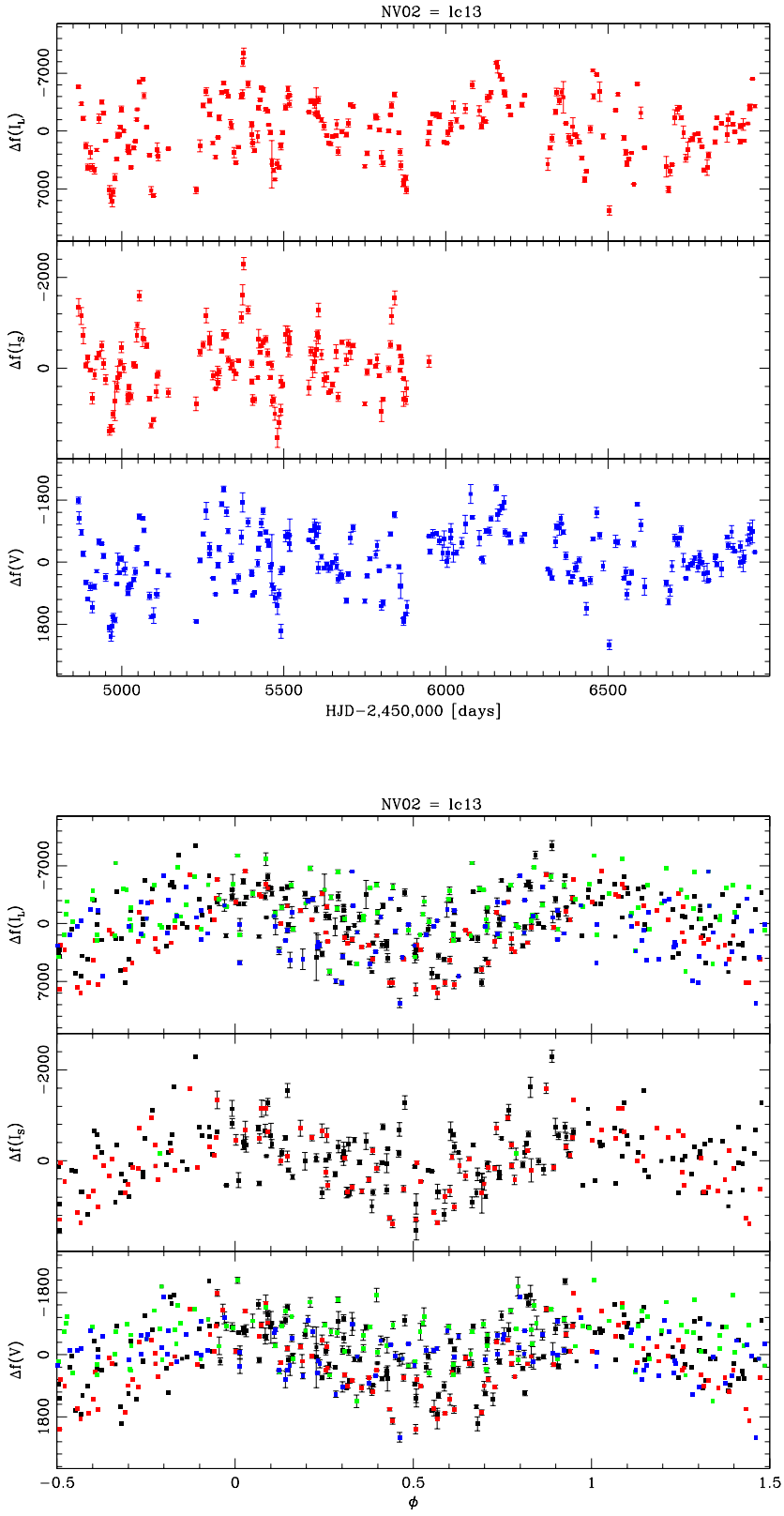

Figure 5.47: Variable NV02 ISIS light curve (top), folded light curve p = 64.2 days (bottom).

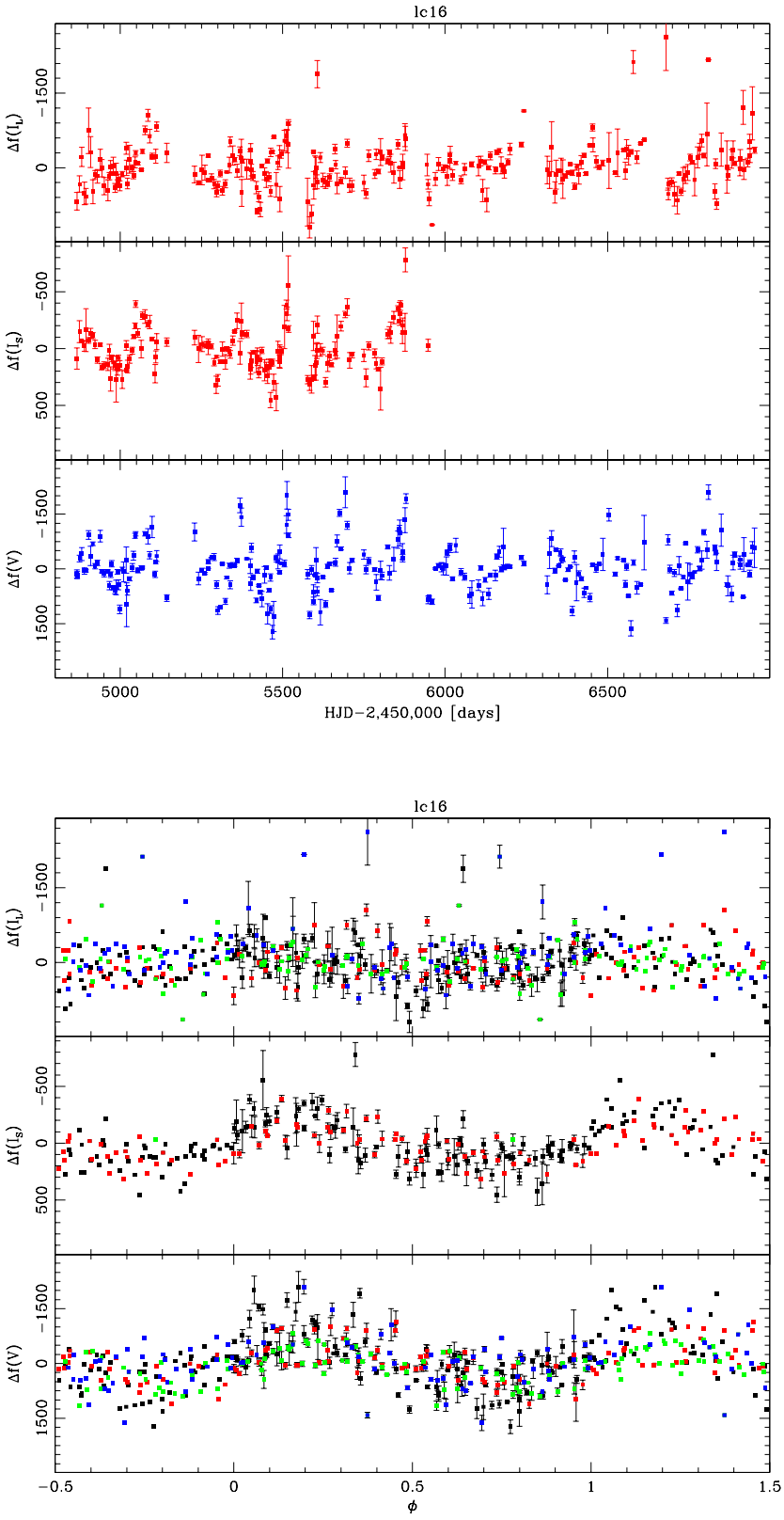

Figure 5.48: Variable LC16 ISIS light curve (top), folded light curve p = 159.4 days (bottom).

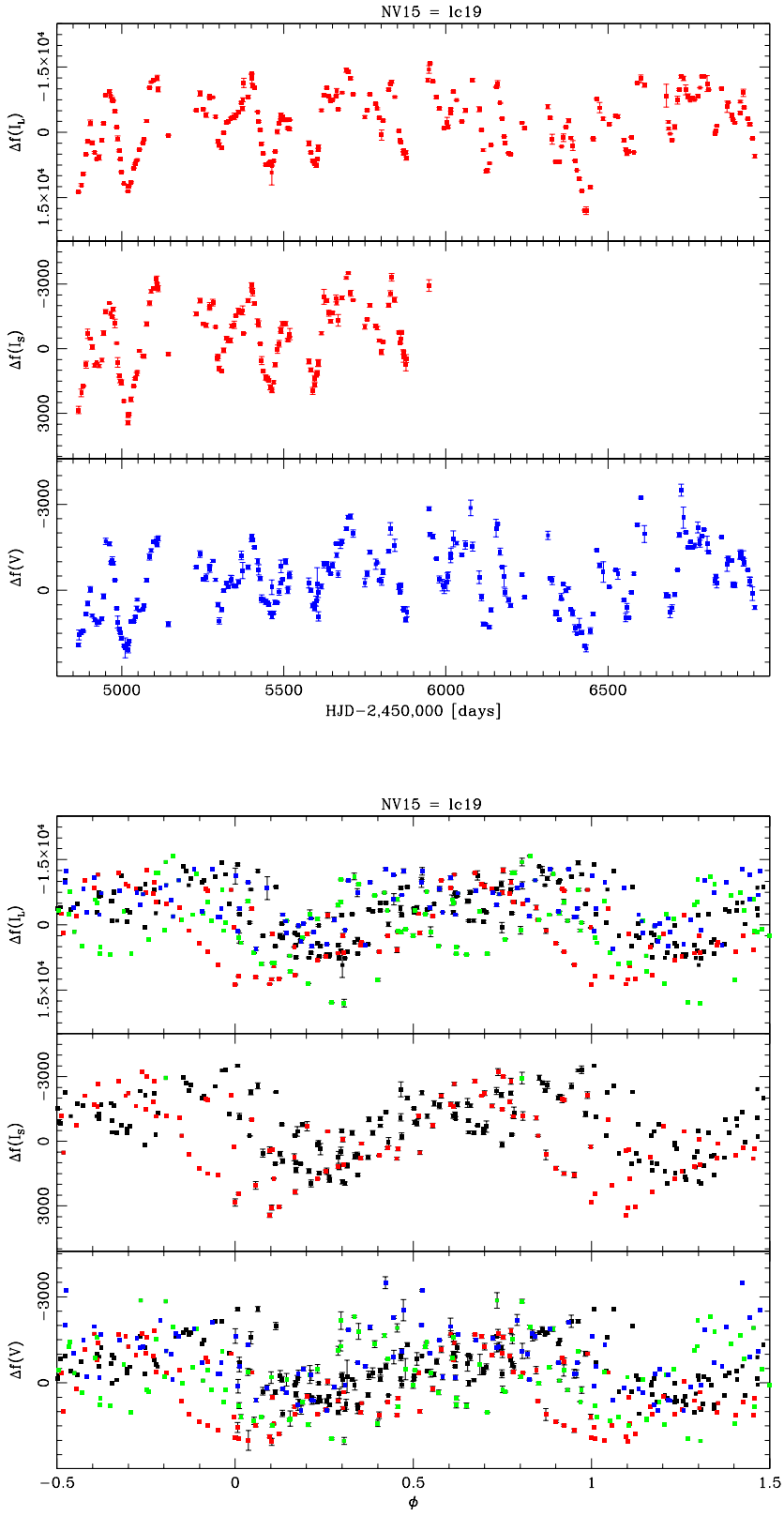

Figure 5.49: Variable NV15 ISIS light curve (top), folded light curve p = 138.5 days (bottom).

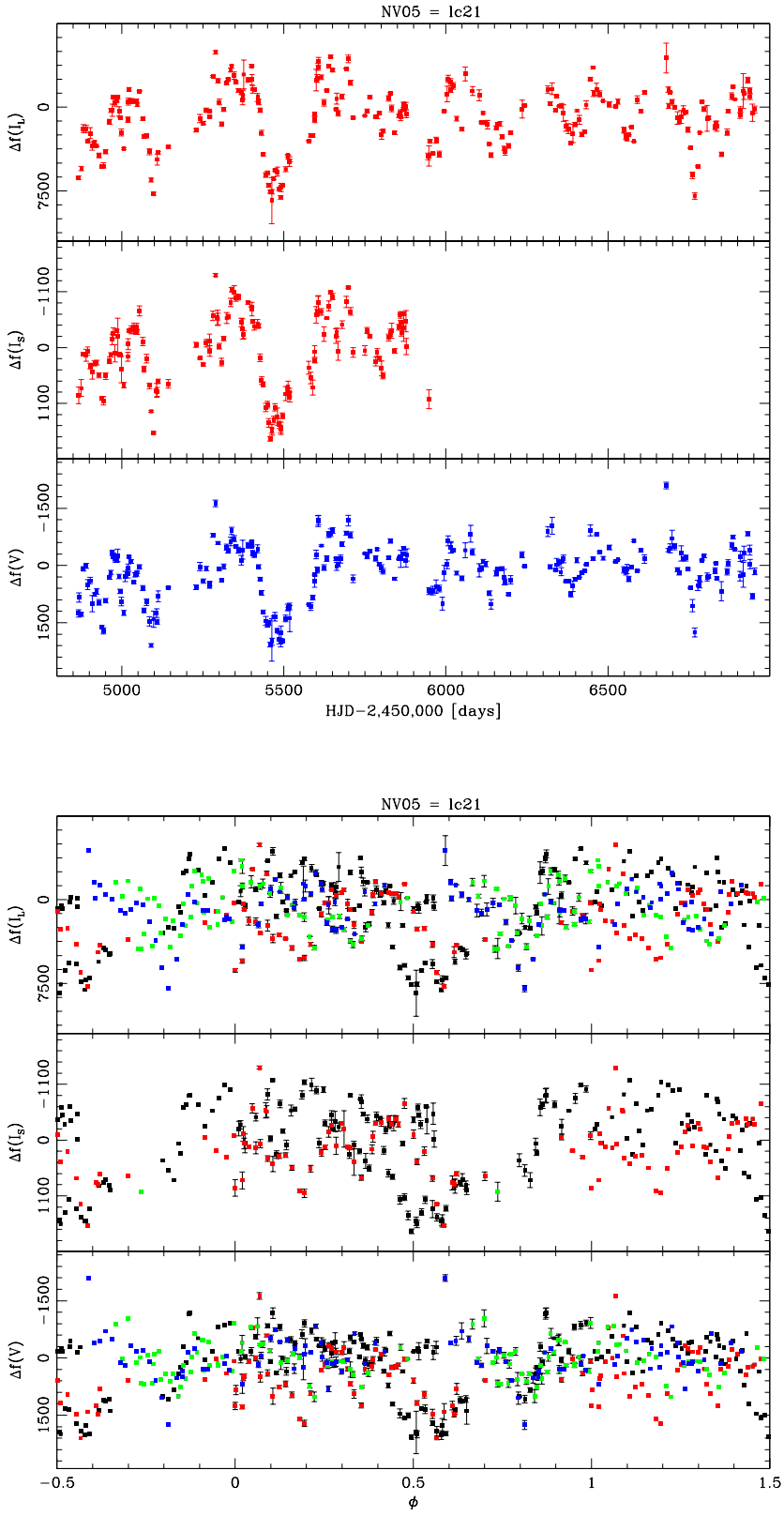

Figure 5.50: Variable NV05 ISIS light curve (top), folded light curve p = 395 days (bottom).

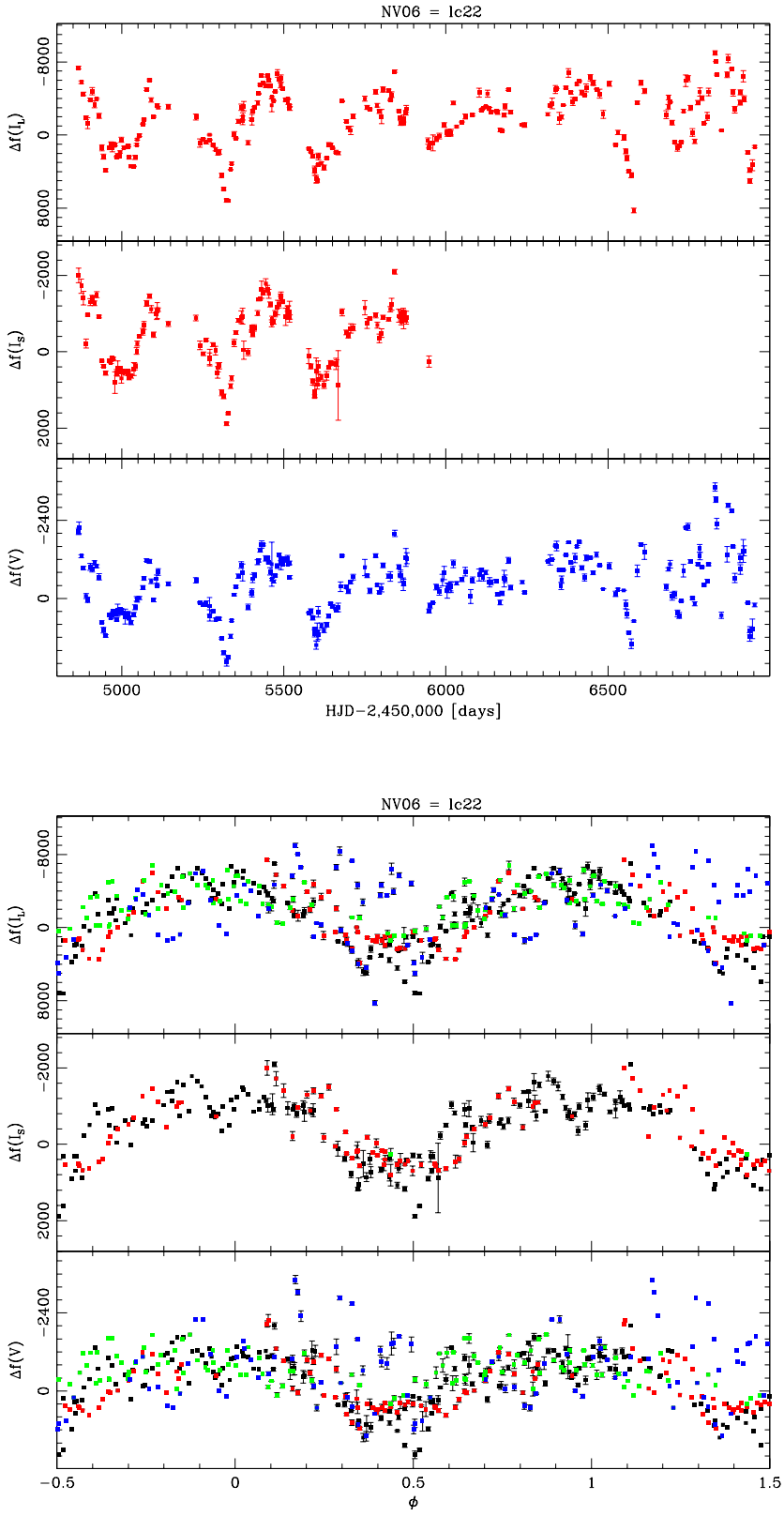

Figure 5.51: Variable NV06 ISIS light curve (top), folded light curve p = 323 days (bottom).

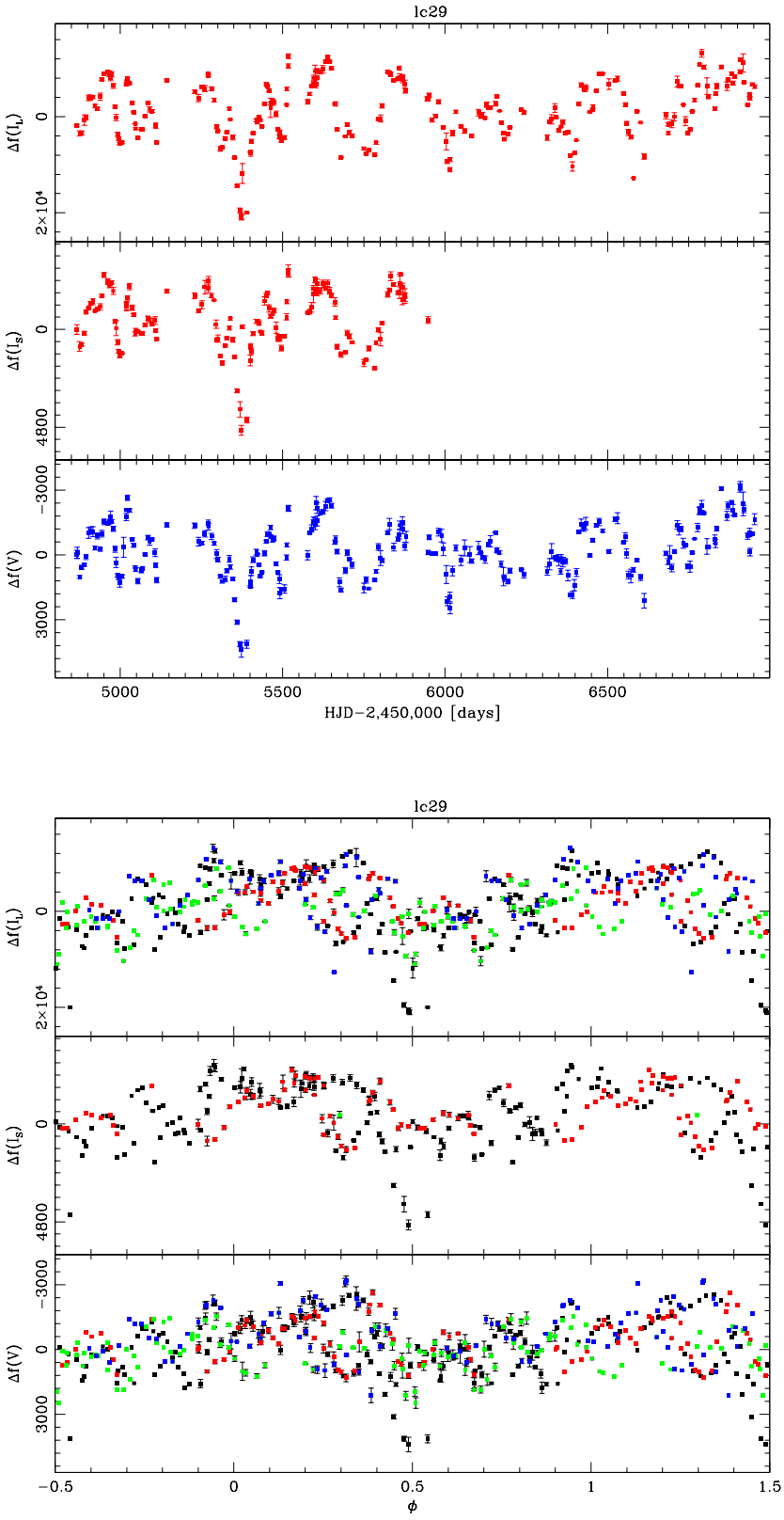

Figure 5.52: Variable LC29 ISIS light curve (top), folded light curve p = 318.3 days (bottom).

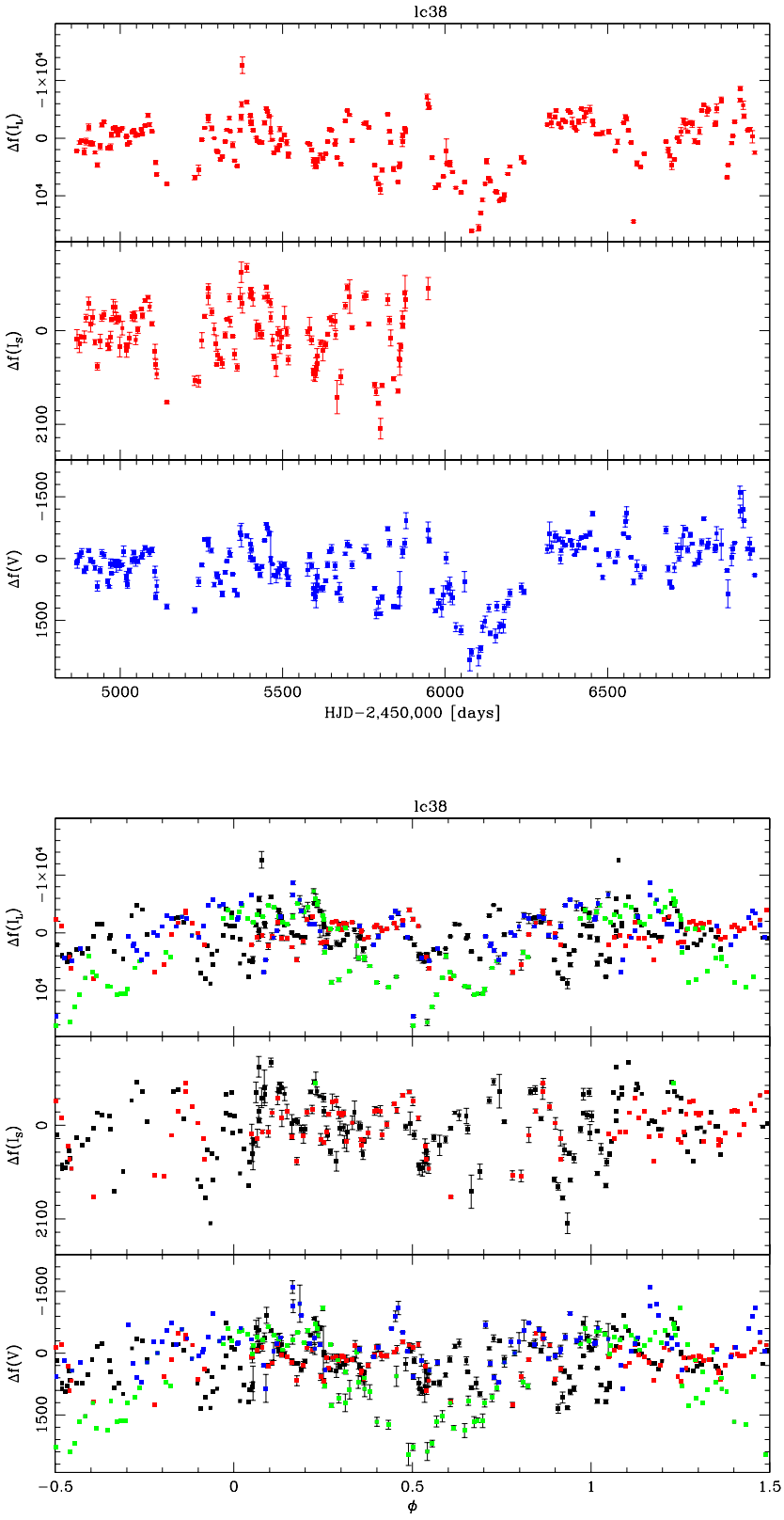

Figure 5.53: Variable LC38 ISIS light curve (top), folded light curve p = 496 days (bottom).

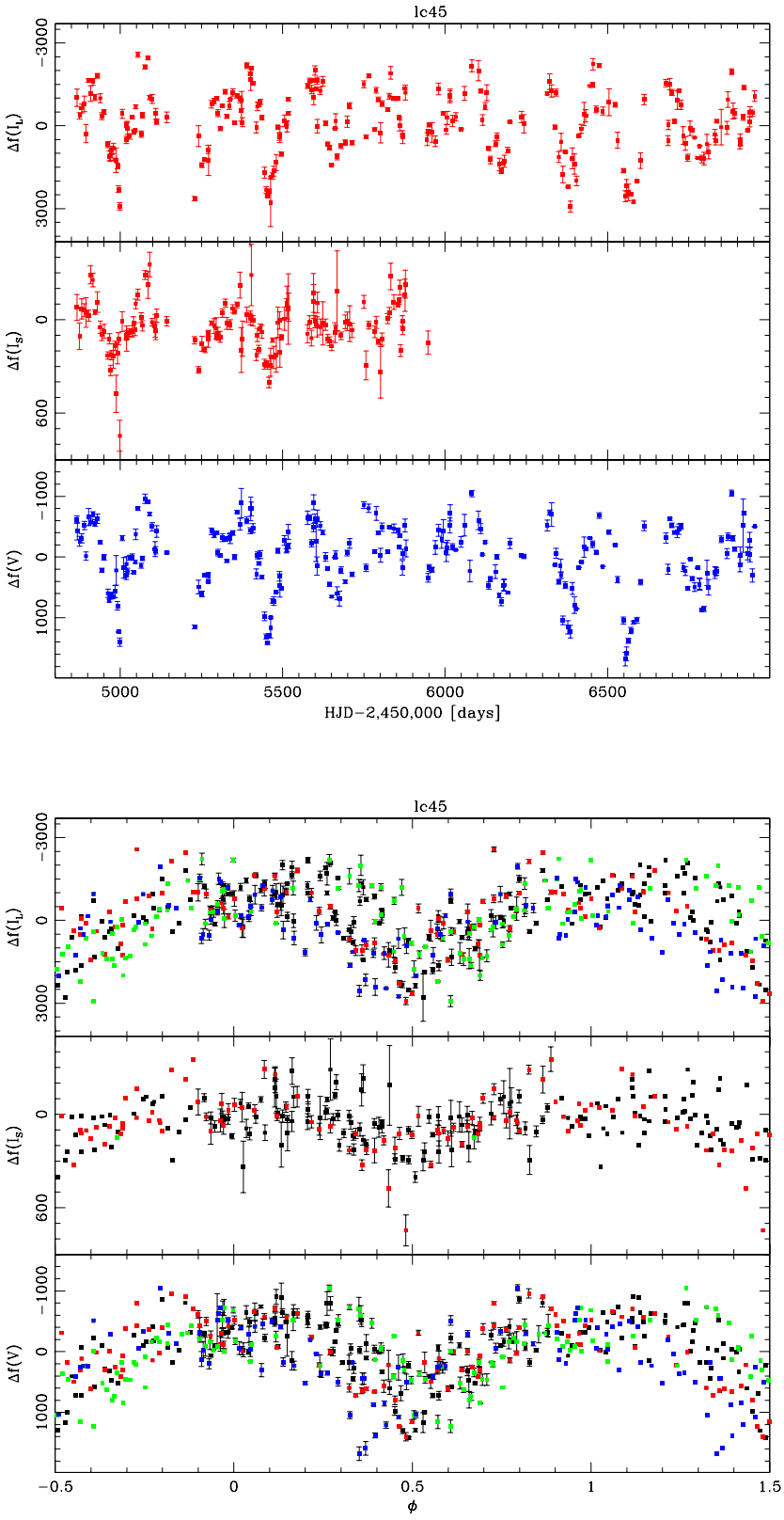

Figure 5.54: Variable LC45 ISIS light curve (top), folded light curve p = 226.5 days (bottom).

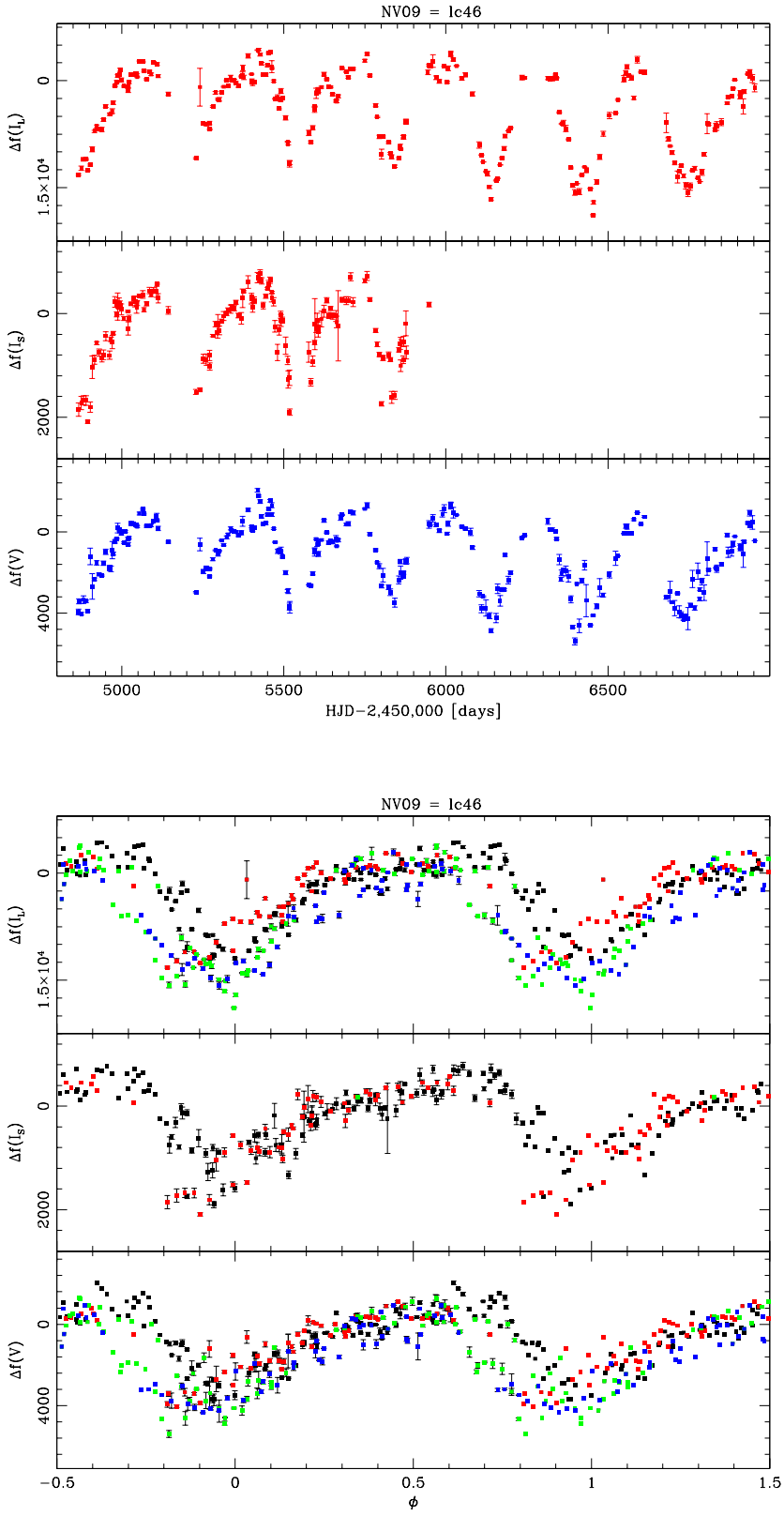

Figure 5.55: Variable NV09 ISIS light curve (top), folded light curve p = 305.917 days (bottom).

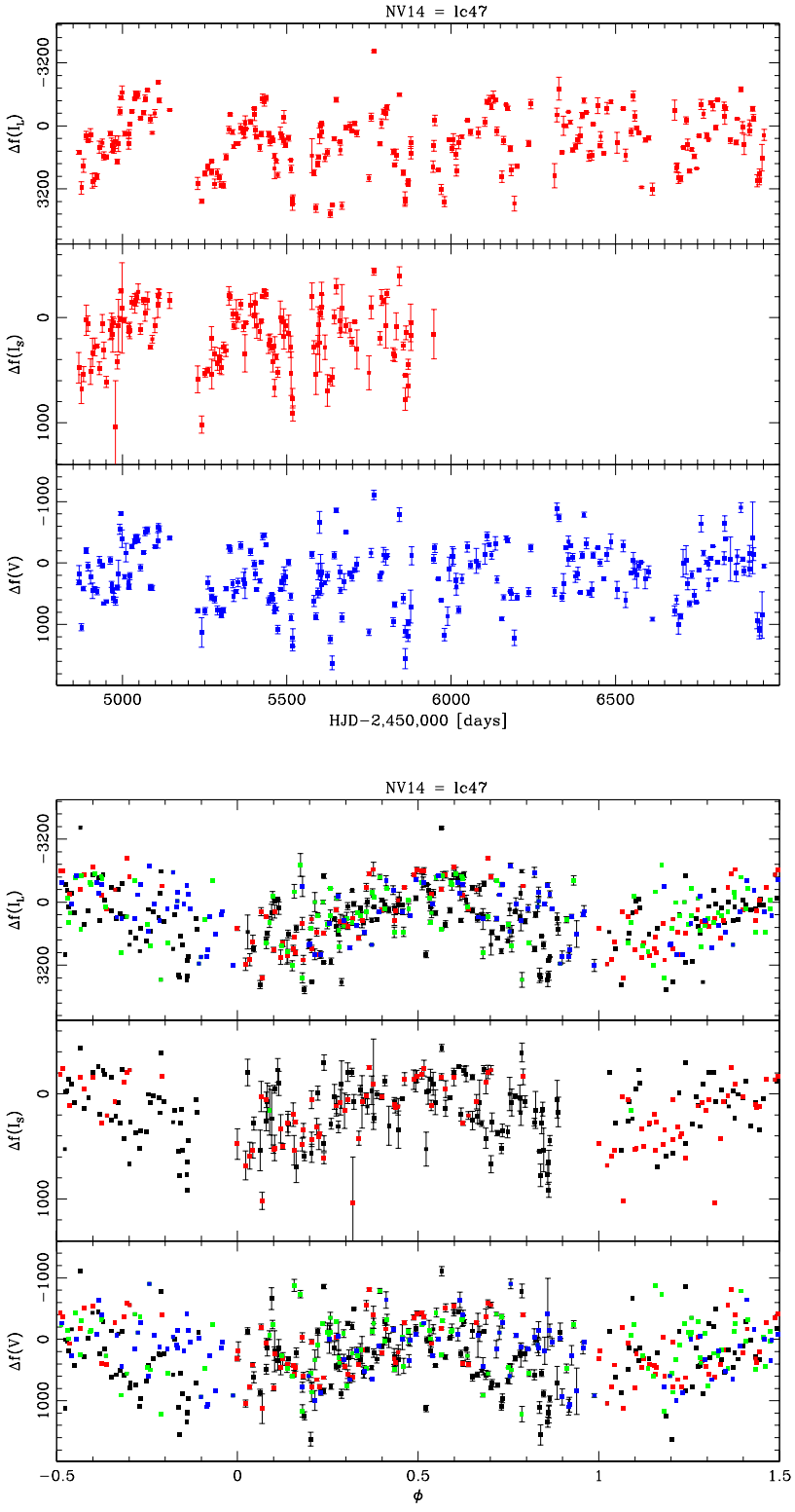

Figure 5.56: Variable NV14 ISIS light curve (top), folded light curve p = 350 days (bottom). Note the gap in the folded I_S light curve is due to the short time baseline (~3 years) relative to the period.

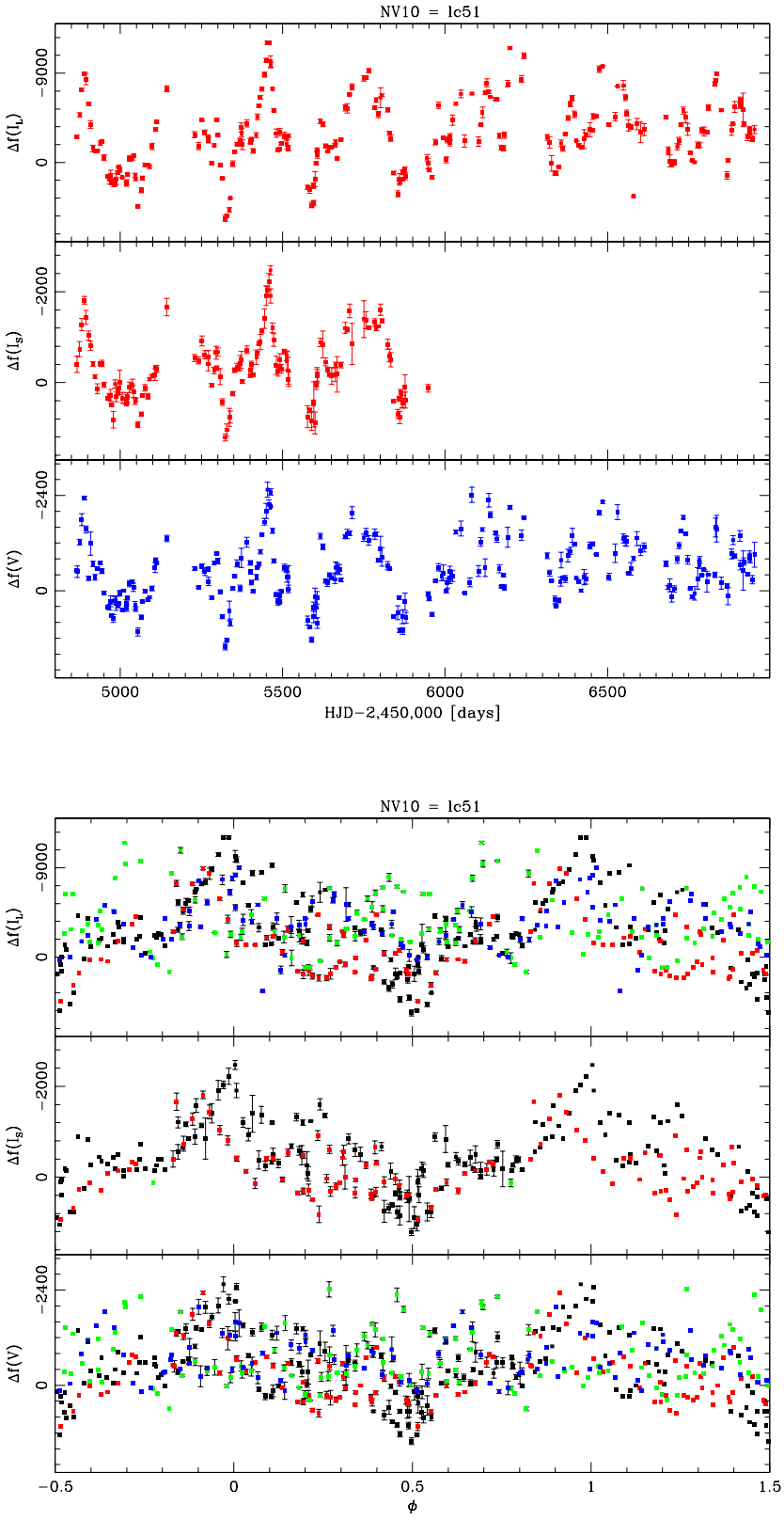

Figure 5.57: Variable NV10 ISIS light curve (top), folded light curve p = 274 days (bottom).

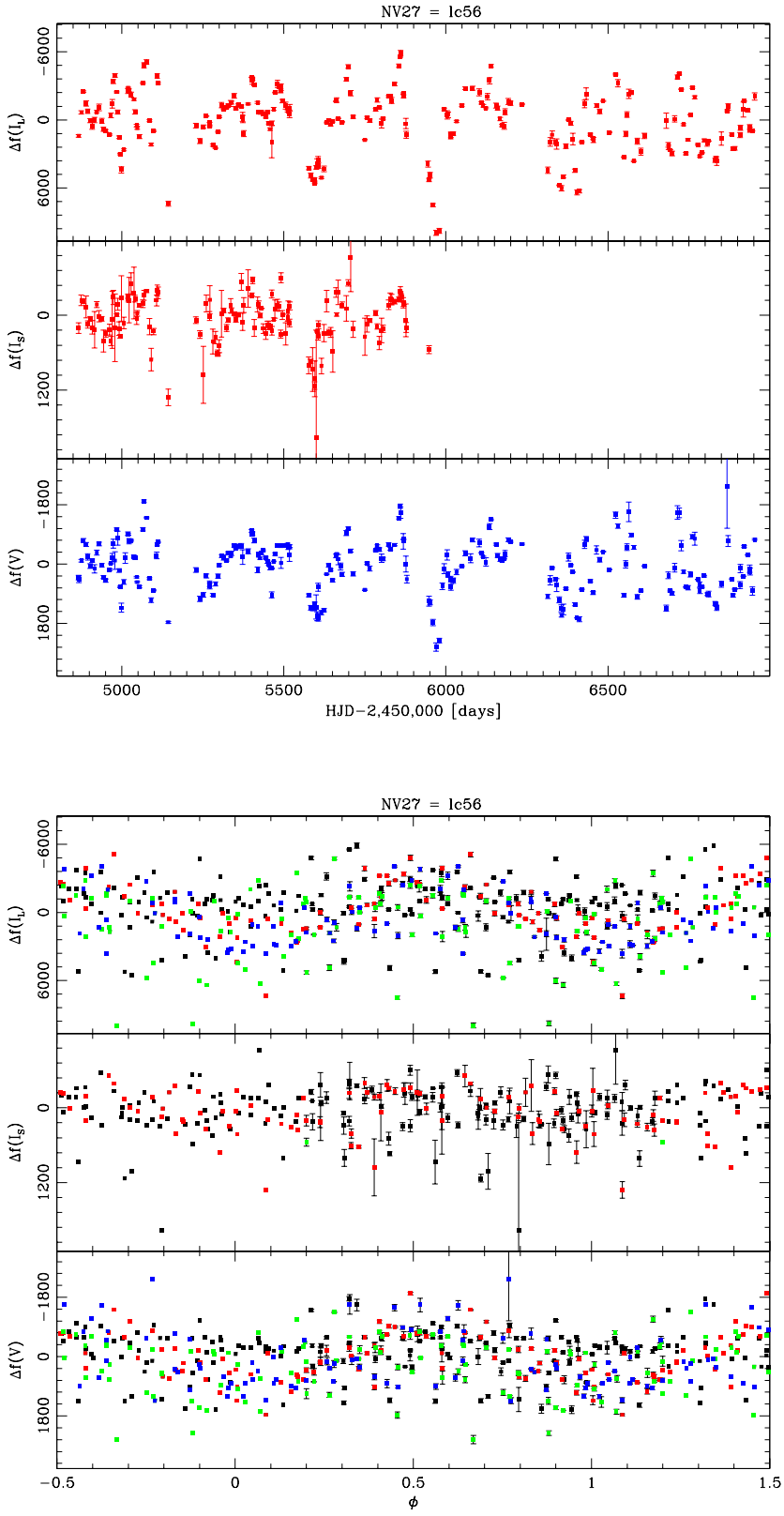

Figure 5.58: Variable NV27 ISIS light curve (top), folded light curve p = 47 days (bottom).

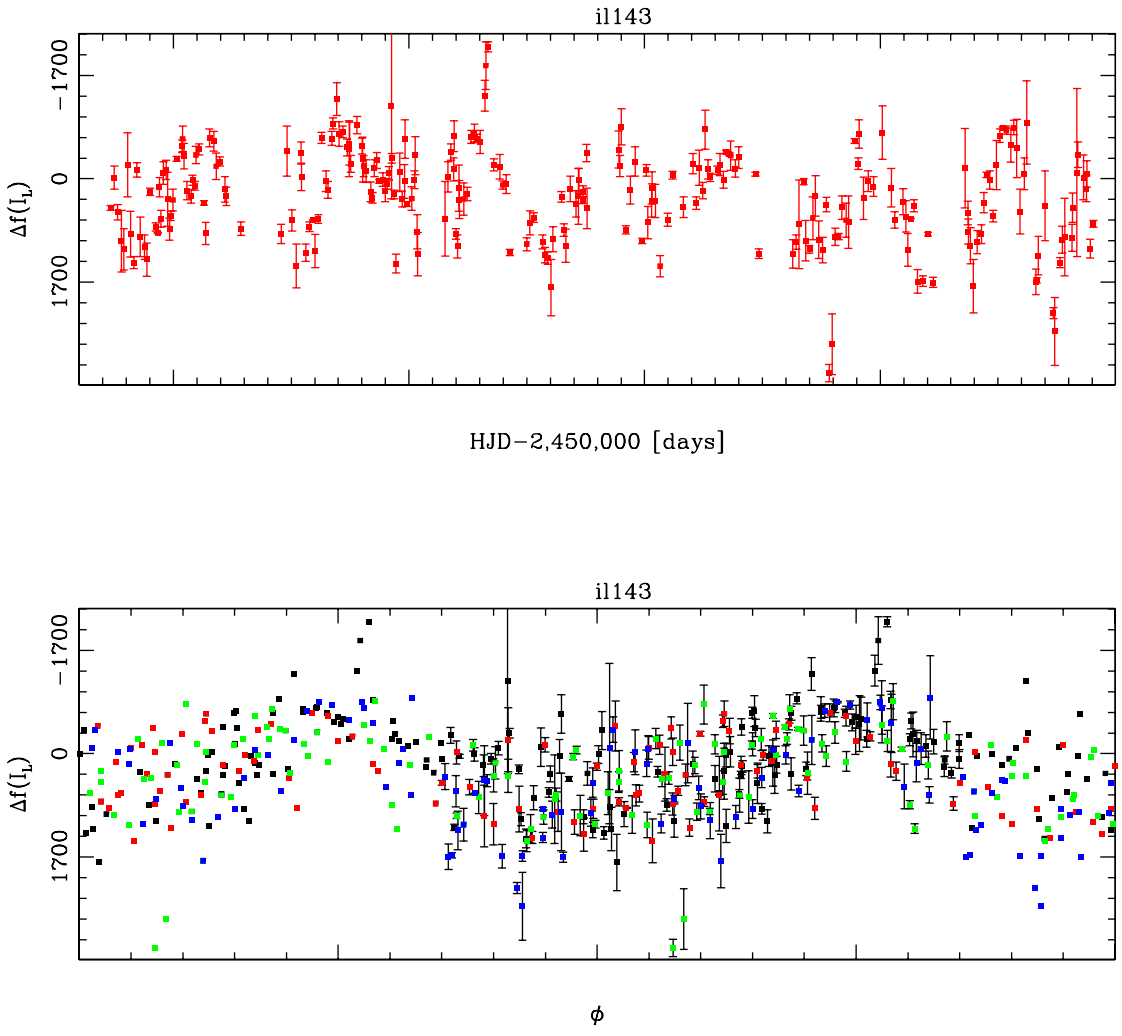

Figure 5.59: Variable IL143 ISIS light curve (top), folded light curve p = 280 days (bottom).

5.6 SPVs – W Virginis variables

Although our main aim in this research is the detection and classification of LPVs, the large amount of data available allows us to provide accurate measurements of the periods of many SPV stars in our FOV, some of which even improve on the published literature values. The first type of SPVs is W Virginis variables, a subtype of Population II Cepheids. These variable stars were abundant in our images. They are also useful as standard candles, much like classical Cepheids, meaning our period measurements can also be used to constrain the distance to the cluster after accounting for reddening. This section also includes the light curves for V77, an anomalous Cepheid ("AC" in GCVS nomenclature) that are believed to be too bright for their periods (Skottfelt et al., 2015). Below is a collection of their light curves (regular and folded), as well as a summary table.

Star ID	x (px) (V)	y (px) (V)	R_p (arcmin)	Period Obs. (days)	Period Lit. (days)	Type (lit.)	V Mag	I Mag
V18	333.52	459.70	0.903	2.8761 ± 0.0008	2.89	CW	N/A	N/A
V29	349.67	390.23	0.346	1.8653 ± 0.0003	1.8652	CWB	N/A	N/A
V36	429.37	409.84	0.517	3.146 ± 0.001	3.1	CW	14.919	12.555
V37	385.81	340.90	0.416	10.759 ± 0.014	10	CW	14.303	13.033
V63*	396.80	380.51	0.127	2.0376 ± 0.0007	2.038	CWB	12.573	11.16
V67^{IL}	161.40	250.09	2.551	2.179 ± 0.003	2.27	CW	16.99	15.549
V70	389.42	394.70	0.125	12.386 ± 0.025	12.38	CWA	12.879	11.411
V72	389.52	367.81	0.160	18.026 ± 0.034	18.01	CWA	12.786	11.187
V73	383.39	370.40	0.125	26.16 ± 0.10	26.1	CWA	12.306	10.465
V77*	387.42	372.67	0.108	1.8640 + 0.0007 - 0.0005	1.8643	AC	12.415	10.471

Table 5.5: Known W Virginis stars detected and/or recovered, and V77. (1st column): Star ID. Stars marked with an asterisk were manually recovered, marked with I_L were only detected in I_L. (2nd and 3rd column): star coordinates are in pixels of the master reference image (V-exposure). (4th column): Projected radius. (5rd and 6th column): Period as observed and in the literature. NR: Not Recovered. (7th column): Literature classification, no discrepancies were found. CWA/B: W Virginis, AC: anomalous Cepheid. (8th and 9th columns): V and I magnitudes if available from Cardona's database.

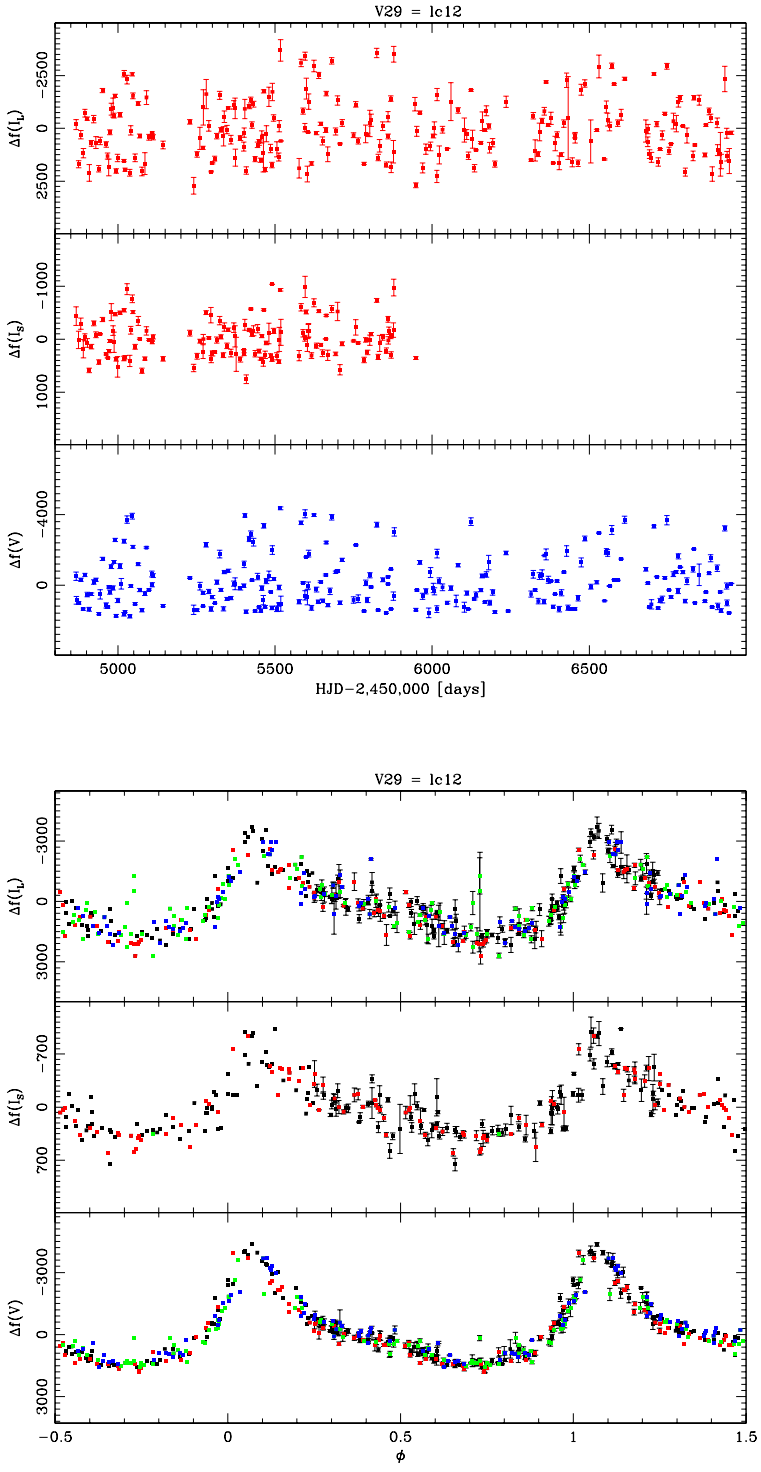

Figure 5.60: Variable V29 ISIS light curve (top), folded light curve p = 1.8653 days (bottom). V29 is classified as CWB, defined as a W Virginis variable with p < 8 days (GCVS, 2009) Note cadence is too low for SPVs, hence the periodic behavior is not evident in the regular light curves.

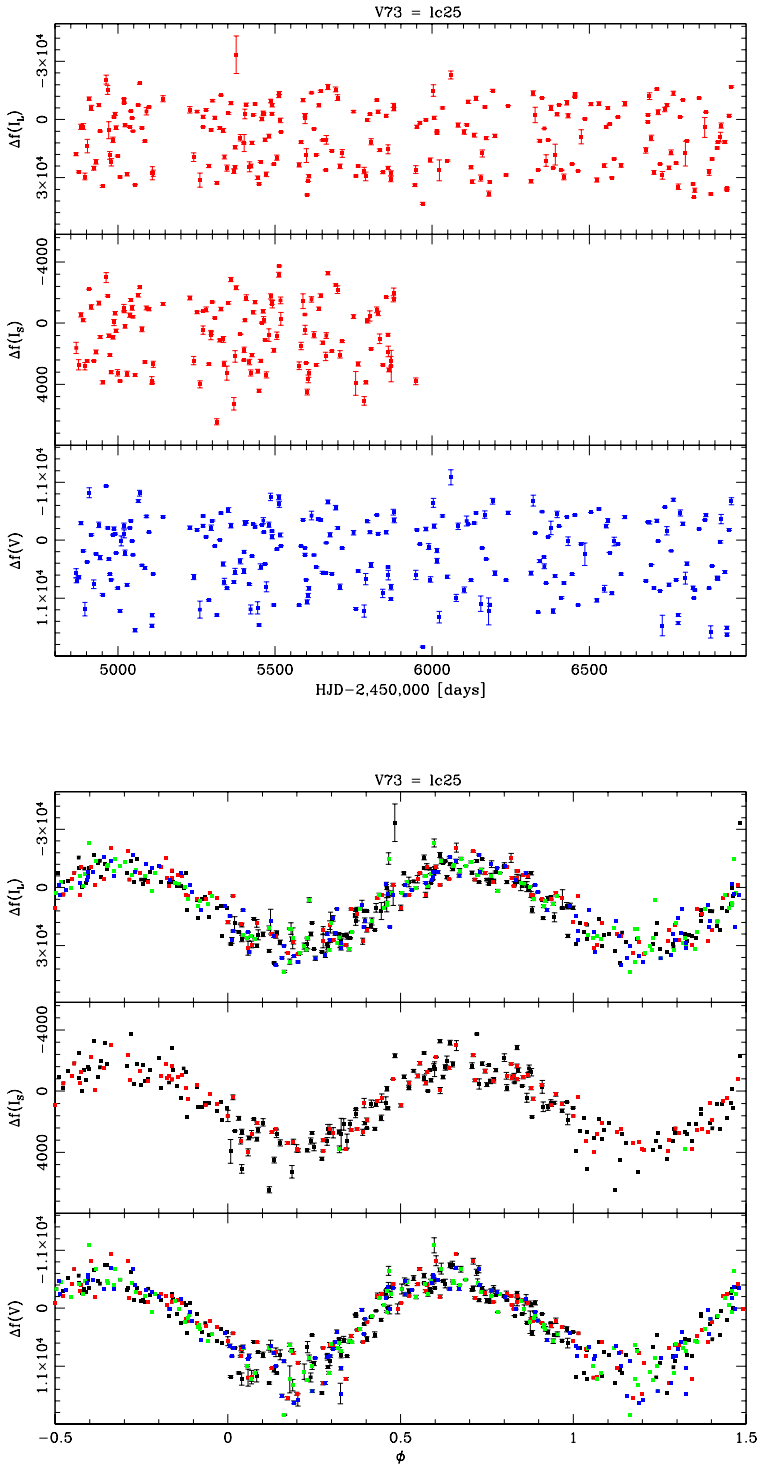

Figure 5.61: Variable V73 ISIS light curve (top), folded light curve p = 26.16 days (bottom). V73 is classified as CWA, defined as a W Virginis variable with p > 8 days (GCVS, 2009). It also has the longest period of all the recovered SPVs in the cluster. Note that discerning periodic behavior from the regular light curve is still difficult.

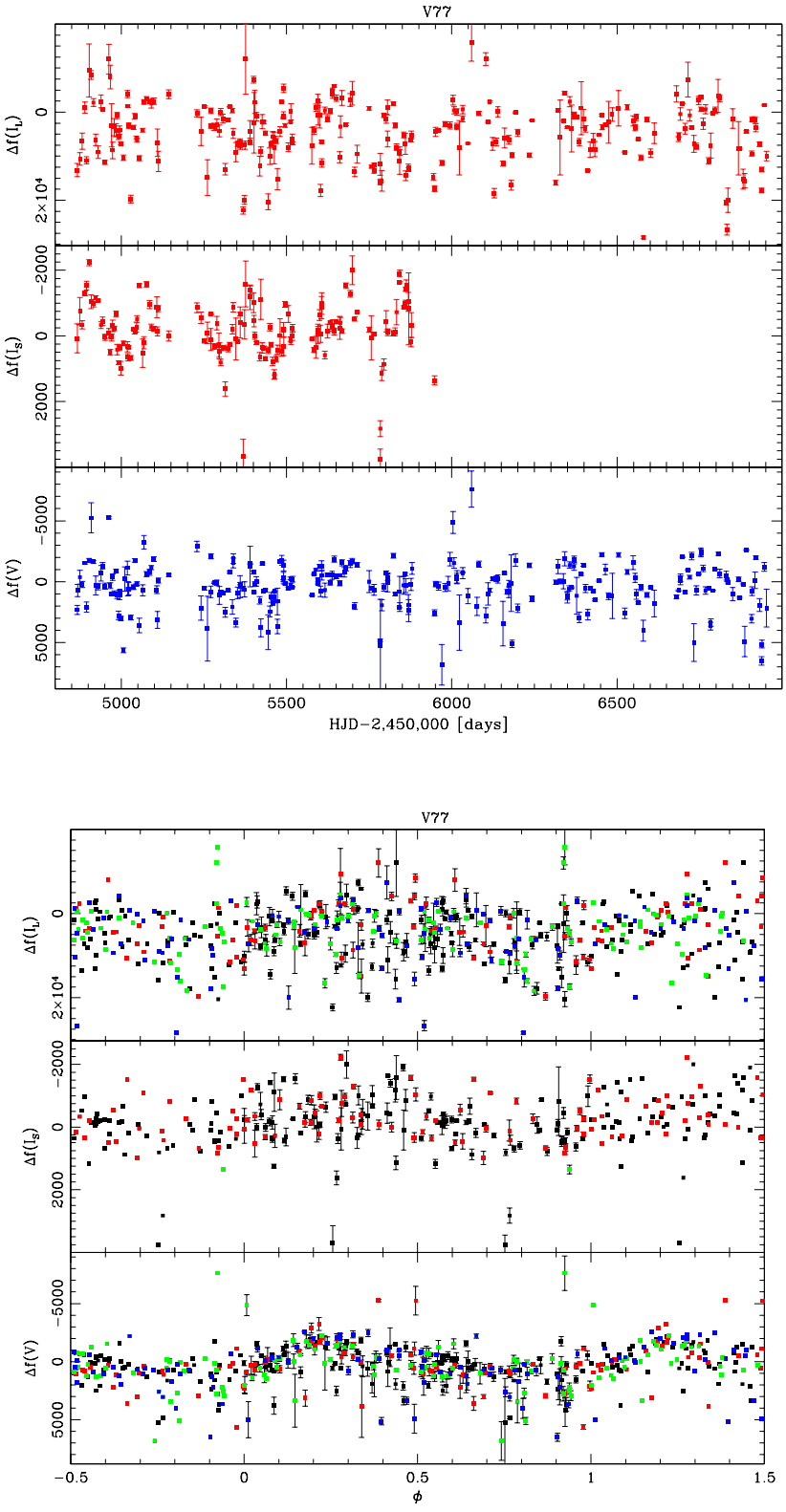

Figure 5.62: Anomalous Cepheid-type Variable V77 ISIS light curve (top), folded light curve p = 1.8640 days (bottom).

5.7 SPVs – RR Lyrae variables

The other SPV variables found, and the most common SPV type, are RR Lyrae variables. Despite the RR Lyraes having short periods with an upper limit of roughly 1 day, the PDM method allows us to leverage our wealth of data, which contained many partially observed cycles, to determine the period very accurately; some variables were determined with an uncertainty on the order of 10^{-4} days (~5 seconds). Much like W Virginis variables, the RR Lyraes are also useful as standard candles. Below is a collection of their light curves (regular and folded), subtype classification (RRab or RRc), as well as a summary table.

Star ID	x (px)	y (px)	R_p (arcmin)	P. Obs. (days)	P. Lit. (days)	Type (lit.)	V Mag	I Mag
V17	319.47	338.71	0.771	0.61142 ± 0.00005	0.611	RR0	N/A	N/A
V20	474.38	452.20	1.118	0.46745 ± 0.00007	0.467	RR1	16.332	15.188
V22	499.48	376.41	1.136	0.58687 ± 0.00004	0.587	RR0	16.706	15.363
V23	80.18	411.58	3.002	0.33762 ± 0.00004	0.338	RR1	16.832	16.002
V26	573.20	276.25	2.136	0.23877 ± 0.00002	0.2390	RR1	17.414	16.608
V28	424.65	297.01	0.936	0.84089 ± 0.00017	0.840	RR0	16.897	15.92
V30	467.52	368.04	0.833	0.95095 ± 0.00018	0.951	RR0?	16.344	15.127
V31	585.37	546.80	2.551	0.34096 ± 0.00005	0.341	RR1	17.142	16.182
V32*	*320.48*	*334.91*	0.785	0.52415 ± 0.00006	0.522	RR1	N/A	N/A
V33	493.88	525.03	1.764	0.55805 ± 0.00007	0.558	RR1	16.767	15.729
V49	404.67	315.29	0.697	0.38425 ± 0.00005	0.384	RR1?	15.14	13.753
V50*	*346.18*	*422.12*	0.535	0.36438 ± 0.00005	0.364	RR1?	14.957	13.584
V51	430.80	337.98	0.639	0.39674 ± 0.00005	0.397	RR1?	15.349	14.023
V53	247.20	443.90	1.473	0.9829 ± 0.0001	0.986	RR0?	16.792	15.688
V55	411.97	273.69	1.110	0.49037 ± 0.00007	0.489	RR1?	15.035	13.184
V58	337.22	372.68	0.473	0.6826 ± 0.0002	0.683	RR0	N/A	N/A
V59	394.78	403.40	0.225	0.58890 ± 0.00006	0.5888	RR0	13.449	11.814
V68	401.71	429.47	0.487	0.9370 ± 0.0001	0.946	RR0?	N/A	N/A
V71	393.28	391.50	0.122	NR	0.854	RR0	N/A	N/A

Table 5.6: Known RR Lyrae stars detected and/or recovered. (1st column): Star ID. Stars marked with an asterisk were manually recovered. (2nd and 3rd column): star coordinates are in pixels of the master reference image (*V*-exposure). (4th column): Projected radius. (5rd and 6th column): Period as observed and in the literature. NR: Not Recovered. (7th column): Literature classification, no discrepancies were found. RR0: RRab, RR1: RRc. (8th and 9th columns): V and I magnitudes if available from Cardona's database.

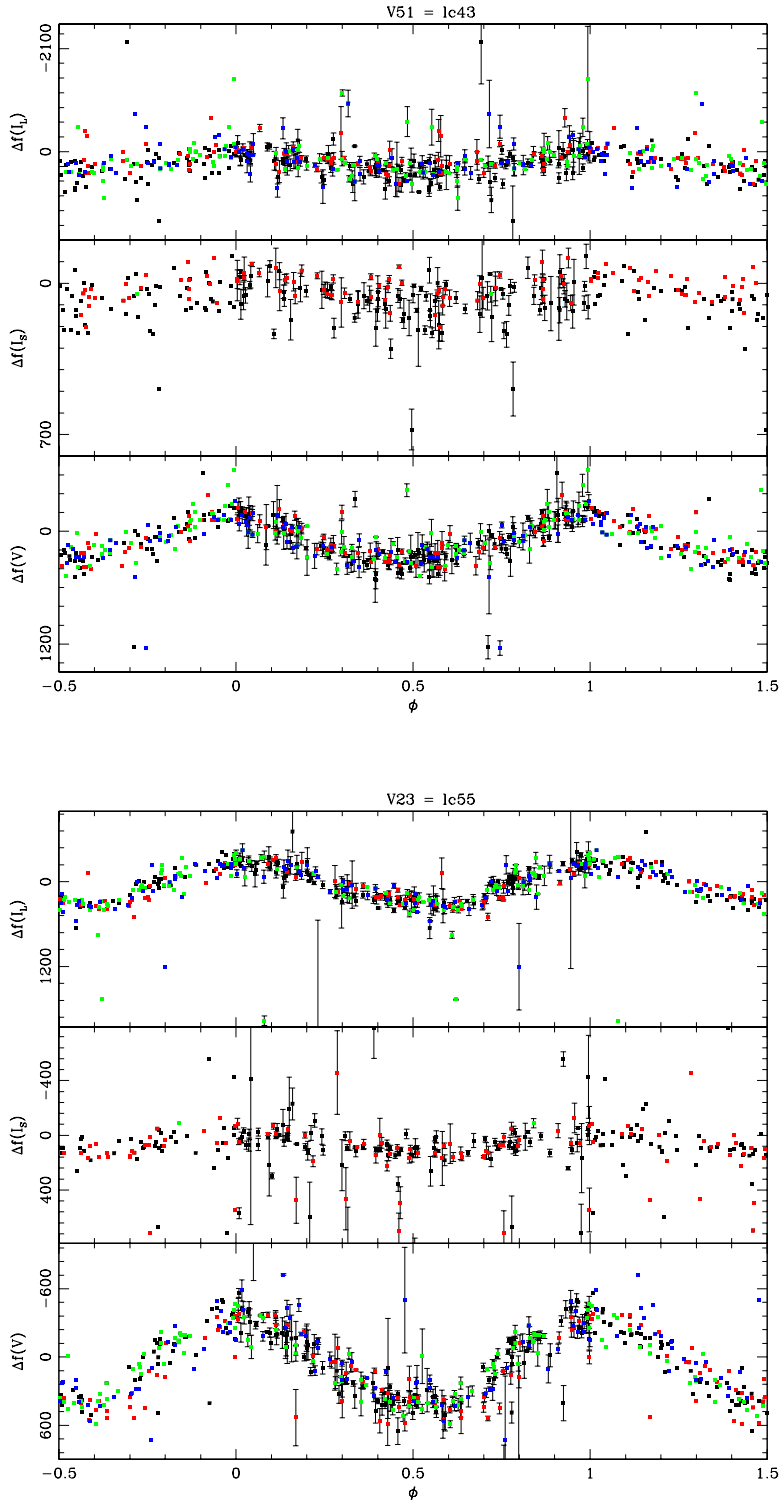

Figure 5.63: ISIS folded light curves for Variable V51, with p = 0.39674 days (top), and Variable V23, with p = 0.33762 days (bottom). V51's period was harder to find than V23 due to the former's higher scatter. The literature classifies both as RRc, but V51's classification is tentative.

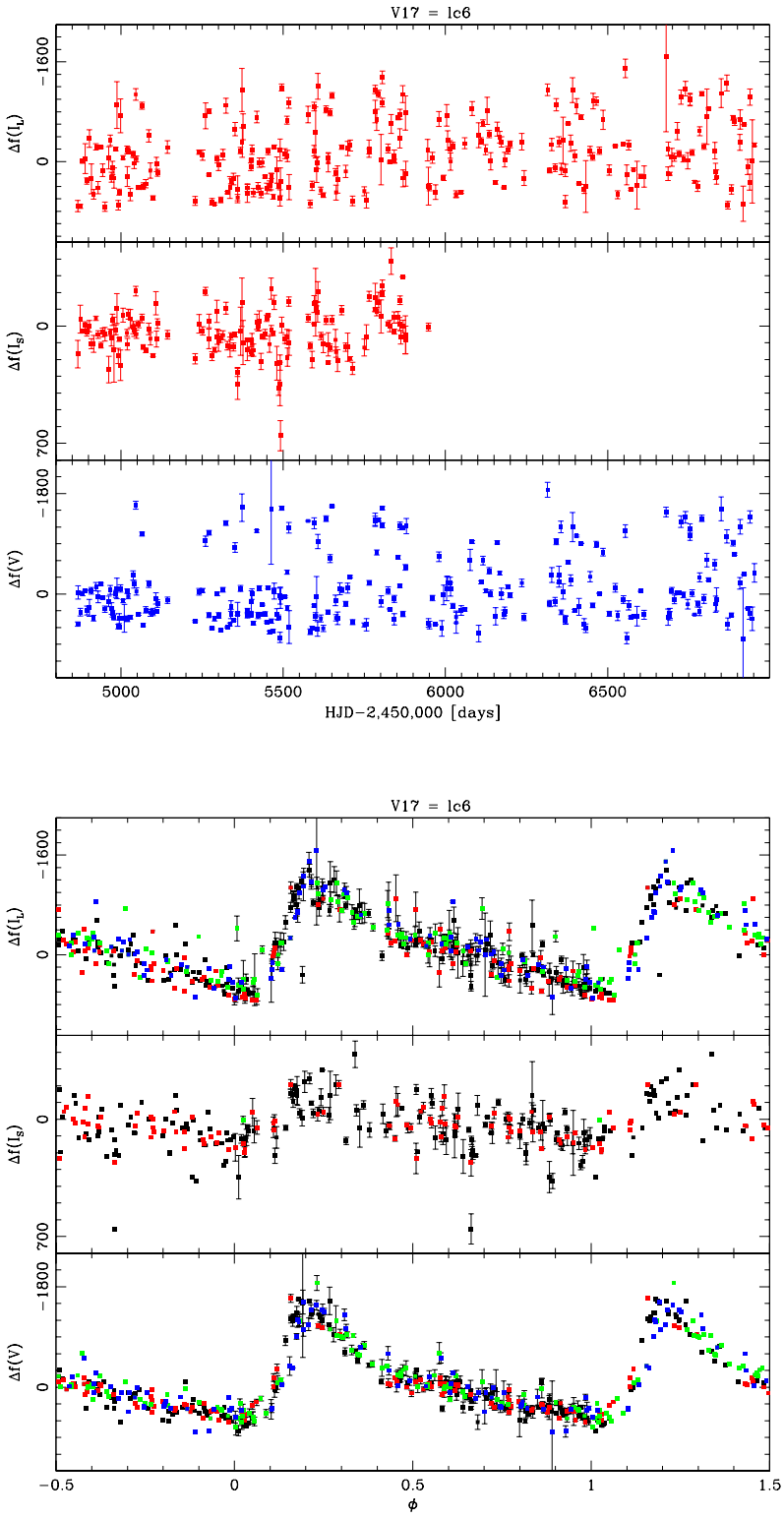

Figure 5.64: Variable V17 ISIS light curve (top), folded light curve p = 0.61142 days (bottom). Classified in the literature as type RRab, as evident in the asymmetry of the folded light curve.

CHAPTER 6. CONCLUSIONS

The main result from the data on LPV variables is the value of extended observations, or a long time baseline, in order to characterize their behavior. Many known LPV stars previously lacked a period or type determination beyond being designated an LPV, and observing them over six years allowed us to discern long-term tendencies as well as their position on the Mira-to-SR-to-IRR continuum. The long time span was achieved using a modest ~40 cm aperture telescope to observe the cluster, for which longer observing campaigns are typically easier to acquire than for larger apertures. Despite the modest resolution (~1.8 arcsec FWHM on good seeing nights) of the PROMPT telescope, we have managed to recover a good number of the known variable stars: 56 stars out of the 104[1] known variables that were in our field of view, with about 39 of the unrecovered 48 stars lying in the crowded central region (see Table 4.3). This was expected given the limits of the resolution as can be seen in Fig. 5.4, which shows that the number of detected variables per surface area drops sharply in the crowded central region. The limited resolution was also evident when plotting these stars' positions on the CMD, where they display positions typical of that of most other stars inside the half-light radius (see Fig. 5.2) due to the overlap of their PSF, affecting the photometry.

The value of extended observations is also evident in the discovery of 16 unpublished LPVs in the cluster, most of which have long periods; the median period for the new variables is about 250 days. Thus they would have been difficult to detect and characterize in earlier variability surveys with shorter time baselines (e.g. Silberman et al. (1994), Pritzl et al. (2002)). Further evidence of this is the fact that six of the discovered variables were not identified by Cardona (2011), who used a smaller two-year subset of our own data set. It was found that our

[1] Number takes into account the duplication of V1 and V2 as V95 and V96, respectively, as detailed in chapter 5 and below.

classifications and periods sometimes differed from Cardona's (2011). This was expected given the larger number of cycles we observed over six years relative to his two. The LPVs that differed were either semi-regulars or irregulars that display some periodicity, and as such cycle-to-cycle variation would mean that a shorter observational timeline would not be sufficient to observe enough cycles to notice the variation between them.

We have determined that 13 new LPVs were cluster members with good confidence given their position on or close to the RGB (see Fig. 5.42), and of the remaining three, one lies within the half-light radius and thus is a probable cluster member (see Table 5.3). We also reported the locations and possible periods of 22 suspected variables that may exist in the cluster, but which require additional observations at higher flux and spatial resolution to confirm or deny their variability. The suspected variables were classified as such due to the lower certainty of their true variability as determined by their light curves, which typically had lower signal-to-noise ratios. This low SNR is possibly due to our observations being hampered by the variables' low variability amplitude, or due to being merged with a neighboring star and thus affecting the flux difference photometry. A good portion of the suspected variables lies on the RGB (see Fig. 5.42 for their locations relative to the new variables).

We have also classified and determined periods of known LPVs that lacked them: 15 stars had their periods determined for the first time, three were classified as semi-regular rather than irregular, and one star (V3) that was previously classified as a Mira was found to be a semi-regular. We have also discovered two duplication errors in the published literature (Skottfelt et al., 2015): V95 is the same star as V1, and similarly V96 is V2, the evidence for which was detailed in their respective pages in section 5.4.

We have found that using PDM was adequate for determining the primary period of the variable star, but that it could not find secondary periods for most of the LPVs displaying multi-periodicity. It is recommended that future work apply Fourier analysis, or some other form of mathematical algorithm specialized for signal analysis, to better determine the periods.

Having obtained periods for LPVs hitherto without ones, or improved upon them (see Tables 4.1, 4.2 and 5.3), we were able to fit an improved LPV Period-Luminosity (PL) relation for the NGC 6388 cluster. The PL relation typically takes the general form:

$$I = a + b * \log(P)$$

where *I* is the magnitude (which can be thought of as the log of the luminosity), in our case the apparent I magnitude (the relation is present across the spectrum and thus can be derived for other filter pass-bands), and *P* is the period in days, with *a* and *b* being the intercept and slope of the fitted line. The PL relation for LPVs can be useful to determine distances, a possibility first noted specifically for Mira-type LPVs by Glass and Lloyd Evans (1981). Although other distance indicators exist, the LPV PL relation can provide another rung on the cosmic distance ladder, or as a way to constrain other distance estimates. LPVs are plentiful (Tabur et al., 2010), especially in old or intermediate-age populations (Whitelock et al., 2008), and luminous, as they are on the RGB/AGB part of the CMD (or the HR for field stars). The PL relation is also useful for probing LPV behavior, as it provide tests for theoretical predictions of luminosity and periodic pulsational behavior, and how they relate to the effects of the metallicity and the general evolutionary history of the stellar population in which the LPVs were formed.

Our PL plot is shown in Fig. 6.1. Data points represent LPV star I magnitudes and periods previously published in the literature, which exist for only six stars, and our own measurements for 34 stars. To estimate the PL relation, line fits were done for both sets of data:

all of the literature values, and a 14 star subset of our own data values. The stars selected for the fit were those on the RGB, as defined in section 5.1.1, and as shown in Fig. 5.3 and Fig. 5.42 for known and new variables, respectively. This was done to avoid using photometry affected by the LPV overlapping with neighboring stars, which was shown to occur in the crowded region in section 5.1.1. The fit parameters were found to be a =13.62 and b = −0.69 for the literature data, and a = 12.45 and b = −0.03 for our own.

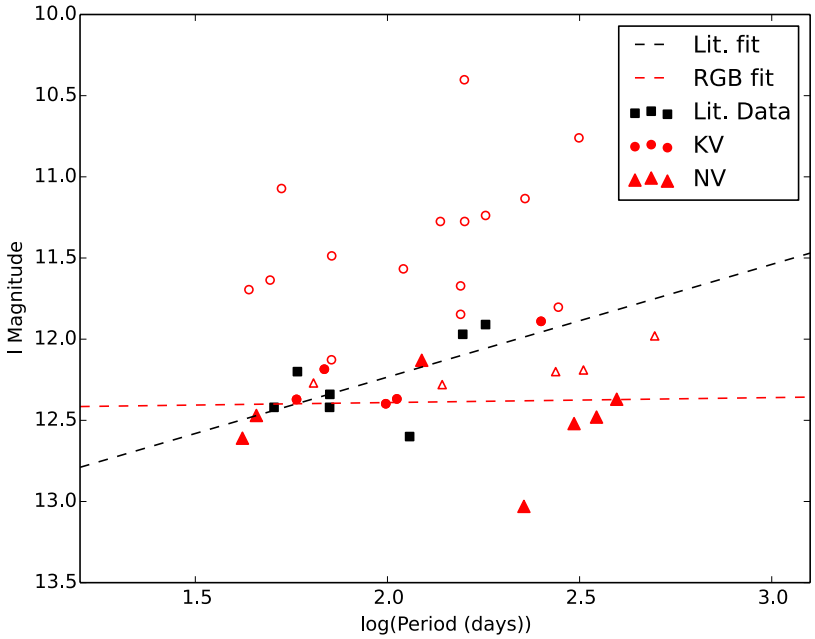

Figure 6.1: Our period-luminosity plot in the I-band. Black squares for previous literature I and P values, red circles and triangles from our data. Red circles and triangles represent known and new LPVs, respectively. Black and red line fits from all literature data (Clement Catalogue, 2015) and a subset of our data. Subset only include I, P of RGB stars as represented by the filled red markers, while open red markers are ignored.

It can be seen that our PL relation has a lower slope; it is nearly flat, which is possibly due to the larger proportion of semi-regular and irregular LPVs with long secondary periods (LSP) in our data relative to the literature. The LPVs in the literature that have a determined period and a measured I magnitude (our criteria for inclusion in the plot) have undergone a

selection effect; it is only those particular LPVs that are regular enough, and with short enough periods, that are detected and their periodicity determined by previous studies, which all had shorter time baselines and thus could not get periods for the semi-regular and irregular LPVs we have characterized, some of which were unknown possibly due to their long periods.

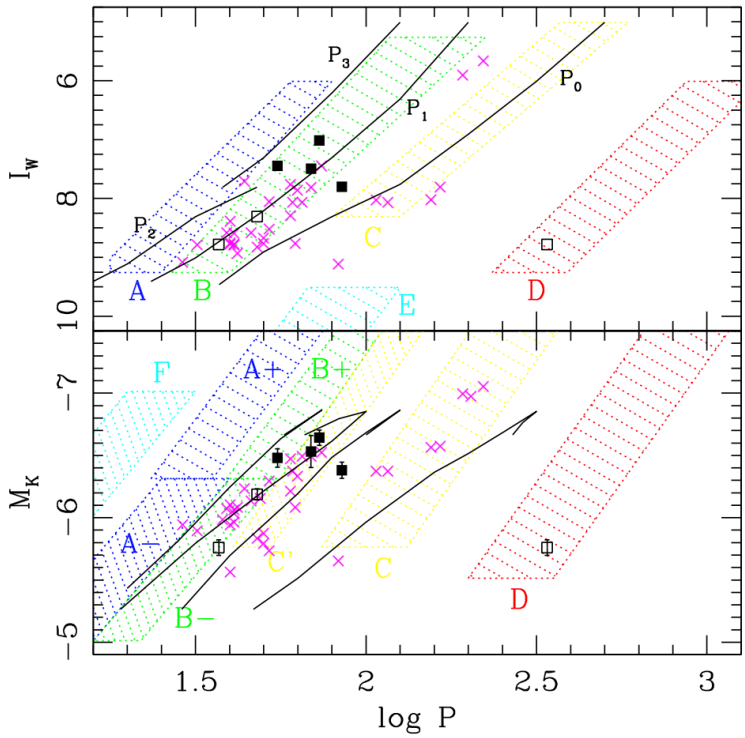

Figure 6.2: Period-luminosity plots sourced from Abbas et al. (2015) in the I and K bands for multiple stellar populations: squares for GC NGC 6496, crosses for GC 47 Tuc, Hatched regions represent LPV pulsational sequences in the LMC.

Our additions tend to have longer periods and/or display a measure of irregularity that only longer periods were detected. They therefore tend to pulsate in the first or second overtone rather than in the fundamental radial mode (Wood, 2000), and thus have different PL relations from Miras and semi-regulars without a LSP. This is illustrated in Fig. 6.2 sourced from Abbas et al. (2015), where the hatched regions each denote a different pulsational mode – or sequence – as detailed in, and sourced from, Wood (2000): Mira-type variables typical follow sequence C,

while semi-regular variables follow the B or C sequence. Thus LPVs have different PL relations as determined by the mode of pulsation. This horizontal spread is also evident in the population of cluster 47 Tuc, represented as crosses in Fig. 6.2. In future work, we will apply a Fourier analysis program to further seek the multiple periods in each star's light curve – in particular, the method will allow us to detect multiple periods in the data, including multiple pulsation periods (simultaneous modes) and LSP(s). We have detected the Long Secondary Period (LSP) as the primary period of the SR/IRR LPVs instead of the shorter pulsational period[1]. This was possibly due to the pulsational period's irregularity/non-uniformity making it difficult to detect using PDM.

Given the aforementioned, and the polluted color-magnitude data of the stars in the core region, a new plot was done (shown in Fig. 6.3) that includes the best available data: I-magnitudes are preferably taken from the literature where possible, and thus solely from Skottfelt et al. (2015) work in the core region due to their superior resolution in that part of the cluster, and periods are preferably from our own work due to our longer time baseline and higher cadence. The obverse is done when an LPV lacks a literature I-magnitude, or when we lack a period for a known LPV. For new LPVs not in the literature, only our data is used.

A new linear fit is also attempted. Given the cut-off of the D-sequence being at roughly log(P) ~ 2.4 in Fig. 6.2, we have filtered out stars with longer periods, thus roughly those with periods greater than 250 days, to avoid the inclusion of stars with detected LSP's along with those whose pulsational periods are known. Stars not on the RGB are also not included in the fit, to assure only the inclusion of cluster members and/or I-magnitude values that would be

[1] An explicit definition could not be found in the literature, but the term appears to designate the period of short, sub-LSP scale pulsations. They are evidenced by the local peak/trough pairs that appear in a light curve on a shorter scale (~30-50 days) than the detected LSP (~250-350 days).

expected of a cluster member. The new linear fit, represented as the solid line in Fig. 6.3, has intercept a = 12.97, slope b = −0.24, and is thus trending upwards; the longer the period, the more luminous the star. This tendency is consistent with that noted by Wood (2000), and the stars of 47 Tuc (see Fig. 6.2) though our PL relation still mixes stars in NGC 6388 pulsating in different modes, an issue that can only be addressed when Fourier analysis is applied to our light curves.

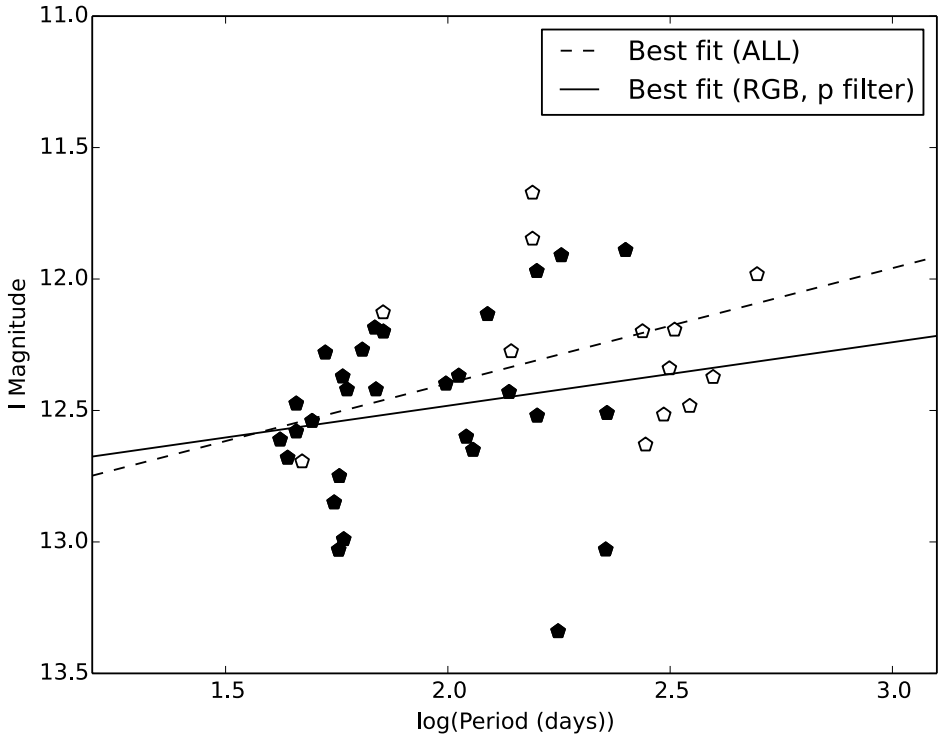

Figure 6.3: PL plot from the best data as described in the main text. Empty, filled markers fitted with dashed, solid lines respectively. Filled markers represent stars that are on the RGB in published literature or our work and whose log(P) < 2.4

In our work, we have defined a variability index to filter out false-positives from the detected variability sources, and it was found to be useful given that the region being searched already has known variables present in it for comparison. It cannot be used when investigating

areas with no known variability sources to calibrate it. It was found to be beneficial, having narrowed the multiple detections returned by ISIS to a smaller, manageable subset.

It was noted in classifying the known and newly discovered variables that the classical definition of irregular and semi-regular LPVs needs to be modified. In our work on multiple known LPVs, some previous classifications were found to be incorrect, or assigned to a star that could defined as either semi-regular or irregular; the semi-regular to irregular LPV transition is continuous, and thus the definition's requirement for regularity is too subjective for work on such a spectrum, and only those at the extremes can be classified with confidence. A bias was also observed in how certain semi-regulars' true regularity can only be observed in more than 3 cycles e.g. V108, which was observed sufficiently by Skottfelt et al. to determine a period, yet no period was reported in the work due to the cycle-to-cycle variation. The opposite is also true, where a previously Mira-classified LPV, V3, was found to be a semi-regular variable with considerable cycle variation. The bias appears to occur in SR LPVs that display a slow variation between sequential pulsational cycles, causing them to appear to more regular than they truly are when observed for a small number of cycles, and in IRR LPVs that display regularity that is only evident across multiple pulsational cycles due to the LSP.

In tackling this problem, we have also defined the regularity index as a way to quantify the regularity of LPVs on a continuous scale. The algorithm did give insight into the classification of long-known LPVs in the Mira-SR portion of the regularity spectrum, and helped underline what were once subjective "judgment calls" based on the light curve shape. That said, it was noted during the classification of new variables that the regularity index calculation algorithm has a shortcoming in accounting for stars that exhibit such irregularity that they cannot form any coherent folded light curve. It is possible if a star is very irregular, or the signal-to-

noise ratio so low, that even the best period detected would generate a curve with such variation that the standard deviation approaches the value of the flux difference range which, according to our definition, would give a very low index value (see Fig. 5.43). That value can approach the range of that of known Mira-type LPVs.

It is our opinion that the technique is promising, and could be useful with further testing. Perhaps if a longer and more mathematically rigorous analysis is undertaken, possibly with the use of synthetic light curve data generated to quantify the effects of measurement accuracy and precision, and intrinsic irregularity and multi-periodicity on the values of the regularity index produced.

In our study, we have identified stars all along the LPV spectrum using a relatively modest aperture telescope, and at a cadence of about 2-3 weeks between observations. This would indicate that the future full sky survey program planned for the Large Synoptic Survey Telescope (LSST) is expected to produce a wealth of high-quality, high-cadence data for LPVs, given the image scale is twice as fine (~0.3 arcsec/pixel) as our own (0.59 arcsec/pixel), and the program's ten-year time baseline (Zinn et al., 2017) is longer than our own six-year baseline. This further underlines the need for a more quantitative definition for semi-regular and irregular LPV behavior.

REFERENCES

Abbas, Mohamad A., Andrew C. Layden, Katherine A. Guldenschuh, D. E. Reichart, K. M. Ivarsen, J. B. Haislip, M. C. Nysewander, A. P. LaCluyze, and Douglas L. Welch. 2015. "Variable Stars in Metal-Rich Globular Clusters. IV. Long-Period Variables in NGC 6496." *The Astronomical Journal* 149 (2): 40. doi:10.1088/0004-6256/149/2/40.

Alard, C. 2000. "Image Subtraction Using a Space-Varying Kernel." *Astronomy and Astrophysics Supplement Series* 144 (June): 363–70. doi:10.1051/aas:2000214.

———. 2016. "ISIS IMAGE SUBTRACTION PACKAGE." *ISIS Tutorial: Photometry and Light Curves*. Accessed March 1. http://www2.iap.fr/users/alard/page5.html.

Alard, C., and Robert H. Lupton. 1998. "A Method for Optimal Image Subtraction." *The Astrophysical Journal* 503 (August): 325–31. doi:10.1086/305984.

Beaulieu, J.-P., W. J. de Wit, H. J. G. L. M. Lamers, J.-B. Marquette, C. Coutures, P. Leisy, S. Totor, et al. 2001. "Blue Irregular Variable Stars in the Small Magellanic Cloud from EROS2: Herbig Ae/Be or Classical Be Stars?" *Astronomy and Astrophysics* 380 (December): 168–76. doi:10.1051/0004-6361:20011313.

Bland-Hawthorn, Jonathan, Patrick L. Shopbell, and David F. Malin. 1993. "Deep Sky Surveys: A Motivation for Stacking Digitized Photographic Plates." *The Astronomical Journal* 106 (November): 2154–60. doi:10.1086/116792.

Cardona Velasquez, Gustavo Adolfo. 2011. "Properties of Bright Variable Stars in Unusual Metal Rich Cluster NGC 6388." Bowling Green State University. https://etd.ohiolink.edu/pg_10?21059774820460::NO:10:P10_ETD_SUBID:49761.

Clement, Christine M., Adam Muzzin, Quentin Dufton, Thivya Ponnampalam, John Wang, Jay Burford, Alan Richardson, Tara Rosebery, Jason Rowe, and Helen Sawyer Hogg. 2001. "Variable Stars in Galactic Globular Clusters." *The Astronomical Journal* 122 (November): 2587–99. doi:10.1086/323719.

Cmglee. Anonymous web graphic artist. *English: Visual Comparison of Convolution, Cross-Correlation and Autocorrelation.* Own work. https://commons.wikimedia.org/wiki/File:Comparison_convolution_correlation.svg.

Corwin, T. Michael, Andrew N. Sumerel, Barton J. Pritzl, Horace A. Smith, M. Catelan, Allen V. Sweigart, and Peter B. Stetson. 2006. "Image-Subtraction Photometry of Variable Stars in the Globular Clusters NGC 6388 and NGC 6441." *The Astronomical Journal* 132 (September): 1014–22. doi:10.1086/505745.

Feast, M. W. 1972. "Red Variables in Globular Clusters, in the Galactic Centre and in the Solar Neighbourhood." *Quarterly Journal of the Royal Astronomical Society* 13 (June): 191.

"General Catalog of Variable Stars (GCVS Database, Version 2012Apr)." n.d.

Harris, William E. 1996. "A Catalog of Parameters for Globular Clusters in the Milky Way." *The Astronomical Journal* 112 (October): 1487. doi:10.1086/118116.

Glass, I. S., and T. Lloyd Evans. "A Period–luminosity Relation for Mira Variables in the Large Magellanic Cloud." *Nature* 291, no. 5813 (May 28, 1981): 303–4. doi:10.1038/291303a0.

Hazen, Martha L., and Betty Hinsdale Hesser. 1986. "The Variable Stars in the Globular Cluster NGC 6388." *The Astronomical Journal* 92 (November): 1094–99. doi:10.1086/114239.

King, Ivan. 1962. "The Structure of Star Clusters. I. an Empirical Density Law." *The Astronomical Journal* 67 (October): 471. doi:10.1086/108756.

King, Ivan R. 1966. "The Structure of Star Clusters. III. Some Simple Dynamical Models." *The Astronomical Journal* 71 (February): 64. doi:10.1086/109857.

Lanzoni, B., E. Dalessandro, F. R. Ferraro, P. Miocchi, E. Valenti, and R. T. Rood. 2007. "The Surface Density Profile of NGC 6388: A Good Candidate for Harboring an Intermediate-Mass Black Hole." *The Astrophysical Journal Letters* 668 (October): L139–42. doi:10.1086/522927.

Lanzoni, B., A. Mucciarelli, L. Origlia, M. Bellazzini, F. R. Ferraro, E. Valenti, P. Miocchi, E. Dalessandro, C. Pallanca, and D. Massari. 2013. "The Velocity Dispersion Profile of NGC 6388 from Resolved-Star Spectroscopy: No Evidence of a Central Cusp and New Constraints on the Black Hole Mass." *The Astrophysical Journal* 769 (June): 107. doi:10.1088/0004-637X/769/2/107.

Lebzelter, T., and P. R. Wood. 2005. "Long Period Variables in 47 Tuc: Direct Evidence for Lost Mass." *Astronomy and Astrophysics* 441 (October): 1117–27. doi:10.1051/0004-6361:20053464.

———. 2007. "The AGB Stars of the Intermediate-Age LMC Cluster NGC 1846. Variability and Age Determination." *Astronomy and Astrophysics* 475 (November): 643–50. doi:10.1051/0004-6361:20078395.

Lloyd Evans, T., and J. W. Menzies. 1973. "Red Variables Stars in Metal Rich Globular Clusters." In , 36:151. doi:10.1007/978-94-010-2590-4_23.

———. 1977. "Near Infrared Photometry of Globular Clusters. III - The Metal-Rich Clusters." *Monthly Notices of the Royal Astronomical Society* 178 (January): 163–93. doi:10.1093/mnras/178.2.163.

Matsunaga, N., and IRSF/SIRIUS Team. 2007. "The Period--Luminosity Relation of Mira Variables in NGC 6388 and NGC 6441." In , 378:86. eprint: arXiv:astro-ph/0610816. http://adsabs.harvard.edu/abs/2007ASPC..378...86M.

Mattei, Janet Akyuz. 1997. “Introducing Mira Variables.” *Journal of the American Association of Variable Star Observers (JAAVSO)* 25: 57–62.

Mink, Jessica. 2017. “WCSTools Sky World Coordinate Systems.” Accessed March 3. http://tdc-www.harvard.edu/wcstools/wcstools.wcs.html.

Monet, D. G. 1998. “The 526,280,881 Objects In The USNO-A2.0 Catalog.” In , 193:120.03. http://adsabs.harvard.edu/abs/1998AAS...19312003M.

Ostlie, Dale A., and Bradley W. Carroll. 1995. *An Introduction to Modern Stellar Astrophysics*. 1st edition. Reading, Mass: Benjamin Cummings.

Otero, Sebastián, Christopher Watson, and Patrick Wils. 2013. “VARIABLE STAR TYPE DESIGNATIONS IN VSX.” AAVSO. https://www.aavso.org/vsx/help/VariableStarTypeDesignationsInVSX.pdf.

Percy, John R., Joseph B. Wilson, and Gregory W. Henry. 2001. “Long-Term VRI Photometry of Small-Amplitude Red Variables. I. Light Curves and Periods.” *Publications of the Astronomical Society of the Pacific* 113 (786): 983–96. doi:10.1086/322153.

Pritzl, Barton J., Horace A. Smith, Márcio Catelan, and Allen V. Sweigart. 2002. “Variable Stars in the Unusual, Metal-Rich Globular Cluster NGC 6388.” *The Astronomical Journal* 124 (August): 949–76. doi:10.1086/341381.

Reichart, D., M. Nysewander, J. Moran, J. Bartelme, M. Bayliss, A. Foster, J. C. Clemens, et al. 2005. “PROMPT: Panchromatic Robotic Optical Monitoring and Polarimetry Telescopes.” *Nuovo Cimento C Geophysics Space Physics C* 28 (July): 767. doi:10.1393/ncc/i2005-10149-6.

Samus, N. N., E. V. Kazarovets, E. N. Pastukhova, T. M. Tsvetkova, and O. V. Durlevich. 2009. “A Catalog of Accurate Equatorial Coordinates for Variable Stars in Globular Clusters.” *Publications of the Astronomical Society of the Pacific* 121 (886): 1378–85. doi:10.1086/649432.

Shapley, Harlow, and Henrietta H. Swope. 1940. “Variable Stars in Low Galactic Latitudes.” *Annals of Harvard College Observatory* 90: 177–88.

Silbermann, N. A., Horace A. Smith, Michael Bolte, and Martha L. Hazen. 1994. “RR Lyrae Stars and Color-Magnitude Diagram of the Globular Cluster NGC 6388.” *The Astronomical Journal* 107 (May): 1764–72. doi:10.1086/116984.

Skottfelt, J., D. M. Bramich, R. Figuera Jaimes, U. G. Jørgensen, N. Kains, A. Arellano Ferro, K. A. Alsubai, et al. 2015. “Searching for Variable Stars in the Cores of Five Metal-Rich Globular Clusters Using EMCCD Observations.” *Astronomy and Astrophysics* 573 (January): A103. doi:10.1051/0004-6361/201424967.

Sloan, G. C., N. Matsunaga, M. Matsuura, A. A. Zijlstra, K. E. Kraemer, P. R. Wood, J. Nieusma, J. Bernard-Salas, D. Devost, and J. R. Houck. 2010. "Spitzer Spectroscopy of Mass-Loss and Dust Production by Evolved Stars in Globular Clusters." *The Astrophysical Journal* 719 (August): 1274–92. doi:10.1088/0004-637X/719/2/1274.

Stellingwerf, R. F. 1978. "Period Determination Using Phase Dispersion Minimization." *The Astrophysical Journal* 224 (September): 953–60. doi:10.1086/156444.

Sterken, C, and C Jaschek. 1996. *Light Curves of Variable Stars a Pictorial Atlas*. Cambridge: Cambridge University Press.

Stetson, Peter B. 1996. "On the Automatic Determination of Light-Curve Parameters for Cepheid Variables." *Publications of the Astronomical Society of the Pacific* 108 (October): 851. doi:10.1086/133808.

Tabur, V., T. R. Bedding, L. L. Kiss, T. Giles, A. Derekas, and T. T. Moon. 2010. "Period–luminosity Relations of Pulsating M Giants in the Solar Neighbourhood and the Magellanic Clouds." *Monthly Notices of the Royal Astronomical Society* 409 (2): 777–88. doi:10.1111/j.1365-2966.2010.17341.x.

Trager, S. C., Ivan R. King, and S. Djorgovski. 1995. "Catalogue of Galactic Globular-Cluster Surface-Brightness Profiles." *The Astronomical Journal* 109 (January): 218–41. doi:10.1086/117268.

Whitelock, Patricia A., Michael W. Feast, and Floor Van Leeuwen. 2008. "AGB Variables and the Mira Period-Luminosity Relation." *Monthly Notices of the Royal Astronomical Society* 386 (May): 313–23. doi:10.1111/j.1365-2966.2008.13032.x.

Wood, P. R. 2000. "Variable Red Giants in the LMC: Pulsating Stars and Binaries?" *Publications of the Astronomical Society of Australia* 17 (April): 18–21. doi:10.1071/AS00018.

Wood, P. R., C. Alcock, R. A. Allsman, D. Alves, T. S. Axelrod, A. C. Becker, D. P. Bennett, et al. 1999a. "MACHO Observations of LMC Red Giants: Mira and Semi-Regular Pulsators, and Contact and Semi-Detached Binaries." In , 191:151. http://adsabs.harvard.edu/abs/1999IAUS..191..151W.

———. 1999b. "MACHO Observations of LMC Red Giants: Mira and Semi-Regular Pulsators, and Contact and Semi-Detached Binaries." In , 191:151. http://adsabs.harvard.edu/abs/1999IAUS..191..151W.

Zinn, J. C., C. S. Kochanek, S. Kozłowski, A. Udalski, M. K. Szymański, I. Soszyński, Ł. Wyrzykowski, et al. 2017. "Variable Classification in the LSST Era: Exploring a Model for Quasi-Periodic Light Curves." *Monthly Notices of the Royal Astronomical Society* 468 (June): 2189–2205. doi:10.1093/mnras/stx586.